Department of Mechanical Engineering
University of Oulu

OULUN YLIOPISTO
UNIVERSITY of OULU

Proceedings of the 11th Finnish Mechanics Days
XI Suomen Mekaniikkapäivät

Oulun yliopisto
29.-30. marraskuuta 2012

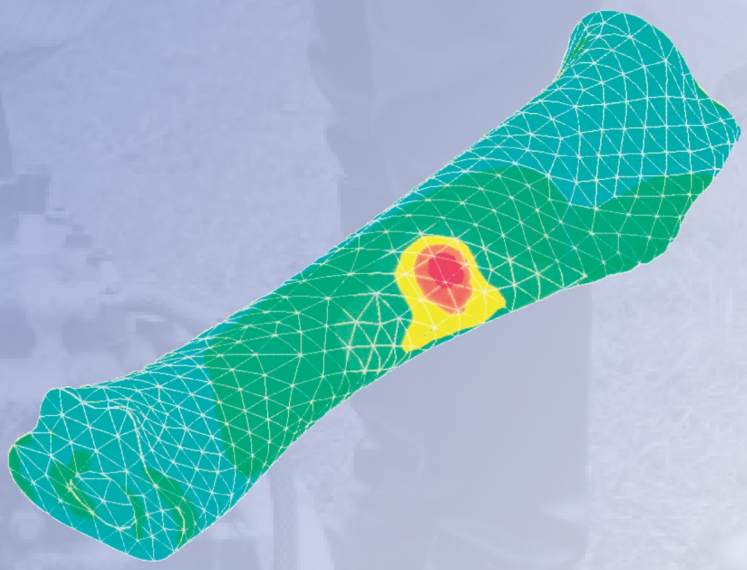

Toimittajat

Hannu Koivurova
Mikko Malaska

Proceedings of the 11th Finnish Mechanics Days
XI Suomen Mekaniikkapäivät

Oulun yliopisto
29. – 30. Marraskuuta 2012

Toimittajat
Hannu Koivurova
Mikko Malaska

University of Oulu
Department of Mechanical Engineering
P.O. Box 4200
FI-90014 University of Oulu
FINLAND

Phone +358 294 482020
Fax +358 8 553 2026
http://me.oulu.fi

ISBN 978-952-62-0006-4

FOREWORD

The 11th Finnish Mechanics Days were held in the University of Oulu, Finland, on 29-30 November 2012. The objective of the conference is to stimulate and promote research and applications within the area of solid mechanics, fluid mechanics and mathematical problems related to mechanics. The conference provides a forum for researchers, designers, teachers and other professionals to network, discuss and share ideas and information.

The first Mechanics Days were held in Oulu 20 years ago, in 1982. The conference has been organized every three years since then.

We are pleased to present these proceedings, which are the record of the contributions by the invited speakers and 36 other presentations. The invited presentations were given by Professor Ivan Argatov, University of Oulu, D.Sc. Roger Rabb, Wärtsilä Finland Oy and Professor Matti Ristinmaa, University of Lund.

We want to thank all of those who provided manuscripts for publication in these proceedings. We also want to give a special thanks to all participants and speakers, the scientific committee and the local organizers for their valuable contributions to the success of the conference.

Mikko Malaska
Hannu Koivurova

Oulu, 2012
On behalf of the organizing committee

SISÄLLYS

Structural Mechanics

Fatique

Failure Mechanics

Applications

Dynamic indentation testing of biological tissues: a mathematical modelling approach

Ivan Argatov

University of Oulu
Department of Mechanical Engineering
PO Box 4100, 90014 University of Oulu

Summary. In recent years, a number of experimental studies have been conducted to investigate the mechanical behaviour, damage mechanisms, and viability of biological materials, like articular cartilage, under quasi-static, dynamic, and impact loading using indentation technique. While well-developed quasi-static indentation methods are suitable for testing in many industrial applications, an enhanced indentation technique is needed for measuring time-dependent material properties of biological tissues by taking into account dynamic effects. At present, there is the need of simple mathematical models, which allow comparing experimental results obtained in dynamic indentation testing with different parameters of indentation protocols.

A variety of sophisticated mathematical models were suggested to describe the stress-strain response of articular cartilage that represents a multiphasic, structurally complex material possessing time-dependent properties. A significant increase of mathematical complexity results in the fact that the mathematical formulation of the corresponding indentation problems turns out to be so complicated that it is often impossible to solve them by analytical methods. At the same time, numerical methods frequently become useless in identifying the essential properties of the studied mathematical model of a biological tissue based on scarce data of indentation tests. To capture the main features of the in vivo indentation tests recently suggested for assessing articular cartilage viability, we explore viscoelastic models. In the present talk, based on the recently developed mathematical models for dynamic indentation, a review and comparison among previous experimental studies on indentation testing of articular cartilage are performed.

Todennäköisyysteoriaan pohjautuva väsymis-analyysi

Roger Rabb

Tiivistelmä. Teollisuutemme kilpailukyvyn ylläpitäminen ja kehittäminen edellyttää jatkuvaa panostusta koneiden ja laitteiden turvallisuuden ja luotettavuuden parantamiseen. Väsymis-analyysin hyvä hallinta nousee tässä pyrkimyksessä keskeiseen asemaan. Jännitykset pystytään nykyään laskemaan kohtalaisen hyvin, mutta materiaalien väsymislujuuteen ja laskenta-kriteereihin liittyvät kysymykset muodostavat usein varsinaisen pullonkaulan. Eräs syy tähän on tietysti se, että väsymisanalyysin kehittäminen vaatii kalliita väsytystestejä ja tiukan budjetti-kurin aikana on yrityksiä usein vaikeaa saada panostamaan tällaiseen pitkäjänteiseen kehitys-työhön. Väsymisilmiön satunnaisluonteen ymmärtäminen on välttämätön edellytys tarkkojen väsymiskriteerien kehittämiseksi testien avulla. Wärtsilä on viime vuosikymmenien aikana suorittanut TkT Rabbin johdolla runsaasti väsymiseen liittyvää testausta ja kehitystyötä. Työn tulokset on arvioitu niin tärkeiksi, että Wärtsilä on tehnyt harvinaisen päätöksen saattaa nämä tutkimustulokset opetuksen ja muun teollisuuden käyttöön kirjan muodossa.

Avainsanat: Väsyminen, väsytystestaus, spektritesti, ainevikajakauma, murtumismekaniikka

Esitys on julkaistu *Rakenteiden mekaniikka lehdessä*: Vol. 45, 2012, Nro 3.

Description of Electroelasticity and its Related Forward and Inverse Motion Problems

Matti Ristinmaa[1], Anna Ask[1], Sara Thylander[1], Andreas Menzel[1,2] and Ralf Denzer[2]

Summary. Electroactive polymers (EAP) deform under electric fields and an advantage of EAP is that they may undergo deformations much larger than those capable by electroactive ceramics, however at comparatively much lower forces. As common for polymers, EAP exhibit time-dependent material behavior, i.e. an electro-viscoelastic effect. Modeling of this behavior is discussed. The forward motion problem follows from the solution of balance of linear momentum and balance equations for the electromagnetic fields, providing the shape and state of the deformed configuration. In the inverse motion problem the deformed state of an elastic body for a given set of loads and boundary conditions is specified and the undeformed configuration is found by solving the resulting boundary value problem, e.g. with the finite element method.

Key words: electro-viscoelasticity, forward motion, inverse motion.

Introduction

Electrostriction is the term used to describe an electrically activated deformation which is proportional to the square of the electric polarization in a dielectric material. In some dielectric elastomers this effect gives rise to deformations which are noticeable also on a macroscopic scale. The typical configuration is a capacitor set-up, with an elastomer film sandwiched between two highly compliant electrodes, and variants of this configuration such as stack actuators or spring-roll actuators.

Electromagnetic fields give rise to forces and torques on polarizable media and the usual balance equations of continuum mechanics must be altered accordingly. The theoretical framework necessary is well established, see e.g. [4]. Works on the numerical treatment of boundary value problems for electroactive elastomers are found e.g. in [7] and constitutive models for electro-viscoelasticity are found in [1, 2, 6].

The inverse motion problem used in a numerical setting for elastic bodies was introduced by Govindjee and Mihalic [3], later this was interpreted in the more general framework of configurational mechanics by Steinmann et al. [5]. In this work, the inverse motion problem for electroelastostatics is considered. By means of the finite element model, representative boundary value problems are then solved.

Numerical examples

As a representative boundary value problem, an electroactive gripper is shown in Fig. 1. The specific material model and material parameters used can be found in [1, 2]. In the loaded state, the gripper is supposed to have a circular shape and the undeformed configuration is calculated. The gripper consists of twelve identical arms. An electric

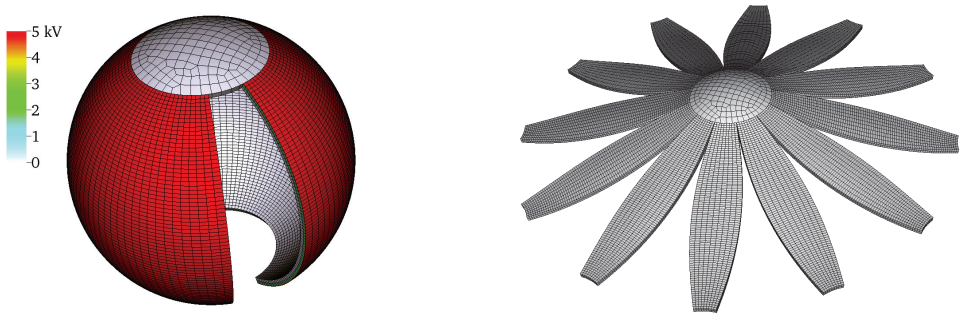

Figure 1. Left: Desired loaded and deformed configuration for the gripper with one arm excluded. Right: Undeformed and unloaded configuration.

potential difference is applied over half of the thickness, inducing bending deformation. In the loaded state, the potential difference is 5 kV. In Fig. 1, left figure, one of the arms is excluded for visualisation purposes.

References

[1] Ask, A., Menzel, A. and Ristinmaa, M., Phenomenological modeling of viscous electrostrictive polymers. *Int. J. Nonlinear Mech.* 47:156–165, 2012.

[2] Ask, A., Menzel, A. and Ristinmaa, M. Electrostriction in electro-viscoelastic polymers. *Mech. Mater.* 50:9–21, 2012.

[3] Govindjee, S. and Mihalic, P.A., Computational methods for inverse deformations in quasi-incompressible finite elasticity. *Int. J. Numer. Meth. Eng.* 43:821–838, 1998.

[4] Ogden, R.W. and Steigmann D.J. (Eds.). *Mechanics and Electrodynamics of Magneto- and Electro-Elastic Materials.* CISM Course and Lectures, Springer, 2011.

[5] Steinmann, P., Scherer, M. and Denzer, R., Secret and joy of configurational mechanics: From foundations in continuum mechanics to applications in computational mechanics. *Z. Angew. Math. Mech.* 89:614–630, 2009.

[6] Thylander S., Menzel A., and Ristinmaa, M., An electromechanically coupled microsphere framework: Application to the finite element analysis of electrostrictive polymers. *Smart Mater. and Struct.*, 21, 094008, 2012

[7] Vu, D.K. and Steinmann, P., Nonlinear electro- and magneto-elastostatics: Material- and spatial settings. *Int. J. Solids Struct.* 44:7891–7905, 2007.

Affiliation 1
Division of Solid Mechchanics, Lund University, P.O. 118, SE-2210 00 Lund, Sweden
`matti.ristinmaa@solid.lth.se, anna.ask@solid.lth.se, sara.thylander@solid.lth.se`

Affiliation 2
Institute of Mechanics, Department of Mechanical Engineering, TU Dortmund, Leonhard-Euler-Str. 5, D-442-27 Dortmund, Germany
`andreas.menzel@tu-dortmund.de, ralf.denzer@tu-dortmund.de`

Saint-Venant's torsion in intrinsic coordinates

Jukka Aalto, Juha Paavola and Eero-Matti Salonen

Aalto University, School of Engineering
Department of Civil and Structural Engineering
PO Box 12100, 00076 Aalto

Abstract. Saint-Venant's torsion is considered in the so-called intrinsic coordinates. Warping function formulation is applied. In connection with thin-walled open cross-sections some inconsistencies are discussed. Certain general relations are derived for a rather general geometry. A weak form suitable for solution by the finite element method is presented. Numerical examples using linear triangular finite elements are finally worked out to demonstrate the efficiency of the new formulation.

Keywords: Saint-Venant torsion, intrinsic coordinates, thin-walled open section, weak form

Esitys on julkaistu *Rakenteiden mekaniikka lehdessä*: Vol. 45, 2012, Nro 3.

Prediction of the Transient Effects in Glassy Polymers

Sami Holopainen

Summary. The objective of this work is to model the mechanical behavior of glassy polymers during non-monotonic loadings involving softening/hardening characteristics, transient effects and necking instabilities. The microstructure of a glassy polymer has a strong influence on the mechanical properties and it is typically described by network models. The most popular approach is the 8-chain version of the Boyce-Parks-Argon (BPA) model. The BPA model is able to capture the monotonic loading well, but for transient effects and long-term behavior, its response is found to deviate significantly from the experimental data. In order to improve the predictions under these conditions, an extension of the BPA model is proposed in this work. The numerical treatment of the proposed model associated with both the ODE-solver and finite element method is discussed. The model is calibrated to the experimental data for various states of deformation. The numerical results indicated that the proposed model is able to predict experimental response under long-term and repeated loadings well.

Key words: Polymers, transient effects, intrinsic material properties, numerical treatment

Introduction

The mechanical properties of amorphous glassy polymers are to a large extent dictated by their chemical composition and microstructure. In amorphous polymers, microstructure is disordered and formed of long polymer chains. The mechanical behavior is characterized by initial yielding and subsequent strain softening, followed by strain hardening due to the reorientation of polymer chains, cf. Argon (1973). Experiments on amorphous glassy polymers also show strong transient effects involving creep/recovery (termed dwell) and nonlinear response during unloading/reloading, cf. Dreistadt *et al.* (2009).

According to the experiments, the micro-structure of a polymer has a strong influence on the mechanical properties. In constitutive models for amorphous polymers, the microstructure is usually represented by an overall chain network which consists of an assembly of individual chains arranged in cubic cells, cf. Fig. 1(a). A successful and maybe most widespread model for glassy polymers was proposed by Arruda and Boyce (1991) (will here be termed the BPA model). The BPA model is able to satisfactorily predict the mechanical behavior of amorphous polymers also in large three-dimensional deformations. Furthermore, the model includes a moderate number of material parameters (10 pcs.) which is of a great importance in practical applications.

Since the initial response of amorphous glassy polymers can be considered nearly elastic, most of state-of-the-art models are based on a linear elastic constitutive assumption. However, such models are not able to satisfactorily reproduce transient effects during non-monotonic loading, which shortcomings are primarily a consequence of neglected viscoelastic effects, cf. Hasan and Boyce (1995). Moreover, the models typically overestimate the long-term creep/recovery. To account for nonlinear deformation behavior in large strains, the models which include both viscoelastic and viscoplastic ingredients

need to be applied, cf. Anand and Ames (2006). In the current models, however, a large number of material parameters need to be identified or the capability of the models is addressed only in a restricted set of loading situations.

In the present paper, we will introduce an extension of the 8-chain BPA model (termed the EBPA model), which significantly improves the prediction of the mechanical response during complex loading situations compared to existing models in this field. For comparison, the predictive capability of the BPA model is evaluated. In order to evaluate the EBPA model predictions also for inhomogeneous deformation, cold drawing experiments on PC are performed and the EBPA model is implemented in a finite element program. Based on the finite element implementation of both the BPA and EBPA model, the cold drawing process of the dumbbell-shaped specimen is simulated and the numerical results are compared with the experimental data.

Extension of the BPA model

To compensate for the shortcomings of state-of-the-art models, both viscoelastic and viscoplastic ingredients are included in the EBPA model. Schematic representations of the models are given in Fig. 1. A brief review for the BPA model can be found Arruda and Boyce (1993) and Holopainen (2012). In the EBPA model, two dashpots in parallel with the nonlinear Langevin spring are used to capture isotropic hardening behavior in the material. The original and extra dashpot are modeled by the internal state variables s_1 and s_2, respectively, which give an additional increase to the shear resistance, i.e.

$$s = s_1 + s_2. \tag{1}$$

The evolution laws for s_1 and s_2 are taken as

$$\begin{aligned} \dot{s}_1 &= h_1(1 - s_1/s_{ss})\dot{\gamma}^p, \quad s_1(0) = s_0, \\ \dot{s}_2 &= h_2(1 - \mathcal{H}(s_2 - \bar{s}_2))\dot{\gamma}^p, \quad s_2(0) = 0 \end{aligned} \tag{2}$$

where s_{ss} is a constitutive parameter and $\mathcal{H}$ is the Heaviside-function which prevents an excessive hardening e.g. during cyclic loading. The threshold $\bar{s}_2$ can be found experimentally. The evolution equation $\dot{\gamma}^p$ for the plastic deformation was originally proposed by Argon (1973) and it was later extended to include the pressure effect, cf. Arruda and Boyce (1991) and Arruda and Boyce (1993). The constitutive parameters h_1 and h_2 control the approach of s_1 and s_2 to s_{ss} and $\bar{s}_2$, respectively. Since $\dot{\gamma}^p$ is positive, cf. Holopainen (2012), a glance at $(2)_2$ reveals that $\dot{s}_2$ is positive and thus, s_2 is monotonically increasing. As a consequence, the amount of isotropic hardening increases in relation to the amount of kinematic hardening. This is of major importance during relaxation simulations at low stresses, where the plastic evolution is particularly governed by the backstress.

To better capture a large strain mechanical response during non-monotonic loadings and in creep, the elastic spring in the BPA model is replaced by a simple Kelvin chain involving a viscoelastic dashpot and an elastic intermediate spring (Kelvin-Voigt element) in series with an elastic spring, cf. Fig. 1(c). The Kelvin-Voigt element is employed for predicting creep and recovery, while its combination with the elastic spring is aimed at describing the stress relaxation. For high stresses and strain rates, the viscoelastic dashpot resists elongation of the parallel spring, whereas the effect of the dashpot in low stress and strain rate levels is attenuated and the intermediate spring contributes to the total

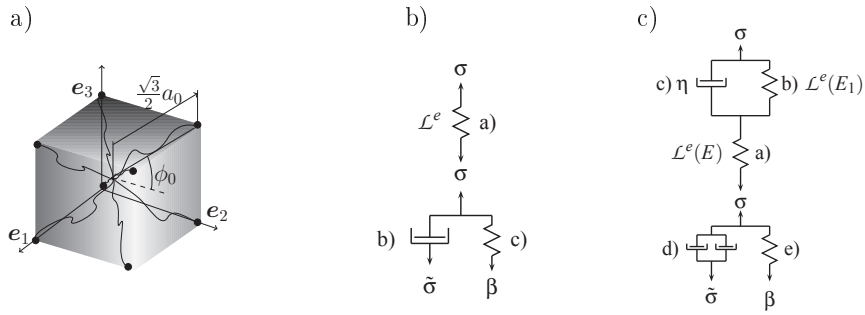

Figure 1: a) The chain geometry according to the 8-chain model. The dimension of the cell is a_0 and the orientation of a chain is determined by the angle ϕ_0. The unit vectors $\boldsymbol{e}_\alpha$, $\alpha = 1, 2, 3$, align with the principal directions of the plastic stretch. Rheological representation of b) the BPA model and c) the EBPA model. The BPA model is governed by the elements: an elastic spring a), a viscoplastic dashpot b) and a nonlinear Langevin spring c). The EBPA model is governed by the elements: two elastic springs a) and b), a viscoelastic dashpot c), two viscoplastic dashpots d) and a nonlinear Langevin spring e).

strain in the system. To improve the accuracy of the linear viscoelastic models in large multi-dimensional deformations, a multiplicative decomposition of the elastic deformation gradient $\boldsymbol{F}^e$ into a viscous and an elastic part needs to be applied, i.e. $\boldsymbol{F}^e = \boldsymbol{F}^e_1 \boldsymbol{F}^e_2$ where $\boldsymbol{F}^e_1$ and $\boldsymbol{F}^e_2$ take the elastic stretching in the spring a) and b) into account, cf. Fig. 1(c). One consequence of the viscoelasticity is that the rate form of the constitutive equation must be derived. In accordance with the BPA model, cf. Arruda and Boyce (1993), the elastic constitutive law is given by

$$\boldsymbol{\tau} = \boldsymbol{\mathcal{L}}^e(E) : \ln \boldsymbol{v}^e_1 = \eta : \frac{d}{dt}(\ln \boldsymbol{v}^e_2) + \boldsymbol{\mathcal{L}}^e(E_1) : \ln \boldsymbol{v}^e_2 \tag{3}$$

where $\boldsymbol{\mathcal{L}}^e$ is the usual fourth order isotropic elasticity tensor. In the equation (3), E and E_1 are the Young's moduli related to the elastic springs a) and b), respectively, and η is the stiffness of the viscous damper. Assuming η to be a scalar, only three new material parameters h_2, E_1 and η enter the EBPA model.

Calibration of the EBPA model

The EBPA model is evaluated by comparing its predictions with the experiments on bisphenol A polycarbonate (BPA-PC) under uniaxial non-monotonic loadings. This homogenous deformation mode allows the numerical integration to be performed using an ODE-solver instead of solving the boundary value problem. [1]

Table 1: Constitutive parameters of the BPA and EBPA model for BPA-PC. The parameters are obtained from the calibration to the uniaxial compression tests, cf. Dreistadt *et al.* (2009).

	E	ν	s_0	s_{ss}	h_1	h_2	$\dot{\gamma}_0$	A	C^R	N	α
	MPa		MPa	MPa	MPa	MPa	s^{-1}	$\text{MPa}^{-1}K$	MPa		
BPA	2300	0.37	99	73	370		$2 \cdot 10^{15}$	241	14.0	1.85	0.08
EBPA	3700	0.37	100	56.5	205	40	$5.6 \cdot 10^{15}$	241	14.0	2.2	0.08

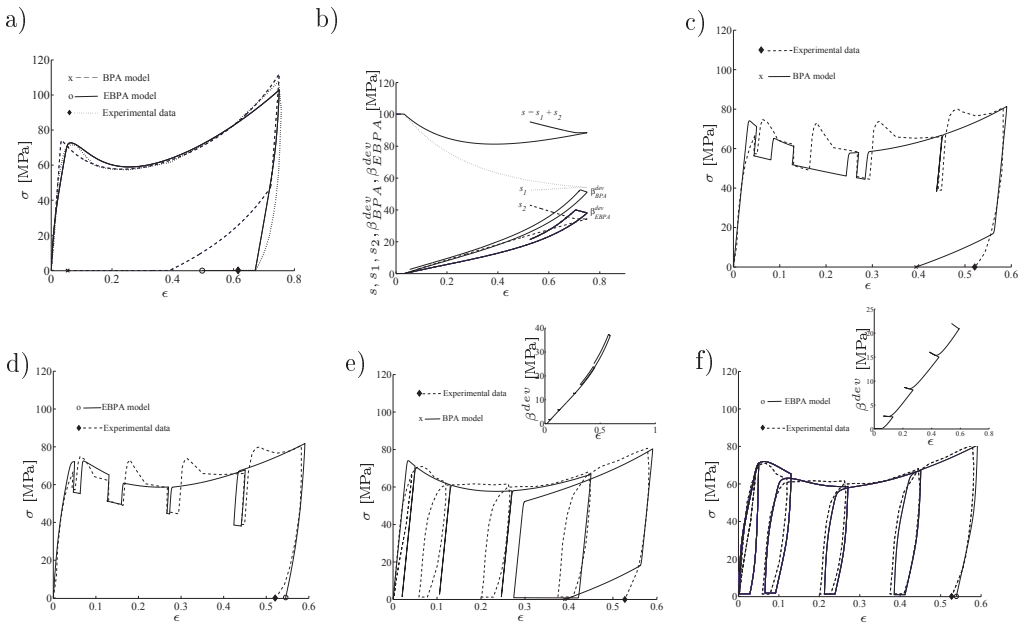

Figure 2: a) True stress vs true strain for uniaxial compression of BPA-PC. The strain rate 0.001 s^{-1} is considered during loading and then the applied load is removed using the constant nominal stress state, $\dot{\pi} = 2.3$ MPa/s. Finally, the specimen is kept unstressed for 400 days. b) Athermal shear strength s and its components s_1 and s_2 according to the EBPA model. β^{dev}_{BPA} and β^{dev}_{EBPA} denote the backstress components in the direction of the applied load. c) - f) Uniaxial compression responses for BPA-PC. The unloadings to $\pi = 59$ MPa and $\pi = 1.2$ MPa are initiated at $\epsilon = 0.05$, 0.13, 0.27, 0.45, and 0.59. After each dwell period of 12.000 s, the specimen is reloaded to the next strain level. The final unloading is performed to zero stress.

Based on the experimental data taken from Dreistadt *et al.* (2009), the EBPA model was calibrated using the least-square fitting (Nelder-Mead simplex algorithm). In the EBPA model, the stiffness of the damper and the intermediate spring are chosen to be $\eta = 5.0{\cdot}10^4$ MPas and $E_1/E = 0.35$, respectively, cf. Fig. 1. In (2), the threshold $\bar{s}_2 = 40$ MPa is employed. The rest of the material parameters resulting from the calibration are given in Table 1. For completeness, the BPA model parameters are also expressed. The calibration for uniaxial homogeneous deformation indicated the following model characteristics:

- During unloading, the BPA model predicts a strong Bauchinger effect, whereas the EBPA model and the experimental response show a smooth transition, cf. Fig. 2(a).
- The original BPA model is not able to predict long-term recovery, but results in a one-magnitude lower permanent strain of 0.062 compared to the experimental data and the EBPA model result, cf. Fig. 2(a).
- The new variable s_2, increases along with the plastic deformation, and as a result the backstress prior to unloading is about 30% greater by the BPA model than the EBPA model, cf. Fig. 2(b).
- In contrast to the experimental and the EBPA responses, the BPA model predicts exaggerated creep during the first two dwell periods, cf. Fig. 2(c)-(d).
- Even though the EBPA model overpredicts the recovery during the first cycle, it is superior to the BPA model during the subsequent cycles when the BPA model predicts almost elastic response or an excessive recovery, cf. Fig. 2(e)-(f).
- The values of the backstress prior to the two last unloadings are much higher predicted by the BPA model than by the EBPA model, cf. Figs. 2(e)-(f).

Investigations on inhomogeneous deformation state

Since long-term behavior will be investigated, the proposed algorithm is based on a fully implicit backward Euler method which allows large time steps to be used. Similar to the BPA model, the elastic rotation $\boldsymbol{R}^e$ in the EBPA model is chosen to be unity and consequently the plastic spin $\bar{\boldsymbol{W}}^p$ is nonzero. The plastic spin is numerically solved by introducing a skew-symmetric algorithmic plastic spin $\tilde{\boldsymbol{W}}^p$, which results from the imposed symmetry of $\boldsymbol{F}^e$ at the end of the integration interval. As with the homogeneous deformation, the viscous damping is described by a scalar targeted to the intermediate elastic stretch, $\boldsymbol{v}_2^e$. To specify the orientation of the elastic intermediate configuration, the first component $\boldsymbol{F}_1^e$ in the decomposition is chosen to be symmetric. In an implicit finite element solution process, the stress-strain relation needs to be linearized. Details for the proposed numerical algorithm as well as the development of the tangent stiffness tensor consistent with the integration algorithm can be found from Holopainen (2012).

Since the material of the test specimen (Lexan® 223R) differing from the PC-polymers given in Table 1, some of the material parameters needs to be recalibrated to the data of the cold drawing experiment. The calibrated parameters for the EBPA model are given in Table 2. Apart from the recalibrated softening parameters $s_0 = 92$ MPa and $s_{ss} = 69$ MPa, the BPA model response is obtained using the material parameters given in Table 1. The development of inhomogeneous deformation at three different phases $u = 10$ mm, $u = 20$ mm and at the end of the last unloading is presented in Fig. 3(e). The average plastic stretch $\bar{\lambda}_{ec}^p$, cf. Holopainen (2012), is chosen to visualize the phenomenon. Based on the calibrations for inhomogeneous deformation the following model characteristics are observed:

- In contrast to the experimental and the EBPA model curve, the BPA model predicts almost linear initial response, which is due to the elastic constitutive description, cf. Fig. 3(b) and (d).
- During continued deformation, the localized zone extends at almost constant force, which indicates that stable neck is present, cf. Fig. 3(a)-(d).
- Once the yield point is passed, inelastic strain localization is developed in the material. The localized zone is not concentrated but expands through the gauge section, i.e. the neck is rather diffuse, cf. Fig. 3(e).
- Unloadings to $f = 60$ N are not satisfactorily captured by the BPA model, which predicts an almost elastic response during the second cycle and a premature Bauchinger effect during the last unloading.
- If an additional loop is performed, cf. the arrow in Fig. 3(b), only a small cyclic shift of the hysteresis loop during this last unloading can be observed, i.e. the BPA model shows the saturated state of hardening.

Table 2: The values of the EBPA model parameters for Lexan® 223R PC. Calibration of the EBPA model is based on the cold drawing experiments of the dumbbell-shaped specimen. The tests were performed in the Laboratory of the Department of Materials Science at TUT.

E	η	s_0	s_{ss}	h_1	h_2	$\dot{\gamma}_0$	A	C^R	N	α
MPa	MPa	MPa	MPa	MPa	MPa	s^{-1}	$\text{MPa}^{-1}K$	MPa		
2550	$1.5 \cdot 10^5$	96	77	720	40	$5.6 \cdot 10^{15}$	241	14	2.2	0.08

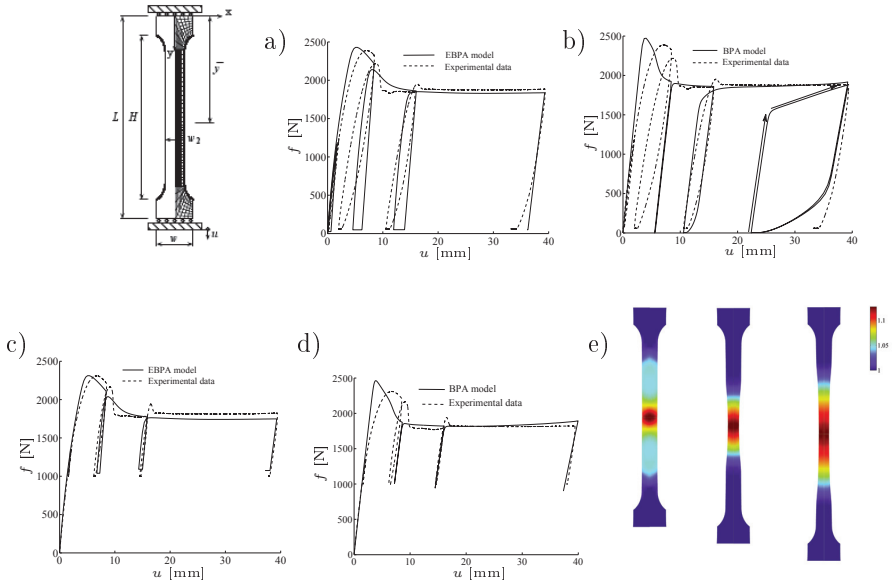

Figure 3: A PC-specimen is subjected to the extension at a cross-head speed $\dot{u} = 2$ mm/s. The unloadings to $f = 60$ N and $f = 1000$ N are initialized at $u = 2.0$ mm, $u = 8.4$ mm and $u = 15.8$ mm, and they are followed by the dwell period of $t = 120$ s. The geometry is given by $H/L \approx 0.89$, $w/L \approx 0.17$, $w_2/L \approx 0.09$ and $t/L \approx 0.035$ where t is the specimen's thickness. The initiation of neck is depicted by $\bar{y} = 0.55L$. The specimen's geometry is specified in ISO 527-2.

It can be concluded that the models are able to capture the characteristic features of the experimental response during monotonic loading. In contrast to the BPA model, the EBPA model captures not only the elongation where the softening is initialized, but also amount of softening as well as creep/recovery during dwell at prescribed forces.

References

Anand, L. and Ames, N. M. (2006). On modeling the micro-indentation response of an amorphous polymer. *Int. J. Plasticity*, **22**, 1123–1170.

Argon, A. S. (1973). A theory for the low-temperature plastic deformation of glassy polymers. *Philosophical Magazine*, **28**(4), 839–865.

Arruda, E. M. and Boyce, M. C. (1991). Anisotropy and localization of plastic deformation. In J. P. Boehler and A. S. Khan, editors, *Proc. Plasticity*, page 483. Elsevier Applied Science, London.

Arruda, E. M. and Boyce, M. C. (1993). Evolution of plastic anisotropy in amorphous polymers during finite straining. *Int. J. Plasticity*, **9**, 697–720.

Dreistadt, C., Bonnet, A. S., Chevrier, P., and Lipinski, P. (2009). Experimental study of the polycarbonate behaviour during complex loadings and comparison with the Boyce, Parks and Argon model predictions. *Materials and Design*, **30**, 3126–3140.

Hasan, O. A. and Boyce, M. C. (1995). A constitutive model for the nonlinear viscoelastic viscoplastic behavior of glassy polymers. *Polym. Engngn. Sci.*, **35**, 331–344.

Holopainen, S. (2012). Modeling of long-term behavior of amorphous glassy polymers. *Accepted for publication in ASME J. Engng. Materials Technol.*

Sami Holopainen
Tampere University of Technology (TUT), Department of Mechanics and Design
P.O.Box 589, FI-331 01 Tampere.
sami.holopainen@tut.fi

Analysing and modeling the geometry of a cellular material

Johanna Sjölund and Jouni Freund

Summary. A way to quantify the geometry of planar cellular structure, such as wood, is presented. A geometric description, that captures the mechanically important features of the actual specimens, is obtained through image and statistical analysis. The relation between geometry and mechanical properties is considered. A method for using the statistical data in order to generate a similar geometry for micromechanical modeling is introduced. A case study of early wood is discussed and the cell structure and thickness of the cell walls are found and restructured for mechanical analysis.

Key words: honeycomb, cellular, geometry, modeling

Introduction

The aim of this paper is to find the geometry of a sheet of cellular material and capture the mechanically important features. The found geometry is described by chosen geometrical parameters and used to create a micromechanical model of the material. The chosen description may contain both random and structured variation. The analysis and modeling procedure presented in this paper can be applied to many cellular materials, such as wood, concrete or foam [3].

The mechanical properties, such as rigidity, depend on the thickness of the cell wall, the shape of the cell and formation of the cell structure. For example, the average (homogenized)strain-stress relationship square cell material with three different wall lengths shown in Figure 1 can be written as

$$\begin{Bmatrix} \epsilon_{xx} \\ \epsilon_{yy} \\ \gamma_{xy} \end{Bmatrix} = \frac{1}{E_s\alpha^2} \begin{bmatrix} \alpha & 0 & 0 \\ 0 & \alpha^2+(\gamma-1)^2\gamma^2 & \gamma(1-3\gamma+2\gamma^2) \\ 0 & \gamma(1-3\gamma+2\gamma^2) & 2+(\alpha^2-3)(\gamma-\gamma^2) \end{bmatrix} \begin{Bmatrix} \sigma_{xx} \\ \sigma_{yy} \\ \sigma_{xy} \end{Bmatrix}, \qquad (1)$$

where h is the cell wall length as shown in the figure, $\alpha = t/h$, t is the thickness of the cell wall, $\gamma = h_1/h$ and E_s is the Young's modulus of the cell wall. The relationship shows that the shape and placement of the cells in relation to each other has a clear effect on the mechanical properties.

Unlike an idealized cell structure, most cellular materials have imperfections and inhomogeneities in their microstructure and material properties. These are obvious in natural materials, but also occur in manufactured honeycombs. As imperfections and irregularities have certainly effect on strength and may affect also rigidity [1, 2], the assumption of a regular cellular structure under constant stress is clearly violated.

Geometrical modeling

When modeling rigidity of a cellular structure, the geometry of the microstructure needs to be accounted for. Firstly, the shape and formation of the cells is considered. Secondly, the

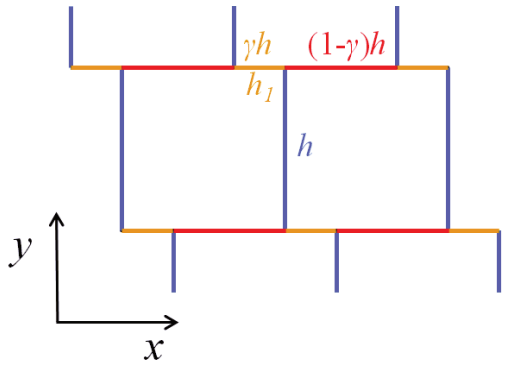

Figure 1. A sheet of material made of square cells.

geometry may have statistical (random) or structured (depending on location) variation. The modelled honeycomb specimen contains information about the shape of cells and irregularities in the cell structure. A good model is as simple as possible and some idealizations are made in order to achieve a compact representation, but not so simple that the features having a clear effect on the mechanical properties are left out.

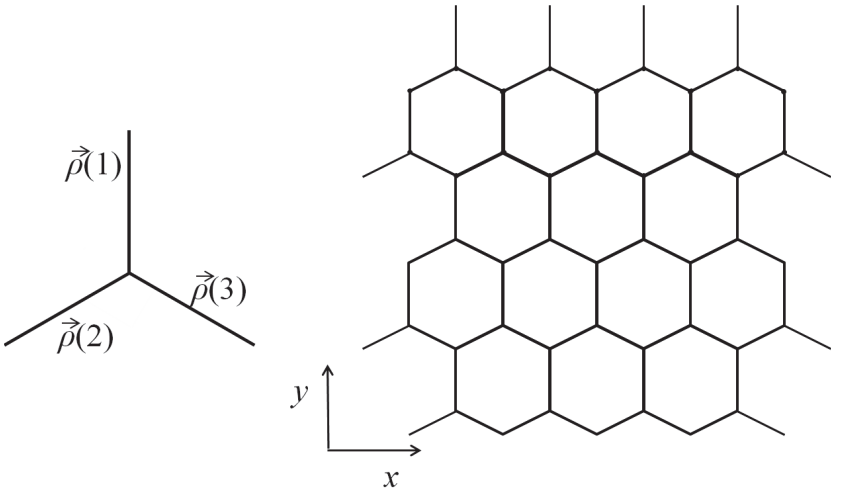

Figure 2. On the left a structural unit and on the right a sheet generated by repeating and translating the structural unit.

Figure 2 illustrates the geometric model of [4] based on the structural unit $\vec{\rho}(k) \quad k \in \{1, 2, 3\}$ of three relative position vectors. Six parameters are used when describing the geometry with the three vectors, for example a square is generated by determining one vector length to be zero.. The structural unit is defined as a geometrical entity which, when repeated, can be used to build a honeycomb by translation mapping as shown on the right of Figure 2. The mapping can be described as

$$\vec{r}(i, j, k) = \vec{r}_0(i, j) + \vec{\rho}(i, j, k), \tag{2}$$

where i and j identify the structural unit and $\vec{r}_0(i, j)$ is the position vector of the center-point which describes the translation of the structural unit. The locations of the vertex

points relative to the centerpoint are described by $\vec{\rho}(i, j, k)$.

Wood sample

A sample of early wood is used as a case study to find the geometrical parameters $\vec{\rho}(k)$ and $t(k)$. The sample is shown in Figure 3, the centers of cells, the vertex points of the structural units and the thicknesses of the cell walls for each vertex point (green circles) are shown in the foreground of the scanned image. The cell regions were first found as closed set of pixels by morphological analysis. After that the centers were calculated as area centroids of the cell regions and the vertex points were obtained by including the cell wall in all cell pixel sets, and defining the vertex points to be centroids of intersection sets of three cell pixel sets.

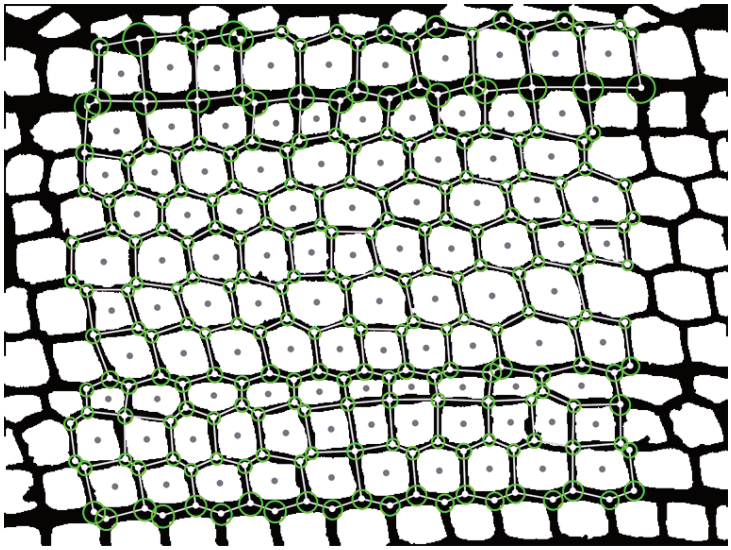

Figure 3. Sample of spruce early wood.

The representative structural units, shown in color in Figure 4, are chosen out of all the structural units found. This way the border regions can be avoided and a desired area can be studied. It is usually best to choose an area where the structural units are similar to each other and study different types of areas separately.

Results

The mean values and the standard deviations of the vectors of the structural units are presented in Table 1. The mean value of the thickness $\mu(t) = 0.036$ mm and standard deviation $\sigma(t) = 0.010$ mm. As one would expect, the variation is larger in the length of the cell wall than for the direction of the cell wall.

Using these parameters the mechanical properties can be derived using a similar compliance matrix as in equation (1). In this case the compliance matrix is more complex, as more variables are used, such as the angles. Using the mean values of the geometrical

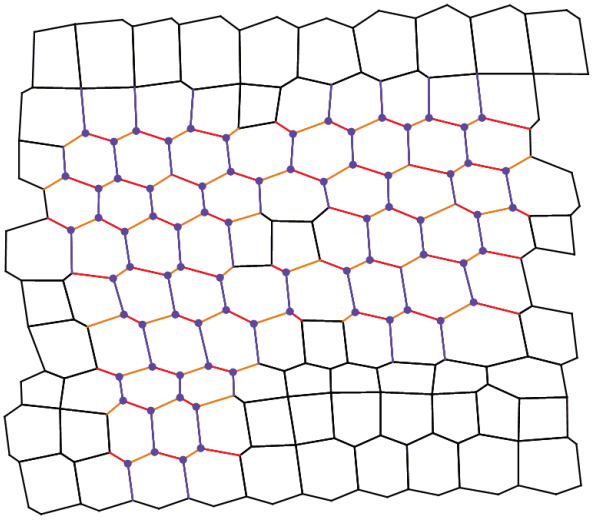

Figure 4. Points chosen of the early wood sample.

Table 1. Geometric parameters of early wood.

	$\mu(\vec{\rho}(1))$	$\mu(\vec{\rho}(2))$	$\mu(\vec{\rho}(3))$	$\sigma(\vec{\rho}(1))$	$\sigma(\vec{\rho}(2))$	$\sigma(\vec{\rho}(3))$
x-axis (mm)	-0.018	0.12	-0.145	0.015	0.036	0.037
y-axis (mm)	0.17	0.054	0.044	0.028	0.012	0.010

parameters the following strain-stress relationship is found

$$\begin{Bmatrix} \epsilon_{xx} \\ \epsilon_{yy} \\ \gamma_{xy} \end{Bmatrix} = \frac{1}{E_s} \begin{bmatrix} 17.08 & -16.19 & -0.85 \\ -16.91 & 35.41 & 8.66 \\ -0.85 & 8.66 & 193.9 \end{bmatrix} \begin{Bmatrix} \sigma_{xx} \\ \sigma_{yy} \\ \sigma_{xy} \end{Bmatrix}. \tag{3}$$

Conclusions

The cellular structure of a early wood sample was analysed and used to calculate the geometric parameters, which take into account the important features of the original structure. The analysis proposed here gives a compact representation of a cellular structure, that can be used to estimate the effective elasticity parameters of material element consisting of large number of cells.

Acknowledgements

This work is part of the Mide project E-wood (Energy Efficient Wood Processing and Machining) funded by Aalto University. To aim of the work is to predict strength statistics of wood by virtual experiments on a micromechanical model.

References

[1] H.X. Zhu J.R. Hobdell, and A.H. Windle. Effects of cell irregularity on the elastic properties of 2D Voronoi honeycombs *Journal of the Mechanics and Physics of Solids*, 49:857–870,2001.

[2] M.J. Silva and L.J. Gibson. The effects of non-periodic microstructure on the elastic properties of two-dimensional cellular solids *International Journal of Mechanical Sciences*, 37:1161–1171,1995.

[3] L.J. Gibson and M.F. Ashby. *Cellular solids: Structure and properties*. Camdridge University Press, Second Edition, 1997.

[4] D.H. Chen. Bending deformation of honeycomb consisting of regular hexagonal cells *Composite Structures*, 93:736–746,2010.

Johanna Sjölund, Jouni Freund
Department of Applied Mechanics, Aalto University
Puumiehenkuja 5 A, 0076 Aalto
johanna.sjolund@aalto.fi, jouni.freund@aalto.fi

Homogenization of Regular Honeycomb Material

Jouni Freund

Summary. The way to homogenize a regular planar honeycomb material starting from a detailed micro-mechanical model is presented. As the outcome one obtains the equilibrium equations of micro-polar elasticity, work conjugate stress and strain definitions, and a way to derive the constitutive equations of micro-polar and classical elasticity. Stress-strain relationships for the rectangular, triangular and hexagonal cell types are given as examples.

Key words: homogenization, honeycomb, cell, elasticity, micro-polar

Introduction

The straightforward micro-mechanical modeling of honeycomb material uses a detailed description of cell geometry and beam equations of the elastic bending and stretching of cell walls. The challenge of this approach is the computational complexity due to the huge difference between the cell and structure scales of practical settings. Therefore, e.g. in wood applications, an approach based on the classical or micro-polar continuum equations and a homogenized constitutive equation is more attractive [1],[2],[3],[4].

Constitutive equations of regular honeycomb material are well-known for the basic cell types. Examples are the hexagonal, square and triangular cell types in connection with the classical elasticity [4],[5]. Micro-polar constitutive equations for a rectangular cell structure are available e.g. in [1] and [3]. The homogenization methods of the references vary from cell-type specific compliance ones to more formal stiffness methods.

The starting point here is a micro-mechanical model based on the detailed cell geometry and Bernoulli beam model for the cell walls. Derivation of the continuum model uses the structural unit concept, principle of virtual work, and a kinematical assumption as the standard tools for dimensional reduction. As the outcome one obtains the equilibrium equations, work conjugate stress and strain definitions, and a method to derive the constitutive equations of micro-polar and classical elasticity.

Structural unit

By definition, a regular honeycomb structure is composed of parts having the same geometry and material properties and called as structural units. To simplify the setting further, the cell material inside the cell is assumed here much softer than the cell wall material and the mechanical behavior of the cell walls is described by Bernoulli beam

theory. Under these assumptions, mechanical properties, like stress-strain relationship of a collection of cells, can be deduced by considering a typical structural unit only.

Figure 1 shows a structural unit of three relative position vectors $\vec{\rho}_i \quad i \in \{1,2,3\}$ representing the centerlines of tree beams having the point 0 in common, the characteristic domain of volume V, and the directed surface areas $\vec{A}_i$ associated with the structural unit. The definitions are chosen to satisfy

$$(\tilde{\nabla} f)_0 = \frac{1}{V} \sum \vec{A}_i f_i \tag{1}$$

in which $f(x,y)$ is linear (scalar, vector,..) and f_i the values of $f(x,y)$ at the vertex points $i \in \{1,2,3\}$ in figure 1. Expression in (1) can be taken as an approximation of the gradient operator in a polygonal domain. Some of its useful consequences are $\sum \vec{A}_i = 0$ and $\sum \vec{A}_i \vec{\rho}_i = V\vec{I}$ ($\vec{I}$ is the unit dyad defined by $\vec{I} \cdot \vec{a} = \vec{a} \cdot \vec{I} = \vec{a} \ \forall \vec{a}$).

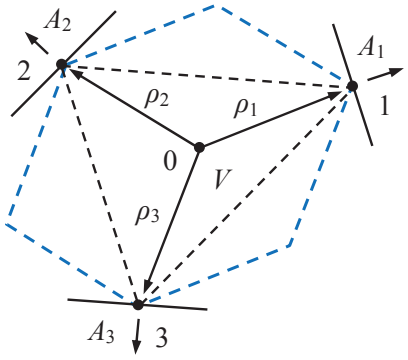

Figure 1 Structural unit of planar honeycomb material consisting of three cell walls

Denoting the rotations and displacement of the points $i \in \{0,1,2,3\}$ by $\vec{u}_i$ and $\vec{\theta}_i$, dividing the displacement of the structural unit into rigid body and deformation parts, and using the truncated Taylor series for the deformation part, gives

$$\begin{Bmatrix} \vec{u}_i \\ \vec{\theta}_i \end{Bmatrix} = \begin{Bmatrix} \vec{u}_r \\ \vec{\theta}_r \end{Bmatrix} + \begin{Bmatrix} \vec{\theta}_r \times \vec{\rho}_i \\ 0 \end{Bmatrix} + \begin{Bmatrix} \vec{v}_0 \\ \vec{\phi}_0 \end{Bmatrix} + \vec{\rho}_i \cdot \begin{Bmatrix} (\nabla \vec{v})_0 \\ (\nabla \vec{\phi})_0 \end{Bmatrix}, \tag{2}$$

in which $\vec{u}_r, \vec{\theta}_r$ are the small rigid body translation and rotation, respectively. Re-arrangement of (2) and the use of (1), gives the strain definition

$$\begin{Bmatrix} \vec{\varepsilon}_0 \\ \vec{\kappa}_0 \end{Bmatrix} = \begin{Bmatrix} (\nabla \vec{v})_0 + \vec{I} \times \vec{\phi}_0 \\ (\nabla \vec{\phi})_0 \end{Bmatrix} = \begin{Bmatrix} \tilde{\nabla} \vec{u} + \vec{I} \times \vec{\theta}_0 \\ \tilde{\nabla} \vec{\theta} \end{Bmatrix}. \tag{3}$$

Above we have used relationship $\vec{\theta} = \vec{\theta}_r + \vec{\phi}$ in which the so-called micro-rotation $\vec{\phi}$ can be non-zero even when the displacement is zero everywhere.

Principle of virtual work

The starting point is the virtual work expression of the structural unit subjected to external and internal force and moments acting on points $i \in \{0,1,2,3\}$

$$\delta W = \delta \begin{Bmatrix} \vec{u}_0 \\ \vec{\theta}_0 \end{Bmatrix}^{\mathrm{T}} \cdot \begin{Bmatrix} \underline{\vec{F}}_0 \\ \underline{\vec{M}}_0 \end{Bmatrix} + \sum \delta \begin{Bmatrix} \vec{u}_i \\ \vec{\theta}_i \end{Bmatrix}^{\mathrm{T}} \cdot \begin{Bmatrix} \underline{\vec{F}}_i - \vec{F}_i \\ \underline{\vec{M}}_i - \vec{M}_i \end{Bmatrix}, \tag{4}$$

where the underbar denotes an external force and moment. Without going into the details, the work conjugate stress definition to (3)

$$\begin{Bmatrix} \vec{\sigma} \\ \vec{\mu} \end{Bmatrix} = \frac{1}{V} \sum \vec{\rho}_i \begin{Bmatrix} \vec{F}_i \\ \vec{M}_i \end{Bmatrix} \tag{5}$$

follows from (4), when the kinematic assumption (2) is substituted there. If further the internal forces of the structural unit satisfy the equilibrium condition according to

$$\delta \begin{Bmatrix} \vec{u}_0 \\ \vec{\theta}_0 \end{Bmatrix}^{\mathrm{T}} \cdot \sum \begin{Bmatrix} \vec{F}_i \\ \vec{M}_i + \vec{\rho}_i \times \vec{F}_i \end{Bmatrix} = 0, \tag{6}$$

the principle of virtual work implies the well-known equilibrium equations

$$\begin{Bmatrix} \nabla \cdot \vec{\sigma} + \vec{f} \\ \nabla \cdot \vec{\mu} - \vec{\sigma} + \vec{m} \end{Bmatrix} = 0 \tag{7}$$

of micro-polar elasticity [1],[3]. Above $\vec{\sigma}$ is the associated vector of the anti-symmetric part of $\vec{\sigma}$. Clearly, if the couple-stress $\vec{\mu}$ is constant, equations (7) boil down to the equilibrium equations of the classical elasticity.

Constitutive equation

Derivation of the relationship between stress and strain i.e. constitutive equation follows the lines of a physical experiments: external stress is applied to the structural unit and strain is recorded. After repeating the experiment for each stress component, the outcome gives the stress-strain relationship in its compliance form.

As here the internal forces are due to the Bernoulli beam model here, the forces and moments are calculated first with the aid of force-stress relationship

$$\begin{Bmatrix} \vec{F}_i \\ \vec{M}_i \end{Bmatrix} = \vec{A}_i \cdot \begin{Bmatrix} \vec{\sigma} \\ \vec{\mu} \end{Bmatrix} \tag{8}$$

associated with (5). This is followed by solving the corresponding displacements and rotations in the usual manner without restricting the rigid body motion. Finally, the strain follows from (3) written as

$$\begin{Bmatrix} \vec{\varepsilon}_0 \\ \vec{\kappa}_0 \end{Bmatrix} = \frac{1}{V} \sum \vec{A}_i \begin{Bmatrix} \vec{u}_i \\ \vec{\theta}_i \end{Bmatrix} + \begin{Bmatrix} \vec{I} \times \vec{\theta}_0 \\ 0 \end{Bmatrix}. \tag{9}$$

It is noteworthy, that the possible rigid body motion is mapped to zero by the strain definition and the outcome is the micro-polar stress-strain relationship in its compliance form. The constitutive equation of classical elasticity follows by further restricting $\vec{\sigma}$ and $\vec{\varepsilon}$ be symmetric.

Regularity of the honeycomb structure implies the condition $\vec{\theta}_i = const.$ (a given parameter) for the force stress loading modes of the specimen. Therefore only the displacements $\vec{u}_i$ are treated as unknowns when solving the displacements.

Classical elasticity compliance

Assuming a properly oriented material coordinate system, the stress-strain relationship of classical elasticity for a regular cell structure can be expressed as

$$\begin{Bmatrix} \varepsilon_{xx} \\ \varepsilon_{yy} \\ \gamma_{xy} \end{Bmatrix} = \begin{bmatrix} 1/E_x & -\nu_{yx}/E_y & 0 \\ -\nu_{xy}/E_x & 1/E_y & 0 \\ 0 & 0 & 1/G_{xy} \end{bmatrix} \begin{Bmatrix} \sigma_{xx} \\ \sigma_{yy} \\ \sigma_{xy} \end{Bmatrix} \tag{10}$$

in which $\nu_{yx}/E_y = \nu_{xy}/E_x$. The material parameters, Young's moduli E_x, E_y, Poisson's ratio ν_{xy}, ν_{yx} and shear modulus G_{xy}, can be determined with the compliance method by considering a single structural unit.

Table 1 Parameters of classical elasticity as functions of $\alpha = t/h$.

	E_x/E_s	E_y/E_s	ν_{xy}	ν_{yx}	G_{xy}/E_s
	α	α	0	0	$\frac{1}{2}\alpha^3$
	$2\sqrt{3}\frac{\alpha+\alpha^3}{3+\alpha^2}$	$2\sqrt{3}\frac{\alpha+\alpha^3}{3+\alpha^2}$	$\frac{1-\alpha^2}{3+\alpha^2}$	$\frac{1-\alpha^2}{3+\alpha^2}$	$\frac{\sqrt{3}}{4}(\alpha+\alpha^3)$
	$\frac{4}{\sqrt{3}}\frac{\alpha^3}{1+3\alpha^2}$	$\frac{4}{\sqrt{3}}\frac{\alpha^3}{1+3\alpha^2}$	$\frac{1-\alpha^2}{1+3\alpha^2}$	$\frac{1-\alpha^2}{1+3\alpha^2}$	$\frac{1}{\sqrt{3}}\frac{\alpha^3}{1+\alpha^2}$
	α	$\frac{16\alpha^3}{1+16\alpha^2}$	0	0	$\frac{4\alpha^3}{5+\alpha^2}$

The outcome for some simple cell types are given in table 1 as functions of the cell wall thickness ratio $\alpha = t/h$ and it's Young's modulus E_s. The geometries of the table, except the triangle one, can be treated with the three-cell-wall structural unit. It is noteworthy that triangular and hexagonal cell materials are isotropic and therefore the material parameters satisfy the condition $G = E/(2+2\nu)$. Cell wall bending and stretching dominated behaviours are indicated by the presence of α^3 and α in the numerators, respectively. For the usual thickness ratios, stretching dominated behaviour makes a material exceptionally stiff.

Micro-polar compliance

In micro-polar elasticity [1], the strain-stress relationship involves force- and couple stress components that do not satisfy symmetry 'a priori'. Also the strain components are non-symmetric. The micro-polar stress-strain relationship of the hexagonal honeycomb material in (11) gives (10) if $\sigma_{xy} = \sigma_{yx}$ and $\gamma_{xy} = \varepsilon_{xy} + \varepsilon_{yx}$.

$$\begin{Bmatrix} \varepsilon_{xx} \\ \varepsilon_{yy} \\ \hline \varepsilon_{xy} \\ \varepsilon_{yx} \\ \hline h\kappa_{xz} \\ h\kappa_{yz} \end{Bmatrix} = \frac{\sqrt{3}}{4E_s\alpha^3} \left\{ \begin{array}{cc:cc:cc} 1+3\alpha^2 & -1+\alpha^2 & 0 & 0 & 0 & 0 \\ -1+\alpha^2 & 1+3\alpha^2 & 0 & 0 & 0 & 0 \\ \hdashline 0 & 0 & 3+\alpha^2 & -1+\alpha^2 & 0 & 0 \\ 0 & 0 & -1+\alpha^2 & 3+\alpha^2 & 0 & 0 \\ \hdashline 0 & 0 & 0 & 0 & 48 & 0 \\ 0 & 0 & 0 & 0 & 0 & 48 \end{array} \right\} \begin{Bmatrix} \sigma_{xx} \\ \sigma_{yy} \\ \hline \sigma_{xy} \\ \sigma_{yx} \\ \hline \mu_{xz}/h \\ \mu_{yz}/h \end{Bmatrix} \tag{11}$$

Concluding remarks

In this work, a micro-mechanical model of honeycomb material was used as an accurate model to end up with a homogenized model. The examples of homogenized constitutive equations were chosen to be simple to keep the compliance expression concise. The method applies, however, also when the three-cell-wall structural unit consists of beams of variable lengths, angles and material properties.

References

[1] A. C. Eringen, *Microcontinuum field theories; I: Foundations and solids*, Springer, 1998.

[2] S. Gonella, M. Ruzzene, Homogenization and equivalent in-plane properties of two-dimensional periodic lattices, *International Journal of Solids and Structures*, 45:2897–2915, 2008.

[3] R.S. Kumar, D.L. McDowell, Generalized continuum modeling of 2-D periodic cellular structures, *International Journal of Solids and Structures*, 41:7399–7422, 2004.

[4] L.J. Gibson, M.F. Ashby, *Cellular solids, structure and properties*, Cambridge University Press, 1999.
[5] J. Hohe, W. Becker, Effective stress-strain relations for two-dimensional cellular sandwich cores: Homogenization, material models, and properties, *Appl. Mech. Rev.* , 55: 61-87, 2002.

Jouni Freund
Aalto University, School of Engineering, Department of Applied Mechanics
P.O.BOX 14300, FI-00076 AALTO, FINLAND
jouni.freund@aalto.fi

Muistimetallimateriaalimallin käyttö ohuen NiTi-langan mallinnuksessa

Antti-Jussi Vuotikka

Tiivistelmä. Erittäin ohuelle NiTi-muistimetallilangalle on tehty erilaisia mekaanisia materiaalitestejä, joissa tutkitaan langan soveltuvuutta kirurgiseksi ommellangaksi. Langan lujuutta ja käsiteltävyyttä on testattu veto-, vääntö- ja taivutustesteillä, ja langan solmittavuutta puolestaan solmun ja silmukan vetotesteillä.

Tässä työssä pyritään löytämään materiaalimallissa tarvittavat parametrit langan vetokokeiden mittaustuloksia käyttäen. Tämän jälkeen tutkitaan materiaaliparametrien soveltuvuutta langan taivutus- ja vääntötestien mallinnukseen.

Avainsanat: NiTi, ommellanka, materiaalitesti, FEM

Johdanto

NiTi-muistimetallilangan mekaanista soveltuvuutta kirurgisena ommellankana on tutkittu aiemmin [10]. Langan mekaanisia ominaisuuksia testattiin usealla eri testausmenetelmällä. Perusominaisuudet selvitettiin tekemällä vetomurto-, vääntö- ja virumistestejä. Langan käsiteltävyyttä selvitettiin langan taivutus- ja silmukoitumistesteillä. Näiden lisäksi materiaalin käyttäytymistä tutkittiin kahdella erityyppisellä solmun vetotestillä.

Tässä työssä pohditaan materiaalitestauksesta saatujen tulosten käytettävyyttä materiaalin mallinnukseen. Alussa on lyhyesti esitetty mallinnettavaksi valitut ommellankojen testausmenetelmät, jotka ovat veto-, taivutus- ja vääntötesti. Materiaalimallin parametrit sovitetaan materiaalin vetotestin tulokseen. Näiden parametrien avulla pyritään mallintamaan taivutus- ja silmukoitumistestien tulokset.

Materiaalitestit

Materiaali

Kirurgisten ommellankojen testauksessa oli tutkittavana kaksi erilaista NiTi-lankaa, joista toinen on huoneen ja kehon lämpötilassa austeniittisessa muodossa ja toinen on martensiittisessa muodossa. Vertailumateriaalina käytettiin yleisesti käytettyä kirurgista

ommellankaa, Prolene (polypropylene) 6-0. NiTi-langat ovat USP:n [20] luokittelun mukaisesti ei-absorboivia III-luokkaan kuuluvaa ommelmateriaalia. Vertailumateriaali kuuluu I-luokkaan, ja se on myös ei-absorboivaa materiaalia. Langan halkaisija on 0,1 mm. Kaikki langat on testattu siinä tilassa, jossa ne on toimitettu. NiTi-langoille ei ole tehty lämpökäsittelyjä eikä niitä ole stabilisoitu.

Menetelmät

Suoran langan vetokoe

Absorboimatonta kirurgista ommellankaa on testattu kirjallisuudessa monilla eri menetelmillä. Menetelmät voidaan jakaa pääsääntöisesti langan kiinnitysmenetelmien mukaan vetokokeisiin perinteisillä leuoilla [11],[18], lankaleuoilla [3],[21] tai tutkijoiden itse kehittämillä kiinnitysmenetelmillä [2],[5],[9],[13]. USP on standardisoinut suoran langan ja solmitun kirurgisen ommellangan veto-ominaisuuksien testauksen, jonka mukaisesti materiaalin testaus on tehty. Suoran langan testeistä saadaan materiaalin veto-ominaisuudet selvitettyä, ja solmitun langan vetotestistä selvitetään materiaaliominaisuuksien heikkeneminen solmun vaikutuksesta.

Vetolujuus mitataan vetokoneessa välittömästi, kun kappale on poistettu kuljetuspakkauksesta ilman esivalmisteluita. USP mahdollistaa vetotestauksessa käytettävän joko vakiokuormitusnopeutta tai -venymänopeutta. Testit tehtiin austeniittiselle NiTi:lle paremmin sopivalla vakiovenymänopeusmenetelmällä [12] huoneen lämpötilassa. Venymänopeus on USP:n vaatimusten mukaan 50 mm:n mittapituisella koekappaleella 100 mm/min. Langan kiinnitys tehtiin tavallisiin vetokoneen leukoihin. Voima ja langanpään siirtymä on mitattu.

Taivutus- ja vääntökoe

Kirurgisen langan käsiteltävyysominaisuudet ovat erittäin tärkeitä langan mekaanisten ominaisuuksien lisäksi. Vaikka langalla olisi kuinka hyvät kestävyysominaisuudet tai biomekaaniset ominaisuudet, lankaa ei suosita, jos sen käytettävyys on huono ommeltaessa. Käsiteltävyysominaisuuksien vertailua varten useat tutkijat ovat kehittäneet menetelmiä langan taivutusjäykkyyden mittaamista varten, mutta vääntökokeita ei ole tehty kirurgisten lankojen testauksen yhteydessä.

Langan kiertyminen ompelemisen aikana voi aiheuttaa ongelmia langan kestävyydessä ja käytettävyydessä [9]. Kasvavan väännön myötä langan kyky kantaa vetokuormitusta pienenee ja ommellanka voi silmukoitua. Yksittäinen silmukka voi myös rullautua itsensä ympäri langan aksiaalissuuntaa vastaan kohtisuorassa suunnassa. Silmukoitumisen jälkeen aksiaalisen vedon kasvaminen langassa voi aiheuttaa pysyvän vaurion lankamateriaaliin silmukan kiristyessä.

Kirjallisuudessa taivutusjäykkyyden mittaamisessa on käytetty kolmea eri perusmenetelmää, jotka ovat ulokepalkin taivutukseen [1],[15], palkin kolmipistetaivutukseen [16],[18],[19] sekä sauvan vetotestiin [14] perustuvat menetelmät. Materiaalitesteihin valittiin kolmipistetaivutusmenetelmä, jossa 250 mm pitkä lanka tuetaan keskeltä ja molempiin päihin kiinnitetään 16 mg:n painoiset punnukset. Taivutusjäykkyys voidaan määritellä langanpäiden etäisyyden perusteella.

Langan silmukoitumista vääntökuormituksessa on tutkittu kirjallisuudessa tekemällä vääntötestejä [4],[6],[7],[8]. Lankaan muodostetaan tunnettu kiertymä halutulla

vakiovoimalla, ja silmukoituminen aiheutetaan lyhentämällä langan kiinnityspisteiden etäisyyttä.

Materiaaliparametrien selvittäminen

Langan vetokoetulosten avulla on selvitetty materiaaliparametrit, joita tarvitaan muistimetallin materiaalimallissa. Malli on implementoitu Abaqus-ohjelmistoon UMAT-aliohjelmana, ja se pohjautuu suurille siirtymille laajennettuun Lagoudasin pienten venymien materiaalimalliin [17].

Yksittäisten vetokokeiden tulokset austeniittiselle, martensiittiselle ja vertailulangalle on esitetty kuvassa 1. Materiaalimalli kuvaa NiTi-materiaalin superelastista käyttäytymistä, mutta se ei kuvaa martensiittifaasin uudelleen suuntautumista. Tämän takia tässä keskitytään vain austeniittisen langan käyttäytymiseen.

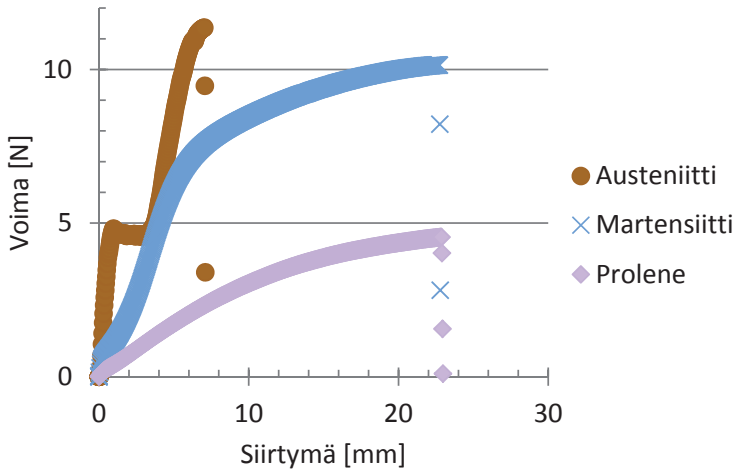

Kuva 1. 50 mm pitkien austeniittisen, martensiittisen ja Prolenelangan vetokoekäyrät. Martensiitti- ja Prolenelangoilla on 46 %:n ja austeniittilangalla 14 %:n murtovenymä.

Langan vetotesteistä saatujen tulosten avulla on etsitty tarvittavat materiaaliparametrit, jotka on esitetty taulukossa 1. Langan vetokokeen tuloksiin sovitettu käyrä on esitetty kuvassa 2. Koska langanvetotestauksia on tehty vain yhdessä lämpötilassa ja langan murtumiseen saakka, vetokokeen tuloksien avulla saadut materiaaliparametrit eivät määräydy yksiselitteisesti ja osittain ei voida antaa edes arviota materiaalin käyttäytymisestä [12]. Kuvassa 2 esitettyä materiaalimallin palautumista martensiittitilasta austeniittitilaan ei ole todettu kokeellisesti.

Taivutus- ja vääntötestien mallintaminen oli seuraavana vaiheena, jossa käytettiin edellä saatuja parametreja. Taivutuskokeen tuloksia ja materiaalimallin antamia tuloksia on verrattu kuvassa 3. Vääntötestin mallinnuksesta ei ehditty saada tuloksia.

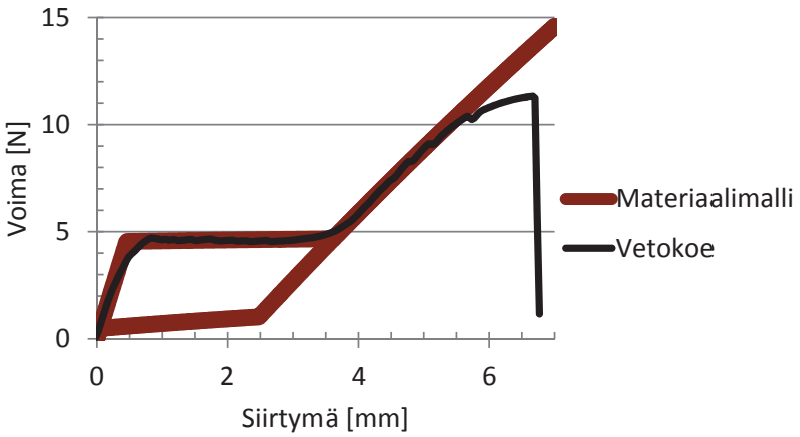

Kuva 2. Austeniittisen langan vetokokeeseen sovitettu superelastinen materiaalimalli.

Taulukko 1. Materiaalimallin parametrit. Testituloksiin sovitus on tehty vahvistettuja lukuja säätämällä.

Materiaaliparametri		Austeniitti-faasi	Muutos-alue	Martensiitti-faasi	Yksikkö
Kimmokerroin	E_A, E_M	**63,8**		**22,9**	GPa
Poisson vakio	ν	0,3		0,3	-
Lämpölaajenemiskerroin	α_A, α_M	22E-6		10E-6	1/K
Faasimuutoslämpötila	As, Ms	**290**		251	K
	Af, Mf	**291**		247	K
Transformaatiovenymä	H		**4,25**		%
Entropian erotus	ρΔS		**-0,67**		MPa/K

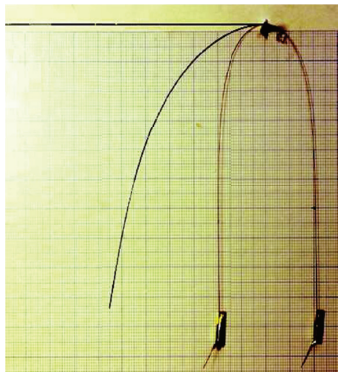

Kuva 3. Abaqus-mallin lähtö- ja lopputilaa verrataan austeniittilangan taivutuskokeen tuloksiin. Austeniittilangan päissä näkyy 16mg:n punnukset.

Langan maksimipääjännitys 133 MPa on tuella, ja se on selvästi alle faasitransformaation kynnysjännityksen 570 MPa. Tämän perusteella materiaali pysyy austeniittisena testin aikana. Lähteen [16] mukaan austeniittiselle langalle voidaan laskea taivutusjäykkyys painojen ja langanpäiden välisen etäisyyden perusteella. Taivutustestissä jäykkyydeksi saadaan 35 $mNmm^2$. Mallin ennustama jäykkyys on lähes 10 kertaa suurempi eli 332 $mNmm^2$. Tämä ero voi osittain johtua liian suuresta austeniittifaasin kimmokertoimesta. Liian nopea kuormitusnopeus vaikuttaa myös faasitransformaation kynnysjännitykseen [12], jolloin todellisuudessa osa materiaalista voikin olla martensiittia pienentäen materiaalin taivutusjäykkyyttä.

Yhteenveto

Kirurgiselle ommellangalle tehdyt testit eivät ole riittävät materiaaliparametrien määrittämiseen. Kuormituksen poistamista ei ole testattu austeniittisella langalla, ja testejä ei ole tehty vähintään kahdessa eri lämpötilassa, jolloin parametrit eivät määräydy yksiselitteisesti. Materiaali suositellaan stabiloimaan ennen mittauksia, mutta tässä tapauksessa asialla ei ole merkitystä, koska lankaa käytetään suoraan toimitusmuodossa. Suurempana ongelmana on se, että materiaalin kuormitusnopeus on ollut huomattavan suuri. Se vaikuttaa voimakkaasti materiaalin käyttäytymiseen ja siten saataviin mallin parametreihin.

Viitteet

[1] F.Baltenneck,A.Franbourg,F.Leroy,M.Mandon,C.Vayssié, A new approach to the bending properties of hair fibers, Journal of Cosmetic Science, 52:355-368, 2001.

[2] K.Baumgarten,M.D.Brodt,M.J.Silva,R.W.Wright, Anin vitro analysis of the mechanical properties of 16 arthroscopic knots, Knee Surg Sports Traumatol Arthosc 16:957-966, 2008.

[3] C.C.Chu, Mechanical Properties of Suture Materials, Ann.Surg. 193(3):365-371, 1981.

[4] N.S.Ermolaeva,J.Regelink,M.P.M.Krutzen, Hockling behaviour of single- and multiple-rope systems, Engineering Failure Analysis, 15:142-153, 2008.

[5] C.Gerber,A.G.Schneeberger,M.Beck,U.Schlegel, Mechanical Strength of Repairs of the Rotator Cuff, The Journal of Bone and Joint Surgery, 76B(3):371-379, 1994.

[6] V.G.A.Goss, G.H.M van der Heijden,J.M.T.Thompson and S.Neukirch, Experiments on snap buckling, hysteresis and loop formation in twisted rods, Experimental Mechanics, 45(2):101-111, 2005.

[7] G.H.M.van der Heijden,S.Neukirch,V.G.A.Goss,J.M.T.Thompson, Instability and self-contact phenomena in the writhing of clamped rods, International Journal of Mechanical Sciences, 45:161-196, 2003.

[8] L.Heller,A.Kujawa,P.Sittner,M.Landa,P.Sedlák and J.Pilch, Quasistatic and dynamic functional properties of thin superelastic NiTi wires, The European Physical Journal Special Topics, 158:7-14, 2008.

[9] D.B.Hennessey,E.Carey,C.K.Simms,A.Hanly,D.C.Winter, Torsion of monofilament and polyfilament sutures under tension decreases suture strength and

increases risk of suture fracture, Journal of the Mechanical Behaviorof Biomedical Materials, 12:168-173, 2012.
[10] T.Karjalainen,S.Kujala,A.Vuotikka,J.Näpänkangas,T.Jämsä,J.Ryhänen,The Material And Knotting Properties Of Martensite and Superelastic Nitinol Wires, to be published.
[11] J.C.Kim,Y.K.Lee,B.S.Lim,S.H.Rhee,H.C.Yang, Comparison of tensile and knot security properties of surgical sutures, Journal ofMaterial Science: Materials in Medicine 18:2363-2369, 2007.
[12] D. C. Lagoudas, Shape Memory Alloys, Modeling and Engineering Applications, Springer, 2008.
[13] L.Nobile,L.Checchi,G.Monaco, Experimental analysis of tensile properties of some suturing materials, Journal of Materials Science: Materials in Medicine, 8:53-56, 1997.
[14] G.T.Rodeheaver,J.G.Thacker,J.Owen,M.Strauss,T.Masterson,R.F.Edlich, Knotting and Handling Characteristics of Coated Synthetic Absorbable Sutures, Journal of Surgical Research 35:525-530, 1983.
[15] G.T.Rodeeaver, T.A.Powell,J.G.Thacker and R.F.Edlich, Mechanical Performance of Monofilament Synthetic Absorbable Sutures, The American Journal of Surgery, 154:544-547, 1987.
[16] G.V.Scott and C.R.Robbins, Stiffness of human hair fibers, Journal of Society of Cosmetic Chemists, 29:469-485, 1978.
[17] J.Teeriaho, An extension of a shape memory alloy model for large deformations based on an exactly integrable Eulerian rate formulation with changing elastic properties, Journal of Plasticity, submitted.
[18] K.Tomihata,M.Suzuki and N.Tomita, Handling characteristics of poly(L-lactide-co-ε-caprolactone) monofilament suture, Bio-Medical Materials and Engineering, 15:381-391, 2005.
[19] N.Tomita,S.Tamai,T.Morihaa,K.Ikeuchi and Y.Ikada, Handling Characteristics of Braided Suture Materials for Tight Tying, Journal of Applied Biomaterials, 4:61-65, 1993.
[20] United States Pharmacopeia 2002. United States Pharmacopeia Convention. Rockville, MDm cop. 2001:1636-1638, 2079-2081.
[21] A.Wada, H.Kubota, H.Hatanaka, H.Miura and Y.Iwamoto, Comparison of Mechanical Properties of Polyvinylidene Fluoride and Polypropylene Monofilament Sutures used for Flexor Tendon Repair, The Journal of Hand Surgery, 26B(3):212-216, 2001.

Antti-Jussi Vuotikka
Oulun yliopisto, Konetekniikan osasto
antti-jussi.vuotikka@oulu.fi

Strain engineering in VO_2 Thin Films

Matti Kangaspuoskari[1], Jyrki Lappalainen[2] and Jarkko Puustinen[2]

[1] Structural Engineering and Construction Technology Laboratory, University of Oulu, P.O. Box 8000, FIN-90014, Finland

[2] Microelectronics and Materials Physics Laboratories, University of Oulu, P.O. Box 8000, FIN-90014, Finland

email: matti.kangaspuoskari@oulu.fi

Summary

Metal-insulator transition (MIT) material undergoes a phase transition in which its crystal structure changes from one symmetry into another. This transformation has severe consequences to the materials properties like degree of conductivity and optical transmittance. Of the many different materials that can be considered, *vanadium oxide* VO_2 is found to be the most interesting from the technological point of view. In recent years, many papers and references considered possibilities to active phase transition control in single crystal VO_2 under of key parameters such as temperature, pressure or stress. Over the decade's experimental result were interpreted to support one or the other of these control scenarios.

Although MIT effect was found already during 1950's, the material science community has just recently started to study these materials for thin-film structures where epitaxial VO_2 layer is tensioned or compressed on top of substrate. The influence of stress-strain effects to phase transition in thin film structures is a new and promising research area.

In thin-film structures, stress and strain state in VO_2 film depends on substrate lattice orientation, thermal stresses, phase transition stresses, and external mechanical loads. These four loading components offer a wide variety to plan a phase transition based electromechanical devices. Modeling using the stress-strain relationship offer possibility to plan MIT effect component so that material goes to phase transition under mechanical loads. Numerical modeling of strain state effects on MIT in VO_2 thin films can be called strain engineering and is essential for design of component performance.

The aim of the this paper is to present how strain engineering techniques can be used in VO_2 thin film structures. The strain is induced in the VO_2 by using substrates with a smaller or larger lattice constant. Phase diagram between phase transition temperature and strain as control parameter in VO_2 bulk- and thin film structures is presented.

Key words: VO_2 thin films, MIT, strain engineering, phase transformation

Introduction

The interest on intelligent materials has grown in the last decades due to their remarkable properties. This class of materials, usually applied as sensors and actuators in the so called intelligent structures, has the ability of changing its electrical and optical properties, shape, stiffness, among other properties, through the imposition of electrical, electric-magnetic, temperature, or stress fields. Nowadays, the most used materials on intelligent structures applications are the shape memory alloys, the piezoelectric ceramics, the magnetostrictive materials, and the electro- and magnetorheological fluids. A common denominator for most of these applications is that their undergoing phase transformations from one crystal structure to another. These transformations have been studied widely for decades by the experimental and theoretical analyses [1].

Very similar phenomenon *Metal-insulator-transition* (MIT) has not got the same interest in macroscopic material modeling, but still it has been studied widely from other point of views [2]. MIT material undergoes a phase transition in which its crystal structure changes from one symmetry into another. This transformation has severe consequences to the materials properties like degree of conductivity and conductivity mechanisms, magnetic ordering, optical transmittance, and refractive index, as shown in figure 1. The underlying mechanism of this transformation lays in the lattice distortions induced by some external force, such as thermal expansion, mechanical force, or electrostrictive effect, leading to a new electronic occupation densities and energy band structure in solid.

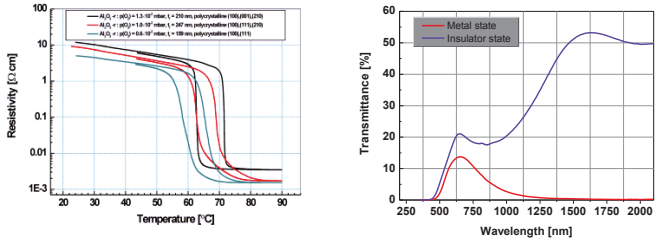

Figure 1. (a) Measured resistivity change of VO_2 thin films as a function of temperature in MIT and (b) optical transmittance spectra $T(\lambda)$ measured in insulator state (black line) and in metal state (red line) as in Ref. [3].

Several material groups and different systems are found to present MIT effect with large diversity in structural complexity, electrical and optical properties, and transition characteristics. Of the many different materials that can be considered, *vanadium oxide compounds* are found to be the most interesting from the technological point of view, not only due to their specific optical properties, simplicity of processing and thin-film deposition, but also due to the possibility of simple tailoring of the transition temperature. VO_2 is particularly interesting because of its low transition temperature 68 ^{o}C [3].

Strain – T_{MIT} phase diagram

Bulk vanadium dioxide (VO_2) undergoes a Mott type metal-insulator transition at T_{MIT} = 68 °C. At this temperature a single crystal VO_2 undergoes a first-order metal-insulator phase transition from the low-temperature insulating monoclinic (M1 or M2) phase to high-temperature metallic tetragonal (R) phase. The MIT in VO_2 is complicated by two low-temperature phases called M1 and M2. In M1 phase vanadium atoms zigzag along *a*-axis ($a_{M1} = (100)_{M1} = (001)_R$) while in M2, only the other half of vanadium atoms zigzag, the other half are strongly organized along the a_{M1} direction. Uncoupling the zigzag structure leads to longer lattice and tensile strain relaxation in a_{M1} direction. In bulk VO_2 at room temperature, M2 phase is unstable structure but it can be stabilized by doping or applied tensile strain. In epitaxial thin film structures, misfit strain behaves similar to doping in single crystals.

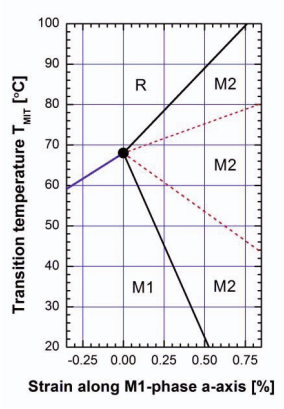

MIT is usually induced by chancing the temperature, pressure or stress in single crystal VO_2. Obviously we need a loading independent parameter to describe the change of transition temperature as function of external load. In early literature control parameter was lattice parameter a_{M1}, *i.e.* lattice parameter in *a*-axis direction in M1 phase. Later control parameter is ε_{aM1}, *i.e.* engineering strain in *a*-axis direction in M1 phase, see later in this paper and in figure 2.

It is interesting to note, that the control parameter of the MIT has always been one dimensional strain or lattice.

Figure 2. Phase equilibrium diagram of single crystal VO_2.

Determination of Poisson ratio

Before further analysis, material properties E and ν must be determined. Young's modulus E = 140 GPa is found from literature [4]. Poisson ratio ν can be determined using three dimensional isotropic linear elastic stress-strain relations $\{\boldsymbol{\sigma}\}=[\boldsymbol{E}]\{\boldsymbol{\varepsilon}\}$ and phase transition control parameter ε_{aM1} shown in figure 2. In Ref. [4], single-crystal VO_2 beams were grown on high temperature along R phase *c*-axis with (110) planes. At room temperature corresponding axis is a_{M1}. Active control of strain was induced by three-point bending so that the strain is ε_{aM1}. A uniaxial compressive strain was measured by strain gauge. Assuming linear one dimensional material model as done in Ref. [4], the stress can be found by using one dimensional Hooke's law shown in formula (1)

$$\sigma_{aM1} = E\varepsilon_{aM1} \tag{1}$$

In Ref. [4], measured total strain ε_{aM1} in full transition at room temperature was ~1.9%

Under the conditions of hydrostatic pressure p, isotropic linear elastic stress-strain relations $\{\boldsymbol{\sigma}\}=[\boldsymbol{E}]\{\boldsymbol{\varepsilon}\}$ can be reduced to the simple form

$$\varepsilon_x = \varepsilon_y = \varepsilon_z = \frac{1-2\upsilon}{E} p \tag{2}$$

Pressure driven phase transition is found in monoclinic VO_2 [5] at room temperature over p = 10 GPa hydrostatic pressures. Using ε_{aM1} in control parameter formulas (1) and (2) lead us to Poisson's ratio $\nu = 0.367$.

Strain induced MIT in VO_2 thin-film structures

Obviously, novel electronic components based on strain induced non-metal to metal transitions in materials such as VO_2 are difficult to develop by single-crystal techniques. More promising idea is to use epitaxial thin films on proper substrates. Strain induced phase transition can be used also in the case of thin films on substrates, which is not yet reported on VO_2 thin films in literature. The main problem is to find a substrate where orientation relationship, *i.e.* misfit strains, between the films and the substrates produces high enough compressive stress along the a_{M1} direction in VO_2.

Strain state in epitaxial VO_2 thin film on substrate

The strain definition is based on an **initial state** against which the current state is compared. In uniaxial extension the **Cauchy strain** or **engineering strain** (strain) is expressed as the ratio of the change in length ΔL per unit of the original length L of a material line element

$$\varepsilon = \Delta L \Big/ L_0 \tag{3}$$

In this expression $\Delta L = L_1 - L_0$, where L_0 is the original length of the material line element and L_1 is the final length of the material line element.

In epitaxial film strain theory the original length, *i.e.* initial state, of the material line element is lattice parameter in bulk material with M1 phase, and the final length is substrates lattice parameter on the surface of substrate. It should be noted, that between initial state and final length the film material undergoes elastic deformation process which consists of stretching/compressing corresponding to substrate lattice, a possible stress relaxation by phase transformation, and finally possible dislocation and/or fracture indicated by the secondary strain relaxation.

Analysis of thin films on substrates is similar to plane stress conditions since this problem is two-dimensional. In the usual notation, the film loaded in the x-y plane, and the zero stress components are $\sigma_z = \tau_{yz} = \tau_{zx} = 0$. It can be shown that isotropic linear elastic stress-strain relation and the strain component ε_z, *i.e.* film thickness direction, takes the following simple forms:

$$\begin{pmatrix} \varepsilon_x \\ \varepsilon_y \\ \gamma_{xy} \end{pmatrix} = \frac{1}{E} \begin{bmatrix} 1 & -\upsilon & 0 \\ -\upsilon & 1 & 0 \\ 0 & 0 & 2(1+\upsilon) \end{bmatrix} \begin{pmatrix} \sigma_x \\ \sigma_y \\ \tau_{xy} \end{pmatrix} \quad \text{and} \quad \varepsilon_z = \frac{-\upsilon}{E}\left(\sigma_x + \sigma_y\right) = \frac{-\upsilon}{1-\upsilon}\left(\varepsilon_x + \varepsilon_y\right) \tag{4}$$

Example of epitaxial VO_2 thin-film

Next, we consider epitaxial VO_2 thin film on *r*-plane Al_2O_3 substrate. Orientation of the thin-film-substrate structure is now VO_2 (100) [010] // Al_2O_3 (1102) [1120], and stress-strain state in VO_2 film can be written by three dimensional linear elastic material model shown in formula (4). Lattice orientations are shown in figure 3.

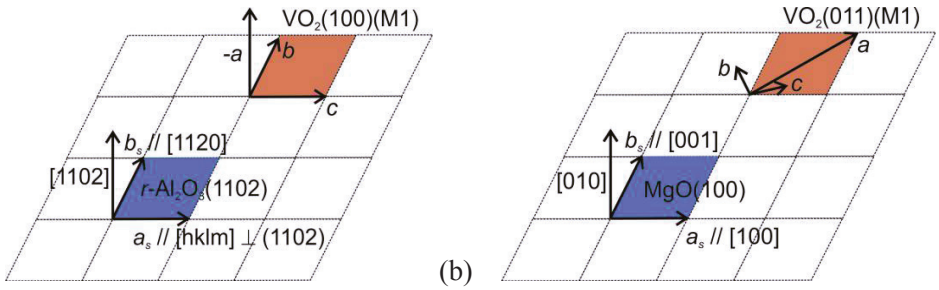

Figure 3. (a) Lattice orientation in VO_2 thin film on *r*-plane Al_2O_3 and (b) on MgO substrate [6].

Results and discussion

Using these lattice parameters, misfit strains in VO_2 thin film in M1 phase on *r*-plane Al_sO_3 substrate can be written as shown in formula (3)

$$\varepsilon_{bM1} = \frac{b_s - b_{M1}}{b_{M1}} = +5.3\% \qquad \text{and} \qquad \varepsilon_{cM1} = \frac{a_s - c_{M1}}{c_{M1}} = -4.6\% \tag{5}$$

Assuming plane stress state in thin film (σ_a = 0), the strain ε_a can be written using formula (4), such that

$$\varepsilon_{aM1} = \frac{-\upsilon\,(\varepsilon_b + \varepsilon_c)}{(1-\upsilon)} = -0.40\% \tag{6}$$

Strain in a_{M1}-axis direction in negative and VO_2 film is in M1 phase (see figure 2).

Table 1. Lattice parameters of substrates and VO_2 thin films.

a-Al_2O_3 (1120)		*r*-Al_2O_3 (1102)		*c*-Al_2O_3 (0001)		MgO		VO_2		
a_s (Å)	b_s (Å)	a_s (Å)	b_s (Å)	a_s (Å)	b_s (Å)	b_s (Å)	c_s (Å)	a_{M1} (Å)	b_{M1} (Å)	c_{M1} (Å)
5.544	5.512	5.125	4.763	5.500	5.500	4.216	4.216	5.743	4.517	5.375

In figure 4, measured transition temperatures T_{MIT} in VO_2 thin films on four different substrates reported. On *a*-plane Al_2O_3 and *r*-plane Al_2O_3 substrates, VO_2 a_{M1}-axis is in film thickness direction, as shown in figure 3a. The lattice constant a_{M1} has been measured by X-ray diffraction and T_{MIT} vs. ε_{aM1} is shown in figure 4.

On *c*-plane Al_2O_3 and MgO substrates, VO_2 a_{M1}-axis is in substrate surface direction, as shown in figure 3b. In these cases, the lattice constant a_{M1} could not be measured in used θ–2θ construction. For solid-solid reactions, the ratio $dT/d\varepsilon$ is nearly constant, *i.e.* a linear relationship between the stress and the temperature occurs. The slope of the linearity, *i.e.* $dT/d\varepsilon$, is determined and strain ε_{aM1} corresponding to measured T_{MIT} is calculated. Results are shown in figure 4.

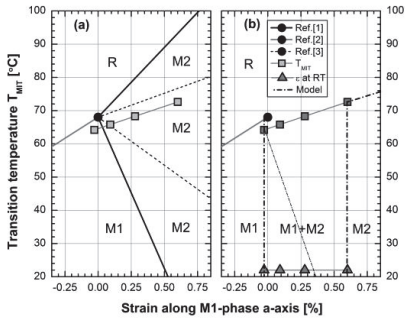

In the case of calculated example VO_2 on *r*-plane Al_2O_3, the strain ε_{aM1} = – 0.40% means that transition temperature is 6.6 ºC lower than in single crystal (see figure 2). The results did not match measured value shown in figure 4.

X-ray diffraction results indicated highly orientated VO_2 thin films [7] but numerical modeling above showed that films cannot be epitaxial without stress relaxation by M1-M2 phase transition and/or dislocations.

Figure 4. Phase equilibrium diagram of VO_2 thin film on substrate [7].

References

[1] W.D. Callister Jr., *Materials Science and Engineering*, *An Introduction*, John Wiley & Sons, 2007.

[2] M. Imada, A. Fujimori, Y. Tokura, Metal-insulator transitions. *Reviews of Modern Physics*, 70:1039–1263, 1998.

[3] J. Lappalainen, S. Heinilehto, H. Jantunen and V. Lantto, Electrical and Optical Properties of Metal-Insulator-Transition VO_2 Thin Films, *Journal of Electroceramics*, 22:73-77, 2009.

[4] J. Cao, E. Ertekin, V. Srinivasan, W. Fan, S. Huang, H. Zheng, J. W. L. Yim, D. R. Khanal, D.F. Ogletree, J.C. Grossman & J. Wu, Strain engineering and one-dimensional organization of metal–insulator domains in single-crystal vanadium dioxide beams, *Nature Nanotechnology*, 4:732-737, 2009.

[5] L.A. Ladd and W. Paul, Optical and transport properties of high quality crystals of V_2O_4 near the metallic transition temperature, *Solid State Communications*, 7(4): 425-428, 1969.

[6] J. Lappalainen, M. Kangaspuoskari and J. Puustinen, Phase-Coexistence Phenomenon in Metal-Insulator-Transition of VO_2 Thin Films, *Abstract book of Electroceramics XIII – 2012*, Twente, Netherlands, 24-27 June 2012.

[7] M. Kangaspuoskari, J. Lappalainen and J. Puustinen, Strain Engineering of Metal-Insulator-Transition Phenomenon of VO_2 Thin Films. *Proceedings of the 46th annual meeting of the Finnish Physical Society*, Physics Days, University of Eastern Finland, Joensuu, 13–15 March 2012 (http://www.uef.fi/fp2012).

Numerical modelling of ice rubble with three dimensional discrete element method

Arttu Polojärvi and Jukka Tuhkuri

Abstract. Numerical simulations on ice rubble were performed using three dimensional discrete element method. In this modelling technique, rubble is modelled as discontinuum i.e. each block in the rubble is modelled and the rubble deformation is due to the motion of the individual blocks within it. The model was applied on simulations of ice rubble punch through experiments, in which a flat indentor penetrates floating rubble mass. This experimental technique is commonly used to derive ice rubble properties, even if the accurate interpretation of the experiment results is far from straightforward. The model was successfully validated using the results from a series of laboratory scale punch through experiments on rubble consisting of plastic blocks. The simulations helped in gaining insight on the interpretation of the punch through experiment results. The results clearly showed, that the evolution of deformation patterns was related to the load records demonstrating the need for the numerical model to correctly present the deformation of the rubble mass. Further, the behaviour earlier interpreted as rubble material softening during an experiment was observed to be due to a change in the rubble geometry.

Keywords: Discrete element method, ice mechanics, ice loads

Introduction

Punch through experiments are an important method for testing ice rubble properties. In a punch through experiment, a flat indentor platen penetrates a rubble mass floating in the water, while the force applied by the rubble on the indentor is measured. The force records are then used to derive some rubble material properties. The accurate interpretation of the results in terms of material modelling is anyhow very challenging. Punch through experiments have been performed in laboratory and full scale by several authors [1].

In this work, laboratory scale punch through experiments were performed using rubble consisting of plastic blocks and numerically modelled using 3D discrete element method (DEM) [2]. The motivation of using plastic blocks in the experiments instead of ice blocks was to simplify the interpretation of the results. In the numerical model, the rubble consisted of individual rigid blocks which interacted through contacts. In ice mechanics, discrete approach in modelling has been earlier used e.g. in studies of ice ridging [3], ice pile-up against structures [5] and punch through experiments [6, 7].

In the following, we present and compare some results from the experiments and the simulations of the experiments. Through the comparison we validate the model and demonstrate its applicability in ice mechanics. Then we use the simulation results to further analyze the experiments. Using the model, we showed, that the evolution of the deformation patterns was closely related to the indentor force records, and observed that the behaviour earlier interpreted as rubble material softening during an experiment was due to a change in the rubble geometry. This work is reported in detail in [6].

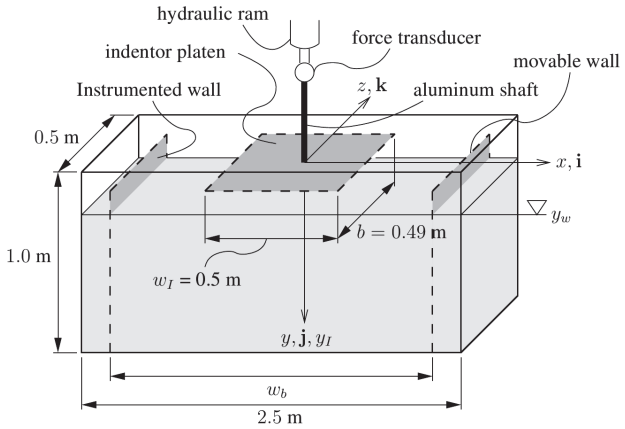

Kuva 1. Experimental set up. Direction of the indentor motion y_I is indicated. The figure does not show the rubble floating in the water (gray) nor the covers used in some experiments for clarity. In the figure, w_b is the basin width that could be altered.

Experiments

Our test basin with its dimensions is illustrated in Figure 1. The basin was made of transparent acrylic glass (PMMA) and was supported by a steel frame. The indentor platen was made of polyethylene (PE). The basin had movable PE walls attached to the basin frame which enabled to change its width (w_b). In some experiments PE covers were installed into the basin. The plastic rubble blocks had a shape of a rectangular cuboid and were sawn out of $0.09 \times 0.05 \times 0.02$ m in size.

Two different types of punch through experiments with various rubble thicknesses were conducted: uncovered and covered basin experiments. The experiment types differed by the boundary conditions on the top of the rubble. In the covered basin experiments, the rubble besides the indentor platen was covered. These boundary conditions can be compared to the ones in a punch through experiment on ice rubble with frozen consolidated layer on top of the rubble. In uncovered basin experiments the covers were not used and in this case the experiments can be compared to those performed on loose ice rubble. More data on the experiments can be found from [6].

The experiments were recorded and the video recordings were post processed using a motion tracking software, which detected and tracked the block corners throughout the experiment giving their trajectories. These trajectories were used in the analysis of rubble deformation as described in detail in [6].

Simulations

In the 3D discrete numerical model used, the rubble pile consisted of numerous individual rigid blocks interacting through contacts. In addition to forces due to contacts, the block forces were due to buoyancy, gravitation and a simple model for water drag. The properties and size of the simulated blocks and the simulation domain were chosen after the blocks used in the experiments. The simulations were explicit. The initial configuration of the rubble in the simulations was random (see Figure 2). See [6] for more details on simulations.

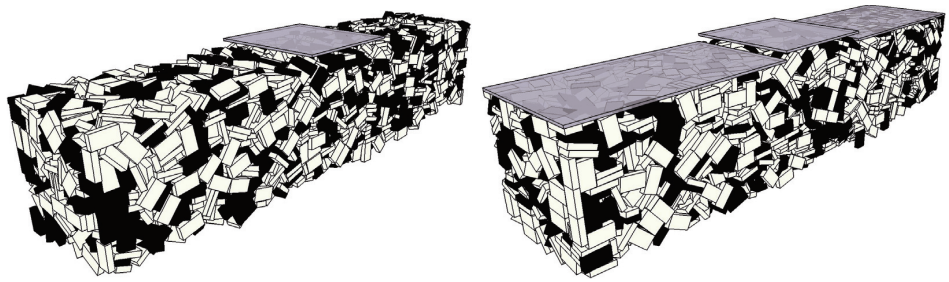

(a) (b)

Kuva 2. The simulations of (a) uncovered and (b) covered experiments showing the random initial configurations of the rubble.

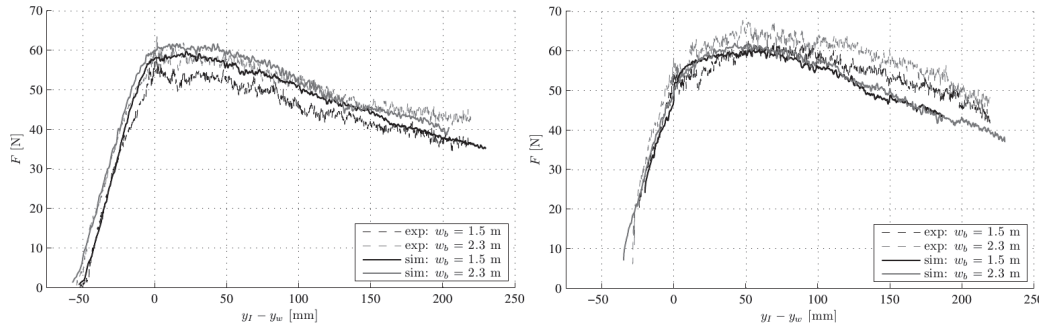

Kuva 3. The mean rubble load $\bar{F}_R$ records from the experiments and the simulations of experiments and simulations with both basin widths w_b: (a) uncovered and (b) covered basin. The x-axis shows the indentor position in relation to the water surface y_w.

Results and validation of the numerical model

The rubble load-indentor displacement, $\bar{F}_R - y_I$, records from the experiments and simulations were in very good agreement (see Figure 3): $\bar{F}_R$ first increased with the same rate and reached its maximum with approximately equal indentor displacement. The maximum rubble load $\bar{F}_R^m$ values were also approximately equal in the experiments and the simulations (see Figures 4 a and b). The basin width had no major effect on F_R records nor F_R^m values as Figures 3 and 4 show.

Snapshots in Figure 5 illustrate rubble deformation in covered basin experiments and corresponding simulations. In the first snapshot with $y_I = 35$ mm, the indentor platen has reached the water surface and a wedge shaped volume of rubble under the indentor is observed to move downwards with it (polygon with red border including rubble moved by more than $0.9y_I$ in the figure). The next snapshot with $y_I = 80$ mm shows the deformation patterns at the maximum rubble load F_R^m. The volume of displaced rubble has increased from the previous snapshot due to widening of the rubble volumes moved by less than $0.9y_I$. The last snapshot with $y_I = 240$ mm shows rubble deformation still being similar in the simulations and experiments. Lateral movement of the rubble towards the indentor center line above the indentor platen is observed.

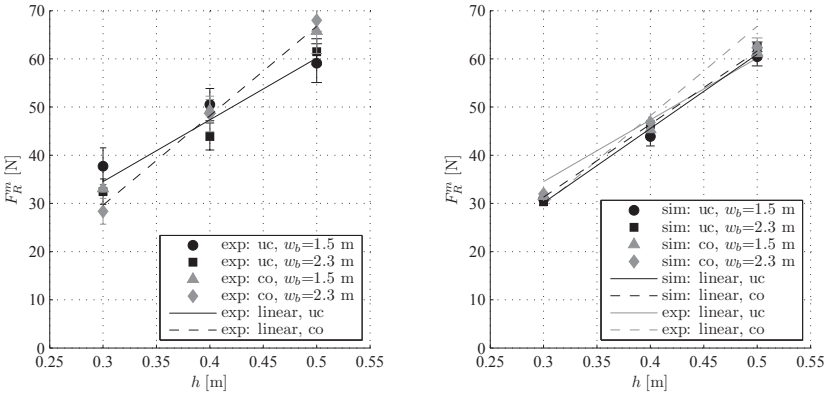

(a) (b)

Kuva 4. Maximum rubble load F_R^m in (a) uncovered (un) and covered (co) basin experiments and in (b) corresponding simulations. The linear fits in the figures for different experiment types include data from experiments and simulations with both basin widths w_b.

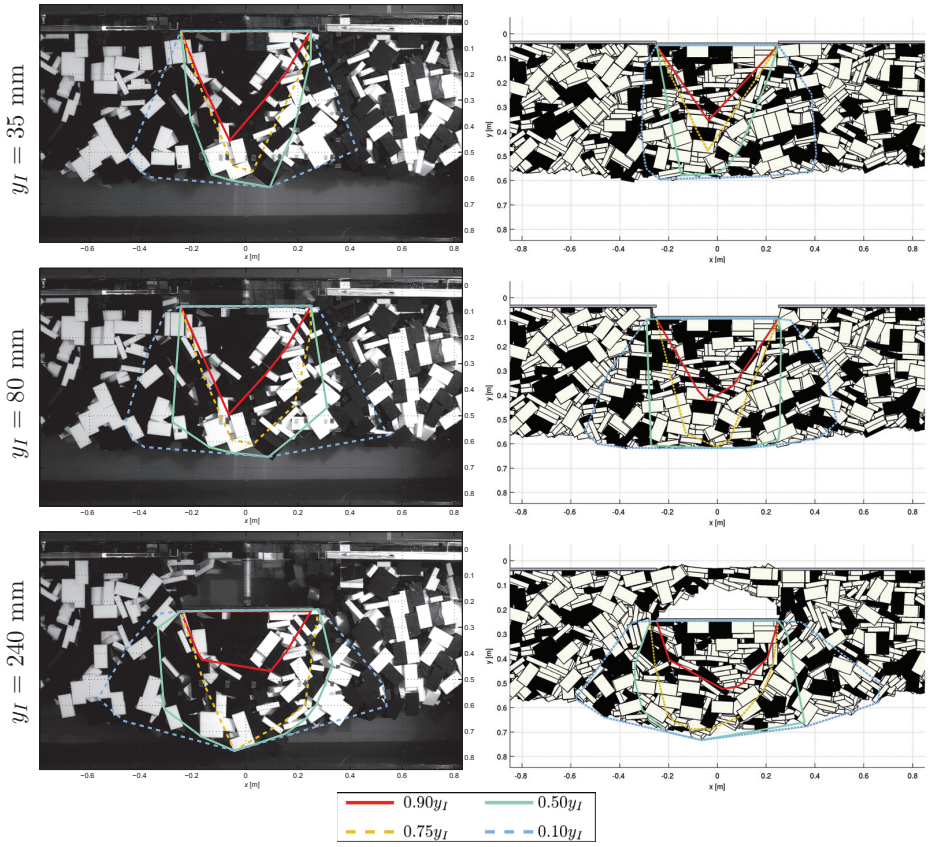

Kuva 5. Two sequences of snapshots from a covered basin experiment (left) and a corresponding simulation (right) illustrating rubble deformation patterns with increasing indentor displacement y_I. The volumes of rubble moved by various ratios of y_I are indicated with colored lines.

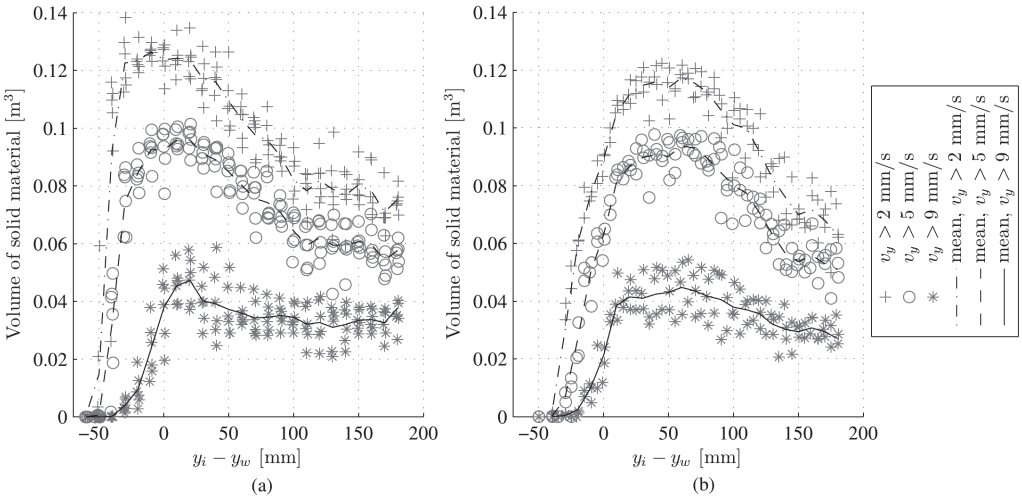

Kuva 6. The volumes of blocks moving downwards in simulated experiments with velocities $v_y = 9, 5$ and 2 mm/s: (a) uncovered and (b) covered basin simulations. The x-axis shows the indentor position y_I in relation to the water line y_w. In all simulations shown rubble thickness $h = 0.5$ m and rubble thickness $v_I = 10$ mm/s. Data from simulations with both basin widths is included in the figures.

Analysis and discussion

The simulation data was used to analyze the relation between the load $\bar{F}_R$ and rubble deformation fields in more detail as the analysis was not limited only on the visible part of the rubble. The displacing rubble volume during simulated experiments is illustrated by Figures 6 a and b using the velocities of the blocks. The figures show the total volume of blocks with their centroids having the downward velocities $v_y > 2$ mm/s, $v_y > 5$ mm/s, and $v_y > 9$ mm/s in simulations with indentor velocity $v_I = 10$ mm/s.

Figure 6 shows two distinct features: (1) the experiment type has an effect on the evolution of the displacing rubble volumes and (2) the volume of displacing rubble is at its maximum close to the maximum rubble load F_R^m. As a consequence of downwards moving rubble volume increasing during longer displacement interval in the covered than in the uncovered basin experiments, the maximum rubble load F_R^m is reached later in covered experiments.

As Figure 6 further shows, the volume of solid material moving downwards decreased in all simulations towards the end of the indentor stroke. This resulted into a decrease in $\bar{F}_R$. The decrease in $\bar{F}_R$ has earlier been mistaken as material softening. A numerical model needs to correctly represent the rubble deformation and its mass flow to simulate this phenomena.

Conclusions

Laboratory scale punch through tests on floating rubble consisting of plastic blocks were conducted and simulated with a 3D discrete numerical model. The discrete numerical method simulated the experiments well: the experimental force records and the deformation patterns of the rubble during indentor stroke were in good agreement with the simulation results. The model was then used to analyze the experiments.

References

[1] Liferov, P. and Bonnemaire, B. (2005). Ice rubble behaviour and strength: Part I. review of testing and interpretation of results. *Cold Regions Science and Technology*, 41:135–151.

[2] Cundall, P. and Strack, O. (1979). A discrete numerical model for granular assemblies. *Géotechnique*, 29:47–65.

[3] Hopkins, M. (1998). Four stages of pressure ridging. *Journal of Geophysical Research*, 103(C10):21,883–21,891.

[4] Paavilainen, J., Tuhkuri, J., and Polojärvi, A. (2011). 2D numerical simulations of ice rubble formation process against an inclined structure. *Cold Regions Science and Technology*, 68(1-2).

[5] Paavilainen, J., Tuhkuri, J., (2012). Pressure distributions and force chains during simulated ice rubbling against sloped structures. *Cold Regions Science and Technology*, accepted manuscript.

[6] A. Polojärvi, A., J. Tuhkuri, J., Korkalo, O. (2012a). Comparison and analysis of experimental and virtual laboratory scale punch through tests. *Cold Regions Science and Technology*, 81 (2012), pp. 11-25.

[7] Polojärvi, A. and Tuhkuri, J. (2012b). On modeling cohesive ridge keel punch through tests with a combined finite-discrete element method. *Cold Regions Science and Technology*, accepted manuscript.

Arttu Polojärvi and Jukka Tuhkuri
Aalto University, School of Engineering
Department of Applied Mechanics
P.O.Box 14300, FI-00076 Aalto
E-mail: `arttu.polojarvi@aalto.fi, jukka.tuhkuri@aalto.fi`

Akustisen aallon sironta elastisesta kappaleesta

Timo Lähivaara ja Tomi Huttunen

Tiivistelmä. Työssä tarkastellaan kytkettyjen aalto-ongelmien (akustinen ja elastinen aaltoyhtälö) ratkaisuja kolmidimensionaalisissa sirontaongelmissa. Esimerkkiongelmana tutkitaan merenpohjassa olevasta pallonmuotoisesta elastisesta kappaleesta heijastuvaa akustista aaltokenttää. Käytetyssä laskentamallissa aaltoyhtälöiden paikkaderivaatat ratkaistaan käyttäen epäjatkuvaa Galerkinin (engl. *discontinuous Galerkin*) menetelmää ja aikaderivaatat eksplisiittisellä *low-storage Runge-Kutta* aikaintegrointimenetelmällä.

Avainsanat: epäjatkuva Galerkinin menetelmä, eksplisiittinen aikaintegrointi, numeerinen vaimennuskerroin, sirontaongelmat

Johdanto

Lukuisilla tekniikan ja fysiikan osa-alueilla on tarpeen simuloida värähtelypulssien etenemistä ongelmissa, jotka sisältävät sekä elastisen että akustisen väliaineen. Näitä tutkimuskohteita ovat esimerkiksi rakenteiden mekaaniset värähtelyt, seismologia tai ultraäänellä tehtävä rakennetutkimus. Tässä työssä keskitytään meren pohjassa olevien elastisten kappaleiden tunnistamiseen niiden sirottaman akustisen kentän perusteella.

Tutkimuksessa aaltopulssin simulointiin käytetään epäjatkuvaa Galerkinin (engl. *discontinuous Galerkin (DG)*) [1] menetelmää. Menetelmän etuina ovat muun muassa geometrinen joustavuus ja tehokas rinnakkaistuminen moniprosessoritietokoneille. Kattava lähdeteos DG menetelmään on Hesthavenin ja Warburtonin vuonna 2007 kirjoittama kirja [2]. Tässä työssä käytetty laskentamalli on kuvattu viitteessä [3].

Tutkimus on jatkoa julkaisuun [4], jossa tarkasteltiin akustisen aallon sirontaa merenpohjaan sijoitetusta sylinterimuotoisesta kappaleesta. Ratkaistava fysikaalinen malli (kytketty akustinen ja elastinen aaltoyhtälö) on esitetty viitteessä [4]. Tämän tutkimuksen motiivina on tarkastella, kuinka suuri vaikutus havaittavaan heijastukseen on kappaleen upotuksella sedimenttiin. Numeerisissa esimerkeissä käytetään kolmea sirottavan kappaleen kappaleen upotussyvyyttä:

1) kappale sijaitsee sedimentin pinnalla,

2) kappale on puoliksi upotettu vesi-sedimentti rajapintaan,

3) kappale on kokonaan vesi-sedimentti rajapinnan alapuolella.

Sironnutta kenttää havainnoidaan aika-taajuuskuvaajana (spektrogrammi).

Numeeriset esimerkit

Esimerkissä tarkastellaan tasoaallon sirontaa merenpohjaan sijoitetusta pallonmuotoisesta kappaleesta. Kappale on sijoitettu kolmelle syvyydelle ks. Kuva 1. Kyseistä ongelmaa

on tutkinut Zampolli kollegoineen viitteessä [5]. Heidän tutkimuksessa ongelmaa tarkastellaan taajuustasossa, mutta tässä työssä aallon etenemistä ja sirontaa käsitellään aikatason ongelmana.

Kuvassa 1 on esitetty tutkittavan esimerkkiongelman geometriat. Alueet on määritelty seuraavasti vesi: $\Omega_1 = [-2,\ 2] \times [-2,\ 2] \times [0,\ 2]$ m^3 ja sedimentti: $\Omega_2 = [-2,\ 2] \times [-2,\ 2] \times [-2,\ 0]$ m^3. Alueen ulkoreunalle on lisätty numeerinen vaimennuskerros, jonka paksuus on 50 cm (tarkemmin kuvattu viitteessä [4]). Tutkittavan alueen ulkoreunalle asetetaan absorboiva reunaehto [8]. Sirottava kappale on 0.5 m säteinen pallo, jonka kuoren paksuus on 1 cm [5]. Kappale on sijoitettu kolmelle eri syvyydelle z_r (0.5 m, 0 m, -0.7 m). Ongelman fysikaaliset parametrit on listattu Taulukossa 1.

Taulukko 1. Tutkittavan sirontaongelman fysikaaliset parametrit [5].

	c_P (m/s)	c_S (m/s)	ρ (kg/m^3)
vesi	1500	-	1000
sedimentti	1600	-	1800
kuori	3500	1400	3000
täyte	2500	1200	2000

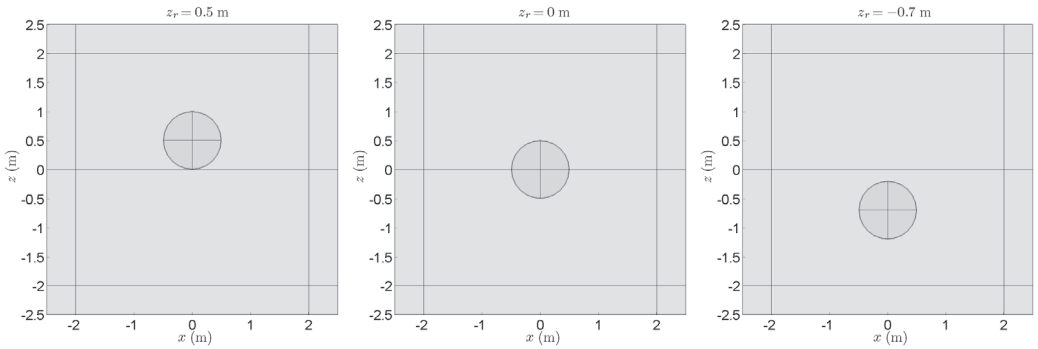

Kuva 1. Tutkittavan ongelman geometria. Sirottavan kappaleen keskipisteen z-koordinaatti on nähtävillä kuvien otsikossa.

Tutkittavan alueen ulkoreunalla käytettävä numeerinen vaimennuskerros [7, 4] estää tasoaaltoherätteen tuottamisen alueen ulkoreunalta (esimerkiksi epähomogeenisella reunaehdolla). Tämän vuoksi tasoaalto tuotetaan PML ja ei-PML alueiden väliseltä rajapinnalta Γ_{vesi} (vain vesialueessa). Koska käytetyssä laskentamallissa (epäjatkuva Galerkinin menetelmä) jatkuvuus elementtien rajapinnoilla määritellään jatkuvuusehtojen (paine ja nopeus) avulla, voidaan tätä rajapintaa käyttää myös tuottamaan tasoaalto alueeseen [4].

Tutkimuksessa herätteenä käytetään *Ricker*-wavelettia, joka voidaan kirjoittaa seuraavasti

$$g(t) = \left(0.5 + \alpha\,(t - t_0)^2\right) \exp\left(\alpha\,(t - t_0)^2\right) \quad \forall t \geqslant 0, \quad \text{rajapinnalla} \quad \Gamma_{vesi}, \tag{1}$$

missä $\alpha = -(f_c \pi)^2$ ja $t_0 = 0.3$ ms. Keskitaajuudeksi f_c valitaan 5 kHz. Tutkittavan ongelman loppuaika on määrätty arvoon $t_{\max} = 5$ ms, jonka aikana pulssi etenee ko-

konaisuudessaan tutkittavan alueen läpi. Tasoaallon tulosuunnaksi asetetaan 25-astetta xz-tasossa.

Paineen spektrogrammit (kaikille sirottajan upotussyvyyksille z_r) havaintopisteessä $(x_o, y_o, z_o) = (-1.6, 0, 0.8)$ m on esitetty Kuvassa 2. Spektrogrammien laskentaan käytetään Matlabin funktiota *spectrogram*, jossa asetetaan aikaikkunaksi 0.38 ms ja päällekkäisten havaintojen ajaksi 0.37 ms. Kuvaajat on esitetty havaitulle signaalille $p_{total} = p_{tuleva} + p_{sironnut}$, joten jokaisessa kuvaajassa havaitaan samanmuotoinen herätesignaali (ajanhetkellä ~ 0.9 ms). Edelleen, ajanhetkellä ~ 1.4 ms havaintaan vesi-sedimentti rajapinnasta syntynyt heijastus ja ajanhetkellä $\sim$ 2.4-3.0 ms sylinterin pinnasta syntyvä ensimmäinen takaisinheijastus (aikaväli johtuu upotussyvyydestä).

Sirottavan kappaleen pinnalta tuleva ensimmäinen heijastunut aalto on amplitudiltaan merkittävästi pienempi $z_r = -0.7$ m tapauksessa. Muutenkin $z_r = -0.7$ m tapauksessa havaittu spektrogrammi on merkittävästi vaimeampi suhteessa kahden muun upotussyvyyden tuloksiin. Syvyyksillä $z_r = 0$ m ja $z_r = 0.5$ m havaituista spektrogrammeista nähdään selkeästi monimutkaisempi resonanssirakenne, joka helpottaa kappaleen tunnistamista.

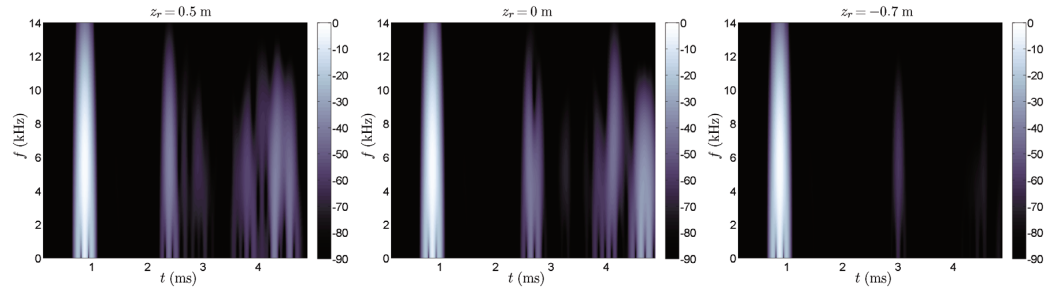

Kuva 2. Paineen spektrogrammit havaintopisteessä $(x_o, y_o, z_o) = (-1.6, 0, 0.8)$ m. dB-asteikko määritellään $\mathrm{SPL(dB)} = 20 \log_{10}(|p|/p_{ref})$, missä $p_{ref} = 10^{-6}$ Pa.

Pohdinta

Työssä tutkittiin aalto-ongelmia kytketyissä ongelmissa. Tutkimuksessa kytketyillä malleilla tarkoitetaan mallinnusongelmia, jotka sisältävät akustisen ja elastisen väliaineen. Työssä tarkasteltiin sirontaongelmia tapauksissa, joissa sirottava kappale sijoitetaan eri syvyyksille vesi-sedimentti rajapinnalla. Akustinen heräte (*Ricker*-wavelet) tuotettiin laskenta-alueeseen mielenkiintoalueen ulkoreunalta.

Laskentamallina käytettiin epäjatkuvaa Galerkinin menetelmää ratkaisemaan tutkittavan fysikaalisen ongelman paikkaderivaatat. Aikaderivaattoja arvioitiin eksplisiittisellä *low-storage Runge-Kutta* lähestymistavalla. Laskentamalli on rinnakkaistettu MPI:llä (engl. *message passing interface*), joten se soveltuu hyvin käytettäväksi supertietokoneissa ja laskentaklustereissa. Laskentaympäristönä käytettiin Tieteen tietotekniikka keskuksen (CSC) *Louhi* supertietokonetta.

Tutkimuksen seuraavassa vaiheessa tavoitteena on ratkaista käänteisongelma, missä sironneesta signaalista lasketaan sirottavan kappaleen sijainti ja määritetään kappaleen sisäinen rakenne.

Viitteet

[1] W. Reed ja T. Hill, *Triangular mesh methods for the neutron transport equation*, Technical report, Los Alamos National Laboratory, 1973.

[2] J. Hesthaven ja T. Warburton, *Nodal Discontinuous Galerkin Methods: Algorithms, Analysis, and Applications*, Springer, 2007.

[3] T. Lähivaara ja T. Huttunen, *A non-uniform basis order for the discontinuous Galerkin method of the 3D dissipative wave equation with perfectly matched layer*, Journal of Computational Physics, 229(13):5144–5160, 2010.

[4] T. Lähivaara ja T. Huttunen, *Akustisen aallon sironta elastisesta kappaleesta*, Rakenteiden Mekaniikka, 45(1):34–44, 2012.

[5] M. Zampolli, F.B. Jensen ja A. Tesei, *Benchmark problems for acoustic scattering from elastic objects in the free field and near the seafloor*, Journal of the Acoustical Society of America, 125(1):89–98, 2009.

[6] R.J. Leveque, *Finite Volume Methods for Hyperbolic Problems*, Cambridge Texts in Applied Mathematics, 2002.

[7] S. Abarbanel ja D. Gottlieb, *On the construction and analysis of absorbing layers in CEM*, Applied Numerical Mathematics, 27:331:340, 1998.

[8] B. Engquist ja A. Majda, *Absorbing boundary conditions for the numerical simulation of waves*, Mathematics of Computation, 31(139):629–651, 1977.

Timo Lähivaara
Itä-Suomen yliopisto
Sovelletun fysiikan laitos
PL 1627
70211 Kuopio
timo.lahivaara@uef.fi

Tomi Huttunen
Kuava Oy
PL 1188
70211 Kuopio
Itä-Suomen yliopisto
Sovelletun fysiikan laitos
PL 1627
70211 Kuopio
tomi.huttunen@uef.fi

Optimized low-order explicit Runge-Kutta schemes for the high-order spectral difference method

Matteo Parsani, David I. Ketcheson and Willem Deconinck

Summary. Optimal explicit Runge-Kutta (ERK) schemes with large stable step sizes are developed for method-of-lines discretizations based on the spectral difference (SD) spatial discretization on quadrilateral grids. These methods involve many stages and provide the optimal linearly stable time step for a prescribed SD spectrum and the minimum leading truncation error coefficient, while admitting a low-storage implementation. Using a large number of stages, the new ERK schemes lead to efficiency improvements larger than 60% over standard ERK schemes for 4^{th}- and 5^{th}-order spatial discretization.

Key words: Optimized explicit Runge-Kutta, High-order spectral difference method, Wave propagation.

Introduction

Throughout the past two decades, the development of high-order accurate spatial discretization has been one of the major fields of research in computational fluid dynamics (CFD), computational aeroacoustics (CAA), computational electromagnetism (CEM) and in general computational physics. High-order discretizations have the potential to improve the computational efficiency required to achieve a desired error level by allowing use of coarser grids. Moreover, since computational science is increasingly used as an industrial design and analysis tool, high-order accuracy must be achieved on unstructured grids, which are required for efficient meshing. These needs have been the driving force for the development of a variety of higher order schemes for unstructured meshes such as the Discontinuous Galerkin (DG) method [1], the Spectral Volume (SV) method [2], the Spectral Difference (SD) method [3], the Energy Stable Flux Reconstruction [4], etc.

High-order schemes are usually much stiffer than lower-order ones, so the maximum stable CFL number usually decreases rapidly with increasing order of accuracy. Therefore, the step size is often based on stability considerations when obtaining time-accurate solutions with explicit schemes.

This work focuses on the development of new optimized ERK schemes for accurate and efficient computation of wave propagation problems with high-order SD methods. A two-step optimization procedure is used to design optimal ERK schemes. First, a new, robust, fast and accurate optimization algorithm is employed to find the optimal stability function that maximizes the linear stable step size of the ERK scheme for a prescribed SD Fourier footprint computed by discretizing the two-dimensional (2D) advection equation. A second optimization step is used to determine the Butcher coefficients of the scheme, optimized for a small leading truncation error constant and constrained to be implementable in a low-storage form.

In [5] has been shown that the SD discretization error typically dominates, when both spatial and temporal discretizations have the same accuracy. Therefore, for a fixed order

of accuracy the error is almost independent of the CFL number and large time steps can be used. This feature has led to a new ongoing line of research where the ultimate goal is to investigated if efficient and accurate low-order ERK schemes can be developed for high-order SD discretizations. In fact, the coefficients of a low-order method must satisfy fewer order conditions which implies a larger number of free parameters in the optimization process. Following this idea, we present the performance of low-order ERK schemes for a 4^{th}-order SD discretization applied to a compressible Euler flow past a wedge.

Spectral difference method

Consider a problem governed by a general system of conservation laws given by Equation (1) and valid on a domain $\Omega \subset \mathbb{R}^d$ and completed with consistent initial and boundary conditions.

$$\frac{\partial \mathbf{w}}{\partial t} + \vec{\nabla} \cdot \vec{\mathbf{f}} = 0, \tag{1}$$

The domain is divided into N non-overlapping cells. In order to achieve an efficient implementation of the SD method, all hexahedral cells in the physical domain are mapped into cubic elements using local coordinates $\vec{\xi} = [\xi_1, \xi_2, \xi_3]^T$. Such a transformation is characterized by the Jacobian matrix $\vec{\vec{\mathrm{J}}}_i$ with determinant $det(\vec{\vec{\mathrm{J}}}_i)$. Therefore, system (1) can be written in the mapped coordinate system as

$$\frac{\partial \mathbf{w}_i^{\vec{\xi}}}{\partial t} = -\frac{\partial \mathbf{f}_{1,i}^{\vec{\xi}}}{\partial \xi_1} - \frac{\partial \mathbf{f}_{2,i}^{\vec{\xi}}}{\partial \xi_2} - \frac{\partial \mathbf{f}_{3,i}^{\vec{\xi}}}{\partial \xi_3} = -\vec{\nabla}^{\vec{\xi}} \cdot \vec{\mathbf{f}}_i^{\vec{\xi}}, \qquad 1 \leq i \leq N, \tag{2}$$

where $\mathbf{w}_i^{\vec{\xi}} \equiv det(\vec{\vec{\mathrm{J}}}_i)\,\mathbf{w}$ and $\vec{\nabla}^{\vec{\xi}}$ are the conserved variables and the divergence differential operator in the mapped coordinate system, respectively.

For a $(p+1)$-th-order accurate d-dimensional scheme, N^s *solution collocation points* with index j are introduced at positions $\vec{\xi}_j^s$ in each cell i, with N^s given by $N^s = (p+1)^d$. Given the values at these points, a polynomial approximation of degree p of the solution in cell i can be constructed. This polynomial is called the *solution polynomial* and is usually composed of a set of Lagrangian basis polynomial $L_j^s\left(\vec{\xi}\right)$ of degree p:

$$\mathbf{W}_i\left(\vec{\xi}\right) = \sum_{j=1}^{N^s} \mathbf{W}_{i,j}\, L_j^s\left(\vec{\xi}\right), \qquad 1 \leq i \leq N. \tag{3}$$

The interpolation coefficients $\mathbf{W}_{i,j}$ are the unknowns of the SD method.

The divergence of the mapped fluxes $\vec{\nabla}^{\vec{\xi}} \cdot \vec{\mathbf{f}}^{\vec{\xi}}$ at the solution points is computed by introducing a set of N^f flux collocation points with index l and at positions $\vec{\xi}_l^f$, supporting a polynomial of degree $p+1$. The evolution of the mapped flux vector $\vec{\mathbf{f}}^{\vec{\xi}}$ in cell i is then approximated by a flux polynomial $\vec{\mathbf{F}}_i^{\vec{\xi}}$, which is obtained by reconstructing the solution variables at the flux points and evaluating the fluxes $\vec{\mathbf{F}}_{i,l}^{\vec{\xi}}$ at these points. The flux is also represented by a Lagrange polynomial:

$$\vec{\mathbf{F}}_i^{\vec{\xi}}\left(\vec{\xi}\right) = \sum_{l=1}^{N^f} \vec{\mathbf{F}}_{i,l}^{\vec{\xi}}\, L_l^f\left(\vec{\xi}\right), \tag{4}$$

The solution at a face is in general not continuous and requires the solution of a Riemann problem to maintain conservation at a cell level. Approximate Riemann solvers, such as the Roe solver, are typically used. The tangential component of $\vec{\mathbf{F}}^{\vec{\xi}}_{\text{num}}$ is usually taken from the interior cell.

Taking the divergence of the flux polynomial $\vec{\nabla}^{\vec{\xi}} \cdot \vec{\mathbf{F}}^{\vec{\xi}}_i$ in the solution points results in the following modified form of (2):

$$\frac{d\mathbf{W}_{i,j}}{dt} = -\vec{\nabla} \cdot \vec{\mathbf{F}}_i \Big|_j = -\frac{1}{J_{i,j}} \vec{\nabla}^{\vec{\xi}} \cdot \vec{\mathbf{F}}^{\vec{\xi}}_i \Big|_j = \mathbf{R}_{i,j}, \tag{5}$$

where $\mathbf{R}_{i,j}$ is the SD residual associated with $\mathbf{W}_{i,j}$. This is a system of ODEs, in time, for the unknowns $\mathbf{W}_{i,j}$ which will be solved with the new optimized ERK schemes presented in this work.

Optimized Runge–Kutta schemes

In general, the stability function $\psi(z)$ for an s-stage, order p, ERK method is a polynomial of degree s that differs from the exponential function by terms of order z^{p+1}:

$$\psi(z) = \sum_{j=0}^{s} \beta_j z^j = \sum_{j=0}^{p} \frac{1}{j!} z^j + \sum_{j=p+1}^{s} \beta_j z^j, \tag{6}$$

where z is in general a complex number.

It is natural then to design optimal polynomials by choosing the coefficients β_j in (6) so as to maximize maximum linearly stable CFL number ν_{stab}. The optimization problem may be stated formally as follows

Problem 1 (Stability polynomial optimization)

$$\begin{aligned} &\textit{maximize} \quad \nu \\ &\text{subject to} \\ &\qquad |\psi(\nu\lambda)| \leq 1 \quad \textit{for all } \lambda \in \sigma(\mathbf{L}) \\ &\qquad \psi(z) - \exp(z) = \mathcal{O}(z^{p+1}). \end{aligned}$$

We solve Problem 1 using a convex optimization approach and bisection with respect to the CFL number ν, as described in [6]. This approach allows us to optimize methods with large numbers of stages in order to improve the maximum absolutely stable time step ν_{stab}. The optimization is carried out for 2^{nd}- to 5^{th}-order accurate schemes; the constraint points λ are taken as the spectrum of the SD semi-discretization of the 2D advection equation [5].

The choice of stability polynomial does not fully determine the method; an ERK method of s stages has $s(s+1)/2$ coefficients and only s of them are constrained by the stability polynomial. We use the remaining degrees of freedom to satisfy additional nonlinear order conditions ($\tau_i^{(j)}(\mathbf{A}, \mathbf{b}) = 0$), to obtain a low-storage implementation, and ensure that the truncation error coefficients $C^{(p+1)}$ is not too large. This leads to the computation of the so called Butcher's coefficients $\mathbf{A}, \mathbf{b}$. The optimization problem may be stated formally as follows:

Method	s	ν_{stab}/s	$C^{(p+1)}$
Kutta's ERK(4,4)	*4*	3.9534×10^{-02}	1.4505×10^{-02}
Optimal ERK(9,4) [5]	9	5.6977×10^{-02}	5.0640×10^{-04}
Optimal ERK(18,4) [5]	18	6.5233×10^{-02}	1.1087×10^{-04}
Optimal ERK(4,1)	4	6.6877×10^{-02}	1.6427×10^{-02}
Optimal ERK(9,1)	4	6.8593×10^{-02}	3.9650×10^{-04}
Optimal ERK(18,1)	18	6.8832×10^{-02}	4.1898×10^{-08}

Table 1. Effective step size and leading truncation error coefficient of the optimal ERK methods used in this work. The 4-stage method (corresponding to the values in italics) is the classic ERK method.

Problem 2 (RK method optimization)

$$
\begin{aligned}
&\textit{minimize} \quad C^{(p+1)} \\
&\text{subject to} \\
&\qquad \tau_i^{(j)}(\mathbf{A},\mathbf{b}) = 0 \quad (0 \le j \le p) \\
&\qquad \mathbf{b}^T\mathbf{A}^{j-1}\mathbf{e} = \beta_j \quad (0 \le j \le s) \\
&\qquad \Gamma(\mathbf{A},\mathbf{b}) = 0
\end{aligned}
$$

Here $\mathbf{b}^T\mathbf{A}^{j-1}\mathbf{e} = \beta_j$ and $\Gamma(\mathbf{A},\mathbf{b}) = 0$ represent the prescribed stability polynomial coefficients β_j and the conditions necessary for the method to be written in low-storage form [7], respectively.

We have computed optimized methods for $s \le 20$, because for larger values of s, the convex solvers used in the algorithm of [6] often fail due to poor numerical conditioning. The order of accuracy of the SD scheme has been fixed to four ($p = 3$) whereas the order of accuracy of the optimized ERK schemes has been varied from one to three (i.e. $p-1$). In this work we show present three new 1$^{\text{st}}$-order accurate optimized ERK schemes with respectively 4, 9 and 18 stages (i.e., ERK(4,1), ERK(9,1) and ERK(18,1)) and we compare their performance with the optimized 4$^{\text{tt}}$-order methods with the same number of stages recently presented in [5].

Table 1 lists the value of the effective time step and the leading truncation error coefficient of the optimized ERK schemes used for the test problem in the next section.

Flow past a wedge

In this section, the compressible Euler flow past a triangular wedge is discretized using a highly unstructured mesh and is used to study the performance of two new 1$^{\text{st}}$-order ERK schemes. In Figure 1 the density contour at $t = 200$ is shown, where the incoming flow is from left to right. The wedge is placed on the centerline $y = 0$ of the computational domain and it is characterized by a length L. At the left boundary (the inflow) the flow is prescribed to be uniform with zero angle of attack and free-stream Mach number of 0.2. Both inlet density and inlet pressure are set to one. A pressure outlet boundary condition is imposed on the right boundary of the domain which is placed about 20 L away from the wedge. Far-field boundary conditions (i.e. uniform Dirichlet boundary conditions for the conserved variables) are imposed both on the top and bottom boundaries.

An unstructured grid with $2,952$ quadrilateral cells with a maximum aspect ratio of 1.6 is used. The total number of DOFs is $47,232$. Several computations are performed using the CFL number ν_{stab} for each scheme and measuring the error after 0.1 seconds.

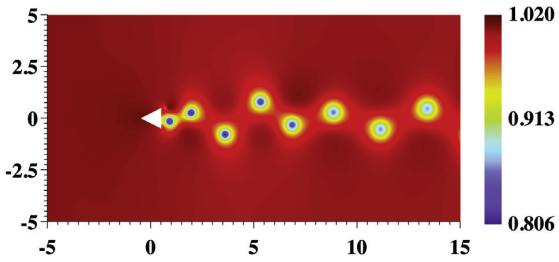

Figure 1. Density contour of the flow past a wedge at $t = 200$.

A reference solution is numerically computed by solving the problem on the mesh with $11,686$ quadrilateral cells with the 5^{th}-order SD method ($292,150$ DOFs) and the explicit 6-stage 5^{th}-order Runge–Kutta–Fehlberg (ERKF(6,5)) scheme. A CFL number $\nu = 0.1$ is used for the reference computation.

Starting with an already developed solution, several computations are performed using the CFL number ν_{stab} for each scheme and measuring the error after 0.1 seconds. Figure 2 shows the maximum norm of the error and the CPU time for the classical 4-stage 4^{th}-order ERK(4,4) scheme, the 4^{th}-order optimized methods presented in [5] and the new 1^{st}-order time stepping.

Remarkably, we observe that the new schemes, designed using linear advection on a uniform grid, perform very well also for the compressible Euler equations on an unstructured quasi-uniform grid.

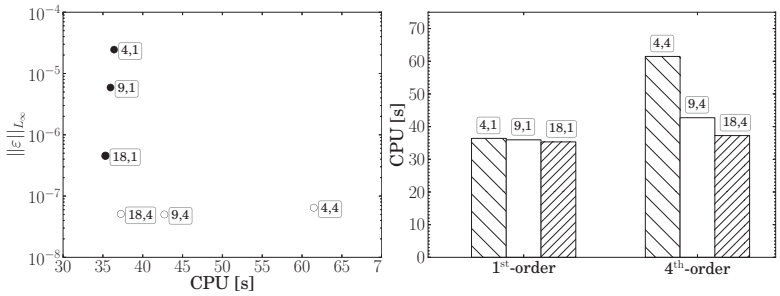

(a) Error versus CPU time. (b) CPU time for each simulation.

Figure 2. Error and CPU time for the wedge problem. The labels s, p for each point indicate the number of stages s and the order p of the corresponding scheme. Open circles are used for the reference methods.

By using a lower order of accuracy we have been able to increase the linearly stable step size of the solver by about 60% and 17%, respectively, over the standard ERK(4,4) scheme and the ERK(9,4) method presented in [5]. However, for the 18 stage method the gain is about 5%. Such improvements are obtained with some sacrifices in accuracy, though the global error obtained by using the ERK(18,1) method is still small.

Conclusions and future directions

In this work the performance of new optimized first-order ERK schemes for the high-order spectral difference method on unstructured quasi-uniform tensorial cell grids have

been presented. A comparison with the recently proposed optimized 4^{th}-order schemes reported in [5] has also been reported. We have observed that if a small or a medium number of stages is used and an integration error of about $10^{-4} - 10^{-5}$ is acceptable the low-order accurate ERK schemes represent a valid alternative to the standard high-order methods when simulations running on expensive supercomputers for hundreds of hours must be integrated as fast as possible.

The optimization of low-order ERK schemes for the SD methods is still an ongoing research and will be completed in the near future with the development of ERK schemes with embedded error estimators.

References

[1] Hesthaven, Jan S. and Warburton, Tim. *Nodal Discontinuous Galerkin Methods: Algorithms, Analysis, and Applications*. Texts in Applied Mathematics, **54**. Computational Science & Engineering, Springer Publishing Company, Incorporated (2007).

[2] Sun, Y., Wang, Z. J. and Liu Y. *Spectral (finite) volume method for conservation laws on unstructured grids VI: extension to viscous flow*. J. of Comput. Phys., **215**(1), 41–58 (2006).

[3] May, G. and Jameson, A. *A spectral difference method for the Euler and Navier-Stokes equations on unstructured meshes. AIAA paper* 2006-304. 44th AIAA Aerospace Sciences Meeting, Reno, Nevada, USA, January 9-12, 2006.

[4] Castonguay, P., Vincent P. and Jameson, A. *Application of High-Order Energy Stable Flux Reconstruction Schemes to the Euler Equations. AIAA paper* 2011-686. 49th AIAA Aerospace Sciences Meeting including the New Horizons Forum and Aerospace Exposition, Orlando, Florida, USA, January 4-7, 2011.

[5] Parsani, M., Ketcheson, David I. and Deconinck, W. *Optimized explicit Runge-Kutta schemes for the spectral difference method applied to wave propagation problems*. Submitted, (2012).

[6] Ketcheson, David. I. and Ahmadia, Jamil A. *Optimal Runge-Kutta stability regions*. Submitted, (2012); http://arxiv.org/abs/1201.3035.

[7] Ketcheson, David I. *Runge–Kutta methods with minimum storage implementations*. J. of Comput. Phys., **229**(5), 1763–1773 (2010); http://arxiv.org/abs/1207.5830.

Matteo Parsani, David I. Ketcheson
King Abdullah University of Science and Technology
Division of Mathematical and Computer Sciences and Engineering
23955-6900 Thuwal, Saudi Arabia
matteo.parsani@kaust.edu.sa, david.ketcheson@kaust.edu.sa

Willem Deconinck
Vrije Universiteit Brussel
Department of Mechanical Engineering
Pleinlaan 2, 1050 Brussels. Belgium
willem.deconinck@vub.ac.be

Geometric approach in numerical eigenproblem analysis

Alexis Fedoroff[1] and Reijo Kouhia[2]

[1]Department of Civil and Structural Engineering, Aalto University
P.O. Box 12100, FI-00076 Aalto, Finland
[2]Department of Mechanics and Design, Tampere University of Technology
P.O. Box 589, FI-33101 Tampere, Finland

Summary. Non-linear eigenproblems can be encountered in a wide range of physical systems, stability analysis being an important source of such problems. The current technique used in commercial finite element code to solve non-linear eigenproblems consists in linearizing the criticality equation with respect to the bifurcation parameter evaluated at the origin. Since the numerical technique is approximative, it is essential to assess the error both on the eigenvalue and the eigenmode. The latter one is of particular importance, since the eigenmode is typically used as initial imperfection in imperfection sensitivity analysis.

In this paper the authors propose a new geometric approach, in which the eigenvector is considered as a locally smooth function de?ned on the criticality manifold. Given two such eigenvectors, one for the non-linear eigenproblem and one for the linear one, it is possible to evaluate the error between the two eigenvectors considering the location of their respective arguments on the criticality manifold and the intrinsic properties of the criticality manifold itself. Simple, illustrative examples taken from structural stability will be shown for the sake of clarity as well as numerical computations on engineering problems.

Key words: Non-linear eigenproblems, Riemannian geometry, Structural stability

Esitys on julkaistu *Rakenteiden mekaniikka lehdessä*: Vol. 45, 2012, Nro 3.

Non-Linear Finite Element Modeling of Hydraulic Driven Multibody System

Antti Ylinen, Jari Mäkinen and Heikki Marjamäki

Summary. This paper studies the modeling of a hydraulic driven flexible fusion reactor maintenance robot using non-linear finite element method. The mechanical part of the maintenance robot is modeled using geometrically exact Reissner's beam element and mass elements. The hydraulic system is partitioned into elements which can be assembled together likewise in the finite element method. A subsystem that contains the transmission line with orifices or volumes at the ends of transmission line can be considered as an element of hydraulic system. In this paper, we shall introduce models also for hydraulic pump and pressure relief valve. In the finite element analysis, the basic idea is to divide the whole hydraulic system into elements that can be assembled together. This assembling procedure gives the ordinary differential equation system and the Jacobian matrix for whole the hydro-mechanical system. Hydraulic and mechanical systems are coupled in the hydraulic cylinder where oil pressure gives movement for the cylinder rod, giving also displacements for the mechanical system. The governing equations of motion in the dynamic case are solved by using an implicit Newmark time integration method.

Key words: finite element method, hydraulic systems, modeling, simulation, coupled system, non linear

Introduction

Hydraulic-driven multibody systems are very common in lifting vehicles, robotic manipulators, timber logging and mining etc. where hydraulics is a powerful power transferor. Here we introduce modeling technique where the hydraulic system is partitioned into elements likewise in finite element method. Idea is to build the whole hydro-mechanical system using elements as in the element method. Depending on the component or the part in the structure, we can use either mechanical elements or hydraulic elements and the state equation of the whole system can then be assembled. Traditionally coupled hydro-mechanical systems have been modeled as separate systems where interaction between these two systems is dealt with the displacements and velocities of the hydraulic actuators and by forces induced by the actuators. These kinds of systems are usually solved separately by an iterative approach. Iterative solution has a drawback because it adds instability in the sense of convergence and it is computationally inefficient. In addition, the tangential matrices between the hydraulic and the mechanical systems are not properly coupled, that is called inconsistent formulation. The modeling technique presented in this paper removes this inconsistence because the system can be solved as one set of ordinary differential equations.

Fluid Transmission Line Models

In this section we introduce the fluid transmission line model for laminar flow. These models are needed in modeling of the coupled hydro-mechanical system. There are three different kinds of models: a Q-model, where flow rates at the boundaries are given as inputs; a P-model, where pressures as given inputs and finally PQ-model, where we give flow rate as an input on the other boundary and pressure on the other end. More thorough presentation on these elements can be found in papers [1,2] where models are given in transfer function form. In this paper we present the models using state space form though, they are adapted more easily for finite element formulation.

In this paper we introduce first the Q-model transmission line element. Graphical representation of all these elements and their boundary values are in Figure 1

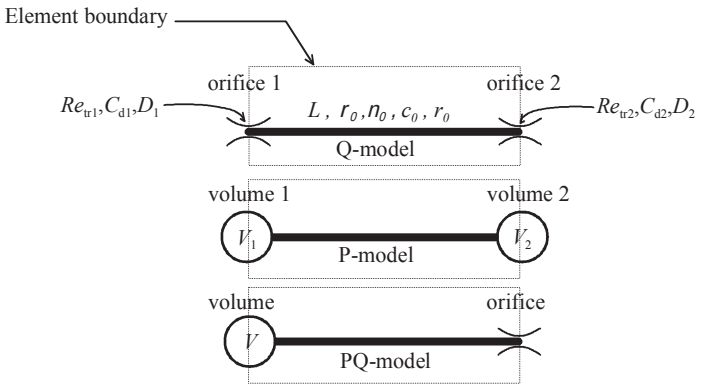

Figure 1: Fluid transmission line parameters and positive flow rate directions

The space state formulation for the Q-model can be written for *n* modes for the pressure oscillation as

$$\begin{aligned} \dot{\mathbf{x}} &= \mathbf{A}\mathbf{x} + \mathbf{B}\mathbf{Q} \\ \mathbf{P} &= \mathbf{C}\mathbf{x} \end{aligned} \tag{1}$$

where the input vector **Q**, describing the fow rates, the output vector of pressures **P** and the state variable vector **x** and the state space matrices are

$$\mathbf{Q} = \begin{pmatrix} Q_1 & Q_2 \end{pmatrix}^{\mathrm{T}}, \quad \mathbf{P} = \begin{pmatrix} P_1 & P_2 \end{pmatrix}^{\mathrm{T}}, \quad \mathbf{x} = \begin{pmatrix} p_0 & r_1 & p_1 & \cdots & r_n & p_n \end{pmatrix}^{\mathrm{T}}$$

$$\mathbf{A} = \mathrm{diag}\left(0, \mathbf{A}_1, \mathbf{A}_2, \ldots, \mathbf{A}_n\right), \quad \mathbf{A}_i = \begin{pmatrix} 0 & -\dfrac{\omega_i^2}{T^2} \\ 1 & -\dfrac{\varepsilon_i}{T} \end{pmatrix}, \quad \mathbf{B} = \begin{pmatrix} \mathbf{B}_0 \\ \mathbf{B}_1 \\ \vdots \\ \mathbf{B}_n \end{pmatrix}_{2n+1\times 2} \quad \begin{aligned} \mathbf{B}_0 &= \frac{Z_0}{T}\begin{pmatrix} 1 & -1 \end{pmatrix} \\ \mathbf{B}_{2i-1} &= \frac{2Z_0 w_{2i-1}}{T^2}\begin{pmatrix} \varepsilon b_n & \varepsilon b_n \\ T & T \end{pmatrix} \\ \mathbf{B}_{2i} &= \frac{2Z_0 w_{2i}}{T^2}\begin{pmatrix} \varepsilon & -\varepsilon \\ T & -T \end{pmatrix} \end{aligned} \tag{2}$$

$$\mathbf{C} = \begin{pmatrix} 1 & 0 & 1 & 0 & 1 & 0 & 1 & \cdots \\ 1 & 0 & -1 & 0 & 1 & 0 & -1 & \cdots \end{pmatrix}_{2\times 2n+1}$$

The modal natural frequency ω_i and the modal damping coefficient ε_i are

$$\omega_i = \alpha_i - \frac{1}{4}\sqrt{\alpha_i \varepsilon} + \frac{1}{16}\varepsilon, \quad \varepsilon_i = \frac{1}{2}\sqrt{\alpha_i \varepsilon} + \frac{1}{8}\varepsilon, \quad \varepsilon := \frac{8\nu_0 L}{r_0^2 c_0}, \quad i = 1,2,...,n \tag{3}$$

The series impedance $Z_0 := (\rho_0 c_0)/(\pi r_0^2)$, where ρ_0 is the density of fluid, c_0 is the speed of sound, and r_0 is the inner radius of the pipe. The wave time is defined as $T := L/c_0$, where L is the length of transmission line. ν_0 is the mean kinematic viscosity. The attenuation factors with Riemann windowing are given as $w_i = \sin\beta_i/\beta_i$. For Q-model, the model parameters can be written

$$\alpha_i = i\pi, \quad \beta_i = \frac{i\pi}{n+1}, \quad b_n = \left(8\sum_{i=1,3,...}^{n-1} w_i/\omega_i^2\right)^{-1} \tag{4}$$

For the P and PQ model we can write corresponding matrices which are shown in [8].

Modeling of hydraulic components

The transmission line elements by themselves aren't adequate to model actual hydraulic systems. Therefore we need models for volume and orifice. As we can see in Figure 1 the transmission line uses orifices or volumes at the ends of the line. These components can be interpreted as boundary conditions for the transmission line element.

For the orifice a simple first order differential equation can be written as

$$\dot{Q}_{\text{or}} = \frac{1}{V_{\text{or}}}\left(\frac{\Delta P_{\text{or}} A_{\text{or}}^2}{\rho_0} - \frac{Q_{\text{or}}|Q_{\text{or}}|}{2C_d^2}\right) \tag{5}$$

where V_{or} is the volume of the fluid particle in the orifice and C_d is the discharge coefficient 33 [3].

For hydraulic volume the change in pressure is

$$\dot{P}_{\text{v}} = \frac{B}{V_{\text{v}}}\left(\sum_{i=1}^{n_{\text{in}}}(Q_{\text{in}})_i - \sum_{i=1}^{n_{\text{out}}}(Q_{\text{out}})_i\right) \tag{6}$$

where *B* is the bulk modulus of the fluid.

To model hydraulic systems, we also need hydraulic actuator, cylinder in this case. Hydraulic cylinder can be treated as volume pair with hydraulic variables but at the same time it has mechanical variables, displacements at the ends of the cylinder. Though the cylinder couples the hydraulic system with the mechanical system. The force that the cylinder produces can be expressed using the chamber pressures

$$f_{\text{c}} = A_A P_A - A_B P_B \tag{7}$$

and the pressure change is

$$\begin{pmatrix} \dot{P}_A \\ \dot{P}_B \end{pmatrix} = \begin{pmatrix} \dfrac{Q_A - A_A \dot{x}_c}{V_A + A_A x_c} c_0^2 \rho_0 \\ \dfrac{-Q_B + A_B \dot{x}_c}{V_B - A_B x_c} c_0^2 \rho_0 \end{pmatrix} \tag{8}$$

Hydraulics with finite element method

The transmission line elements in state space realization can be implemented into finite element method using quite straight forward methods. The transmission line element itself describes only the state variables within the elements boundary. The elements are connected via orifices or volumes at the ends of the transmission lines. When two Q-elements are connected, they share the same flow rate at the connecting node.

The global hydraulic state matrix is then created using same techniques as in finite element method. The residual vector for the transmission line elements consists of pressures, flow rates and inner variables and if values of these are shared in a node, we can create the coupling between these elements. See more on [8].

The coupling between hydraulic system and mechanical system occurs in the cylinder element. As we can see in Eqn (7), the cylinder element has hydraulic variables as well as mechanical variables. When the inner force and stiffness matrix of the cylinder element are derived from this equation we get accurate coupling.

Results

In this chapter we present the results for the simulation model. The mechanical structure is based on the ITER fusion reactor divertor maintenance robot [9]. 3D model of the robot is on Figure 2. Although the actual robot is waterhydraulic servo system, the model in this paper is considered as traditional hydraulic system. The basic idea is to compare the displacement results and response of the system when the cylinder element is modeled as a length controlled rod element and with the hydraulic system and hydraulic cylinder. This comparison is adequate for in mechanisms the cylinder element is usually treated as length controlled rod element.

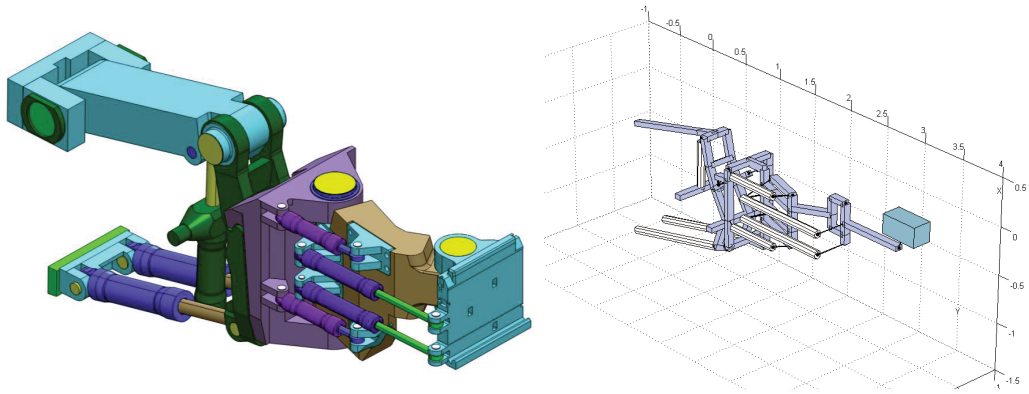

Figure 2: The divertor maintenance robot and the beam element model of the robot

The problem with this element is, that in more complicated cases the right function for the length variation. First assumption for the length function is to calculate it the from the stationary flow to the hydraulic cylinder. We know the maximum pressure and orifice areas and thus the flow rate to the cylinder and the length change in fixed time. The length function can also be discussed. The most obvious choice is linear function, but intuitively it can be said, that it might not be the best choice. Therefore also Hermite polynomial is used in the analysis. The displacement and velocity profiles are presented in Figure 3 on the left hand side.

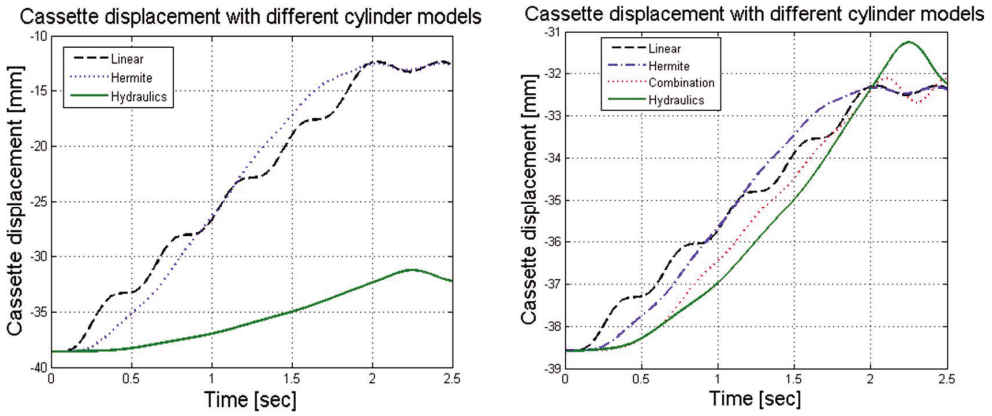

Figure 3: Cassette displacement and velocity with different cylinder modeling methods [9]

As we can see from Figure 3 the assumption for the stationary condition is poor in this case where the cylinder doesn't reach the stationary velocity on the fixed time period. Therefore we redo the simulation by taking the length value from the first simulation. We also introduce new function for the length change in form of combination of Hermite polynomial and linear function. The length change starts by Hermite polynomial and ends usin linear growth. The ratio of these functions has been fitted so that the cylinder displacement follows the model with the hydraulic cylinder in position wise.

When the length change is taken from the output of the hydraulic system, we get better results for the cassette displacement. However the results aren't still matching the results from the hydraulic system completely. This is due to the mass effects of the system because it isn't enough to match the displacements if the velocities and

accelerations are incorrect. Therefore the simulation of the hydraulic system produces better results than the length controlled rod element.

References

[1] Mäkinen J. and Piché R and Ellman A. Fluid Transmission Line Modeling Using a Variational Method. *ASME Journal of Dynamic Systems, Measurement, and Control 122*, (2000), 153-162.

[2] Mäkinen J. and Marjamäki H. Modelling Hydraulic Systems as Finite Elements, *The 17th IASTED International Conference on Applied Simulation and Modelling (ASM-2008)*, Corfu, Greece, 23–25 Jun 2008.

[3] Ellman A and Piché R. A two regime orifice flow formula for numerical simulation. ASME *Journal of Dynamic Systems, Measurement, and Control 121*, (1999), 721-724.

[4] Marjamäki H. and Mäkinen J. (2007), The Raising Movement of a Hydro-Mechanical Lift Frame, In: *COMPDYN 2007 First International Conference on Computational Methods in Structural Dynamics and Earthquake Engineering (COMPDYN 2007)*, Papadrakakis, M., Charmpis, D., Lagaros, N. & Tsompanakis, Y. (eds.). Rethymno, Greece, 13-16 June 2007.

[5] Marjamäki H. and Mäkinen J. Different Approaches in Modelling Boom Lifting Movement, *The III European Conference on Computational Mechanics - Solid, Structures and Coupled Problems in Engineering (ECCM-2006)*, Lisbon, Portugal, 5-9 June 2006.

[6] Marjamäki H. and Mäkinen J. Modelling a Telescopic Boom - The 3D Case: Part II, *Computers & Structures 84*, 29-30 (2006), 2001-2015.

[7] Kauranne H. and Kajaste J. and Vilenius M., *Hydraulitekniikan perusteet*, WSOY, 2003.

[8] Mäkinen J.; and Pertola P and Marjamäki H. Modelin Coupled Hydraulic-Driven Multibody Systems using Finige Element Method *The 1st Joint International Conference on Multibody System Dynamics* May 25-27, 2010 Lappeenranta Finland

[9] Ylinen, A: *Methods For Modelig Coupled Hydraulic Driven Flexible Multibody Systems*, Master's thesis, 2011, TTY.

Antti Ylinen
antti.ylinen@tut.fi

Jari Mäkinen
jari.m.makinen@tut.fi

Heikki Marjamäki
heikki.marjamaki@tut.fi

Traveling Waves on a Viscoelastic Cylinder Cover Due to Rolling Contact - A Numerical Study using FEM

Anssi T. Karttunen, Raimo von Hertzen

Summary. In this paper, traveling waves which appear at high speeds in the polymer cover of a cylinder due to rolling contact are studied using a 2D finite element (FE) model for a two-cylinder system. It is found that an infinite number of natural mode families exist for the cylinder cover due to its finite thickness. A critical speed below which the traveling waves do not appear can be calculated on the basis of a resonance condition using the modal information. Traveling waves in the cover are identified as modified quasi-elastic Rayleigh waves composed of the eigenmodes of the polymer cover. The critical speed according to the resonance condition is also the minimum phase velocity of the waves propagating in the cover. It is found that the traveling wave phenomenon is best described as a Rayleigh wave resonance in which contact-induced modified quasi-elastic Rayleigh waves arising at critical and supercritical speeds superpose to form a strong traveling shock wave.

Introduction

Dynamic physical phenomena, which have been traditionally considered to be matters of minor importance, are starting to play a pivotal role in industrial rolling contact machines because of increasing operating speeds. This creates a need for a thorough understanding of the dynamic behavior of high-speed rolling contact systems coated with viscoelastic polymers and sets new requirements for the design and development of industrial machines.

In this paper, we investigate a traveling wave phenomenon occurring at high rolling velocities in the polymer cover of a cylinder which is in rolling contact with a steel cylinder. The novelty of the utilized two-dimensional plane strain finite element (FE) model in comparison to thin shell, ring, tensioned beam, membrane etc. models is that the plane strain approach provides true insight into the polymer cover throughout its thickness. The FE analysis is done using the FE software package Abaqus 6.10.

The traveling waves studied in this paper are closely related to the widely studied standing waves in car tires, which emerge at high rolling velocities from the contact area, the nip, between road and tire, and can be seen along the tire circumference. A study giving a solid resonance-based physical interpretation on the phenomenon was made by Soedel [1]. Other approaches have also been used to characterise tire standing waves, for example, see [2, 3].

Methods

The two-cylinder rolling contact system under investigation consists of a steel cylinder having a radius of 0.4 m and a cylinder with a total radius of $R = 0.21$ m including a 6 mm thick viscoelastic polymer cover attached to a steel core (see Fig. 1).

For the 2D computational model used in this work, the steel core of the polymer-covered cylinder is modeled as rigid and the polymer as a linear isotropic viscoelastic

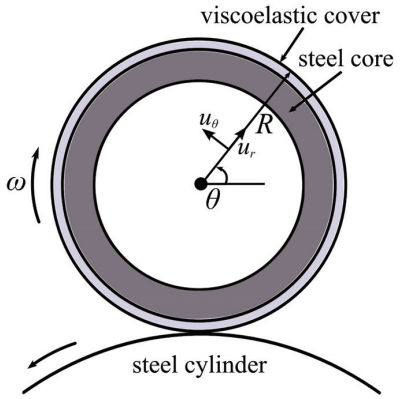

Figure 1. Two-dimensional rolling contact system with a rubber-like viscoelastic polymer cover on the other cylinder.

material. The steel cylinder is modeled as a rigid surface. The contact between the cylinders is frictionless. In the used frame of reference which is fixed to the viscoelastically covered cylinder, the other cylinder moves in rolling contact around the covered cylinder which in this frame appears to be at rest. Linear isoparametric quadrilateral plane strain elements are used with unit thickness[1].

Within the context of small strains, the constitutive equation for an isotropic viscoelastic material can be written in a hereditary integral form as

$$\boldsymbol{\sigma}(t) = \int_0^t 2G(t-\tau)\frac{d\mathbf{e}}{d\tau}(\tau)d\tau + \mathbf{I}\int_0^t K(t-\tau)\frac{d\phi}{d\tau}(\tau)d\tau \ , \tag{1}$$

where $\boldsymbol{\sigma}$ is the Cauchy stress tensor, G is the shear modulus, K is the bulk modulus, $\mathbf{e}$ is the deviatoric part of the strain, ϕ is the volumetric part of the strain, t is current time, τ is past time and $\mathbf{I}$ is the identity tensor [4]. In the calculations, the moduli in Eq. (1) are represented in terms of the Prony series which corresponds to a generalization of the classical Maxwell model of viscoelasticity, which in 1D consists of a spring and Maxwell elements assembled in parallel [4].

The natural frequencies and mode shapes of the cover layer of the polymer-coated cylinder are computed using the shifted block Lanczos method. In the computations, the frequency-dependent behavior of the viscoelastic polymer is taken into account. Thus, the elastic properties of the polymer need to be evaluated at a chosen ("dependent") frequency before performing the eigenmode analysis. The material properties of the polymer cover for the eigenmode analysis are determined according to the resonance condition, that is to say, the dependent frequency to determine the material parameters is matched with the computed natural frequency by iteration for each mode. The contact between the cylinders is not considered in the eigenmode computations.

The dynamic simulations are performed by using Abaqus/Explicit. The explicit time integration method is suitable for achieving high resolution solutions for high-speed transient dynamic events and, especially, if contact conditions need to be updated within small time intervals. To model the frictionless contact between the cylinders, a penalty contact algorithm is used to enforce the contact constraints. The role of the contact loading is mainly to act as a supply of energy required to propagate and sustain a wave.

[1]Abaqus elements CPE4H (eigenmode analysis) and CPE4R (explicit dynamic analysis)

Results and discussion

Natural frequencies and modes

Fig. 2 shows close-up views of two different mode families of the polymer cover. In both mode families, every individual mode possesses an integer number of waves on the cylinder circumference. For the shown modes the number of waves is one hundred, thus the principal mode number in both cases is $N = 100$. Fig. 2a shows the sine wave-type primary mode. Secondary mode family I is presented in Fig. 2b. For the modes in Figs. 2a and 2b, the corresponding natural frequencies are 5016 and 8296 Hz, respectively. For the primary mode in Fig. 2a the radial displacement does not change sign along an initially straight radial line from the bottom to the surface of the polymer cover. For the secondary mode I in Fig. 2b, the sign changes once. For the secondary mode II the sign would change twice in the radial direction. Due to the finite thickness of the cover layer, there are an infinite number of higher mode families, each of which corresponds to a secondary mode number.

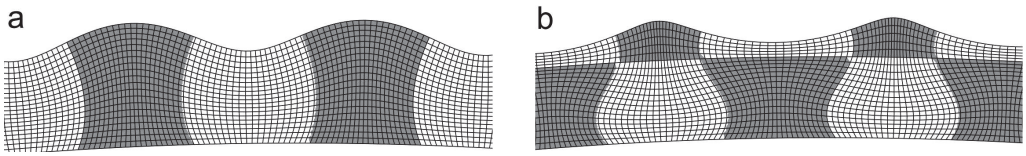

Figure 2. Two mode families. The principal mode number in both cases is $N = 100$. The dark and white areas represent positive and negative radial displacements, respectively. a) Primary mode, $f_{100} = 5016$ Hz, b) Secondary mode I, $f_{100} = 8296$ Hz.

Traveling waves due to harmonic load

A harmonic load with the frequency 5016 Hz corresponding to the natural frequency f_{100} of the primary mode is exerted on five adjacent surface nodes on the cover. A modified quasi-elastic Rayleigh wave, which is generated by the load and propagates along the circumference of the polymer cover, is shown in Fig. 3. An identical wave travels in the opposite direction. For the viscoelastic parameter values of the present work the radiated traveling waves attenuate fast when the primary mode $N = 100$ is excited. The frequency of the traveling wave equals the natural frequency f_{100}.

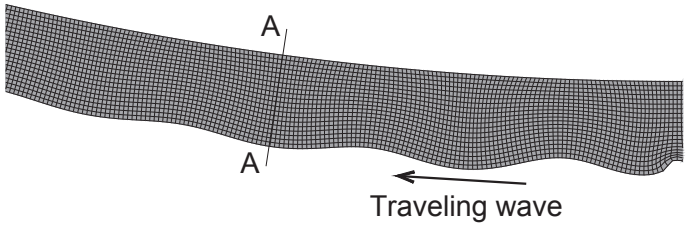

Figure 3. Traveling wave in the viscoelastic cylinder cover in steady-state. A harmonic load is exerted on five surface nodes. Due to the finite depth of the polymer layer and elastic-like behavior of the viscoelastic material, the wave is classified as a modified quasi-elastic Rayleigh wave according to [5] and [6]. Due to symmetry only the left part of the cover is shown.

Physical interpretation and critical speed

A resonance condition for the system is given by $f = f_N/N$, where $f = \omega/2\pi$ is the rotational frequency of a load moving on the circumference of the covered cylinder [1]. The computed values of f_N/N and equivalently the Rayleigh wave phase velocity $v_p/2\pi R$ are shown in Fig. 4 as a function of the principal mode number N. The curve of the primary modes approaches a constant value around 39 Hz at higher modes, indicating that there is a cutoff rotational frequency, or a critical speed (51.5 m/s), under which the resonance condition is not fulfilled by any mode.

Considering the wave propagation, one can see that also the phase velocity of the modified quasi-elastic Rayleigh waves approaches a constant value at higher frequencies. This means that the high frequency waves in the cover layer become non-dispersive, as is the case for Rayleigh waves over an elastic half-space. The phase velocity of the Rayleigh waves in an elastic half-space is given by the approximate formula $c_R = \frac{0.87+1.12\nu}{1+\nu}\sqrt{G/\rho}$, where ν is the Poisson ratio, G the elastic shear modulus and ρ the density of the polymer. With the parameter values of this work, the equation gives $c_R = 51.7$ m/s, which is very close to the critical speed 51.5 m/s in Fig. 4.

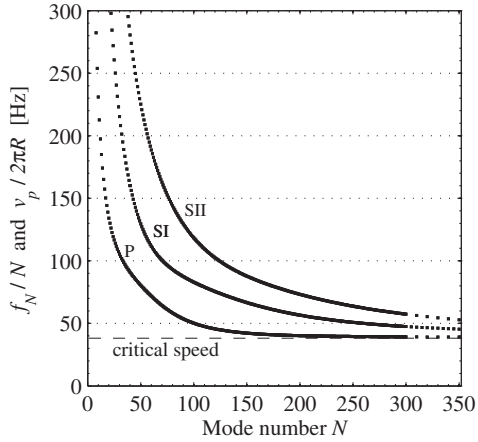

Figure 4. Natural frequencies divided by the principal mode number for the primary and secondary modes and equivalently the Rayleigh wave phase velocity as a function of the principal mode number. Every mode up to $N = 350$ was calculated. From $N = 300$ to $N = 350$ only selected modes are shown.

It is known that if the velocity of a semi-infinite uniform loading on an elastic half-space equals the velocity of the Rayleigh wave for the medium, a so-called Rayleigh wave resonance takes place [7]. When this happens, the Rayleigh waves arising at the front end of the load will have a common front, which moves together with the load. Thus, in the neighborhood of the front end of the load, a superposition of Rayleigh waves with the same phase occurs. As a result, the energy transmitted by the waves accumulates in the vicinity of the front end of the load.

Traveling waves due to rolling contact

Figs. 5a and 5b present the deformed shapes and the von Mises stresses of the polymer cover at the rotational frequencies $f = 50.16$ and 80.5 Hz, which have been chosen according to the primary modes $N = 100$ and 50, respectively, on the basis of the resonance

condition $f = f_N/N$. At both rotational frequencies, a steady-state traveling wave due to rolling contact moving together with the nip at the same speed forms. The traveling wave behavior conforms perfectly to the Rayleigh wave resonance explanation given by Goldstein [7]. It can be seen in Fig. 5 that the traveling waves bring about high stresses that spread along a considerable distance in the polymer cover. Actually, shock wave formations with reflections from the rigid bottom are clearly displayed, especially in Fig. 5b.

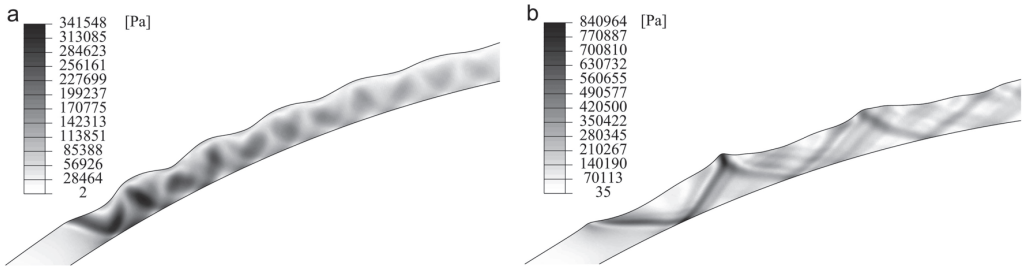

Figure 5. Deformed shape of the polymer cover with the von Mises stress contour [Pa] at the rotational frequencies a) $f = 50.16$ Hz and b) $f = 80.5$ Hz. The contact load due to the rigid cylinder is moving in the counterclockwise direction near the lower left corner in both cases. The stresses are concentrated at the shock wave fronts.

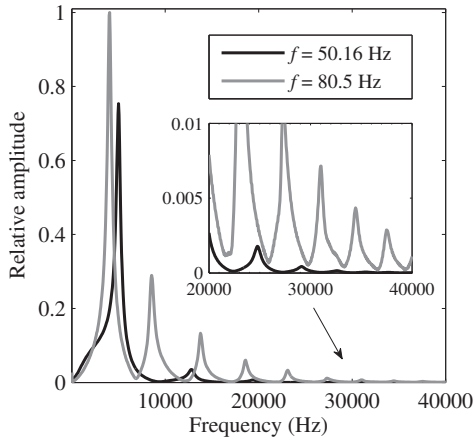

Figure 6. Frequency spectrum calculated by FFT from the radial displacement of a single surface node executing free oscillations for $f = 50.16$ and 80.5 Hz. The highest amplitude peaks are located at 5025 and 12830 Hz for $f = 50.16$ Hz and at 4030, 8555 and 13780 Hz for $f = 80.5$ Hz.

In both constant speed cases, that is, $f = 50.16$ and 80.5 Hz, a single surface node on the polymer cover is chosen and a frequency spectrum is calculated by the Fast Fourier Transform (FFT) from the radial displacement of the node after the nip has passed it and the node has oscillated freely outside the nip for a short time interval (~ 0.005 s) during which the waves have passed the node. The result, Fig. 6, gives the modal decomposition (without phase information) of the traveling waves, and the peaks correspond to the resonating modes according to $f = f_N/N$ and Fig. 4, and to the higher mode families. Each amplitude peak has a certain width in Fig. 6 which indicates that instead of a single

natural mode from each family being active, a large number of modes are activated. This is a manifestation of the fact that a modified quasi-elastic Rayleigh wave corresponding to a certain mode family is a superposition of the modes in that family. These waves arising from the different mode families during the Rayleigh wave resonance combine into the wave which we refer to as *the traveling wave due to rolling contact*. Furthermore, the critical speed is also the minimum phase velocity of the traveling waves in the polymer cover.

Conclusions

In this study, contact-induced traveling waves appearing at high rolling speeds on a viscoelastic cylinder cover in a two-cylinder rolling contact system were investigated using a two-dimensional plane strain finite element model. It was found that an infinite number of different natural mode families exist for the polymer cover due to its finite thickness. A critical speed for the traveling wave phenomenon could be calculated on the basis of the eigenmode results for the rolling contact system. At the critical speed of the system, there is, depending on the degree of viscosity in the system, little or no wave dispersion when the onset of the traveling wave phenomenon takes place as quasi-elastic modified Rayleigh waves start to arise at the front end of the contact area, the nip. At the critical speed, the speed of the nip equals the minimum phase velocity of the modified Rayleigh waves and a conventional shock wave with a common front with the nip forms. Therefore, a superposition of waves with the same phase occurs and a traveling wave arises. The phenomenon is essentially a Rayleigh wave resonance.

References

[1] Soedel W. On the dynamic response of rolling tires according to thin shell approximations. J Sound Vib 1975;41(2):233-46.

[2] Chatterjee A, Cusumano JP, Zolock JD. On contact-induced standing waves in rotating tyres: Experiment and theory. J Sound Vib 1999;227(5):1049-81.

[3] Krylov VV, Gilbert O. On the theory of standing waves in tyres at high vehicle speeds. J Sound Vib 2010;329(21):4398-408.

[4] Dassault Systemes Simulia Corp. Abaqus 6.10 Theory Manual. 2010.

[5] Allard JF, Atalla N. Propagation of sound in porous media: Modelling sound absorbing materials. Wiley; 2009.

[6] Currie PK, O'Leary PM. Viscoelastic Rayleigh-waves. Q Appl Math 1977;35(1):35-53.

[7] Goldstein RV. Rayleigh waves and resonance phenomena in elastic bodies. PMM-J Appl Math Mec+ 1965;29(3):608-19.

Anssi T. Karttunen, Raimo von Hertzen
Aalto University, School of Engineering, Department of Applied Mechanics,
P.O. Box 14300, FI-00076 Aalto, Finland
anssi.karttunen@aalto.fi, raimo.von.hertzen@aalto.fi

Timber building optimization

Jussi Jalkanen

Summary. The topic of this study is the structural optimization of the timber frame of an industrial building. Mathematical optimization theory has been applied to practical civil engineering problem in order to find a more economic solution compared to traditional design methods. The frame of building consists of cantilever type glulam columns and double tapered beams. Also the secondary roof beams made of LVL and the concrete pad foundations have been considered in optimization. Particle swarm optimization (PSO) and tabu search (TS) are used as the optimization algorithms. Both are simple heuristic algorithms.

Key words: structural optimization, timber structure, particle swarm optimization, tabu search

Introduction

Wood is as a construction material traditional and rather popular in Finland and other northern countries where there are wide forests and corresponding industry. Timber is not used only in traditional single family houses but also in all kind of buildings up to demanding long span applications like sport arenas, bridges etc. Large scale timber buildings are usually made of glulam or laminated veneer lumber (LVL).
Design codes such as European eurocode 5 ([1] and other parts) give design rules for timber buildings and bridges. In addition to these there are e.g a special design guide for nail plate trusses and some guidance for timber products offered by manufacturers. Also the manufacturing of glulam and other glued timber structures is specified and quality controlled. In many civil engineering offices there are some engineers or a whole department which is focused to the design of timber buildings.
The next natural step in the design of timber structures is optimization. Previously optimization is studied in the case of steel structures ([2] and [3]) and there are no reasons which would prevent the use of this approach in the design of timber structures.

Structural optimization

Structural optimization means the systematical seek of good design solutions by using the methods of mathematical optimization theory and modern computers. It offers a new way to go further than the traditional analysis of a few candidate structures selected based on designer's experience and intuition. The aim is to find such solutions which would be left undiscovered using traditional design methods. In addition to numerical

algorithms and computing power it is essential to understand the nature of design task so that optimization problem can be formulated reasonable.

Particle swarm optimization and tabu search

Heuristic means a deduction which does not fulfill all strict logical requirements but still often leads to a correct or a good answer. This means a stochastic or deterministic optimization algorithm which usually works but does not necessarily produce the optimum and may sometimes fail. The selection of heuristic optimization algorithms is large and there are also several different combinations. The wide applicability and the ability to solve, at least approximately, computationally hard discrete and mixed-integer problems have made heuristic algorithms popular in structural optimization.

The basic idea of stochastic particle swarm optimization (PSO) is to model the social behavior of a swarm (e.g. birds or fishes) in nature. A swarm of particles tries to adapt to its environment by using previous knowledge based on the experience of individual particles and the collective experience of the swarm. It is useful for a single member, and at the same time for the whole swarm, to share information among other members to gain some advantage. PSO belongs to the class of population based optimization methods, like genetic algorithm, because there is the group of solutions instead of a single solution. It can be seen that the group can offer some extra benefit compared to a single individual.

The idea of tabu search (TS) is always to look for the best point in the neighborhood of the current solution and take it as a new iteration point. All points in the neighborhood are not allowed since there is so called tabu list that contains forbidden solutions. When TS proceeds to a new solution the previous one will be put into the tabu list and usually the oldest one will be removed from the list. Sometimes all the same kind of solutions are prohibited at the same time and not just only one solution. If some point in the neighborhood is unfeasible it can be rejected directly. In the beginning TS works like the discrete deepest descent method. However, the tabu list makes it possible to avoid to get stuck in a poor solution and try to find the global minimum.

Optimization problem and results

The industrial building the material cost of which should be minimized is presented in Fig. 1. The frame of building consists of cantilever type columns and double tapered beam made of glulam GL32c. In spite of smaller loads there are no lighter frames at the ends of building due to possible future enlargement plans. Wind columns at the end of building are not included to optimization. The load carrying roof structure consists of secondary Kerto-S beams (distance 900 mm) and plywood panels. The weight of roof without Kerto-beams is 0,5 kN/m^2. The pad foundations (concrete + reinforcing steel) have been also considered in optimization. Proper base connection for column is chosen based on foundation loads and column dimensions. Walls are made of light polyurethane or wool sandwich panels and they are not included in optimization.

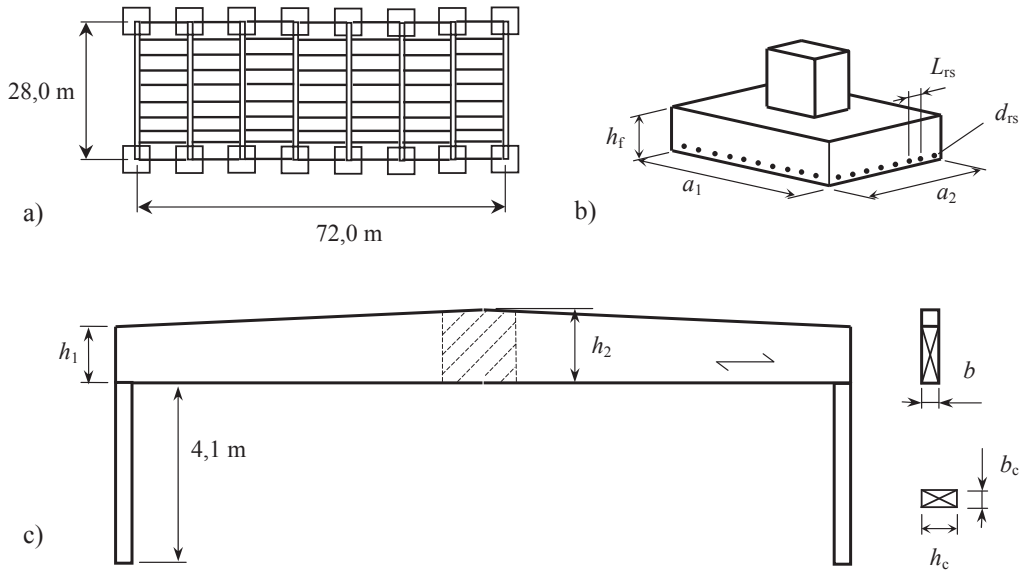

Figure 1. The optimized industrial building. a) Top view. b) Pad foundation. c) The main frame.

Design variables are connected to the number of frames (n), timber cross section dimensions (h_1, h_2, b, h_c, b_c and x_{sb}) and foundation dimensions (a_1, a_2, h_f, d_{rs} and L_{rs}). Some of these are discrete since the number of frames is integer, there are commercially available only certain thicknesses for glulam (90, 115, 140, 165, 190, 215, 240 and 265 mm) and the selections of Kerto-beams and reinforced steel bars are limited (44 and 8 pieces). x_{sb} is an ordinary number between 1 to 44. The rest design variables (h_1, h_2, h_c, a_1, a_2, h_f, and L_{rs}) could be continuous but due to practical reasons they are also treated as discrete and they will change in 10 mm steps (L_{rs} in 50 mm steps). Thus all the design variables are discrete.

The minimized objective function (1) contains the material cost of wooden members and foundations. In addition to this also the costs of foundation connections (foundation and secondary roof beam) are included.

$$C(\mathbf{x}) = c_{\text{glulam}}\left(V_{\text{b}}(\mathbf{x}) + V_{\text{c}}(\mathbf{x})\right) + c_{\text{LVL}}V_{\text{LVL}}(\mathbf{x}) + C_{\text{f}}(\mathbf{x}) + C_{\text{rest}}(\mathbf{x}) \tag{1}$$

Coefficients c_{glulam} and c_{LVL} are the prices of glulam GL32c and Kerto-S (Table 1). $C_{\text{f}}(\mathbf{x})$ means the cost of and $C_{\text{rest}}(\mathbf{x})$ includes the cost of connection parts.

Table 1. The material prices.

Material	Price
Glulam GL322	800 eur/m^3
Kerto-S	900 eur/m^3
Concrete C25/30	135 eur/m^3
Steel A500HW	0,86 eur/kg

Constrains take care that structure is strong enough to carry snow and wind loads in Tampere region (snow load s_k = 2,5 kN/m^2, terrain category II and the maximum allowed ground pressure 200 kPa). All the appropriate design code checks have been made for beam, columns, secondary roof beams and foundations. In order to compensate the deflection of beam there is 50 mm precamber in the beam.

Results

At first optimization is done using PSO with randomly selected initial population (population size 50 and with 15 feasible particles). Since PSO is stochastic algorithm the number of optimization runs must be enough. In this case it has been 30 and Fig. 2 shows the progress of the objective function during these runs. It should be noted that in all runs it takes several hundred trials to choose 15 feasible members to initial population.

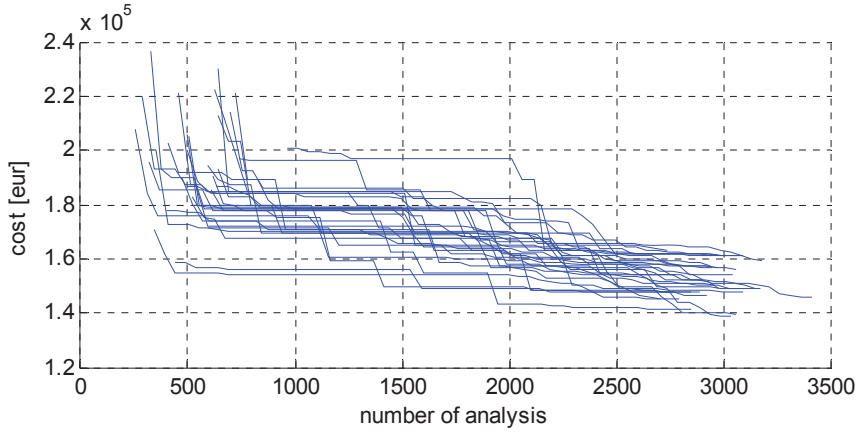

Figure 2. The improvement of the objective function during PSO optimization runs.

Table 2 presents the best found solution which gives for the whole building the objective function value 150 101 eur. Corresponding values for constraints are given in Table 3.

Table 2. The best found solution (f^* = 150101 eur) from PSO runs. The number of frames is $n = 18$ (distance between frames 4000 mm).

Beam	Column	Secondary beams	Foundation
h_1 = 1000 mm	h_c = 350 mm	x_{sb} = 2 (27 mm × 225 mm)	a_1 = 1690 mm
h_2 = 2210 mm	b_c = 140 mm		a_2 = 1320 mm
b = 165 mm			h_f = 500 mm
			d_{rs} = 32 mm
			L_{rs} = 200 mm

Table 3. Utilization rates for the best found solution from PSO runs.

Beam	Column	Secondary beams	Foundation
Bending in tapered part 73 %	Bending 33 %	Bending 97 %	Ground pressure 77 %
Bending in apex 56 %	Shear 14 %	Shear 59 %	Shear 13 %
Lateral torsional buckling 79 %	Compression 24 %		Bending 3 %
Transverse tension in apex 90 %	Buckling 99 %		Punching 11 %
Shear 90 %			
Deflection 99 %			

In the second stage the optimization problem is solved using TS and the best found solution from PSO runs is the feasible initial guess. Tabu search is deterministic algorithm and thus only one optimization run is enough. The best found solution from this run can be seen in Table 4 and corresponding values for constraints from Table 5.

Table 4. The best found solution (f^* = 144 261 eur) from TS run. The number of frames is $n = 18$ (distance between frames 4000 mm).

Beam	Column	Secondary beams	Foundation
h_1 = 1010 mm	h_c = 350 mm	x_{sb} = 2 (27 mm × 225 mm)	a_1 = 1570 mm
h_2 = 2200 mm	b_c = 140 mm		a_2 = 1070 mm
b = 165 mm			h_f = 200 mm
			d_{rs} = 16 mm
			L_{rs} = 400 mm

Table 5. Utilization rates for the best found solution from TS run.

Beam	Column	Secondary beams	Foundation
Bending in tapered part 73 %	Bending 33 %	Bending 97 %	Ground pressure 100 %
Bending in apex 56 %	Shear 14 %	Shear 59 %	Shear 100 %
Lateral torsional buckling 79 %	Compression 24 %		Bending 89 %
Transverse tension in apex 89 %	Buckling 99 %		Punching 64 %
Shear 89 %			
Deflection 100 %			

By comparing results from PSO and TS runs it can be seen that the tabu search managed to improve the final cost 5840 euros (3,9 %). All the other design variables and utilization rates are the same or almost the same except those which are connected to foundation.

The cost distribution from TS run is presented in Fig. 3.

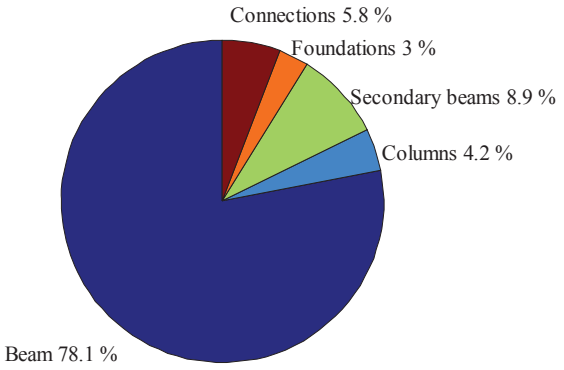

Figure 3. The final cost distribution after PSO and TS optimization runs.

Conclusions

In the timber building design it is better to exploit the advantage of structural optimization than to abide by the analysis of few candidate structures selected based on designer's experience and intuition. All the needed tools like algorithms and computers are nowadays available.

Based on the results it can be seen that the traditional 6 meters distance between frames is not optimal. The cost of glulam beam is the most significant and other costs are rather small compared to it. However it should be kept in mind that material prices might change and if the manufacturing cost is included the result might be different. For example foundation cost would be probably much more than just 3 % if more than material cost is taken into account.

References

[1] EN 1995-1-1 Eurocode 5: Design of timber structures. Part 1-1: General. Common rules and rules for buildings.
[2] Jalkanen, J. 2007, *Tubular truss optimization using heuristic algorithms*. Dissertation, Tampere University of Technology.
[3] Farkas, J., Jármai, K. 2008, *Design and Optimization of Metal Structures*, Horwood Publishing.

Jussi Jalkanen
KPM-Engineering
Kalevantie 7 C, 33100 Tampere, Finland
jussi.jalkanen@kpmeng.fi

Steel building optimization applying metamodel techniques

Teemu Tiainen, Markku Heinisuo, Timo Jokinen, Mikko Salminen

Metallirakenteiden tutkimuskeskus, TTY
PL 600 33101 Tampere

Summary. The paper demonstrates the use of metamodels in a cost optimization of single story industrial or commercial steel building including one span symmetric tubular steel roof trusses. A cost optimal solution for truss+wall combination is presented by varying the unit cost of the wall. One span truss metamodel is used. The main conclusions are: Optimize larger compositions, not only one product; cost optimal span/height ratio for one span Warren-type truss is 10; for low cost walls, say 50 - 70 e /m2, the optimal span/height ratio is 12; for more expensive walls the span/height ratio should be more than 12; careful building of metamodels enables their use in many kinds of optimization problems to quickly get results for the preliminary design; the metamodels are essential tools in optimization still a long time, although software and hardware are getting more and more efficient.

Key words: Metamodel, tubular steel truss cost optimization, truss+wall optimization

Esitys on julkaistu *Rakenteiden mekaniikka lehdessä*: Vol. 45, 2012, Nro 3.

Rakenteen vasteiden estimointi metamallien avulla

Lauri Halonen, Sami Pajunen

Tiivistelmä Artikkelissa on sovellettu muutamia yleisesti käytössä olevia metamalleja rakenteiden vasteiden approksimointiin. Ensimmäisen ja toiseen asteen polynomiregressiolla sekä Krigingin stokastisella mallilla on estimoitu erityyppisten analyyttisten testifunktioiden arvoja, jotta saataisiin käsitys eri mallien vaatimasta työmäärästä ja tarkkuudesta. Metamallien yhteydessä on tutkittu myös eri koesuunnittelumenetelmien ominaisuuksia ja niiden vaikutuksia tulosten tarkkuuteen. Metamalleja on sovellettu lisäksi törmäysvaimentimen transienttiin tarkasteluun ANSYS- ja MatLab-ohjelmilla.

Key words: metamalli, korvikemalli, koesuunnittelu, vastinpinta, Kriging

1. Johdanto

Metamallilla tarkoitetaan tässä yhteydessä rakenteesta tehdystä laskentamallista muodostettua yksinkertaistettua ja laskennallisesti tehokasta mallia, joka jäljittelee alkuperäisen laskentamallin käyttäytymistä rakenteen muuttujien saadessa eri arvoja. Metamalli, eli korvikemalli, muodostetaan laskemalla rakenteen haluttuja vasteita erillisissä koepisteissä, joissa muuttujat eli faktorit saavat tietyt arvot. Tyypillisesti faktorit ovat rakenteen mittoihin, geometriaan tai topologiaan liittyviä suureita ja koepisteiden paikat määritetään systemaattisesti jollakin koesuunnittelumenetelmällä. Koepisteiden välillä rakenteen vasteita approksimoidaan metamallin tyypistä riippuen joko polynomifunktioilla tai stokastisilla funktioilla. Metamallin muodostamisessa yksi oleellinen tekijä on approksimoinnissa syntyvän virheen kontrolloiminen ja laskentatyömäärän pitäminen pienenä mahdollisimman tarkoituksenmukaisella koepistevalinnalla. Tyypillisesti metamalleja käytetään kantavien rakenteiden optimoinnin yhteydessä, jossa saavutetaan suuri etu, kun kohde- ja rajoitusfunktioiden arvoja on laskettava useita kertoja. Metamalleja voidaan hyödyntää myös esimerkiksi herkkyysanalyysissä käytännön insinöörisuunnittelussa, kun halutaan tietää miten rakenteen vasteet muuttuvat, kun olemassa olevaa rakennetta muutetaan eri tavoilla. Tässä artikkelissa on esitelty lyhyesti polynomiregression ja Kriging-menetelmän keskeisimmät yhtälöt luvuissa 2 ja 3. Luvussa 4 on esitelty muutamia yleisimpiä koesuunnittelun menetelmiä, joilla koepisteiden paikat määritetään. Luvussa 5 on esitetty sovellusesimerkki, jonka avulla on havainnollistettu eri menetelmien toimintaa.

2. Regressiomalli

Tarkastellaan rakenteen mielivaltaista vastetta y, joka riippuu jatkuvista muuttujista x_i siten, että

$$y = f(x_1, x_2, \cdots, x_n) \tag{1}$$

Funktion f määrittämiseksi tarvitsee tietää vasteen y arvo faktoreiden x_i eri arvoilla. Yleisessä tapauksessa kun vasteita on useampia, ne voidaan esittää matriisimuodossa

$$\mathbf{y} = \mathbf{X}\boldsymbol{\beta} \tag{2}$$

jossa $\mathbf{X}$ on datamatriisi ja $\boldsymbol{\beta}$ on regressiomallin parametrit β_i sisältävä vektori. Datamatriisi $\mathbf{X}$ sisältää k faktorin arvot N koepisteissä siten, että

$$\mathbf{y} = \begin{bmatrix} y_1 \\ y_2 \\ \vdots \\ y_N \end{bmatrix}, \qquad \mathbf{X} = \begin{bmatrix} 1 & x_{11} & x_{12} & \cdots & x_{1k} \\ 1 & x_{21} & x_{22} & \cdots & x_{2k} \\ \vdots & \vdots & \vdots & \ddots & \vdots \\ 1 & x_{N1} & x_{N2} & \cdots & x_{Nk} \end{bmatrix} \tag{3}$$

Mikäli koepisteitä on enemmän kuin tarvittava minimimäärä, regressiomallin kertoimien β_i määrittäminen tehdään pienimmän neliösumman menetelmällä. Tämä johtaa vasteen $\mathbf{y}$ estimaatin $\hat{\mathbf{y}}$ yhtälöön [1]

$$\hat{\mathbf{y}} = \mathbf{X}\mathbf{b} \tag{4}$$

jossa

$$\mathbf{b} = \left(\mathbf{X}^{\mathrm{T}}\mathbf{X}\right)^{-1}\mathbf{X}^{\mathrm{T}}\mathbf{y} \tag{5}$$

Yleensä funktioksi f valitaan polynomi (1. tai 2. asteen), jolloin menetelmästä käytetään nimeä vastepintamenetelmä.

3. Kriging-malli

Kriging-mallin tuntematon funktio $y(x)$ koostuu kahdesta osasta

$$y(x) = f(x) + Z(x) \tag{6}$$

jossa $f(x)$ on approksimaatiofunktio (yleensä vakio tai 1. asteen polynomi), joka kuvaa mallin globaalia käyttäytymistä ja $Z(x)$ on funktio joka kuvaa tilastollista osuutta mallissa sekä paikallista muutosta [2]. Mallia luodessa asetetaan stokastisen prosessin odotusarvo nollaksi ja kovarianssi nollasta poikkeavaksi. Kovarianssimatriisi funktiolle $Z(x)$ saadaan muodostettua pisteiden x^i ja x^j välille muodossa

$$Cov\left[Z\left(\mathbf{x}^{\mathrm{i}}\right), Z\left(\mathbf{x}^{\mathrm{j}}\right)\right] = \sigma^2\mathbf{R}\left(\left[R\left(\mathbf{x}^{\mathrm{i}}, \mathbf{x}^{\mathrm{j}}\right)\right]\right) \tag{7}$$

jossa σ^2 on varianssi ja $\mathbf{R}$ korrelaatiomatriisi, joka muodostetaan korrelaatiofunktion R avulla. Korrelaatiofunktio R pyrkii kuvaamaan millainen korrelaatio koepisteiden x^i ja x^j välillä on. Korrelaatiofunktio voidaan valita vapaasti, mutta yleisesti käytössä olevia korrelaatiofunktioita ovat Gaussin funktio, lineaarinen ja neliöllinen korrelaatiofunktio. Gaussin korrelaatiofunktio pisteiden x^i ja x^j välille voidaan esittää muodossa

$$R\left(\mathbf{x}^{\mathrm{i}}, \mathbf{x}^{\mathrm{j}}\right) = \exp\left[-\sum_{k=1}^{n_{\mathrm{d}}} \theta_k \left|x_{\mathrm{k}}^{\mathrm{i}} - x_{\mathrm{k}}^{\mathrm{j}}\right|^2\right] \tag{8}$$

jossa n_d on faktorien lukumäärä ja θ_k on faktoria k vastaava korrelaatiokerroin. Korrelaatiokerroin voi olla jokaiselle faktorille sama, mutta tarkin malli saadaan, kun korrelaatiokerroin lasketaan optimoimalla [3,4]. Näin muodostettu korrelaatiomatriisi **R** on symmetrinen *n*x*n*-matriisi, jonka lävistäjällä on ykkösiä. Käyttämällä pienimmän neliösumman menetelmää, päädytään lopulta vasteen estimaatin yhtälöön [3]

$$\hat{\mathbf{y}} = \mathbf{f}\hat{\beta} + \mathbf{r}^{\mathrm{T}}\mathbf{R}^{-1}\left(\mathbf{y} - \mathbf{f}\hat{\beta}\right) \tag{9}$$

jossa **f** on koepisteessä $\boldsymbol{x}$ muodostettu vektori ja estimaatti $\hat{\beta}$ on

$$\hat{\beta} = \left(\mathbf{f}^{\mathrm{T}}\mathbf{R}^{-1}\mathbf{f}\right)^{-1}\mathbf{f}^{\mathrm{T}}\mathbf{R}^{-1}\mathbf{y} \tag{10}$$

ja korrelaatiovektori pisteen **x** ja koepisteiden välillä lausutaan muodossa

$$\mathbf{r}^{\mathrm{T}} = \left[\mathbf{R}\left(\mathbf{x},\mathbf{x}^{1}\right),\mathbf{R}\left(\mathbf{x},\mathbf{x}^{2}\right),\cdots,\mathbf{R}\left(\mathbf{x},\mathbf{x}^{\mathrm{n}}\right)\right]^{\mathrm{T}} \tag{11}$$

4. Koesuunnittelu

Täydessä kahden tai kolmen tason faktorikokeessa kaikki faktorit saavat skaalattuja arvoja joukosta [-1,1] tai [-1,0,1], mutta myös huomattavasti monimutkaisempiakin koesuunnitteluja on olemassa [1]. Esimerkiksi klassinen CCD–menetelmä (Central Composite Design) on eräs paljon käytetty menetelmä, jossa faktoreiden arvotasoja on viisi. Faktoreiden lukumäärän kasvaessa käytetään usein osittaisia faktorikokeita, joilla koepisteiden lukumäärä rajoitetaan kohtuulliseksi jättämällä merkityksettömiä faktorikombinaatioita pois. Koesuunnittelumenetelmiä, joissa pyritään kattamaan faktoriavaruus mahdollisimman hyvin eri kriteereihin perustuen, ovat esimerkiksi LHS (Latin Hypercube Sampling) ja *D*-optimaalinen koesuunnittelu. Nämä menetelmät eivät ole sidottuja mihinkään tiettyyn arvotasolukumäärään ja niitä käytetään yleisesti sekä polynomiregressiomallin että Kriging–mallin yhteydessä.

5. Mallien vertailua

Edellä esitettyjä malleja ja niissä esiintyviä lukuisia variaatioita on testattu kattavasti työssä [5]. Tässä yhteydessä esitetään vain yhden testitapauksen tuloksia kuvailevasti. Tarkastellaan kuvassa 1 esitettyä rakennetta, joka koostuu teräksisestä ohutseinäisestä sylinteristä (osa 1) ja hyvin jäykästä kuristimesta (osa 2). Sylinterin päähän keskeisesti törmäävä 5000 kg massa mallinnettiin levynä, joka on alkutilanteessa kiinni sylinterin toisessa päässä eikä pääse irtoamaan sylinteristä törmäyksen aikana. Massan alkunopeus on 1 m/s. Muuttujiksi valittiin kolme rakenteen käyttäytymiseen oleellisesti vaikuttavaa tekijää – sylinterin seinämän paksuus *t* (kuvssa 8 mm), kuristimen sisäosan kaltevuus α (10^{O}) sekä loppuosan halkaisija *d* (208 mm). Estimoitaviksi vasteiksi valittiin sylinterin tunkeuma kuristimen sisään sekä sylinterin muodonmuutosenergia. Estimointi tehtiin faktoriavaruuteen, jossa $t \in$[6.5mm, 8.5mm], $\alpha \in [9^{\mathrm{O}}, 11^{\mathrm{O}}]$, $d \in$[200mm, 208mm].

Mallin käyttäytymistä estimoidaan lineaarisella ja neliöllisellä polynomiregressiolla sekä Kriging-mallilla. Polynomiregressiossa käytetään minimimäärää koepisteitä, joten lineaarinen vastepinta muodostetaan neljällä koepisteellä ja toisen asteen malli kymmenellä koepisteellä. vastaavasti Kriging-mallia luodessa on käytetty 15 *D*-optimaalisella suunnittelukriteerillä valittua koepistettä. Koepisteiden lukumääräksi valittiin 15, koska ennalta tiedetään, että Kriging-mallia ei saada viritettyä tarpeeksi tarkaksi jos koepisteitä on liian vähän [5]. Näin ollen jokaisen mallin muodostamiseen käytettiin koepisteiden minimimäärää, ja jokaista mallia olisi mahdollisuus tarkentaa koepisteitä lisäämällä.

Eri mallien antamia tuloksia sekä tunkeumalle että muodonmuutosenergialle on esitetty kuvassa 2 siten, että kuvissa kuristimen loppuosan halkaisija on kiinnitetty arvoon d = 208 mm.

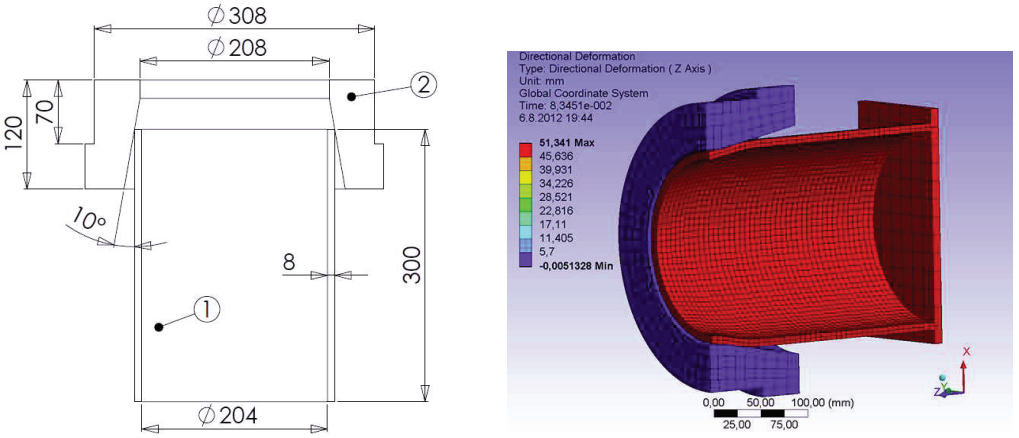

Kuva1. Vaimentimen rakenne ja lähtötiedot sekä deformoitunut rakenne lopputilassa

Kuvasta 2 nähdään selkeä yhdenmukaisuus eri mallien välillä. Virhetarkastelu osoittaa, että lineaarisessa mallissa virhe jakautuu epätasaisesti pinnan alueelle ja on suurimmillaan nurkissa [5]. Tämä antaa viitteitä siitä, että pinta ei todellisuudessa ole lineaarinen. Toisen asteen mallin virhejakauma puolestaan on hyvin tasainen, joten on selvää, että se pystyy kuvaamaan todellista mallia tarkemmin kuin lineaarinen pinta [5]. Kriging-menetelmän tuloksesta nähdään, että se poikkeaa muista malleista nimenomaan mallinnetun alueen nurkka-alueilla. Kuvassa 3 on esitetty vastaava Kriging-mallin tulos hiukan rajatulle faktoriavaruuden osalle, jonka nurkkapisteet ovat koepisteitä. Tällöin vaste on kvalitatiivisesti samanlainen polynomipintojen kanssa. Tämä vahvistaa aiemmissa testeissä todetun säännön Kriging-mallille [5]: Gaussin korrelaatiofunktiota käytettäessä ei tulisi mennä kovin paljon koepisteiden suunnittelussa käytettyjen rajojen ulkopuolelle ettei mallin tarkkuus romahtaisi.

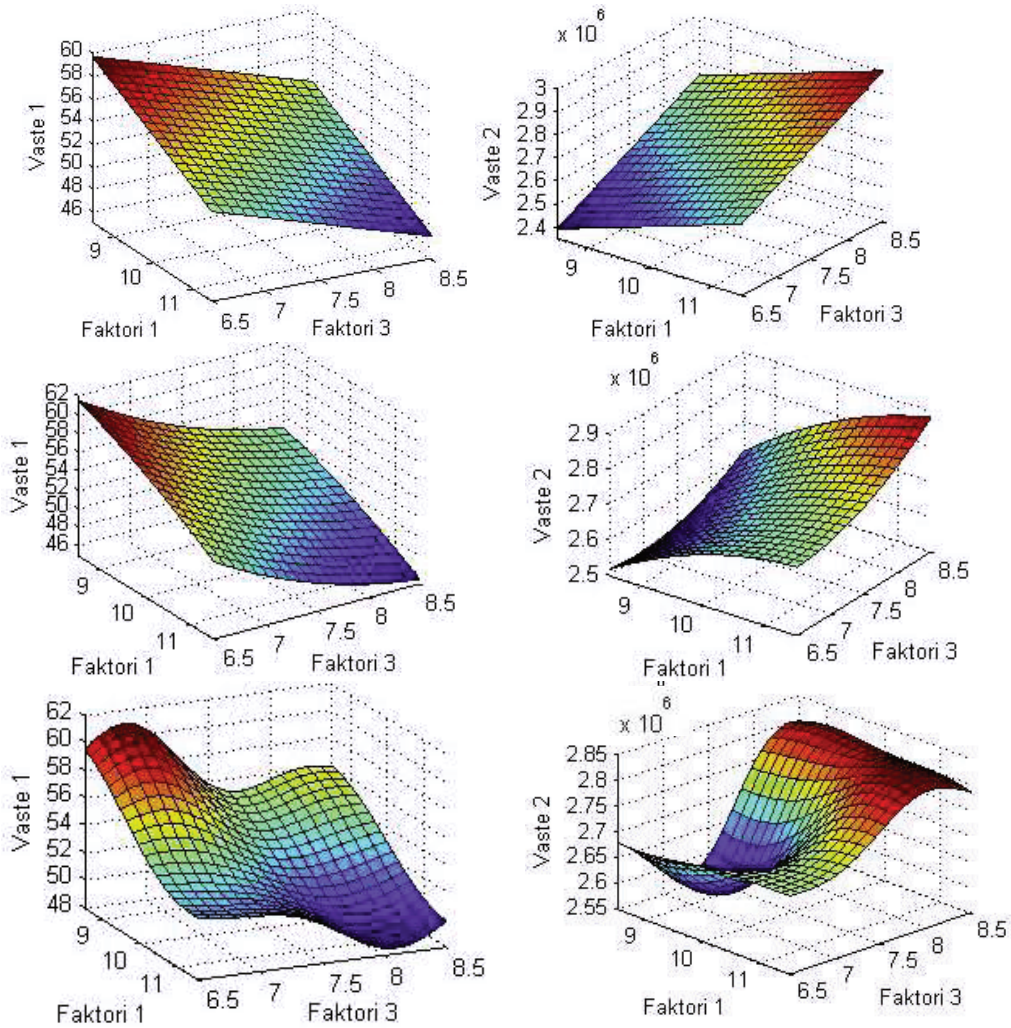

Kuva 2. Tunkeuman (mm) ja muodonmuutosenergian vastepintoja (ylinnä lineaarinen malli, keskellä toisen asteen malli, ja alinna Kriging-malli)

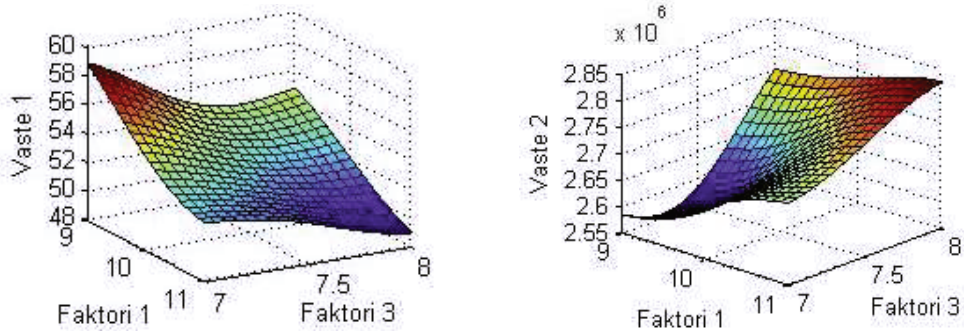

Kuva 3. Kriging-mallin tulokset pienemmälle aliavaruudelle.

6. Johtopäätökset ja jatkotutkimus

Työssä on sovellettu eri metamalleja rakenteiden mekaniikan analyysiin ja tutkittu eri menetelmien parametrien vaikutusta estimointitarkkuuteen. Yleisenä johtopäätöksenä voidaan todeta, että lineaarinen ja toisen asteen polynomiregressiomalli riittävät käytännössä kaikkiin vastinpintoihin, mutta ongelmaksi tulee sopivan avaruuden koon määrittäminen. Merkittäväksi tämä tulee etenkin monimutkaisemmissa ja epälineaarisesti käyttäytyvissä tehtävissä joissa ei tiedetä kovin hyvin vasteen käyttäytymistä. Esimerkkinä tällaisesta tehtävästä on esitetty törmäysvaimentimen analysointi. Kriging-malli taas toimii hyvin lähes aina, kunhan koepisteitä on riittävästi. Jos koepisteitä ei ole riittävästi, θ-parametrien arvot poikkeavat paljon optimiarvoista, joka taas johtaa epätarkkaan malliin. Gaussin korrelaatiofunktio ja vakio regressiofunktio ovat lukuisten testiesimerkkien valossa riittävä kombinaatio tehtävätyypistä riippumatta, mutta ko. funktioita muuttamalla voi säätää mallin käyttäytymistä lineaarisemmaksi jos se on tarpeen mallin stabiloimiseksi.

Jatkossa tutkimuksessa tehtyjä malleja käytetään rakenteiden optimoinnin yhteydessä, jossa metamallit tuovat laskennallista tehokkuutta. Optimoinnin yhteydessä tarvitaan myös vasteiden herkkyysderivaattoja, joiden evaluoinnissa syntyviin approksimaatiovirheisiin ei vielä tässä työssä ole otettu kantaa. Lisäksi jatkotutkimuksen yhtenä suuntana on kehittää testi, jonka avulla voitaisiin mahdollisimman pienellä lisätyöllä arvioida, mikä metamalli soveltuu tarkastelun kohteena olevalle tehtävätyypille parhaiten, ja kuinka suuren suunnittelumuuttuja-avaruuden sillä voi kattaa.

Viitteet

[1] R.H. Myers, D.C. Montgomery, C.M. Anderson-Cook, *Response Surface Methodology: process and Production Optimization Using Designed Experiments*, John Wiley & Sons, 2009.

[2] N. Cressie, The Origins of Kriging, *Mathematical Geology*, 22(3), 1990.

[3] T. W. Simpson,T. M. Mauery, J. J. Korte, F. Mistree, Kriging models for global approximation in simulation-based multidisciplinary design optimization, *AIAA Journal*, 39 (12):2233-2241, 2001.

[4] S.N. Lophaven, H.B. Nielsen, J. Sondergaard, DACE - A Matlab Kriging Toolbox, *Technical Report.* Technical University of Denmark, 2002.

[5] L. Halonen, Metamallien soveltaminen kantavien rakenteiden parametriseen laskentaan. Diplomityö, Tampereen teknillinen yliopisto, 2012.

Lauri Halonen
Lujuuslaskija
FSDynamics
lauri.halonen@fsdynamics.fi

Sami Pajunen
Yliopistonlehtori
PL 589 33101 Tampere
sami.pajunen@tut.fi

Sekalukuformulointi ristikkorakenteiden topologian optimointiin

Kristo Mela ja Juhani Koski

Tiivistelmä. Ristikoiden topologian optimoinnissa etsitään parasta mahdollista sauvottelua ja sauvojen profiileja. Lähtökohtana on niin sanottu perusrakenne, jossa on suuri määrä solmuja ja sauvoja, ja optimoinnissa sauvojen annetaan poistua. Tavallisissa tehtävänasetteluissa sauvojen poistumisesta aiheutuu vakavia teoreettisia ja numeerisia ongelmia. Tässä työssä esitellään topologian optimoinnin formulointi, joka välttää nämä ongelmat ja mahdollistaa lineaaristen sekalukualgoritmien käyttämisen tehtävän ratkaisemiseen.

Avainsanat: Ristikko, topologian optimointi, sekalukuoptimointi

Johdanto

Ristikkorakenteiden suunnitteluprosessi voidaan osittain automatisoida pukemalla suunnitteluongelma matemaattiseksi optimointitehtäväksi, joka ratkaistaan sopivalla optimointialgoritmilla. Tällöin suunnittelijan ei tarvitse tehdä rakennetta parantavia muutoksia käsityönä, vaan ratkaisualgoritmi etenee automaattisesti, kunnes ennalta määrätty lopetuskriteeri toteutuu.

Ristikoiden optimointitehtävät jaetaan pääsääntöisesti kolmeen kategoriaan. *Mitoitusoptimoinnissa* rakenteen solmujen ja sauvojen paikat on kiinnitetty ja tavoitteena on löytää sauvojen optimaaliset poikkipintaprofiilit. *Geometrian optimoinnissa* sauvojen profiilien lisäksi voidaan muutella solmujen sijaintia, jolloin ristikon muoto muuttuu. *Topologian optimoinnissa* solmujen ja sauvojen lukumäärä, solmujen sijainti, sauvojen kytkeytyminen ja niiden profiilit ovat muuttujina. On selvää, että viimeksi mainittu tehtävätyyppi on haastavin, mutta samalla se tarjoaa parhaat mahdollisuudet uudenlaisten rakennekonseptien löytämiseksi.

Ristikoiden topologian optimoinnissa lähtökohtana on ns. *perusrakenne (ground structure)*, joka sisältää suuren määrän sauvoja ja solmuja [2]. Optimoinnin aikana sauvat ja solmut voivat hävitä, mikä johtaa topologian muutoksiin. Tyypillisesti sauvojen poistaminen hoidetaan antamalla poikkipinta-alan mennä nollaksi, jolloin sauva häviää rakennemallista. Tällä tekniikalla on kuitenkin vakavia teoreettisia ja numeerisia seurauksia, jotka johtavat suuriin hankaluuksiin tehtävän ratkaisemisessa.

Tässä artikkelissa tarkastellaan ristikoiden topologian optimointitehtäviä, joissa sauvaprofiilit valitaan diskreetistä vaihtoehtojen joukosta. Työssä esitellään formulointi, jossa tehtävästä tulee lineaarinen sekalukuoptimointiongelma (*mixed-integer linear programming, MILP*). Formuloinnin pääasiallisena etuna on, että sen avulla vältetään topologian optimoinnin teoreettiset ongelmat, jotka liittyvät perusrakenteesta poistettaviin sauvoihin. Lisäksi tehtävä voidaan ratkaista deterministisellä ns. *branch-and-cut*-algoritmilla, jolla on mahdollista suotuisissa tapauksissa löytää globaali optimi.

Artikkeli on jaoteltu seuraavasti. Aluksi esitellään lyhyesti ristikon rakenneanalyysi siinä muodossa kuin sitä myöhemmin käytetään. Sitten esitellään optimointitehtävän

muuttujat, rajoitusehdot ja kohdefunktio. Lopuksi tarkastellaan formuloidun sekalukutehtävän ratkaisemista.

Rakenneanalyysi

Rakenneanalyysi tehdään lineaarisen kimmoteorian mukaisesti siirtymämenetelmään perustuen. Poikkeuksellisesti jäykkyysyhtälö hajotetaan elementtitasolle, millä vältetään jäykkyysmatriisin singulaarisuus sauvojen poistuessa rakenteesta. Kolme tarvittavaa ehtoa ovat solmujen voimatasapaino, yhteensopivuusehdot sekä voima-siirtymä-relaatiot. Olkoon perusrakenteessa n_E sauvaa ja n_d siirtymävapausastetta. Kuormitustapauksen k solmujen tasapainoehdot voidaan kirjoittaa muodossa

$$\mathbf{B}\mathbf{N}^k = \mathbf{p}^k \tag{1}$$

missä $\mathbf{B} \in \mathbb{R}^{n_d \times n_E}$ on rakenteen staattinen matriisi, $\mathbf{N}^k \in \mathbb{R}^{n_E}$ on sauvojen normaalivoimien vektori ja $\mathbf{p}^k \in \mathbb{R}^{n_d}$ on kuormitusvektori. Sauvan i normaalivoima kuormitustapauksessa k on

$$N_i^k = \frac{E_i A_i}{L_i} \mathbf{b}_i^{\mathrm{T}} \mathbf{u}^k \tag{2}$$

missä E_i on kimmomoduuli, L_i on sauvan pituus, $\mathbf{b}_i$ on matriisin $\mathbf{B}$ sarake i, $\mathbf{u}^k$ on globaali solmusiirtymävektori ja A_i on sauvan poikkipinta-ala.

Yhtälöt (1) ja (2) riittävät yhdessä ristikon analysointiin. Yhtälö (2) sisältää sekä yhteensopivuusehdot, että voima-siirtymä-yhtälön.

Optimointimuuttujat

Tehtävässä on sekä binäärisiä että jatkuvia muuttujia. Binäärimuuttujat määräävät sauvojen ja solmujen olemassaolon sekä profiilin valinnan. Jatkuvat muuttujat ovat sauvojen normaalivoimat ja solmusiirtymät, jotka siis tässä sisällytetään optimointitehtävään muuttujina.

Sauvan i olemassaolon määrittää muuttuja y_i, joka saa arvon 1, jos sauva valitaan rakenteeseen ja 0 muuten. Vastaavasti solmuun ℓ liitetään binäärimuuttuja z_ℓ, joka saa arvon 1, jos solmu on rakenteessa ja 0 muuten.

Oletetaan, että valittavissa on n_S kappaletta profiileja, jotka on asetettu poikkipinta-alan mukaan kasvavaan järjestykseen. Poikkipinta-alojen ja neliömomenttien joukkoja merkitään $\mathcal{A} = \{\hat{A}_1, \hat{A}_2, \ldots, \hat{A}_{n_S}\}$ ja $\mathcal{I} = \{\hat{I}_1, \hat{I}_2, \ldots, \hat{I}_{n_S}\}$. On huomattava, että $\hat{A}_i < \hat{A}_{i+1}$, mutta $\hat{I}_i \geq \hat{I}_{i+1}$ on mahdollinen.

Sauvan profiilin valinta tehdään binäärimuuttujien y_{ij} avulla, jotka määritellään:

$$y_{ij} = \begin{cases} 1 & \text{jos profiili } j \text{ valitaan sauvalle } i \\ 0 & \text{muuten} \end{cases} \tag{3}$$

Yksikäsitteinen profiili valitaan lisäämällä tehtävään seuraava rajoitusehto kaikille sauvoille:

$$y_i = \sum_{j=1}^{n_S} y_{ij} \tag{4}$$

Jos yhtälössä (4) muuttuja y_i saa arvon 0, on kaikkien muuttujien y_{ij} oltava myös nollia. Vastaavasti, jos $y_i = 1$, on tarkalleen yhden profiilimuuttujan saatava arvo 1.

Normaalivoimamuuttujat määritellään jokaisen sauvan jokaiselle profiilille kaikissa kuormitustapauksissa. Tällöin merkitään [6]

$$N_{ij}^k = \frac{E_i}{L_i}\hat{A}_j \mathbf{b}_i^{\mathrm{T}} \mathbf{u}^k y_{ij} \quad \forall\,(i,j,k) \tag{5}$$

Formuloinnin tärkein askel on epälineaarisen yhtälön (5) muuntaminen lineaariseen muotoon. Tätä varten on ensin asetettava solmusiirtymille ala- ja ylärajat, $\underline{u}_\ell$ ja $\overline{u}_\ell$. Tällöin voimamuuttujille saadaan rajat [6]

$$\underline{N}_{ij}^k = \min_{\underline{\mathbf{u}} \le \mathbf{u}^k \le \overline{\mathbf{u}}} \left\{ \frac{E_i}{L_i}\hat{A}_j \mathbf{b}_i^{\mathrm{T}} \mathbf{u}^k \right\} = \frac{E_i \hat{A}_j}{L_i} \left(\sum_{\ell : b_{i\ell} > 0} b_{i\ell} \underline{u}_\ell + \sum_{\ell : b_{i\ell} < 0} b_{i\ell} \overline{u}_\ell \right) \tag{6}$$

$$\overline{N}_{ij}^k = \max_{\underline{\mathbf{u}} \le \mathbf{u}^k \le \overline{\mathbf{u}}} \left\{ \frac{E_i}{L_i}\hat{A}_j \mathbf{b}_i^{\mathrm{T}} \mathbf{u}^k \right\} = \frac{E_i \hat{A}_j}{L_i} \left(\sum_{\ell : b_{i\ell} > 0} b_{i\ell} \overline{u}_\ell + \sum_{\ell : b_{i\ell} < 0} b_{i\ell} \underline{u}_\ell \right) \tag{7}$$

Voidaan osoittaa [6], että (5) on ekvivalentti seuraavien lineaaristen epäyhtälöiden kanssa:

$$\underline{N}_{ij}^k y_{ij} \le N_{ij}^k \le \overline{N}_{ij}^k y_{ij} \tag{8}$$

$$(1 - y_{ij})\underline{N}_{ij}^k \le \frac{E_i}{L_i}\hat{A}_j \mathbf{b}_i^{\mathrm{T}} \mathbf{u}^k - N_{ij}^k \le (1 - y_{ij})\overline{N}_{ij}^k \tag{9}$$

Solmumuuttujien ja solmun siirtymien välillä on yhteys

$$\underline{u}_{j\ell} z_\ell \le u_{j\ell}^k \le \overline{u}_{j\ell} z_\ell \quad \forall (j,\ell,k) \tag{10}$$

missä $\underline{u}_{j\ell}$ ja $\overline{u}_{j\ell}$ ovat solmun ℓ siirtymän j ala- ja ylärajat ja $u_{j\ell}^k$ on solmun ℓ siirtymä j kuormitustapauksessa k.

Edellä esitellyt muuttujat voidaan koota vektoriksi

$$\mathbf{x} = \{\mathbf{y}\ \mathbf{N}_1^1\ \mathbf{N}_2^1\ \ldots\ \mathbf{N}_{n_E}^1\ \mathbf{u}^1 \ldots \mathbf{N}_1^{n_L}\ \mathbf{N}_2^{n_L}\ \ldots\ \mathbf{N}_{n_E}^{n_L}\ \mathbf{u}^{n_L}\ \mathbf{Y}\ \mathbf{z}\} \tag{11}$$

missä $\mathbf{y} = \{y_{11}\ \ y_{12}\ \ldots y_{n_E,n_S}\}$, $\mathbf{Y} = \{y_1\ \ y_2 \ldots y_{n_E}\}$ ja $\mathbf{z} = \{z_1\ \ z_2 \ldots z_n\}$.

Rajoitusehdot

Rakenneanalyysi rajoitusehtoina

Yhtälö (2) sisältyy voimamuuttujien määritelmään. Solmujen tasapainoyhtälöjen (1) toteutuminen varmistetaan ottamalla ne yhtälörajoitusehdoiksi. Ne on kuitenkin lausuttava voimamuuttujien avulla. Kootaan sauvan i voimamuuttujat kuormitustapauksessa k vektoriksi $\mathbf{N}_i^k = \{N_{i1}^k\ \ N_{i2}^k\ \ \ldots N_{in_S}^k\} \in \mathbb{R}^{n_S}$, jolloin yhtälö (1) voidaan kirjoittaa muodossa [6]

$$\hat{\mathbf{B}}\hat{\mathbf{N}}^k = \mathbf{p}^k \tag{12}$$

missä $\hat{\mathbf{N}}^k = \{\mathbf{N}_1^k\ \mathbf{N}_2^k\ \cdots\ \mathbf{N}_{n_E}^k\}$ ja

$$\hat{\mathbf{B}} = \begin{matrix} \mathbf{b}_1 & \mathbf{b}_1 & \cdots & \mathbf{b}_1 & \vdots & \mathbf{b}_2 & \mathbf{b}_2 & \cdots & \mathbf{b}_2 & \vdots & \cdots & \vdots & \mathbf{b}_{n_E} & \mathbf{b}_{n_E} & \cdots & \mathbf{b}_{n_E} \end{matrix} \tag{13}$$

Sauvojen lujuus

Sauvojen lujuuden rajoitusehdot lausutaan voimamuuttujien avulla seuraavasti:

$$-\underline{\sigma}\hat{A}_j y_{ij} \leq N_{ij}^k \leq \overline{\sigma}\hat{A}_j y_{ij} \quad \forall\,(i,j,k) \tag{14}$$

missä $\underline{\sigma}$ ja $\overline{\sigma}$ ovat puristus- ja vetopuolen suurimmat sallitut jännitykset. Yhtälöstä (4) seuraa, että vain sauvalle valittavalle profiilille yhtälö (14) on epätriviaali.

Sauvojen nurjahdus

Sauvojen nurjahduksen estävä ehto voidaan kirjoittaa yleisesti muodossa

$$N \geq -f_B(E,L,A,I) \tag{15}$$

missä f_B on nurjahdustapauksesta riippuva suurimman sallitun puristusvoiman määrittävä funktio. Eulerin nurjahduksessa

$$f_B = f_B(E,L,I) = \pi^2 \frac{EI}{L_n^2} \tag{16}$$

missä L_n on sauvan nurjahduspituus. Vastaavasti Eurokoodi 3:n mukaan [3]

$$f_B = f_B(E,L,A,I) = \chi(E,L,A,I)A\frac{f_\mathrm{y}}{\gamma_{M1}} \tag{17}$$

missä χ on nurjahduskestävyyden pienennystekijä, f_y on materiaalin myötöraja ja γ_{M1} on osavarmuuskerroin.

Nurjahdusrajoitusehto kirjoitetaan optimointitehtävään muodossa

$$N_{ij}^k \geq -f_B(E_i, L_i, \hat{A}_j, \hat{I}_j)y_{ij} \quad \forall\,(i,j,k) \tag{18}$$

On merkittävää, että mutkikkaistakin funktion f_B lausekkeista huolimatta rajoitusehto on lineaarinen, sillä f_B evaluoidaan kullekin profiilille ja sauvalle erikseen.

Topologisia rajoitusehtoja

Binäärimuuttujat mahdollistavat ristikon topologiaan liittyvien ehtojen lausumisen yksinkertaisin lausekkein. Niiden pääasiallinen tarkoitus on helpottaa tehtävän ratkaisemista. Sekalukutehtävien ratkaiseminen riippuu näet oleellisesti käytetyn formuloinnin kyvystä rajata käypä joukko tehokkaasti, ja tehtävän koko ei kerro kaikkea sen vaikeudesta.

Olkoon $\mathcal{I}_\ell$ niiden sauvojen joukko, jotka liittyvät solmuun ℓ. Tällöin kyseisen solmumuuttujan ja sauvojen välille voidaan kirjoittaa ehto

$$y_i \leq z_\ell \quad \forall \ell = 1,2,\ldots,n_N, i \in \mathcal{I}_\ell \tag{19}$$

Toisin sanoen, jos solmu poistetaan perusrakenteesta, $z_\ell = 0$, on solmuun liittyvien sauvojenkin hävittävä. Läsnäolevaan solmuun on liityttävä minimimäärä sauvoja. Tuettuihin solmuihin on liityttävä vähintään yksi sauva ja vapaisiin solmuihin vähintään kaksi sauvaa, jotta rakenne voi olla kinemaattisesti stabiili. Tämä voidaan lausua rajoitusehtona

$$\sum_{i \in \mathcal{I}_\ell} y_i \geq C z_\ell \quad \forall \ell = 1,2,\ldots,n_N \tag{20}$$

missä $C = 1$, jos solmu on tuettu ja $C = 2$ jos solmu on vapaa.

Myös ristikon kinemaattisen stabiilisuuden välttämätön ehto voidaan lausua binäärimuuttujien avulla. Ristikko on kinemaattisesti stabiili, jos

$$b + r \geq DN_c \tag{21}$$

missä b on sauvojen, r tukireaktioiden ja N_c solmujen lukumäärä. Lisäksi D on ristikon geometrian dimensio (2 tai 3). Binäärimuuttujien avulla lausuttuna tämä ehto on [4]

$$\sum_{i=1}^{n_E} y_i + \sum_{s \in \mathcal{S}} R_s z_s \geq D \sum_{\ell=1}^{n} z_\ell \tag{22}$$

missä $\mathcal{S}$ on tuettujen solmujen indeksijoukko ja R_s on tuetun solmun s tukireaktioiden lukumäärä.

Kohdefunktio

Tavallisin ristikoiden optimoinnissa käytetty kohdefunktio on rakenteen paino, ja sitä käytetään tässäkin työssä. Paino voidaan ilmaista suunnittelumuuttujienavulla muodossa

$$W(\mathbf{x}) = \sum_{i=1}^{n_E} \rho_i L_i A_i = \sum_{i=1}^{n_E} \rho_i L_i \left(\sum_{j=1}^{n_S} \hat{A}_j y_{ij} \right) = \sum_{i=1}^{n_E} \sum_{j=1}^{n_S} \rho_i L_i \hat{A}_j y_{ij} \tag{23}$$

missä ρ_i on sauvan i materiaalin tiheys.

Tehtävänasettelu

Edellä esitetyn perusteella ristikon painon minimointiongelma voidaan kirjoittaa optimointitehtäväksi

$$\begin{aligned} \min_{\mathbf{x}} \quad & W(\mathbf{x}) \\ \text{siten, että} \quad & \mathbf{x} \text{ toteuttaa ehdot (4), (8), (9), (10), (12), (14), (18), (19), (20), (22).} \end{aligned} \tag{24}$$

Tehtävän ratkaiseminen

Edellä esitetty optimointitehtävä kuuluu lineaaristen sekalukutehtävien joukkoon. Nykyisin sekalukutehtäviä ratkotaan pääasiassa ns. *branch-and-cut*-menetelmällä, jossa yhdistetään hyvin tunnettu *branch-and-bound*-menetelmä (B&B) leikkaustasoihin [7]. Branch and bound -menetelmän ideana on hajottaa käypä joukko binäärimuuttujien suhteen pienempiin erillisiin osiin, joissa tehtävän ratkaiseminen on helpompaa. Kussakin osajoukossa ratkaistaan tehtävän *relaksaatio*, jossa binäärimuuttujia käsitellään jatkuvina. Relaksaatio on lineaarinen optimointitehtävä (LP), jonka ratkaiseminen on erittäin helppoa alkuperäiseen sekalukutehtävään nähden. Relaksaation ratkaisuna saadaan tehtävän optimille alaraja. Jos kaikki binäärimuuttujat saavat relaksaation ratkaisussa kokonaislukuarvon, on löytynyt sekalukutehtävän käypä ratkaisu, josta saadaan optimille yläraja. Käypiä ratkaisuja voidaan etsiä myös heuristisin menetelmin. Algoritmin edetessä optimin alaraja ja yläraja lähestyvät toisiaan, ja kun niiden ero on riittävän pieni, algoritmi lopetetaan. Tällöin on tutkittu koko käypä joukko, ja tuloksena on tehtävän globaali optimi.

Branch and bound -algoritmin keskeinen ongelma on relaksaation tuottaman alarajan heikkous ja sen hidas kasvaminen. Relaksaatiota voidaan oleellisesti tehostaa lisäämällä kussakin tutkittavassa osajoukossa tehtävään leikkaustasoja, joilla relaksaation käyvästä joukosta rajataan pois sellaisia alueita, joissa binäärimuuttujat saavat reaalisia arvoja. Leikkaustasot voivat olla yleisille rajoitusehdoille sopivia tai tietyille rajoitusehtotyypeille räätälöityjä [5].

Yhdessä B&B ja leikkaustasot muodostavat *branch and cut* -menetelmän. Viime vuosina tämän menetelmän kehitys on ollut voimakasta, ja kyky ratkaista suurempia sekalukutehtäviä on kasvanut selvästi [1]. Koska ristikon topologian optimoinnin sekalukuformulointi johtaa helposti suureen optimointitehtävään, mahdollistaa tämä algoritmissa tapahtunut kehitys formuloinnin käyttökelpoisuuden myös käytännön tehtäviin.

Johtopäätökset

Esitetyn formuloinnin keskeinen ominaisuus on tehtävän lineaarisuus. Formuloinnin laajennuksissa tulisi lineaarisuus pyrkiä säilyttämään, sillä epälineaaristen sekalukuongelmien ratkaisu on huomattavasti vaikeampaa kuin lineaaristen. Binäärimuuttujat mahdollistavat haastavienkin topologisten vaatimusten lausumisen yksinkertaisin rajoitusehdoin. Rakenneanalyysin osalta formulointi voidaan laajentaa myös kehärakenteille, mutta silloin ei ole selvää, että lujuuden ja stabiilisuuden rajoitusehdot pysyvät lineaarisina.

Viitteet

[1] R. Bixby and E. Rothberg. Progress in computational mixed in programming – a look back from the other side of the tipping point. *Mathematical Programming*, 149:37–41, 2007.

[2] W. Dorn, R. Gomory, and M. Greenberg. Automatic design of optimal structures. *Journal de Mecanique*, 3:25–52, 1964.

[3] EC 3. *Eurocode 3: Design of Steel Structures. Part 1-1: General rules and rules for buildings.* CEN, 2005.

[4] A. Faustino, J. Júdice, I. Ribeiro, and A. Neves. An integer programming model for truss topology optimization. *Investigação Operacional*, 26:111–127, 2006.

[5] H. Marchand, A. Martin, R. Weismantel, and L. Wolsey. Cutting planes in integer and mixed integer programming. *Discrete Applied Mathematics*, 123:397–446, 2002.

[6] M. Rasmussen and M. Stolpe. Global optimization of discrete truss topology design problems using a parallel cut-and-branch method. *Computers and Structures*, 86:1527–1538, 2008.

[7] L. A. Wolsey. *Integer Programming.* John Wiley & Sons, 1998.

Kristo Mela
Konstruktiotekniikan laitos
Tampereen teknillinen yliopisto
PL 589, 33101 Tampere
s-posti: `kristo.mela@tut.fi`

On selecting weight factors in the least-squares finite element method

Julien Francois[1], Reijo Kouhia[1], Miikka Mikkola[2], and Eero-Matti Salonen[3]

[1] Department of Mechanics and Design, Tampere University of Technology, P.O. Box 589, 33101 Tampere, Finland,
[2] FS Dynamics Finland Oy Ab, Hermiankatu 1, 33720 Tampere, Finland
[3] Department of Civil and Structural Engineering, Aalto University, P.O. Box 12100, 00076 Aalto, Finland

Summary. The paper discusses the selection problem of weight factors in the least-squares finite element method. Simple diffusion equation is used as an example problem. The least-square functional is formed from the system containing both the balance- and the constitutive equations. Standard nodal interpolation is used for heat flux vector and temperature.

Key words: least-squares, finite element method, heat transfer, weight factor

Introduction

The finite element method can be understood as a method of weighted residuals. In a domain Ω we have to solve the following boundary value problem

$$\mathbf{L}\boldsymbol{u} - \boldsymbol{b} = \boldsymbol{0}, \tag{1}$$

where $\mathbf{L}$ is some differential operator and $\boldsymbol{u}$ is a column vector with the unknown quantities to be solved and $\boldsymbol{b}$ is a given source or load vector. Solving the problem with the method of weighted resuduals can be described as

$$\int_\Omega \boldsymbol{w}^{\mathrm{T}}(\mathbf{L}\boldsymbol{u} - \boldsymbol{b})\,\mathrm{d}\Omega = 0, \tag{2}$$

where $\boldsymbol{w}$ a column vector containn the weighting functions. If we choose the weight factors to be the residuals multiplied with a symmetric weight factor matrix $\boldsymbol{W}$ as $\boldsymbol{W}^{\mathrm{T}}\boldsymbol{r} = \boldsymbol{W}^{\mathrm{T}}(\mathbf{L}\boldsymbol{u} - \boldsymbol{b})$ we end up to the least-squares functional

$$I(\boldsymbol{u}) = \frac{1}{2}\int_\Omega \boldsymbol{r}^{\mathrm{T}}\,\boldsymbol{W}\boldsymbol{r}\,\mathrm{d}\Omega. \tag{3}$$

From the stationary condition of I, i.e. $\delta I = 0$ we get the following equation system

$$\int_\Omega (\mathbf{L}\delta\boldsymbol{u})^{\mathrm{T}}\,\boldsymbol{W}(\mathbf{L}\boldsymbol{u} - \boldsymbol{b})\,\mathrm{d}\Omega = 0. \tag{4}$$

With trial functions $\tilde{\boldsymbol{u}} = \boldsymbol{\Psi}\boldsymbol{a} \approx \boldsymbol{u}$, the variation $\delta\boldsymbol{u}$ becomes $\delta\tilde{\boldsymbol{u}} = \boldsymbol{\Psi}\delta\boldsymbol{a}$ and the system (4) transforms into the discrete form

$$\delta\boldsymbol{a}^{\mathrm{T}}\int_\Omega (\mathbf{L}\,\boldsymbol{\Psi})^{\mathrm{T}}\,\boldsymbol{W}(\mathbf{L}\,\boldsymbol{\Psi}\,\boldsymbol{a} - \boldsymbol{b})\,\mathrm{d}\Omega = 0. \tag{5}$$

Example - heat conduction

The energy balance and the Fourier's constitutive equation for an isotropic material can be written as

$$\boldsymbol{r} = \begin{pmatrix} \operatorname{div} \boldsymbol{q} - s \\ \boldsymbol{q} + k \operatorname{grad} \theta \end{pmatrix} = \boldsymbol{0}, \tag{6}$$

where the unknown functions $\boldsymbol{q}$ and θ are the heat flux vector and temperature, respectively.

Dividing the domain Ω in sub-domains Ω^{e} and using the FE-interpolation in each of these subdomains, the discretized weak form can be written in matrix form as

$$\delta \boldsymbol{a}^{\mathrm{T}} (\boldsymbol{A}\boldsymbol{a} - \boldsymbol{f}) = 0, \tag{7}$$

in which the coefficient matrix $\boldsymbol{A}$ is assembled from the elemental contributions

$$\boldsymbol{A}^{\mathrm{e}} = \int_{\Omega^{\mathrm{e}}} \boldsymbol{B}^{\mathrm{T}} \boldsymbol{W} \boldsymbol{B} \, \mathrm{d}\Omega. \tag{8}$$

If standard C_0-interpolation functions are used for each of the flux vector components and temperature, the matrix $\boldsymbol{B}$ can be formed as

$$\boldsymbol{B} = \begin{bmatrix} \boldsymbol{B}_1 & \cdots & \boldsymbol{B}_m \end{bmatrix}, \tag{9}$$

where m is the number of nodes in an element. The nodal contributions $\boldsymbol{B}_i$ can be written in a rectangular cartesian coordinate system as

$$\boldsymbol{B}_i = \begin{bmatrix} N_{i,x} & N_{i,y} & N_{i,z} & 0 \\ N_i & 0 & 0 & kN_{i,x} \\ 0 & N_i & 0 & kN_{i,y} \\ 0 & 0 & N_i & kN_{i,z} \end{bmatrix}, \tag{10}$$

in which N_i is the interpolation function associated to a node i.

The right hand side term $\boldsymbol{f}$ is assembled from the element contributions

$$\boldsymbol{f}^{\mathrm{e}} = \int_{\Omega^{\mathrm{e}}} \boldsymbol{B}^{\mathrm{T}} \boldsymbol{W} \boldsymbol{b} \, \mathrm{d}\Omega, \quad \text{where} \quad \boldsymbol{b} = \begin{pmatrix} s \\ \boldsymbol{0} \end{pmatrix}. \tag{11}$$

Weight factors

In the literature the weight factor matrix $\boldsymbol{W}$ is usually chosen to be a diagonal one [1]. However, in the reference [2] it is demonstrated for a one-dimensional case that the following type constant weight matrix

$$\boldsymbol{W} = \begin{bmatrix} w_{11} & w_{12} \\ w_{12} & w_{22} \end{bmatrix} = \begin{bmatrix} 1 & \beta \\ \beta & 0 \end{bmatrix}. \tag{12}$$

resulted in much better solution for the temperature than the diagonal form. However, in this case the minimum property of the least-squares functional is lost, and in addition the resulting coefficient matrix $\boldsymbol{A}$ is indefinite. It should also be noted that this kind of indefinite weight might yield singular coefficient matrix $\boldsymbol{A}$.

In the matrix $\boldsymbol{W}$ the weight w_{11} is related to the the balance equation. Without loosing generality, it can be assumed that $w_{11} = 1$ and to obtain dimensionally homogeneous functional (3) the weight matrix can be written as

$$\boldsymbol{W} = \begin{bmatrix} 1 & \omega_{12}h^{-1} & \omega_{13}h^{-1} & \omega_{14}h^{-1} \\ & \omega_{22}h^{-2} & \omega_{23}h^{-2} & \omega_{24}h^{-2} \\ & & \omega_{33}h^{-2} & \omega_{34}h^{-2} \\ & \text{symm.} & & \omega_{44}h^{-2} \end{bmatrix}, \tag{13}$$

where h iis a characteristic length of an element. If the material model is isotropic and the element not much elongated, then it is plausible to assume the following form

$$\boldsymbol{W} = \begin{bmatrix} 1 & \omega_1 h^{-1} & \omega_1 h^{-1} & \omega_1 h^{-1} \\ & \omega_0 h^{-2} & \omega_2 h^{-2} & \omega_2 h^{-2} \\ & & \omega_0 h^{-2} & \omega_2 h^{-2} \\ & \text{symm.} & & \omega_0 h^{-2} \end{bmatrix}. \tag{14}$$

Numerical example

A two-dimensional heat conduction problem in a square domain $\Omega = \{(0, L) \times (0, L))$ with zero prescribed temperature on the whole bondary and a constant source s, is used as a test case. Uniform and distorted meshes are used, see Fig. 1. For the distorted meshes, the internal nodes (except the center node) are displaced by a distance of 30% of the element edge-length in a random direction. The relative error in maximum temperature at the center point P_{center}

$$\text{err}(u_h) = 100\frac{|u_h(P_{\text{center}}) - u(P_{\text{center}})|}{u(P_{\text{center}})} \tag{15}$$

is recorded in Table 1 as well as the number of iterations of the unpreconditioned conjugate gradient (CG) method to solve the resulting linear equation system. Only diagonal weights are used and $w_{ii} = 1$.

The Fourier-series solution for temperature can be expressed as

$$\theta(x, y) = \sum_{m=1,3,5,\ldots} \sum_{n=1,3,5,\ldots} a_{mn} \sin(m\pi x/L) \sin(n\pi y/L), \tag{16}$$

where

$$a_{mn} = \frac{16sL^2}{\pi^4 mn(m^2 + n^2)k}. \tag{17}$$

The effect of the weight ω_0 for the accuracy on the temperature is shown in Fig. 2 for both linear triangles and bilinear quadrilaterals. Notice, that reducing the value of the weight ω_0 puts more weight to the balance than to the constitutive equation. In Fig. 3 relative error in the flux vector is shown as a function of the weight ω_0. It is seen that the smallest error in the maximum flux is obtained when $\omega_0 \sim (h/L)$.

Since the value of the weight ω_0 affects the condition number of the global coefficient matrix, it has a direct influence to the speed of convergence of the iterative solution of the system. In Fig.4 the number of unpreconditioned conjugate gradient iterations for the uniform 10×10 mesh are shown as a function of the weight ω_0 for both linear triangles and bilinear quadrilaterals. For distorted meshes the behaviour is similar.

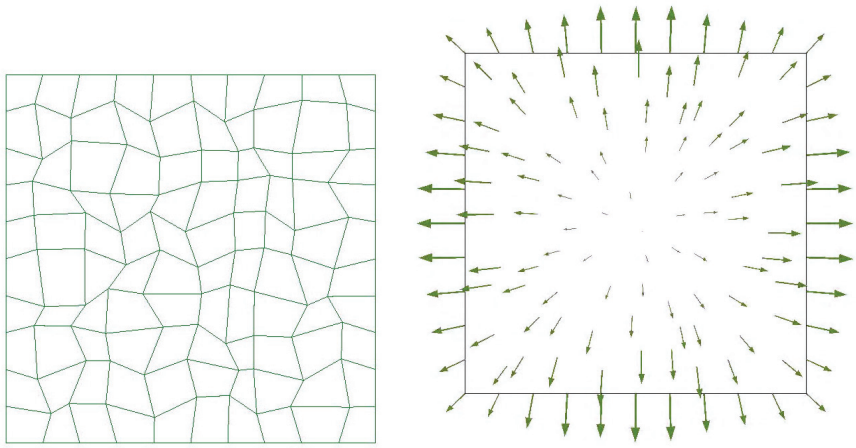

Figure 1. Distorted mesh and the flux vector.

Table 1. Error in maximum temperature and number of CG-iterations. Bilinear elements.

			uniform mesh		distorted mesh	
method	mesh	n	err(u_h)	iter	err(u_h)	iter
standard FEM	10x10	81	0.7986	9	0.8005	19
standard FEM	100x100	9801	0.0077	102	0.0450	149
LS-FEM	10x10	323	1.0562	46	0.9572	126
LS-FEM	30x30	2763	0.1227	221	0.0868	299
LS-FEM	100x100	30203	0.0112	631	0.0448	934

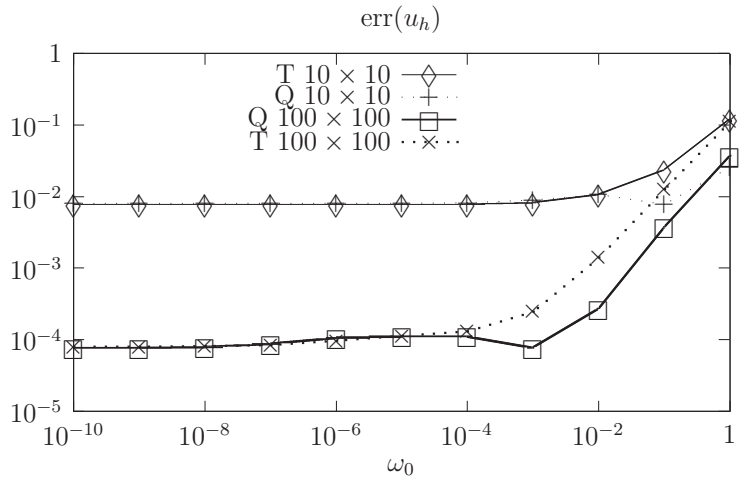

Figure 2. Error in maximum temperature w.r.t. the weight ω_0, uniform meshes.

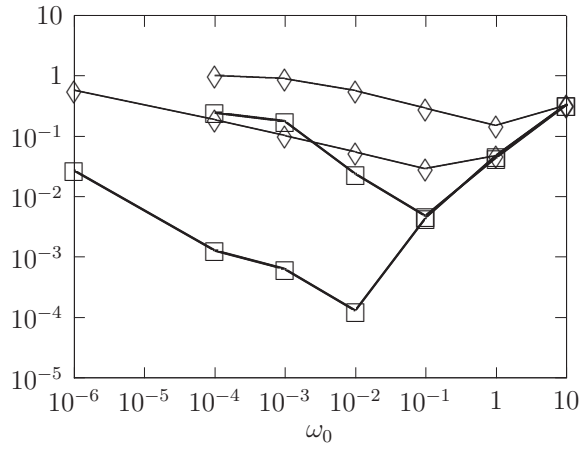

Figure 3. Error in the flux vector w.r.t. the weight ω_0, uniform meshes. Diamonds correspond to the maximun relative error and quads to the relative error in the maximum flux. Upper curves are from 10×10 mesh and the lower ones from 100×100 mesh.

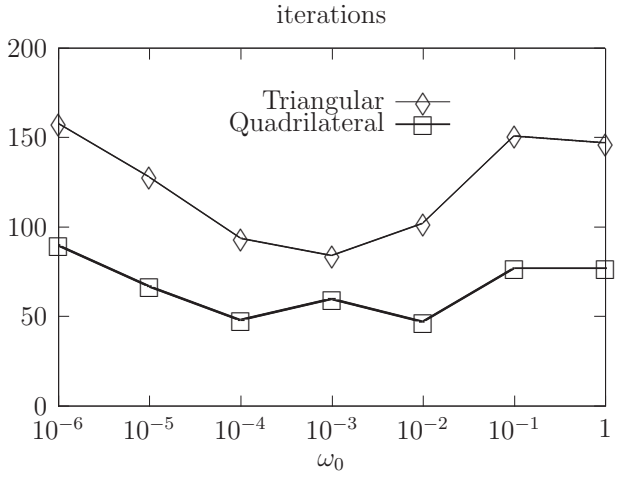

Figure 4. Number of unpreconditioned CG iterations w.r.t. the weight ω_0, uniform 10×10 mesh.

Error in the flux vector concentrates to the corners, see Fig. 5a. If the error is measured as the maximun error of the flux vector for all nodes, the convergence is slow, see the upper curves in Fig 5b. When the error is measured in the maximum flux the convergence is faster and it is seen to be near the optimal rate.

Concluding remarks

The least-squares finite element method is applied to the simple heat condction problem, where the least-squares functional contains both the balance and constitutive equations. Nodal C_0-interpolation is used for the components of the flux vector and temperature. Inevitably the problem size increases considerably in comparison to the standard FEM,

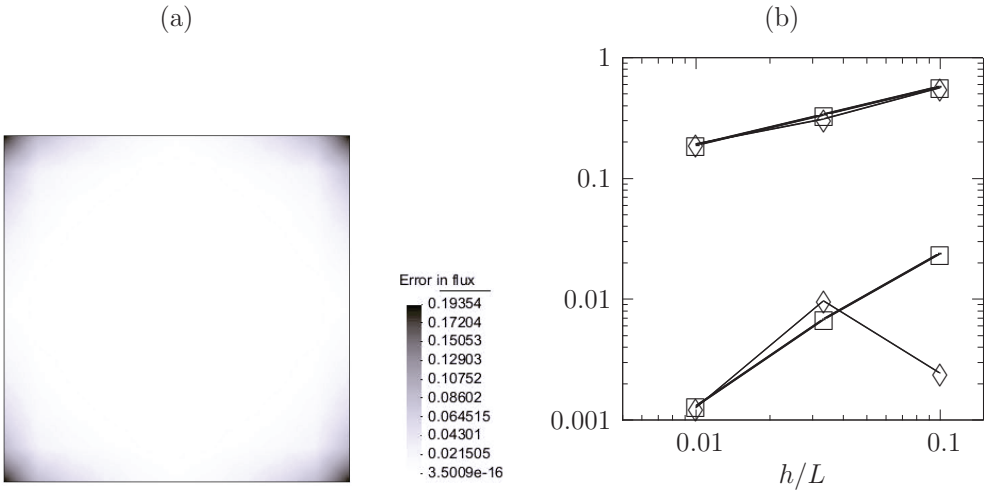

Figure 5. (a) error in flux vector, (b) convergence of the relative error in flux vector. The upper curves indicate the maximun relative error for all nodes and the lower ones to the error in the maximum flux. The squares correspond to the uniform quadrilateral meshes and the diamonds to the distorted meshes.

especially in three dimensional space. For this simple diffusion model there seems to be no benefits in using the least-squares formulation. However, the situation might be different for more complex problems.

References

[1] P.B. Bochev, M. D. Gunzburger, *Least-Squares Finite Element Method*, Applied Mathematical Sciences 166, Springer, 2009.

[2] E.-M. Salonen, J. Freund, On the weight factors in the least squares finite element method, *Rakenteiden Mekaniikka*, **33**,2000,1:3-16.

On the procedures for critical point computations in solid and structural mechanics

Alexis Fedoroff[1], Reijo Kouhia[2], Jari Mäkinen[2], and Miroslav Tůma[3]

[1]Department of Civil and Structural Engineering, Aalto University
P.O. Box 12100, FI-00076 Aalto, Finland
[2]Department of Mechanics and Design, Tampere University of Technology
P.O. Box 589, FI-33101 Tampere, Finland
[3] Institute of Computer Science, Academy of Sciences of the Czech Republic
Pod vodárenskou věží 2, 18207, Prague 8, Czech Republic

Summary. Determination of critical points along an equilibrium path of a structure is a non-linear eigenvalue problem. Several techniques exist to compute the critical equilibrium states and the corresponding modes. In this paper special emphasis is given to large scale stability computations.

Introduction

Determination of a critical point is the primary problem in structural stability analysis. Mathematically it means solution of an eigenvalue problem, which in general is non-linear, together with the equilibrium equations. However, if the pre-buckling displacements are negligible, it is usually sufficient to solve the linearized eigenvalue problem, where the linearization is performed with respect to the undeformed configuration.

The non-linear stability eigenvalue problem constitutes of solving the equilibrium equations simultaneously with the criticality condition. First appearance of this idea seems to be from 1973 by Keener and Keller [1]. In their approach the criticality condition is augmented as an eigenvalue equation, such approach has been used also in Refs. [2–5]. Another approach uses a scalar equation indicating the criticality [6, 7] or expansion to a higher order polynomial eigenvalue problem [8, 9].

In computational structural analysis, direct solution of the critical points along the equilibrium path requires complete kinematical description of the underlying kinematical model. In particular, for dimensionally reduced models, like beam- and shell models, the description has to be capable to handle large rotations. Development of a geometrically exact model with large rotations is not a trivial task [10–12].

Stability eigenvalue problem

The problem of finding a critical point along an equilibrium path can be stated as: find the critical values of $\boldsymbol{q}, \lambda$ and the corresponding eigenvector $\boldsymbol{\phi}$ such that

$$\left\{ \begin{array}{rcl} \boldsymbol{f}(\boldsymbol{q},\lambda) & = & \boldsymbol{0} \\ \boldsymbol{f}'(\boldsymbol{q},\lambda)\boldsymbol{\phi} & = & \boldsymbol{0} \end{array} \right. \tag{1}$$

where $\boldsymbol{f}$ is a vector defining the equilibrium equations and $\boldsymbol{f}'$ denotes the Gateaux derivative (Jacobian matrix) with respect to the state variables $\boldsymbol{q}$, i.e. the stiffness matrix. At the critical point the equilibrium equations $(1)_1$ has to be satisfied at the same time with the criticality condition $(1)_2$, which states the zero stiffness in the direction of the critical eigenmode $\boldsymbol{\phi}$. Such a system is considered in Refs. [3, 5, 13].

The equilibrium equation $(1)_1$ constitutes the balance of internal forces $\boldsymbol{r}$ and external loads $\boldsymbol{p}$, which is usually parametrized by a single variable λ, the load parameter, defining the intensity of the load vector:

$$\boldsymbol{f}(\boldsymbol{q}, \lambda) \equiv \boldsymbol{r}(\boldsymbol{q}) - \lambda \boldsymbol{p}_{\mathrm{r}}(\boldsymbol{q}). \tag{2}$$

If the loads do not dependend on deformations, like in dead-weight loading, the reference load vector $\boldsymbol{p}_{\mathrm{r}}$ is independent of the displacement field $\boldsymbol{q}$.

The system (1) consists of $2n+1$ unknowns, the displacement vector $\boldsymbol{q}$, the eigenmode $\boldsymbol{\phi}$ and the load parameter value λ at the critical state. Since the eigenvector $\boldsymbol{\phi}$ is defined uniquely up to a constant, the normalizing condition can be added to the system (1). In addition some stabilizing conditions might also be needed. In general, the full augmented system can be written as

$$\boldsymbol{g}(\boldsymbol{q}, \boldsymbol{\phi}, \boldsymbol{\lambda}) = \begin{cases} \hat{\boldsymbol{f}}(\boldsymbol{q}, \boldsymbol{\lambda}) \equiv \boldsymbol{f}(\boldsymbol{q}, \lambda) + \boldsymbol{f}_0(\boldsymbol{q}, \boldsymbol{\lambda}) = \boldsymbol{0} \\ \boldsymbol{h}(\boldsymbol{q}, \boldsymbol{\phi}, \boldsymbol{\lambda}) \equiv \boldsymbol{f}'(\boldsymbol{q}, \boldsymbol{\lambda})\boldsymbol{\phi} + \boldsymbol{h}_0(\boldsymbol{\phi}, \boldsymbol{\lambda}) = \boldsymbol{0} \\ \boldsymbol{c}(\boldsymbol{q}, \boldsymbol{\phi}, \boldsymbol{\lambda}) = \boldsymbol{0}, \end{cases} \tag{3}$$

where $\boldsymbol{\lambda}$ is a vector of control and auxiliary parameters and $\boldsymbol{c}$ is a vector of constraint or stabilizing equations, dimension of these vectors is $p \geq 1$. The additional functions $\boldsymbol{f}_0$ and $\boldsymbol{h}_0$ are chosen such that $\boldsymbol{f}_0 = \boldsymbol{h}_0 = \boldsymbol{0}$ at the solution point. The Newton step can be written as

$$\begin{bmatrix} \boldsymbol{K}_f & \boldsymbol{0} & \boldsymbol{P} \\ \boldsymbol{Z} & \boldsymbol{K}_h & \boldsymbol{N} \\ \boldsymbol{C}_q & \boldsymbol{C}_\phi & \boldsymbol{C}_\lambda \end{bmatrix} \begin{Bmatrix} \delta\boldsymbol{q} \\ \delta\boldsymbol{\phi} \\ \delta\boldsymbol{\lambda} \end{Bmatrix} = - \begin{Bmatrix} \hat{\boldsymbol{f}} \\ \boldsymbol{h} \\ \boldsymbol{c} \end{Bmatrix}, \tag{4}$$

where

$$\boldsymbol{Z} = [\boldsymbol{f}'\boldsymbol{\phi}]', \quad \boldsymbol{C}_q = \boldsymbol{c}' = \frac{\partial \boldsymbol{c}}{\partial \boldsymbol{q}}, \quad \boldsymbol{C}_\phi = \frac{\partial \boldsymbol{c}}{\partial \boldsymbol{\phi}}, \quad \boldsymbol{C}_\lambda = \frac{\partial \boldsymbol{c}}{\partial \boldsymbol{\lambda}}. \tag{5}$$

$$\boldsymbol{K}_f = \boldsymbol{K} + \boldsymbol{f}_0', \quad \boldsymbol{K}_h = \boldsymbol{K} + \frac{\partial \boldsymbol{h}_0}{\partial \boldsymbol{\phi}}, \quad \boldsymbol{P} = \frac{\partial \boldsymbol{f}}{\partial \boldsymbol{\lambda}} \quad \text{and} \quad \boldsymbol{N} = \frac{\partial \boldsymbol{h}}{\partial \boldsymbol{\lambda}} \tag{6}$$

Computation of the matrix $\boldsymbol{Z}$ requires second order derivatives of the residual. In the literature these are usually obtained by numerical differentiation. For the geometrically exact Reissner's beam model analytical derivation of the $\boldsymbol{Z}$-matrix is given in [14].

For the eigenvector normalization the following constraints can be used:

$$\|\boldsymbol{\phi}\|^2 - 1 = 0, \tag{7}$$

$$\lambda\|\boldsymbol{\phi}\|^2 - 1 = 0, \tag{8}$$

$$\boldsymbol{e}_i^{\mathrm{T}}\boldsymbol{\phi} - 1 = 0, \tag{9}$$

$$\lambda(\boldsymbol{e}_i^{\mathrm{T}}\boldsymbol{\phi})^2 - 1 = 0, \tag{10}$$

where $\boldsymbol{e}_i$ is a unit vector having the element 1 at i:th component. The constraint (9) is used by Wriggers and Simo [5]. Constraints (8) and (10) guarantee that the iteration

will converge to a solution with a positive critical value of the load parameter λ [14]. A proper scaling of the constraint equation is also important. For the constraint equation (8) the best numerical performance is obtained when the initial scaling of the eigenvector approximation is of order $\|\boldsymbol{\phi}\| \sim \lambda_{\mathrm{cr}}^{-1}$. Numerical experiments in refs. [14,15] indicate that the constraint (8) results in slightly more efficient scheme than (7).

Block elimination strategy

If the system (4) is solved by using a direct solver, the block elimination scheme is a feasible choice. Let us partition the iterative steps $\delta\boldsymbol{q}$ and $\delta\boldsymbol{\phi}$ as

$$\delta\boldsymbol{q} = \boldsymbol{q}_f + \boldsymbol{Q}_p\delta\boldsymbol{\lambda}, \quad \delta\boldsymbol{\phi} = \boldsymbol{\phi}_h + \boldsymbol{\Phi}_n\delta\boldsymbol{\lambda}, \tag{11}$$

where the vectors $\boldsymbol{q}_f, \boldsymbol{\phi}_h$ and the $n \times p$ matrices $\boldsymbol{Q}_p$, $\boldsymbol{\Phi}_n$ can be solved from equations

$$\boldsymbol{K}_f\boldsymbol{q}_f = -\hat{\boldsymbol{f}}, \qquad \boldsymbol{K}_f\boldsymbol{Q}_p = -\boldsymbol{P}, \tag{12}$$

$$\boldsymbol{K}_h\boldsymbol{\phi}_h = -\boldsymbol{h} - \boldsymbol{Z}\boldsymbol{q}_{\mathrm{f}}, \qquad \boldsymbol{K}_h\boldsymbol{\Phi}_n = -\boldsymbol{N} - \boldsymbol{Z}\boldsymbol{Q}_p. \tag{13}$$

The iterative change of the control parameters can be solved from the constraint conditions resulting in

$$\delta\boldsymbol{\lambda} = -(\boldsymbol{C}_\lambda + \boldsymbol{C}_q\boldsymbol{Q}_p + \boldsymbol{C}_\phi\boldsymbol{\Phi}_n)^{-1}(\boldsymbol{c} + \boldsymbol{C}_q\boldsymbol{q}_f + \boldsymbol{C}_\phi\boldsymbol{\phi}_h). \tag{14}$$

The specific choice by Wriggers and Simo [5] yields $\boldsymbol{K}_h = \boldsymbol{K}_f$, which is computationally very attractive. Solution of the augmented system (4) by the block elimination method requires factorization of one matrix of order n, reductions and backsubstitutions of $2(1+p)$ r.h.s.-vectors. An alternative procedure suitable for the use of preconditioned iterative linear solvers is presented in [15].

Iterative solution of the linearized extended system

When an iterative linear solver is used to solve the extended system (4), the block elimination scheme is not the best choice. In the sequel, the extended system is denoted as $\boldsymbol{A}\boldsymbol{x} = -\boldsymbol{g}$. One of the most used iterative schemes to solve non-symmetric linear systems is the preconditioned bi-conjugate gradient stabilized algorithm. In this work, the Bi-CGSTAB algorithm is implemented in its original form [16].

Preconditioned Bi-CGSTAB algorithm:

1. construct $\boldsymbol{M}$ (or directly $\boldsymbol{M}^{-1}$),
2. initialize $\boldsymbol{r}_0 = -\boldsymbol{g} - \boldsymbol{A}\boldsymbol{x}_0$, choose $\tilde{\boldsymbol{r}}$, compute $\rho_0 = \tilde{\boldsymbol{r}}^T\boldsymbol{r}_0$, set $\boldsymbol{d}_0 = \boldsymbol{r}_0$
3. iterate $i = 0, 1, 2, \ldots$ until convergence:
   (a) apply preconditioner: $\boldsymbol{z} = \boldsymbol{M}^{-1}\boldsymbol{d}_i$,
   (b) compute: $\boldsymbol{v}_i = \boldsymbol{A}\boldsymbol{z}$, $\alpha_i = \rho_i/\tilde{\boldsymbol{r}}^T\boldsymbol{v}_i$, $\boldsymbol{s} = \boldsymbol{r}_i - \alpha_i\boldsymbol{v}_i$,
   (c) apply preconditioner: $\tilde{\boldsymbol{s}} = \boldsymbol{M}^{-1}\boldsymbol{s}$,
   (d) compute: $\boldsymbol{w} = \boldsymbol{A}\tilde{\boldsymbol{s}}$, $\omega_i = \boldsymbol{w}^T\boldsymbol{s}/\boldsymbol{w}^T\boldsymbol{w}$,
   (e) update: $\boldsymbol{x}_{i+1} = \boldsymbol{x}_i + \alpha_i\boldsymbol{z} + \omega_i\tilde{\boldsymbol{s}}$, $\boldsymbol{r}_{i+1} = \boldsymbol{s} - \omega_i\boldsymbol{w}$,
   (f) compute $\rho_{i+1} = \tilde{\boldsymbol{r}}^T\boldsymbol{r}_{i+1}$ and $\beta_{i+1} = (\rho_{i+1}/\rho_i)(\alpha_i/\omega_i)$,
   (g) update $\boldsymbol{d}_{i+1} = \boldsymbol{r}_{i+1} + \beta_{i+1}(\boldsymbol{d}_i - \omega_i\boldsymbol{v}_i)$.

There are three possibilities for breakdown in the Bi-CGSTAB method, i.e. when $\tilde{\boldsymbol{r}}^T\boldsymbol{v}_i \approx 0$, $\boldsymbol{w}^T\boldsymbol{s} \approx 0$ or when $\tilde{\boldsymbol{r}}^T\boldsymbol{r}_i \approx 0$. A good preconditioner does not exclude the risk for breakdown of the Bi-CGSTAB iterations. However, this preconditioned iterative method is considered to be reasonably robust in many applications. Slightly more robust modifications have been presented, e.g. in [17].

In the Bi-CGSTAB algorithm the vector $\tilde{\boldsymbol{r}}$ has to be chosen. A common choice is the initial residual $\boldsymbol{r}_0$.

An efficent preconditioner to the extended system should maximally utilize the block structure of the system matrix $\boldsymbol{A}$. For the present system, a simple and natural choice is proposed in Ref. [15]:

$$\boldsymbol{M} = \begin{bmatrix} \boldsymbol{M}_f & \boldsymbol{0} & \boldsymbol{0} \\ \boldsymbol{Z} & \boldsymbol{M}_h & \boldsymbol{0} \\ \boldsymbol{C}_q & \boldsymbol{C}_\phi & \boldsymbol{D} \end{bmatrix}, \tag{15}$$

where $\boldsymbol{M}_f \approx \boldsymbol{K}_f, \boldsymbol{M}_h \approx \boldsymbol{K}_h$ and the (3,3)-diagonal block $\boldsymbol{D}$ is either $\boldsymbol{C}_\lambda$ if it is non-singular, or otherwise an identity matrix. The inverse of the preconditioner ($\boldsymbol{M}$) is then given by

$$\boldsymbol{M}^{-1} = \begin{bmatrix} \boldsymbol{M}_f^{-1} & \boldsymbol{0} & \boldsymbol{0} \\ -\boldsymbol{M}_h^{-1}\boldsymbol{Z}\boldsymbol{M}_f^{-1} & \boldsymbol{M}_h^{-1} & \boldsymbol{0} \\ -\boldsymbol{D}^{-1}(\boldsymbol{C}_q\boldsymbol{M}_f^{-1} - \boldsymbol{C}_\phi\boldsymbol{M}_h^{-1}\boldsymbol{Z}\boldsymbol{M}_f^{-1}) & -\boldsymbol{D}^{-1}\boldsymbol{C}_\phi\boldsymbol{M}_h^{-1} & \boldsymbol{D}^{-1} \end{bmatrix}. \tag{16}$$

Due to the block structure, the preconditioning operation $\boldsymbol{y} = \boldsymbol{M}^{-1}\boldsymbol{s}$ takes the following form

$$\begin{Bmatrix} \boldsymbol{y}_1 \\ \boldsymbol{y}_2 \\ \boldsymbol{y}_3 \end{Bmatrix} = \begin{Bmatrix} \boldsymbol{M}_f^{-1}\boldsymbol{s}_1 \\ \boldsymbol{M}_h^{-1}(\boldsymbol{s}_2 - \boldsymbol{Z}\boldsymbol{M}_f^{-1}\boldsymbol{s}_1) \\ \boldsymbol{D}^{-1}\left[\boldsymbol{s}_3 - \boldsymbol{C}_\phi\boldsymbol{M}_h^{-1}(\boldsymbol{s}_2 - \boldsymbol{Z}\boldsymbol{M}_f^{-1}\boldsymbol{s}_1) - \boldsymbol{C}_q\boldsymbol{M}_f^{-1}\boldsymbol{s}_1\right] \end{Bmatrix} = \begin{Bmatrix} \boldsymbol{M}_f^{-1}\boldsymbol{s}_1 \\ \boldsymbol{M}_h^{-1}(\boldsymbol{s}_2 - \boldsymbol{Z}\boldsymbol{y}_1) \\ \boldsymbol{D}^{-1}(\boldsymbol{s}_3 - \boldsymbol{C}_\phi\boldsymbol{y}_2 - \boldsymbol{C}_q\boldsymbol{y}_1) \end{Bmatrix}. \tag{17}$$

In the computations the choice $\boldsymbol{M}_f = \boldsymbol{M}_h = \boldsymbol{M}_1$ is used, since $\boldsymbol{K}_f$ and $\boldsymbol{K}_h$ are low rank modifications of the stiffness matrix $\boldsymbol{K}$. Thus only the storage for $\boldsymbol{M}_1$ is needed. Application of the preconditioner $\boldsymbol{M}$ is now equivalent of two preconditioning operations with $\boldsymbol{M}_1$ and a solution of a small system with the coefficient matrix $\boldsymbol{D}$.

Some computational issues

Structures where stability issues are relevant, are usually slender beam and shell like structures. Therefore the condition number of the Jacobian matrix $\boldsymbol{K}$ is usually large and the iterative solution can be difficult and a powerfull preconditioner is needed. In Ref. [15] the second-order preconditioner by Kaporin [18] (denoted as RIC2S) have been tested. Numerical computations performed in [15] were performed on the HP ProLiant DL785 G5 server with quad-core AMD Opteron 8360 SE (Barcelona) 2.5 GHz processor, containing 512 GB memory, at the CSC-IT Center for Science at Espoo, Finland. The FE-code is written in Fortran 90/77 and compiled with the Portland Group Fortran compiler using the `-fastsse` optimization option.

Lagrangian 27-node triquadratic solid element was used to model s cylindtrical shell with thickness to radius ratio 1/400. Uniform 32×32, 64×64 and 128×128 meshes for

a quadrant of the panel were used, resulting in 37053, 147837 and 590589 equilibrium equations. Thus, for the finest mesh the extended system (4) consist of nearly 1.2 million unknowns. To be able to compute this large problem, the FE-code has to be compiled with the `-Mlarge_arrays` option. The condition numbers of the stiffness matrix $\boldsymbol{K}$ were in the range $10^6 \cdots 10^8$.

Highly efficient skyline factorization scheme [19] in which machine optimized level 3 BLAS routines is used with the block elimination stratey. The block size has been 95×192 (diagonal block thus 95×95) which fits well in the level 2 cache memory of the server. The iterative scheme will be faster only for the finest mesh, giving roughly one order reduction in solution times. However, the storage requirements with the iterative procedure are only a fraction as compared to the direct linear solvers.

It should also be noted that the memory requirements for solution of the extended set of equations (4) is of same order than is required to solve a linear generalized eigenvalue problem.

Since the Newton's scheme is only locally convergent, the non-linear iteration might not converge to the solution if the undeformed initial state is used as a starting point. Therefore, to increase the robustness of the direct critical point search algorithm, an automatic procedure to find a better starting state is under development.

References

[1] Keener, J. & Keller, H. Perturbed bifurcation theory. *Archive for Rational Mechanics and Analysis* **50**, 159–175 (1973).

[2] Keener, J. Perturbed bifurcation theory at multiple eigenvalues. *Archive for Rational Mechanics and Analysis* **56**, 348–366 (1974).

[3] Seydel, R. Numerical computation of branch points in nonlinear equations. *Numerische Mathematik* **33**, 339–352 (1979).

[4] Wriggers, P., Wagner, W. & Miehe, C. A quadratically convergent procedure for the calculation of stability points in finite element analysis. *Computer Methods in Applied Mechanics and Engineering* **70**, 329–347 (1988).

[5] Wriggers, P. & Simo, J. A general procedure for the direct computation of turning and bifurcation problems. *International Journal for Numerical Methods in Engineering* **30**, 155–176 (1990).

[6] Abbot, J. An efficient algorithm for the determination of certain bifurcation points. *Journal Computational and Applied Mathematics* **4**, 19–27 (1987).

[7] Battini, J.-M., Pacoste, C. & Eriksson, A. Improved minimal augmentation procedure for the direct computation of critical points. *Computer Methods in Applied Mechanics and Engineering* **192**, 2169–2185 (2003).

[8] Huitfeldt, J. & Ruhe, A. A new algorithm for numerical path following applied to an example from hydrodynamic flow. *SIAM Journal on Scientific and Statistical Computing* **11**, 1181–1192 (1990).

[9] Huitfeldt, J. Nonlinear eigenvalue problems - prediction of bifurcation points and branch switching. Tech. Rep. 17, Department of Computer Sciences, Chalmers University of technology (1991).

[10] Cardona, A. & Huespe, A. Evaluation of simple bifurcation points and post-critical path in large finite rotation problems. *Computer Methods in Applied Mechanics and Engineering* **175**, 137–156 (1999).

[11] Ibrahimbegović, A. & Mikdad, M. A. Quadratically convergent direct calculation of critical points for 3d structures undergoing finite rotations. *Computer Methods in Applied Mechanics and Engineering* **189**, 107–120 (2000).

[12] Mäkinen, J. Total Lagrangian Reissner's geometrically exact beam element without singularities. *International Journal for Numerical Methods in Engineering* **70**, 1009–1048 (2007).

[13] Werner, B. & Spence, A. The computation of symmetry-breaking bifurcation points. *SIAM Journal on Numerical Analysis* **21**, 388–399 (1984).

[14] Mäkinen, J., Kouhia, R., Fedoroff, A. & Marjamäki, H. Direct computation of critical equilibrium states for spatial beams and frames. *International Journal for Numerical Methods in Engineering* **89**, 135–153 (2012).

[15] Kouhia, R., Tůma, M., Mäkinen, J., Fedoroff, A. & Marjamäki, H. Implementation of a direct procedure for critical point computations using preconditioned iterative solvers. *Computers and Structures* **108–109**, 110–117 (2012).

[16] Vorst, H. Bi-CGSTAB: a fast and smoothly convergent variant of Bi-CG for the solution of nonsymmetric linear systems. *SIAM Journal on Scientific and Statistical Computing* **13**, 631–644 (1992).

[17] Sleijpen, G. & Fokkema, D. Bi-cgstab(ℓ) for linear equations involving unsymmetric matrices with complex spectrum. *ETNA* **1**, 11–32 (1993).

[18] Kaporin, I. High quality preconditioning of a general symmetric positive definite matrix based on its $U^TU + U^TR + R^TU$-decomposition. *Numerical Linear Algebra with Applications* **5**, 483–509 (1998).

[19] Marques, O. A partitioned skyline LDL^T factorization. Tech. Rep. TR/PA/93/53, CERFACS (1993).

Comparison of deterministic multibody simulation and random analysis in a linearized model of a vibratory feeder

Emil Kurvinen, Oleg Dmitrochenko, Marko Matikainen, and Aki Mikkola

Summary. This paper compares multibody system and random vibration analyses. Multibody system analysis is a frequently used method for performing dynamic simulations. With multibody system analysis, dynamic performance can be described using the equations of motion in the time domain. Random vibration analysis, in turn, involves analysis in the frequency domain. Multibody simulation in the time domain gives an accurate solution for a load that is given explicitly. In practice, this may not be feasible, as it is difficult to consider all possible loads simultaneously. Alternatively, by extracting parameters from the stationary stochastic input process, one can obtain results in terms of stochastic values, for example, the mean-square acceleration of the feeder unit. In this study, a vibratory feeder that moves ground material is under investigation. The vibration of the feeder unit is produced by spinning an unbalanced mass. This vibration results in movement of the material. Assuming relatively small planar displacements results in a simplified two-dimensional linear multibody model of the vibratory feeder. Once the consistency of its deterministic linear system is validated in the time domain, a linear stochastic model is prepared. Input load parameters given in the form of time histories are converted to a stochastic format, such as spectral density of the load, and the linear equations of motion are transformed into system frequency response. Finally, output is presented in the form of spectral functions of the observed data; statistical parameters of output oscillations are computed and compared with dynamical analysis.

Keywords: frequency domain, multibody system, random vibration, time domain

Introduction

In this research, vibratory feeder behaviour is investigated using two different analytical approaches. The two methods are multibody system analysis and random vibration analysis. Typically, multibody system analysis is used to model the dynamic behaviour of bodies that have large translational or rotational displacements. Kinematic constraints define the appropriate body motions for the simulation, and dynamic performance is described using the equations of motion in the time domain. Analysis with respect to the time domain makes it possible to determine system responses such as mass displacement at any arbitrary time [1, 2]. Random vibration analysis involves calculations made in the frequency domain. It is particularly useful for determining forces. The approach introduced by Popp and Schiehlen is applied here [3]. The overall dynamic behaviour of a system can be solved using either of these two methods. A two-dimensional model of the feeder unit is studied as a test case in this research. The input excitation in the form of rotation of an unbalanced mass was used based on measurements taken from an industrial machine. This test case was analyzed using the multibody system and random vibration analysis methods, and the results from each method were compared. Random vibration describes a system that shakes, trembles, or moves backward and forward in

some unpredictable way. The main concern in random vibration is determining the average characteristics of the randomly excited motion and how the motion relates to the excitation and the dynamic properties (mass, stiffness, and damping) [4]. Historically, random vibration analysis has been applied most often and with success in the aerospace industry (see *e.g.*, [5]). However, the method has been found to be equally suitable for a variety of other engineering applications, *e.g.*, to analyze offshore structures [6], in civil engineering analyses [7], to analyze wind excitation [8], and for analyses of land vehicle and train systems [9].

Background of a linear random vibration analysis

A random process includes one or more random values that vary with time $x(t)$. Road irregularity or sporadic forces applied to a mechanical system are examples of random processes. Random processes are typically represented as an ensemble (a set) of sample functions such as $x_1(t), x_2(t)$, etc., as shown on the left side of figure 1. In general, none of the separate sample functions represent complete information about process $x(t)$. That is why random processes are formulated using the specific stochastic parameters that are briefly outlined in this section. The mean value of process $x(t)$, or the expectation $E[x](t)$

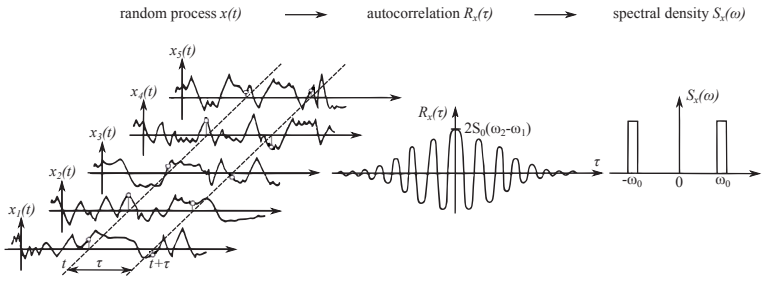

Figure 1. Random process and its main charasterics [4]

is defined as an average computed for all sample functions at any given time moment as follows:

$$E[x](t) = \lim_{n\to\infty} \left[x_1(t) + x_2(t) + x_3(t) + \cdots + x_n(t)\right]/n. \tag{1}$$

If, for the process shown in figure 1, stochastic parameters like $E[x](t)$ and others below are independent of time, process $x(t)$ is called stationary, and $E[x](t) = E[x]$. If averaging across the ensemble (along the dotted line in figure 1) can be substituted by averaging over time t, then the process is called ergodic. For such a process, each of its sample functions, $x_1(t), x_2(t)$, etc. contains full stochastic information about the whole random process. For example expectation (1) can be computed using a single sample function as

$$E[x] = \lim_{n\to\infty} \left[x(0) + x(T/n) + x(2T/n) + \cdots + x(T)\right]/(n+1) = 1/T \int_0^T x(t)\mathrm{d}t. \tag{2}$$

A standard concept that was used here, ' ... for engineering calculations the world is often assumed to be linear, stationary, ergodic, and Gaussian.", was cited by Newland [4], p. 80. The variance $V[x]$ of process $x(t)$ around its mean value $E[x]$ is defined by the value $V[x] = E[x^2] - (E[x])^2$. Value $\sigma_x = \sqrt{V[x]}$ is called the standard deviation. It

represents the amplitude of a constant energy equivalent signal. For the deterministic process $x = A\sin(\omega t)$, the variance $V[x] = A^2/2$ and $\sigma_x = A/\sqrt{2}$. The autocorrelation function of a stationary process is defined as the mean square of the process and itself shifted by time τ, as follows:

$$R_x(\tau) = E\left[x(t)x(t+\tau)\right] \tag{3}$$

Informally, the autocorrelation function keeps information about frequencies in the random process $x(t)$ and shows how fast the 'memory' of its preceding values is lost for relative time τ. See the middle portion of figure 1. Random vibration analysis, like any other type of linear analysis, deals mostly with frequency information, which is analyzed using a Fourier transform as

$$S_x(\omega) = \mathrm{Re}\ FFT[R_x(\tau)] = \mathrm{Re}\ \frac{1}{2\pi}\int_{-\infty}^{\infty} R_x(\tau)e^{-i\omega\tau}\mathrm{d}\tau\ , \tag{4}$$

where the resulting function $S_x(\omega)$ is called the spectral density of random signal $x(t)$, see the right side of figure 1. The spectral density, then, serves as input data for the linear analysis, which results in the corresponding spectral density of the output signal $S_y(\omega)$ as discussed in the next chapter.

Transmission of random input to output for a linear dynamic system

A linear dynamic system is represented by the equation of motion as follows:

$$\mathbf{M}\ddot{\mathbf{y}}(t) + \mathbf{D}\dot{\mathbf{y}}(t) + \mathbf{K}\mathbf{y}(t) = \mathbf{b}x(t) \tag{5}$$

with standard notations for mass matrix $\mathbf{M}$, damping matrix $\mathbf{D}$, and stiffness matrix $\mathbf{K}$. Vector $\mathbf{y}(t)$ is the coordinate vector of the system. The load is represented by a random process $x(t) = x_0 e^{i\omega t}$ with x_0 being a random amplitude; $\mathbf{b}$ is the nodal load vector. The random output is sought in the form $\mathbf{y} = \mathbf{y}_0 e^{i\omega t}$, where $\mathbf{y}_0$ is a vector of random complex amplitudes of the displacement. The relationship between input and output is given in the following form:

$$\mathbf{y}_0 = \mathbf{H}_{\mathbf{y/x}}\mathbf{b}x_0, \qquad \mathbf{H}_{\mathbf{y/x}}(i\omega) = \left[\mathbf{K} - \omega^2\mathbf{M} + i\omega\mathbf{D}\right]^{-1}\ , \tag{6}$$

where $\mathbf{H}_{\mathbf{y/x}}$ is the frequency response matrix. The frequency response connects the spectral densities of input $S_x(\omega)$ and output $\mathbf{S}_\mathbf{y}(\omega)$ in the following way (by [3]):

$$\mathbf{S}_\mathbf{y}(\omega) = \mathbf{H}_{\mathbf{y/x}}(i\omega)\mathbf{b}S_x(\omega)\mathbf{b}^T\mathbf{H}^T_{\mathbf{y/x}}(-i\omega). \tag{7}$$

Finally, the desired output parameters; such as the standard deviations σ of displacements, velocities, and so on; can be computed as

$$\begin{aligned}
&\mathbf{V}_\mathbf{y}\int_0^\infty \mathbf{S}_\mathbf{y}(\omega)d\omega\ ,\quad \sigma_\mathbf{y} = \sqrt{\mathbf{V}_\mathbf{y}}\\
&\mathbf{V}_{\dot{\mathbf{y}}}\int_0^\infty \mathbf{S}_{\dot{\mathbf{y}}}(\omega)d\omega\ ,\quad \sigma_{\dot{\mathbf{y}}} = \sqrt{\mathbf{V}_{\dot{\mathbf{y}}}}\ ,\quad \text{where } \mathbf{S}_{\dot{\mathbf{y}}}(\omega) = \omega^2\mathbf{S}_\mathbf{y}(\omega).
\end{aligned} \tag{8}$$

Comparing Multibody Simulation and Random Vibration Analyses

In this section, the vibratory feeder and simplified two-dimensional model is shown in figure 2. In the model, the feeder body has two degrees of freedom: vertical displacement y and rotation angle θ. Both displacements are assumed to be small. The structure is supported by elastic-dissipative springs in both the rear and front ends of the machine. Parameters l_1 and l_2 represent horizontal translation of the springs relative to the machine centre of gravity.

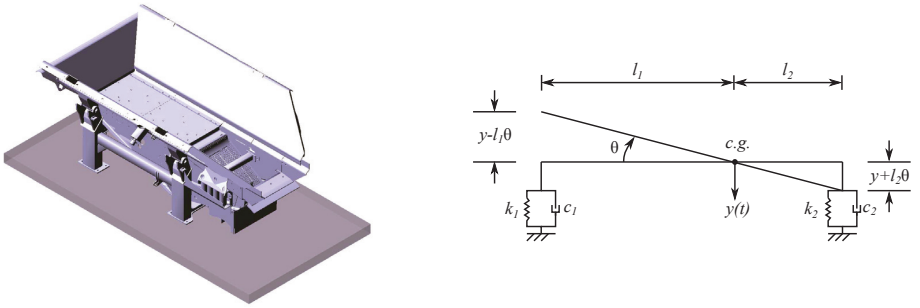

Figure 2. Studied vibratory feeder: vibratory feeder on left, simplified two-dimensional model on right

The equations of motion were defined using Eq. (5), where the vector $\mathbf{y}$ and its time derivative $\dot{\mathbf{y}}$ were introduced as follows:

$$\mathbf{y} = \{y \;\; \theta\}^T \;,\; \dot{\mathbf{y}} = \{\dot{y} \;\; \dot{\theta}\}^T \tag{9}$$

with the following structural matrices used in the equations:

$$\boldsymbol{M} = \begin{bmatrix} m & 0 \\ 0 & I \end{bmatrix}, \boldsymbol{K} = \begin{bmatrix} k_1 + k_2 & k_2 l_2 - k_1 l_1 \\ k_2 l_2 - k_1 l_1 & k_1 l_1^2 + k_2 l_2^2 \end{bmatrix}, \text{and } \boldsymbol{D} = \begin{bmatrix} c_1 + c_2 & c_2 l_2 - c_1 l_1 \\ c_2 l_2 - c_1 l_1 & c_1 l_1^2 + c_2 l_2^2 \end{bmatrix}$$

In the latter formulas for system matrices, the following parameters of the system were used: mass m, inertia moment I of the feeder unit body, spring stiffnesses k_1 and k_2, as well as damping parameters c_1 and c_2 of the springs. The load influence was represented by rotation of a heavy unbalanced mass, which introduced harmonic excitation to the system. Measurements taken from an industrial machine provided the needed angular velocity input data. The measured angular velocity as a function of time is shown in figure 3. This data was transformed to an equivalent input force as shown in figure 4.

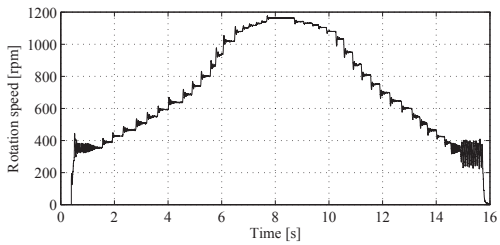

Figure 3. Recorced angular velocity in rpm

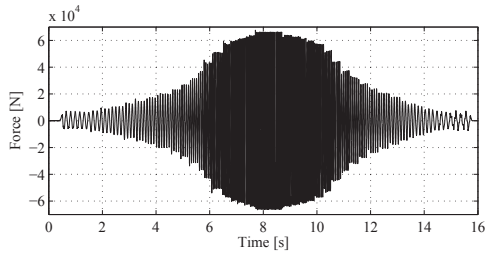

Figure 4. Input force to the recorded angular velocity

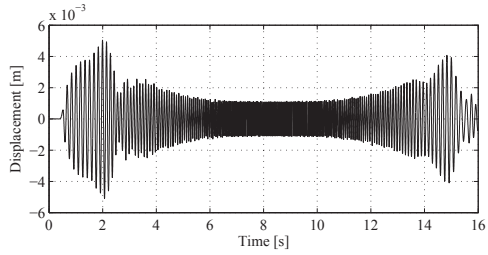

Figure 5. Vertical displacement of vibratory feeder

The results of the multibody simulation solved by ode45 in MATLAB by using equation 5 are presented in figure 5, which plots the vertical displacement of the feeder unit. The results was verified with three-dimensional model in Adams. For the random vibration analysis, the important input signal feature, the autocorrelation function, was computed. See figure 6. The autocorrelation function was used in formulas (4) and (7) to compute the parameters of the output signal. To evaluate the adequateness of the

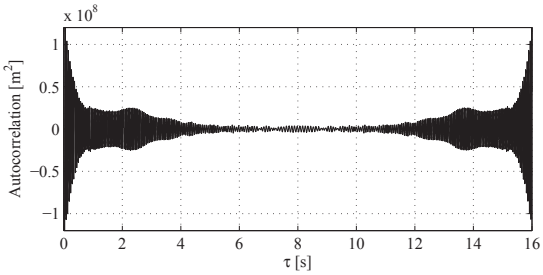

Figure 6. Autocorrelation function of the input force applied to the vibratory feeder

random model, the statistical parameters of the vertical displacement of center of gravity of the feeder unit obtained by using the two analysis methods (time-domain dynamical simulation and frequency-domain random analysis) were compared. The comparison is summarized in table 1. Relative error in this comparison based on measured data is mod-

Table 1. Comparison of output parameters obtained by the two methods

Simulation method	Variance V_y	Standard deviation σ_y
Deterministic	$2.269825 \cdot 10^{-6}$	0.0021306
Random	$1.947134 \cdot 10^{-6}$	0.0019734
Error [%]	16.57	7.97

erate. This can be explained with non-stationary behaviour of the real machine which can be seen from figure 5.

Discussion

If the corresponding stochastic parameters are given as inputs, random vibration analysis provides a straightforward method to obtain the stochastic parameters of the output signal of a linear system. In the preceding discussion, displacements and velocities were offered as examples of typical output parameters. For practical problems, other parameters; such as average reaction forces, amplitude peaks, or frequency of peak values per given time period T; can be useful for estimating overall machine behaviour. See the graphical explanation offered by figure 7. At later stages of research, this data (especially the

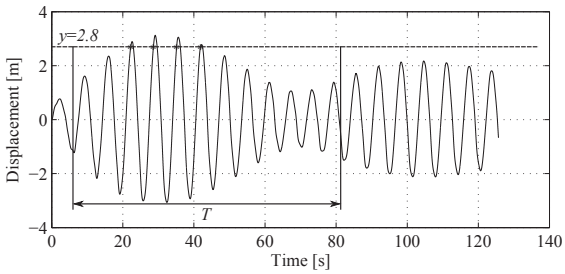

Figure 7. To evaluation of the frequency of peaks

frequency of peaks) might serve as input for fatigue analysis; needed to estimate the life time of the machine, for example.

Conclusions

This study evaluates the applicability of two different analytical approaches, random vibration analysis and multibody simulation, to analyzing vibratory feeder performance. The two methods give statistically equivalent results. For the multibody analysis, simulation time should be longer to accurately calculate dispersion and standard deviation, because of settling time. For random vibration analysis, reduced formulations, such as covariant analysis, are available [3], which can compute the average parameters of the output signal using simple algebraic operations. Further studies must be carried out to extend the application of the random vibration approach to produce useful data for designers. In future research, nonlinear random analysis will be cased analyses of the strains and stresses due to stone dropping to the vibratory feeder.

References

[1] A. Shabana. *Dynamics of multibody systems.* Cambridge University Press, 1998.

[2] A. Shabana. *Computational dynamics.* Wiley-Interscience, 2001.

[3] K. Popp and W. Schiehlen. *Ground vehicle dynamics.* Springer Verlag, 2010.

[4] D. Newland. *An introduction to random vibrations and spectral analysis.* Longman Group Limited, 1975.

[5] H. Press and J. Houbolt. Some applications of generalized harmonic analysis to gust loads on airplanes. *Journal of the Aeronautical Sciences*, 22:17–26, 1955.

[6] M. St Denis and W. Pierson. On the motion of ships in confused seas. *Trans. SNAME*, 61:280–357, 1953.

[7] D. Gasparini and E. Vanmarcke. *Simulated earthquake motions compatible with prescribed response spectra*. Massachusetts Institute of Tehnology, Department of Civil Engineering, Constructed Facilities Division, 1976.

[8] A. Davenport and M. Novak. *Vibration of Structures Induced by Wind*. McGraw-Hill, New York, 2nd edition, 1976.

[9] W. Schiehlen. *Random vehicle vibrations*. Elsevier, Amsterdam, The Netherlands, 1986.

Emil Kurvinen, Oleg Dmitrochenko, Marko Matikainen, Aki Mikkola
Lappeenranta University of Technology
Laboratory of Machine Design
PL 20, 53851 Lappeenranta
emil.kurvinen@lut.fi, oleg.dmitrochenko@lut.fi,
marko.matikainen@lut.fi, aki.mikkola@lut.fi

Stability of moving viscoelastic panels interacting with surrounding fluid

Tytti Saksa, Juha Jeronen and Tero Tuovinen

Department of Mathematical Information Technology
P.O. Box 35 (Agora), FI-40014 University of Jyväskylä

Summary. We study a model describing the out-of-plane vibrations of an axially moving viscoelastic panel submerged in flowing fluid. The panel is assumed to travel at a constant velocity between two fixed supports, and it is modeled as a flat panel made of viscoelastic Kelvin-Voigt material. The fluid flow is modeled with the help of the added mass coefficients. The resulting dynamic equation is a partial differential equation of fifth order in space. Five boundary conditions are set for the studied problem. The behavior of the panel is analyzed with the help of its eigenvalues (eigenfrequencies). These characteristics are studied with respect to the velocity of the panel. In our study, we have included the material (total) derivative in the viscoelastic relations. We study the effects of the surrounding flowing fluid on the behavior of the moving viscoelastic panel. It was found that, in presence of flowing fluid, the critical panel velocity was significantly lower than in the vacuum case. Secondly, for high enough values of viscosity, the panel did not experience instability detected at low values of viscosity in the form of divergence. The flowing fluid was found to diminish the stabilizing effects brought about by material viscosity.

Key words: moving panel, viscoelasticity, eigenvalues, FSI, axial flow, stability, paper industry

Esitys on julkaistu *Rakenteiden mekaniikka lehdessä*: Vol. 45, 2012, Nro 3.

Syklonierottimen kaasuvirtauskentän ajan suhteen tarkka laskenta

Aku Karvinen ja Hannu Ahlstedt

Tiivistelmä. Tässä työssä on laskettu kirjallisuudessa usein vertailutapauksena käytetyn syklonierottimen (Stairmand high-efficiency cyclone) kaasuvirtauskenttä ajan suhteen tarkasti käyttäen avoimen lähdekoodin ohjelmistoa OpenFOAM ja käyttäen turbulenssin mallinnukseen niin sanottua Reynoldsin jännitysmallia. Laskenta on tehty usealla eri tiheyksisellä laskentaverkolla ja usealla eri aika-askeleella diskretoinnin aiheuttamien virheiden selvittämiseksi.

Tuloksista laskettujen aikakeskiarvokenttien vertailu kirjallisuudesta löytyviin mittaustuloksiin osoittaa, että käytetty laskentamenetelmä antaa hyviä tuloksia, mikäli laskentaverkko on riittävän tiheä ja aika-askel lyhyt. Tällöin myös lasketun virtauskentän aikariippuva käyttäytyminen on lähellä mittaustuloksia. Tuloksien vertailu usein virtauslaskennassa käytetyn k-ε-mallin tuloksiin osoittaa kaksiyhtälömallin käyttökelvottomuuden tähän virtaustilanteeseen.

Avainsanat: syklonierotin, URANS, Reynoldsin jännitysmalli, OpenFOAM

Johdanto

Syklonierottimella poistetaan yleensä kiinteitä partikkeleita neste- tai kaasuvirtauksesta. Syklonierottimen partikkeli-kaasuvirtauksen laskennalla pyritään selvittämään mm. syklonin geometrian vaikutus erotustehokkuuteen tai painehäviöön. Lisäksi laskentaa käytetään esimerkiksi partikkelien aiheuttaman eroosion ennustamiseen ja vähentämiseen. [3]

Mikäli partikkelien konsentraatio-osuus on riittävän pieni, voidaan partikkelien liikeratojen laskenta suorittaa niin sanotusti jälkilaskentana [1]. Tällöin kaasuvirtaus (tässä työssä jatkuvana faasina on kaasu) lasketaan ensin olettaen partikkelien vaikutus kaasun virtauskenttään pieneksi. Partikkelien liikeradat lasketaan tämän jälkeen. Tässä työssä on keskitytty näistä kahdesta vaiheesta ensimmäiseen, kaasuvirtauksen kentän laskentaan.

Useat lähteet (esim. [7]) osoittavat, että voimakkaasti kaareutuvan virtauskentän laskentaan ei voida käyttää yleisimmin virtauslaskennassa käytettyjä kaksiyhtälöturbulenssimalleja vaan virtauskentän laskenta pitää tehdä kehittyneemmällä menetelmällä. Lisäksi kirjallisuudessa on osoitettu, että syklonierottimen virtauskenttä ei ole aksiaalisymmetrinen vaan keskiosan virtausrakenne – prekessioliikeessä oleva ydin (precessing vortex core, PVC) – pyörii symmetria-akselin ympäri tietyllä taajuudella, joten virtauskenttää ei voida olettaa aikariippumattomaksi [3].

Tässä työssä on laskettu kirjallisuudessa usein vertailutapauksena käytetyn syklonierottimen (Stairmand high-efficiency cyclone [9]) kaasuvirtauskenttä eräällä Reynoldsin jännitysmallilla ajan suhteen tarkasti ja käyttäen avoimen lähdekoodin ohjelmistoa OpenFOAM 2.1.1 [5, 8]. Laskenta on tehty usealla laskentaverkolla ja usealla eri aika-askeleella diskretoinnin aiheuttamien virheiden minimoimiseksi.

Virtausta hallitsevat yhtälöt ja niiden ratkaisu

Turbulenttia virtausta hallitsevat perusyhtälöt

Reynolds-keskiarvotettaessa virtausta hallitsevat yhtälöt muuttujien hetkelliset arvot jaetaan aikakeskiarvon ja heilahteluarvon summaksi, esimerkiksi nopeuden x_i-komponentti $u_i = \overline{u}_i + u_i'$, missä $\overline{u}_i$ on aikakeskiarvo ja u_i' on heilahteluarvo. Sijoittamalla hajotelmat yleisiin virtausta hallitseviin jatkuvuus- ja liikemääräyhtälöihin ja ottamalla yhtälöistä aikakeskiarvo (ja jättämällä pois päälleviivaukset yksittäisten muuttujien kohdalla) saadaan kokoonpuristumatonta turbulenttia virtausta hallitsevat Reynolds-keskiarvotetut Navier-Stokesin yhtälöt (Reynolds averaged Navier-Stokes, RANS):

$$\frac{\partial u_i}{\partial x_i} = 0, \tag{1}$$

missä u_i on nopeuden x_i-komponentti ja x_i on paikkakomponentti ja

$$\frac{\partial u_i}{\partial t} + u_j \frac{\partial u_i}{\partial x_j} = -\frac{1}{\rho}\frac{\partial p}{\partial x_i} + \nu \frac{\partial^2 u_i}{\partial x_j \partial x_j} + \frac{\partial}{\partial x_j}\left(-\overline{u_i' u_j'}\right). \tag{2}$$

missä ρ on tiheys, p on paine ja ν on kinemaattinen viskositeetti.

Yhtälön (2) viimeinen termi on termi, joka ilmaisee turbulenssin vaikutusta. Termi sisältää niin sanotut Reynoldsin jännitykset $-\overline{u_i' u_j'}$, jotka täytyy mallintaa ylimääräisillä yhtälöillä.

Turbulenssin mallintaminen

Yleisimmin turbulenssin mallinnukseen käytetyissä kaksiyhtälömalleissa (esim. k-ε-malli) käytetään Reynoldsin jännityksille Boussinesq'n pyörreviskositeettimallia, jonka sisältämän oletuksen mukaan Reynoldsin jännitystensorin epäisotrooppisen osan ja aikakeskiarvotetun venymänopeustensorin välille oletetaan lineaarinen yhteys, eli turbulenssi oletetaan isotrooppiseksi. Voimakkaasti kaareutuvassa virtauksessa tämä oletus on väärä.

Reynoldsin jännitysmallissa (Reynolds stress model, RSM) tätä oletusta ei tehdä, vaan jokaiselle Reynoldsin jännitystensorin alkiolle $-\overline{u_i' u_j'}$ on oma yhtälö [6]. Yksittäisiä Reynoldsin jännityksiä käyttäen saadaan Reynolds-keskiarvotettu liikemääräyhtälö (2) sulkeutumaan.

Lähtien Navier-Stokesin yhtälöistä Reynoldsin jännityksille voidaan johtaa yhtälöt:

$$\underbrace{\frac{\partial}{\partial x_k}\left(u_k \overline{u_i' u_j'}\right)}_{C_{ij}\equiv\text{konvektio}} = \underbrace{-\frac{\partial}{\partial x_k}\left[\overline{u_i' u_j' u_k'} + \overline{\frac{p'}{\rho}\left(\delta_{kj} u_i' + \delta_{ik} u_j'\right)}\right]}_{D_{\mathrm{T},ij}\equiv\text{turbulentti diffuusio}} + \underbrace{\frac{\partial}{\partial x_k}\left[\nu \frac{\partial}{\partial x_k}\left(\overline{u_i' u_j'}\right)\right]}_{D_{\mathrm{L},ij}\equiv\text{molekyläärinen diffuusio}}$$
$$\underbrace{-\left(\overline{u_i' u_k'}\frac{\partial u_j}{\partial x_k} + \overline{u_j' u_k'}\frac{\partial u_i}{\partial x_k}\right)}_{P_{ij}\equiv\text{jännitystuotto}} + \underbrace{\overline{\frac{p'}{\rho}\left(\frac{\partial u_i'}{\partial x_j} + \frac{\partial u_j'}{\partial x_i}\right)}}_{\phi_{ij}\equiv\text{painevenymä}} \underbrace{- 2\nu \overline{\frac{\partial u_i'}{\partial x_k}\frac{\partial u_j'}{\partial x_k}}}_{\varepsilon_{ij}\equiv\text{dissipaatio}} \tag{3}$$

missä C_{ij}, $D_{\mathrm{L},ij}$ ja P_{ij} eivät vaadi mallintamista, mutta $D_{\mathrm{T},ij}$, ϕ_{ij} ja ε_{ij} täytyy mallintaa.

Diffuusiotermiä $D_{\mathrm{T},ij}$ mallinnettaessa käytetään turbulentin diffusiviteetin skalaariarvoa:

$$D_{\mathrm{T},ij} = \frac{\partial}{\partial x_k}\left(\frac{\nu_\mathrm{t}}{\sigma_k}\frac{\partial \overline{u_i' u_j'}}{\partial x_k}\right), \tag{4}$$

missä σ_k on turbulenssin kineettisen energian turbulentti Prandtlin luku ja kinemaattinen pyörreviskositeetti $\nu_\mathrm{t} = C_\mu k^2/\varepsilon$, missä C_μ on vakio.

Painevenymätermin ϕ_{ij} malli on merkittävässä roolissa Reynoldsin jännitysmallien kehityksessä ja eri RSM versioiden tulosten erot johtuvat suurelta osin tämän termin mallinnuksen eroista. Termi koostuu kahdesta osasta, hitaasta ja nopeasta painevenymästä:

$$\phi_{ij} = -C_1 \frac{\varepsilon}{k} \quad \overline{u_i' u_j'} - \frac{2}{3} k \delta_{ij} \Big) - C_2 \quad P_{ij} - \frac{2}{3} P \delta_{ij} \Big), \tag{5}$$

missä k on turbulenssin kineettinen energia, $P = P_{kk}/2$ ja C_1 sekä C_2 ovat vakioita.

Dissipaatiotensori ε_{ij} mallinnetaan olettaen paikallinen isotropia, jolloin,

$$\varepsilon_{ij} = \frac{2}{3} \delta_{ij} \varepsilon, \tag{6}$$

missä ε on turbulenssin kineettisen energian dissipaatio ja lasketaan omasta siirtoyhtälöstään.

Yhtälöiden numeerinen ratkaisu

Kaikki laskennat on tehty käyttäen kontrollitilavuusmenetelmään perustuvaa avoimen lähdekoodin ohjelmistoa OpenFOAM 2.1.1 [5, 8]. Kaikkien termien paikkadiskretointi on tehty käyttäen toista kertalukua olevaa keskeisdifferenssiä lukuun ottamatta konvektiotermejä, joiden diskretointiin on käytetty niin sanottua `limitedLinear` diskretointikaavaa ja sen vektorimuotoa (`limitedLinearV`) nopeustermeihin. Menetelmän parametrina on käytetty arvoa 1, jolloin menetelmä on eräs TVD-menetelmistä (Total Variation Diminishing). Paine-nopeuskytkentä on tehty käyttäen PISO-menetelmää [4].

Koska syklonierottimen virtauskenttä on voimakkaasti ajasta riippuva, on laskenta tehty ajan suhteen tarkkana (Unsteady RANS, URANS). Tilannetta on kuitenkin ensin laskettu 1000 iteraatiota käyttäen stationääriä ratkaisijaa `simpleFoam` paremman alkuehdon saamiseksi. Tämän jälkeen laskentaa on jatkettu 2 s aikariippuvana ratkaisijalla `pisoFoam` tilastollisesti ajasta riippumattoman tilanteen saavuttamiskesi. Tämän jälkeen tulosdataa on kerätty jatkamalla laskentaa 1 s. Lopulliset aikakeskiarvotulokset on laskettu tältä aikaväliltä (2 s → 3 s). Aikaintegrointi on tehty käyttäen toista kertalukua oleva implisiittistä menetelmää `backward` [8]. Aika-askeleena on käytetty kolmea eri pituista askelta (Taulukko 1).

Laskenta-alue ja -verkko

Laskettu tilanne (Stairmand high-efficiency cyclone [9]) on esitetty kuvassa 1. Sisäänvirtausnopeuden ja syklonin halkaisijan avulla laskettu Reynoldsin luku $\mathrm{Re}_D = U_\mathrm{in} D/\nu = 280\,000$. Sisäänvirtauskanava on tehty niin pitkäksi ($25D$), että sykloniin tuleva virtaus on täysin kehittynyt kanavavirtaus.

Laskentaverkko on tehty käyttäen ohjelmaa `blockMesh`, joka on OpenFOAMiin kuuluva yksinkertainen laskentaverkon muodostustyökalu. Työkalulle annetaan käsin luotu tiedosto, jossa laskenta-alue on jaettu topologisesti heksaedrin muotoisiin lohkoihin, joihin ohjelma muodostaa laskentaverkon. Lähes koko laskentaverkko (kuvat 2 ja 3) on muodostettu heksaedrin muotoisista kontrollitilavuuksista, ainoastaan sisäänvirtauskanavan alapinnan ja syklonin välisessä rajapinnassa on vähäinen määrä tetraedrin muotoisia kontrollitilavuuksia (kuva 3). Laskentaan on käytetty yhteensä neljää eri laskentaverkkoa, joiden tiheydet ilmenevät taulukosta 1.

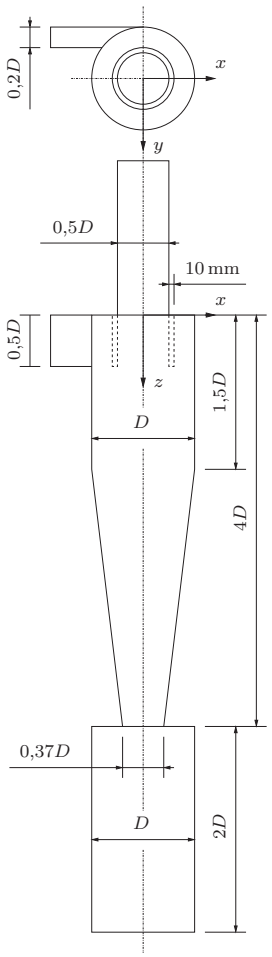

Kuva 1. Geometria, dimensiot ja koordinaatisto. Syklonin halkaisija $D = 290\,\mathrm{mm}$.

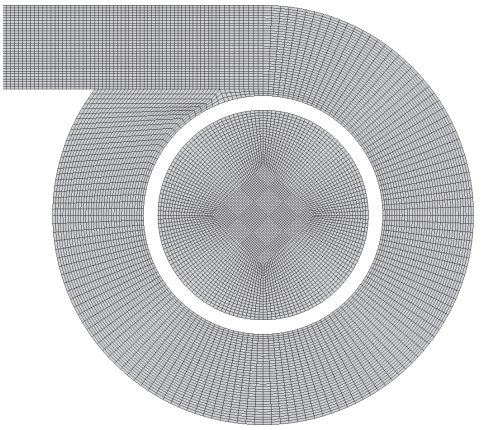

Kuva 2. Laskentaverkko 6 115 890 sisäänvirtauskanavan puolessa välissä tasolla $z = D/4$.

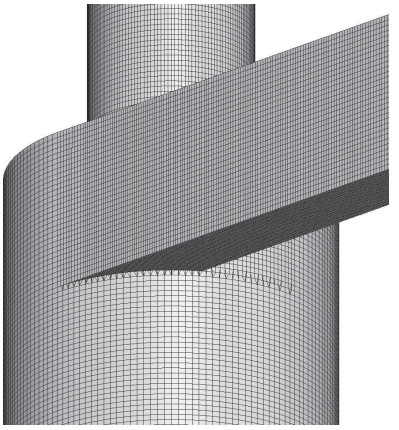

Kuva 3. Laskentaverkko 6 115 890 sisäänvirtauskanavan ja syklonin rajapinnalla.

Taulukko 1. Laskentaverkot, aika-askeleet ja laskenta-ajat.

		`pisoFoam`		
verkko	`simpleFoam`	$\Delta t = 50\,\mu$s	$\Delta t = 25\,\mu$s	$\Delta t = 12{,}5\,\mu$s
538 902	0,036 h	17 h	33 h	60 h
1 787 260	0,13 h	28 h	54 h	110 h
6 115 890	0,50 h	kaatui	250 h	liian pitkä

Tulokset

Tangentiaalinen (kuva 4) ja aksiaalinen (kuva 5) aikakeskiarvonopeus noudattavat hyvin mitattuja tuloksia RSM:ää käytettäessä, kun laskentaverkko on riittävän tiheä ja aika-askel riittävän lyhyt. Kuviin vertailun vuoksi piirretyistä k-ε-mallin (laskettu käyttäen verkkoa 6 115 890 ja aika-askelta $\Delta t = 25\,\mu$s) tuloksista näkyy kaksiyhtälömallin käyttö-

kelvottomuus tällaisessa laskentatilanteessa. Kaksiyhtälömalli antaa tangentiaalinopeudeksi lähes pyörivän kiinteän kappaleen nopeuskentän, kun oikeasti virtaus noudattaa vain sisäalueessa kiinteän kappaleen tangentiaalinopeutta ja ulkoalueessa lähes kitkattoman virtauksen nopeusjakaumaa.

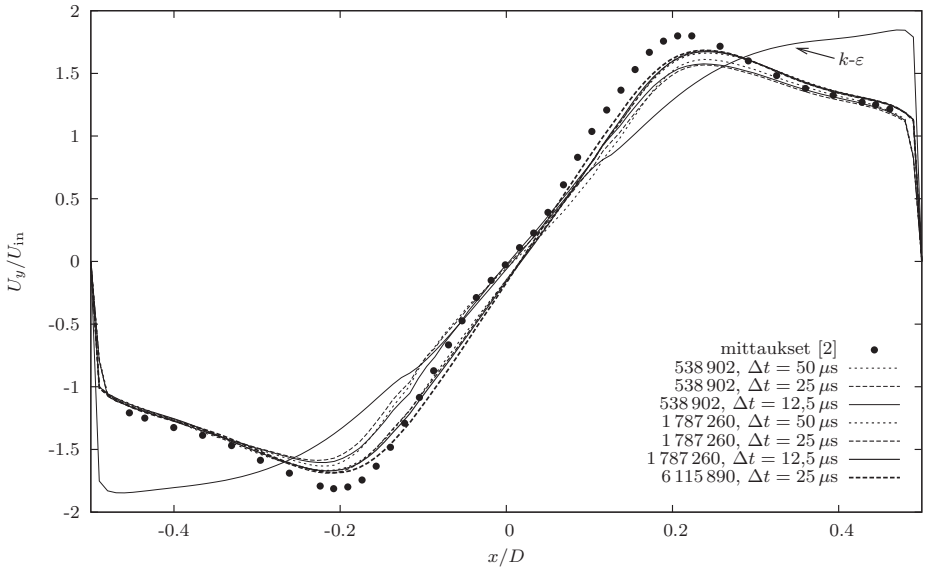

Kuva 4. Tangentiaalisuuntainen aikakeskiarvonopeus suoralla $y = 0$, $z = 1{,}5D$.

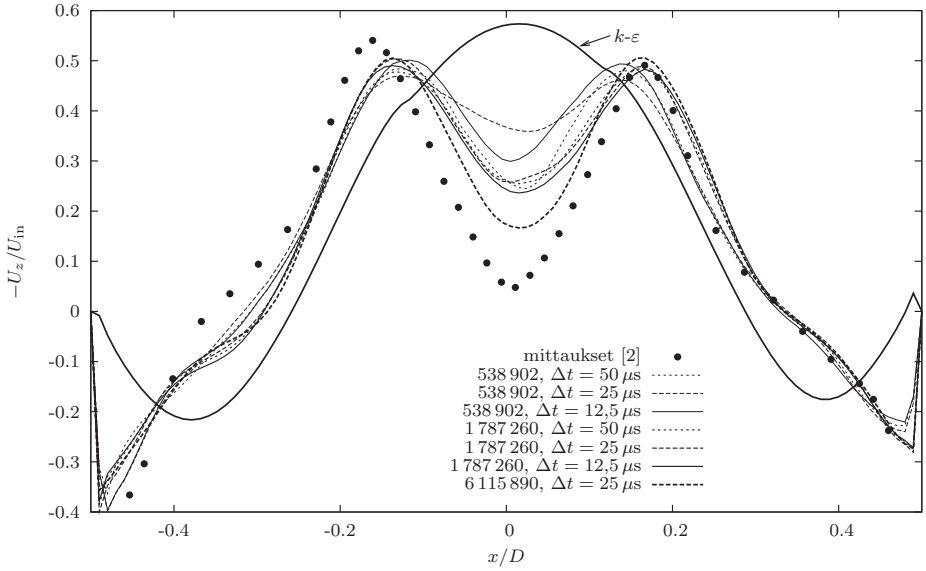

Kuva 5. Aksiaalisuuntainen aikakeskiarvonopeus suoralla $y = 0$, $z = 1{,}5D$.

Prekessioytimen Strouhalin luvuksi ($\mathrm{St}_{\mathrm{PVC}} = f_{\mathrm{PVC}} D/U_{\mathrm{in}}$, missä f_{PVC} on ytimen taajuus ja U_{in} sisäänvirtausnopeus) on mittauksissa [2] saatu $\mathrm{St}_{\mathrm{PVC}} = 1{,}58$. Käytettäessä

laskentaverkkoa 6 115 890 ja aika-askelta $\Delta t = 25\,\mu$s saadaan nopeuden aikakuvaajasta arvioitua Strouhalin luvuksi $\mathrm{St}_{\mathrm{PVC}} \approx 1{,}2$. Harvemmilla laskentaverkoilla ytimen liike ei ole yhtä säännöllistä ja Strouhalin luvun arviointi on vaikeaa.

Taulukon 1 laskenta-ajoista nähdään, että ajasta riippuva virtauslaskenta tiheillä laskentaverkoilla on erittäin laskentaintensiivistä. Kaikki laskennat on tehty käyttäen yhteensä kuuttakymmentä prosessoriydintä. Tiheintä laskentaverkkoa ja pisintä aika-askelta käytettäessä Courantin luvun maksimiarvo oli niin suuri, että laskenta kaatui. Tiheimmän verkon ja lyhyimmän aika-askeleen laskenta taas kesti niin kauan, ettei laskentaa ollut mahdollista saada valmiiksi käytettävissä olleilla laskentaresursseilla.

Johtopäätökset

Syklonierottimen kaasuvirtauksen laskennassa välttämätön ajasta riippuva laskenta on erittäin laskentaintensiivistä. Yleisemmin turbulenssin mallinnukseen käytetyt kaksiyhtälömallit (esim. k-ε-malli) eivät ole tilanteeseen käyttökelpoisia, mutta kehittyneempi Reynoldsin jännitysmalli antaa tuloksia, jotka ovat lähellä mitattuja arvoja, kun laskentaverkko on riittävän tiheä ja aika-askel riittävän lyhyt.

Viitteet

[1] C. Crowe, M. Sommerfeld ja Y. Tsuji. *Multiphase flows with droplets and particles*. CRC Press, Boca Raton, London, New York, Washington, D. C., 1998.

[2] A.J. Hoekstra, *Gas flow field and collection efficiency of cyclone separators*. Väitöskirja, Delft University of Technology, 2000.

[3] A.C. Hoffmann ja L.E. Stein. *Gas cyclones and swirl tubes: Principles, design and operation*. Springer, Berlin, Heidelberg, New York, Barcelona, Hong Kong, London, Milan, Paris, Tokyo, 2002.

[4] R.I. Issa. Solution of implicitly discretized fluid flow equations by operator splitting. *Journal of Computational Physics*, 62:40–65, 1986.

[5] H. Jasak. *Error analysis and estimation for the finite volume method with applications to fluid flows*. Väitöskirja, University of London, 1996.

[6] B.E. Launder, G.J. Reece ja W. Rodi. Progress in the development of a Reynolds-stress turbulence closure. *Journal of Fluid Mechanics*, 68:537–566, 1975.

[7] M. Nallasamy. Turbulence models and their applications to the prediction of internal flows: A review. *Computers and Fluids*, 17:151–194, 1987.

[8] OpenFOAM. www.openfoam.org, June 2012.

[9] C.J. Stairmand. The desing and performance of cyclone separators. *Transactions of the Institution of Chemical Engineers*, 29:356–383, 1951.

Aku Karvinen, Hannu Ahlstedt
Energia- ja prosessitekniikan laitos
Tamperen teknillinen yliopisto
PL 589, 33101 TAMPERE
s-posti: aku.karvinen@tut.fi, hannu.ahlstedt@tut.fi

A Comparison of Two Approaches for the Analysis of Shell Structures: NURBS-based Isogeometric Analysis Versus Bilinear FEM

Antti H. Niemi, Nathan Collier, Lisandro Dalcin, Mehdi Ghommem, and Victor M. Calo

Summary. We study a NURBS-based finite element formulation for shell structures. The formulation is based on a shell model which utilizes curvilinear coordinates and analytic integration thorough the thickness. We examine the accuracy of the approach in the pinched cylinder benchmark problem and present comparisons against the h-version of FEM with bilinear elements.

Key words: shell structures, NURBS, benchmark study

Introduction

Isogeometric analysis is a generalization of standard finite element analysis introduced by Hughes and collaborators in [9]. The goal is to streamline the engineering design and analysis processes by using the same functions for computer aided design and finite element analysis. Popular choices of basis functions are non-uniform rational B-splines (NURBS) and their extension, T-splines, see [3]. Isogeometric approach is suitable for shell analysis since representation of surfaces is customary in computer graphics and shell geometries can be described in terms of the middle surface and its normal vector.

In this study, we introduce a NURBS-based shell model of Reissner-Mindlin type and study its accuracy in the classical pinched cylinder benchmark problem. Our formulation is based on shell model where the displacement, strain and stress fields are defined in terms of a curvilinear coordinate system arising from the NURBS description of the shell middle surface. It should be noted that splines have been employed earlier in shell analysis in the works [9, 3, 10, 5, 4] but also other techniques such as subdivision surfaces have been used in this context, see [6, 11].

Our shell formulation is implemented using the `PetIGA` and `igakit` software packages developed by Collier and Dalcin. The `igakit` package is a Python package used to generate NURBS representations of geometries that can be utilized by the `PetIGA` finite element framework. The latter utilises data structures and routines of the Portable, Extensible Toolkit for Scientific Computation (`PETSc`), see [2, 1]. Our current shell implementation is valid for static, linear problems only, but the software package is well suited for future extensions to geometrically and materially nonlinear regime as well as to dynamic problems.

Isogeometric Shell Analysis using NURBS

In this section we present a summary of representation of surfaces using NURBS and the related finite element analysis. For more detailed discussion, see for instance [13, 8, 7].

B-spline curves

B-splines are piecewise polynomial curves defined in terms of B-spline basis functions. The basis functions of degree p, denoted by $N_{i,p}(\xi)$, associated to a non-decreasing set of coordinates called the knot vector $\mathcal{X} = \{\xi_1, \xi_2, \ldots, \xi_{n+p+1}\}$ are defined recursively as

$$\begin{aligned} N_{i,0}(\xi) &= \begin{cases} 1, & \xi_i \leq \xi < \xi_{i+1} \\ 0, & \text{otherwise} \end{cases} \\ N_{i,p}(\xi) &= \frac{\xi - \xi_i}{\xi_{i+p} - \xi_i} N_{i,p-1}(\xi) + \frac{\xi_{i+p+1} - \xi}{\xi_{i+p+1} - \xi_{i+1}} N_{i+1,p-1}(\xi), \quad p > 0 \end{aligned} \tag{1}$$

for $i = 1, \ldots, n$ and $p \geq 1$. A B-spline basis function is C^∞ between two distinct knots and C^{p-1} at a single knot. If a knot is repeated in the knot vector k times then the continuity is C^{p-k} at that knot. Consequently, the basis becomes interpolatory at knots with multiplicity p whereas knot multiplicity of $p+1$ makes the basis discontinuous and is used at the end points to make the knot vector open.

The B-spline curve of degree p with control points $\mathbf{P}_1, \ldots, \mathbf{P}_n$ is defined on the interval $[a, b] = [\xi_{p+1}, \xi_{n+1}]$ as the linear combination of the control points and basis functions

$$\mathbf{C}(\xi) = \sum_{i=1}^{n} N_{i,p}(\xi) \mathbf{P}_i$$

We recall that the piecewise linear interpolation of the control points is called the control polygon. For open knot vectors, the B-spline curve interpolates the first and last control points and is tangential to the control polygon at these points.

B-spline surfaces

A B-spline surface is defined using tensor products of B-spline basis functions written in two parametric coordinates ξ, η. If $N_{i,p}$ and $M_{j,q}$ denote basis functions of degree p and q associated to the knot vectors $\mathcal{X} = \{\xi_1, \xi_2, \ldots, \xi_{n+p+1}\}$ and $\mathcal{Y} = \{\eta_1, \eta_2, \ldots, \eta_{m+q+1}\}$ and $\mathbf{P}_{ij}$, $i = 1, \ldots, n$, $j = 1, \ldots, m$ is a net of control points in 3-space, the B-spline surface is defined as

$$\mathbf{S}(\xi, \eta) = \sum_{i=1}^{n} \sum_{j=1}^{m} N_{i,p}(\xi) M_{j,q}(\eta) \mathbf{P}_{ij}$$

For open knot vectors, the surface interpolates the control net at the vertices.

NURBS

Non-uniform Rational B-Splines (NURBS) are obtained from integral B-splines by supplementing each control point with a scalar weight. The NURBS surface has the representation

$$\mathbf{S}(\xi, \eta) = \frac{\sum_{i=1}^{n} \sum_{j=1}^{m} N_{i,p}(\xi) M_{j,q}(\eta) w_{ij} \mathbf{P}_{ij}}{\sum_{i=1}^{n} \sum_{j=1}^{m} N_{i,p}(\xi) M_{j,q}(\eta) w_{ij}}$$

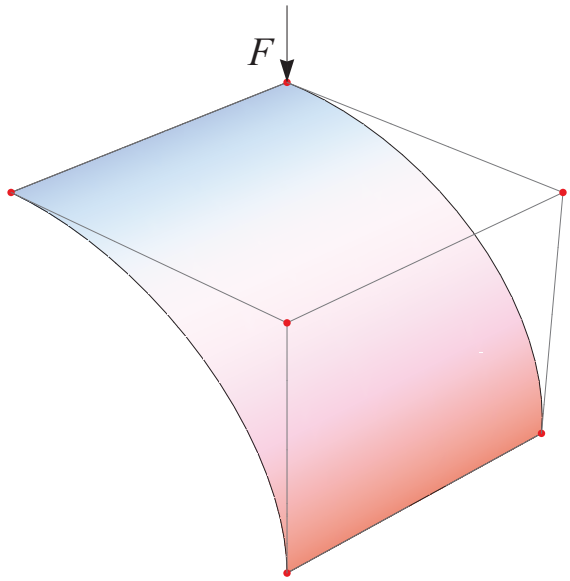

Figure 1. Initial geometry for the pinched cylinder problem.

where the control point net $\mathbf{P}_{ij}$ is augmented with the weights w_{ij} for $i = 1, \ldots, n$ and $j = 1, \ldots, m$. The use of rational functions enables representation of quadric surfaces such as spheres, cones, paraboloids etc.

Finite Element Analysis using NURBS

The isogeometric finite element method is obtained from the exact geometry representation by invoking the isoparametric concept, that is, by using the same basis functions used to represent the geometry to approximate the unknown function. The two basic mechanisms for controlling the accuracy of the approximation in isogeometric analysis are knot insertion and degree elevation. The idea is to enrich the NURBS basis without changing the surface geometrically or parametrically. This can be achieved by changing the number and location of the control points in a suitable way, see [7] for more details. Both refinement techniques are implemented in the `igakit` package.

Numerical Results and Concluding Remarks

We consider as an example a pinched cylinder with end diaphragms which is a classical benchmark problem in shell analysis. The initial geometry consists of a circular cylinder of radius $R = 100$ and length $2L = 100$. The cylinder is loaded by two normal point loads of magnitude $F = 1$ located centrally at the opposite sides of the cylinder. The material parameters are taken to be $E = 3 \cdot 10^7$ and $\nu = 0.3$. By symmetry, it is sufficient to analyze only one eight of the cylinder which can represented using a single quadratic rational NURBS element as shown in Figure 1.

Figures 2 and 3 show convergence of the displacement under the load application point when $R/t = 100$ and $R/t = 1000$, respectively. Quadratic, cubic and quartic NURBS discretizations are compared against the isoparametric bilinear discretization introduced in [12]. The latter formulation also computes the geometric curvature of the shell inside

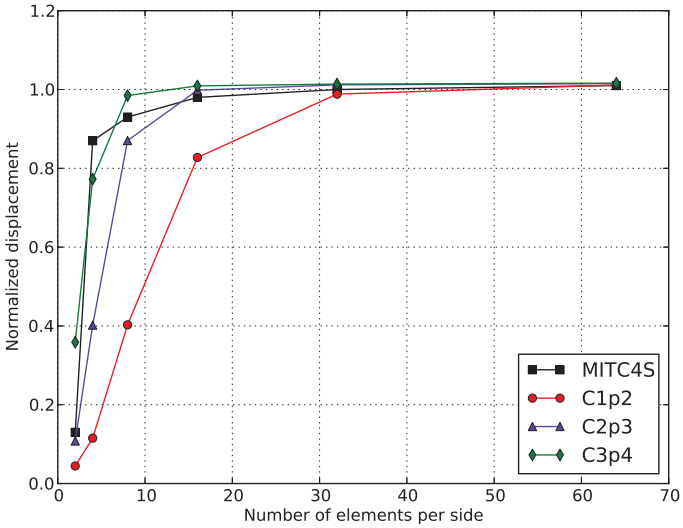

Figure 2. Strain energy convergence of the pinched cylindrical shell at $R/t = 100$. NURBS-based discretizations with maximal continuity vs. bilinear h-FEM.

each element from the nodal normal vectors. This together with reduced strain expressions guarantees excellent coarse-mesh accuracy.

In the NURBS formulation the shell geometry is always represented exactly but no attempt, other than increasing the approximation order, is made to avoid locking. Our results show that the quadratic and cubic NURBS approximations exhibit notably slower convergence under uniform knot insertion as the thickness decreases but the quartic approximation converges relatively quickly.

References

[1] Satish Balay, Kris Buschelman, Victor Eijkhout, William D. Gropp, Dinesh Kaushik, Matthew G. Knepley, Lois Curfman McInnes, Barry F. Smith, and Hong Zhang. PETSc users manual. Technical Report ANL-95/11 - Revision 3.0.0, Argonne National Laboratory, 2008.

[2] Satish Balay, Kris Buschelman, William D. Gropp, Dinesh Kaushik, Matthew G. Knepley, Lois Curfman McInnes, Barry F. Smith, and Hong Zhang. PETSc Web page, 2010. http://www.mcs.anl.gov/petsc.

[3] Y Bazilevs, V M Calo, J A Cotrell, J A Evans, S. Lipton, T J R Hughes, M A Scott, and T W Sederberg. Isogeometric analysis using T-splines. *Computer Methods in Applied Mechanics and Engineering*, 199:229–263, 2010.

[4] D.J. Benson, Y. Bazilevs, M.-C. Hsu, and T.J.R. Hughes. A large deformation, rotation-free, isogeometric shell. *Computer Methods in Applied Mechanics and Engineering*, 200(13-16):1367–1378, March 2011.

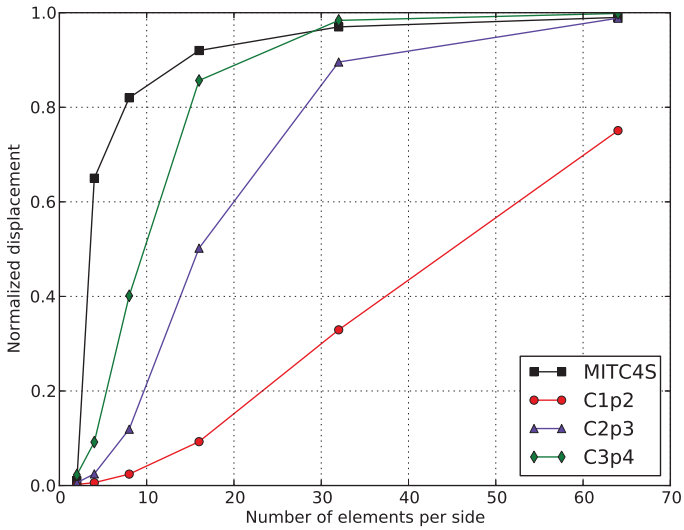

Figure 3. Strain energy convergence of the pinched cylindrical shell at $R/t = 1000$. NURBS-based discretizations with maximal continuity vs. bilinear h-FEM.

[5] D.J. Benson, Y. Bazilevs, M.C. Hsu, and T.J.R. Hughes. Isogeometric shell analysis: The Reissner-Mindlin shell. *Computer Methods in Applied Mechanics and Engineering*, 199(5-8):276–289, January 2010.

[6] Fehmi Cirak, Michael Ortiz, and Peter Schröder. Subdivision surfaces: a new paradigm for thin-shell finite-element analysis. *International Journal for Numerical Methods in Engineering*, 47(12):2039–2072, April 2000.

[7] J. Austin Cottrell, T. J. R. Hughes, and Yuri Bazilevs. *Isogeometric Analysis: Toward Unification of CAD and FEA*. John Wiley and Sons, 2009.

[8] Gerald Farin. *Curves and Surfaces for CAGD: A Practical Guide*. Morgan Kaufmann, 5th edition, 2002.

[9] T.J.R. Hughes, J.A. Cottrell, and Y. Bazilevs. Isogeometric analysis: CAD, finite elements, NURBS, exact geometry and mesh refinement. *Computer Methods in Applied Mechanics and Engineering*, 194(39-41):4135–4195, October 2005.

[10] J. Kiendl, K.-U. Bletzinger, J. Linhard, and R. Wüchner. Isogeometric shell analysis with Kirchhoff-Love elements. *Computer Methods in Applied Mechanics and Engineering*, 198(49-52):3902–3914, November 2009.

[11] Quan Long, P. Burkhard Bornemann, and Fehmi Cirak. Shear-flexible subdivision shells. *International Journal for Numerical Methods in Engineering*, pages n/a–n/a, April 2012.

[12] Antti H. Niemi. A bilinear shell element based on a refined shallow shell model. *International Journal for Numerical Methods in Engineering*, 81:485–512, 2010.

[13] Les Piegl and Wayne Tiller. *The NURBS Book*. Monographs in Visual Communication. Springer, New York, 1995.

Antti H. Niemi
Aalto University
Espoo, Finland
antti.h.niemi@aalto.fi

Nathan Collier, Mehdi Ghommem, and Victor M. Calo
King Abdullah University of Science and Technology (KAUST)
Thuwal, Kingdom of Saudi Arabia
nathan.collier@kaust.edu.sa, mehdi.ghommem@kaust.edu.sa, victor.calo@kaust.edu.sa

Lisandro Dalcin
Consejo Nacional de Investigaciones Científicas y Técnicas
Santa Fe, Argentina
dalcinl@intec.unl.edu.ar

A Simple Method to Determine Critical Temperature and Catenary Force of Simply Supported Steel Beam in Fire

Mikko Salminen, Markku Heinisuo

Summary. This paper presents a simplified method to determine the critical temperature and the corresponding catenary force in a simply supported steel beam in fire when the maximum deflection is defined. The critical temperatures and tensile forces are defined for different kinds of steel I-beams and compared to other well validated method. Moreover, the proposed method is applied in the case of WQ-beam and the results are compared to those obtained using finite element (FE) software ABAQUS.

Key words: steel beam, fire, catenary action

Introduction

When subjected to elevated temperatures, steel structures lose part of their loading capacity and stiffness. Left-hand side of Fig. 1 shows the reductions of yield strength (k_y), elastic modulus (k_E) and proportional limit (k_p) as a function of a temperature according to EN 1993-1-2 [1]. The structural fire design concept of EN 1993-1-2 [1] is adopted from ambient temperature (20 ^oC) design meaning that the beam's critical temperature is calculated based on the bending moment capacity of the beam and large deformations are not taken into account. This has been shown to give very conservative critical temperatures (T_{crit}) for steel beams in most of the cases e.g. in Refs. [2-5] and expensive fire protection is required [2]. The critical temperature can be defined by using advanced calculation models (FE), which are time consuming due to many sources of non-linearities e.g. large deflections, thermal expansion and highly non-linear material behaviour (right-hand side of Fig. 1).

The idea of catenary action is not new, but it has only recently being considered in structural fire engineering [5]. The behaviour of a beam changes from bending to catenary action at large deflections and it can give the beam very high load carrying capacity compared to current design procedure. According to Yin and Wang [2], if large deflection is acceptable, it might be possible to eliminate fire protection to all steel beams in a building.

Yin and Wang [2] have concluded that the utilization of catenary action in realistic applications requires careful consideration of the adjacent structure, including joints. Joints are often the critical elements in fire situation. The test results conducted by Ding and Wang [6] indicated that even relatively simple joints were able to allow the beams to develop substantial catenary action so that the critical temperatures were much higher than those obtained by assuming the beams in pure bending. They also reported

that at the end of the tests, the beams reached deflections $L/5$, where L is span of the beam and even then, the failure always occurred in the joints. In EN 1993-1-2 [1], the deflection limit in fire situation is $L/20$. These results indicate that it is possible to utilize the catenary action in fire but the joints should be very strong and have a high rotational capacity [6]. Recent studies [7] show that so-called extended end-plate connection performs well and enables catenary action in fire situation.

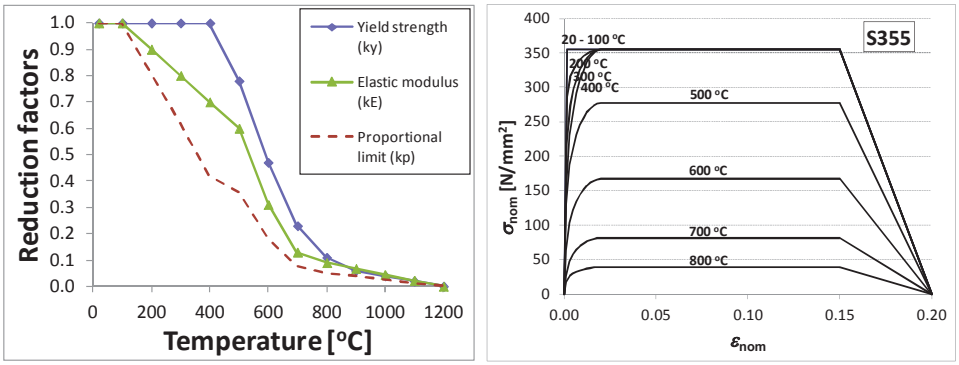

Figure 1. Material behaviour according to the EN 1993-1-2 [1].

Yin and Wang have proposed a simple analysis method of catenary action in steel beams in fire, which is presented in more detail in Refs. [3,4]. The main assumptions in the method are the beam's deflection profile and interaction between axial load and bending moment [3]. This method can be used for uniform and non-uniform temperature distributions, for simply supported, clamped or semi-rigidly supported beams as well as for beams with uniform or point loads. This method is validated with a large number of numerical simulations [3-4]. It should be noted that Yin and Wang assumed a fourth order polynomial as the deflection profile. This leads to a third order equilibrium equation, which means that the method might not be very practical tool in design.

Background of the proposed method

This paper proposes even more simplified method than the method of Yin and Wang [3,4]. Proposed method does not assume a function for the deflection curve of the beam. Instead, it assumes that the beam (with cross-section area A, section modulus W, and yield strength f_y) is in equilibrium and has reached it's maximum deflection δ. Half of the deflected beam is drawn in the middle of Fig. 2. The equilibrium of forces and moment with respect to left support can be written as shown in Fig. 2 ((a)-(c)). Resistance check of the beam is done at support and in the middle of the beam (Fig. 2 (d) and (e)). Linear interaction curves between bending moment- and axial force resistance are assumed for simplicity, which is not the case in reality. However, that assumption is on the safe side. It is assumed that no local or global buckling occur in the beam during heating even though the compressive forces due to thermal expansion may be significant. This study considers simply supported (support moment M_s=0) beam with uniform temperature and loading q. However, different loading conditions and

semi-rigid joints where stiffness of the joint, S, is expressed as $S=M_s/\varphi$ (φ is the rotation of the beam at support) could also be applied to the calculation procedure.

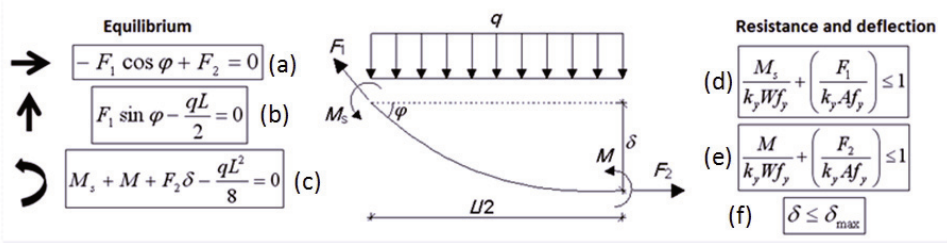

Figure 2. Basic idea of the proposed method.

Benchmark case and design formulas

The proposed method was validated against the results of Yin and Wang's method [3,4] which has been validated very well against test and FE results. The critical temperatures ($T_{crit,prop}$) and catenary forces ($F_{cat,prop}$) were calculated for 36 cases including different I-profiles, lengths of the beam (L = 6-20 m) and loading ratios (LR = 0.2-0.7). The maximum deflection in both methods was taken as $L/10$. The considered cases are named as B1-B12 in Ref. [5]. The temperature distribution in Yin and Wang's cases was slightly non-uniform and $T_{crit,Wang}$ corresponded the hottest temperature of the cross-section. The method proposed in this paper gives the critical average temperature of the beam. Thus, $T_{crit,prop}$ was multiplied by factor 1.08-1.09 depending on the considered cross-section so that the average temperatures in both cases were the same. According to Yin and Wang [2] the temperature distribution has only a minor effect to the critical temperature.

The reduction factor k_y can be solved from equations (a)-(f) of Fig. 2, but the formula is rather complicated. Thus, $T_{crit,prop}$ was first defined using a solver-command of a spreadsheet-calculation software meaning that the minimum value for k_y was found so that the constraints (a)-(f) were satisfied. The minimum value of k_y corresponds the maximum value of $T_{crit,prop}$ as can be seen from Fig. 1. The described optimization problem is rather simple but the purpose of this study was to develop even more simplified method which could be applied e.g. in preliminary design. In the first calculations it was found that the rotation angle φ was in all 36 cases very close to 22.6° (± 0.2°). Thus, the simple Equations (1) and (2) were derived assuming that $\varphi = 22.6°$. It should be noted that assuming a constant value for φ gives in every case lower values for $T_{crit,prop}$ (safe side) but in some cases too low (unsafe side) values for $F_{cat,prop}$ compared to the exact solution of equations (a)-(f). The minimum value of k_y can be solved from Equation (1).

$$k_y = \frac{125qL^2}{(77W + 923A\delta)f_y} \tag{1}$$

The critical temperature is then defined based on EN 1993-1-2 [1] shown also in the left-hand side of Fig. 1. The catenary force can be defined from Equation (2).

$$F_{cat} = F_2 = \frac{923AqL^2}{616W + 7384A\delta} \tag{2}$$

Fig. 3 presents the critical temperatures (left) and catenary forces (right) according to proposed method (Eqs. (1) and (2)) and the method of Yin and Wang [3,4]. The critical temperatures according to EN 1993-1-2 [1] are also shown.

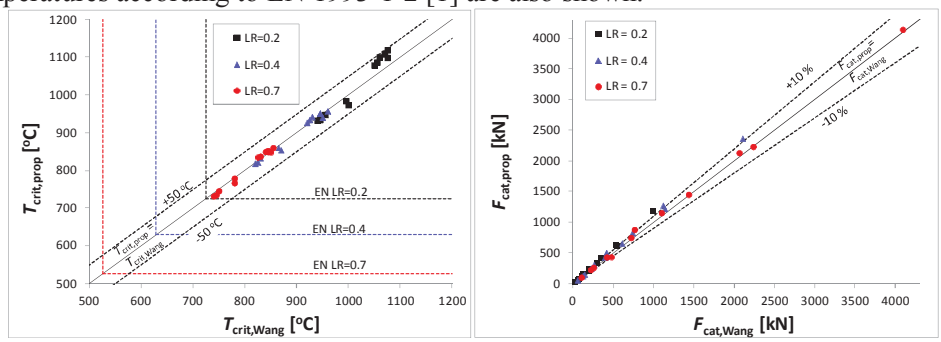

Figure 3. Results of benchmark case.

The proposed method gave almost the same critical temperatures as the method proposed by Yin and Wang [3,4] in the considered cases. The proposed method gave slightly higher catenary force than Yin and Wang's method in most of the cases.

Case study

A simply supported, axially restrained so-called WQ-beam (S355), shown in Fig. 4, was analysed at uniform temperatures 20-1000 °C. The length of the beam was 11.63 m and uniformly distributed loads q = 18.6, 31.0 and 44.3 kN/m (LR = 0.3, 0.5 and 0.71, respectively) were applied on the upper flange before heating of the beam.

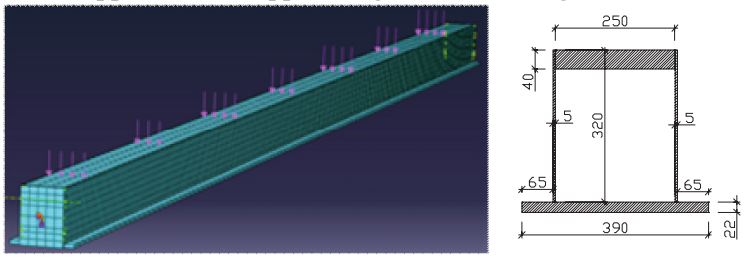

Figure 4. FE model (left) and cross-section of the considered beam.

The numerical analysis was conducted using ABAQUS [8] FE software. The beam was modelled using S4R shell elements. Non-linear behaviour of steel material at elevated temperatures was taken into account according to EN 1993-1-2 [1]. Creep strain is implicitly included in this stress-strain relationship. The following results are applicable for all time-temperature-curves where heating rate is between 2 and 50 K/min [1] and where the temperature does not decrease at any time. True stresses and logarithmic strains were calculated and used in the modelling as defined in EN 1993-1-5 [9].
Table 1 presents the critical temperatures from FE analysis ($T_{crit,FE}$), according to Yin and Wang's method ($T_{crit,Wang}$) and according to the proposed method ($T_{crit,PROP}$) which were calculated using three values for δ. Deflections δ = 582 mm and 1163 mm correspond values $L/20$ [1] and $L/10$, which is the value recommended by Yin and

Wang [5]. Twilt [10] has proposed a deflection limit $\delta = L^2/400h$ = 989 mm (h is height of the beam) which is also considered. Table 2 presents the catenary forces which were defined using the same methods at T_{crit}. The tie force $F_{cat,EN}$ was defined according to EN 1991-1-7 [11].

Table 1. Critical temperatures of WQ-beam.

q [kN/m]	LR	$T_{crit,EN}$ [°C]	$T_{crit,FE}$ [°C]	$T_{crit,Wang}$ [°C]	$T_{crit,prop}$ [°C] (δ=582 mm)	$T_{crit,prop}$ [°C] (δ=989 mm)	$T_{crit,prop}$ [°C] (δ=1163 mm)
18.6	0.30	671	> 1000	1080	870	980	1010
31.0	0.50	590	927	1000	785	875	895
44.3	0.71	521	849	900	745	810	840

Table 2. Catenary forces.

q [kN/m]	LR	$F_{cat,EN}$ [kN]	$F_{cat,FE}$ [kN]	$F_{cat,Wang}$ [kN]	$F_{cat,prop}$ [kN] (δ=582 mm)	$F_{cat,prop}$ [kN] (δ=989 mm)	$F_{cat,prop}$ [kN] (δ=1163 mm)
18.6	0.30	179	332	213	530	315	268
31.0	0.50	298	550	412	884	524	447
44.3	0.71	425	801	775	1255	744	634

The proposed method gave good and safe predictions for T_{crit}. Critical temperatures according to EN 1993-1-2 [1] were more than 300 °C lower than those from numerical analysis. The formula proposed by Yin and Wang [3,4] gave at least 50 °C hotter critical temperatures compared to FE results. Compared to FE analysis, the method of Yin and Wang gave lower catenary forces. The catenary forces according to proposed method were close to those from FE analysis when using the maximum deflection proposed by Twilt [11] (δ = 989 mm). Smaller deflections overestimated and lower underestimated F_{cat}. It should be noted that the catenary forces presented in Table 2 are the upper limits because the support displacements were fixed. According to Yin and Wang, for safe prediction of catenary forces, complete end axial restraint and zero end rotational restrains may be assumed [1]. Different kinds of stability problems were observed during the heating of the beams especially for the beam with the smallest loading ratios. Buckling of the web occurred in the middle area of the beam at temperatures 100–200 °C as shown in the left-hand side of Fig. 5 and lateral torsional buckling was observed at higher temperatures (middle and right-hand side of Fig. 5). The lateral displacement of the upper flange of the beam started to decrease after 600 °C due to tension in the beam. According to Yin and Wang [2] whether there occurs lateral torsional buckling or not will only have some minor effect on the ultimate resistance of a steel beam in catenary action.

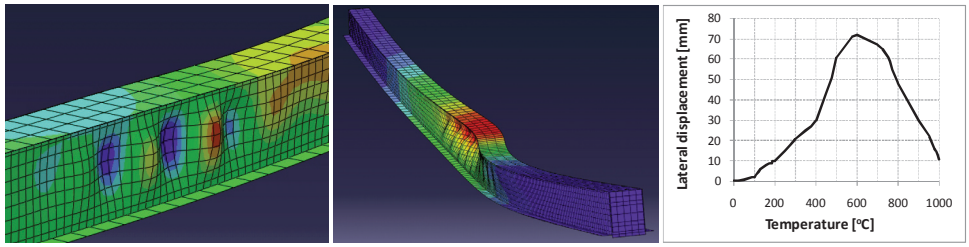

Figure 5. Buckling of the web at T=109 °C (left) and lateral torsional buckling at T=575 °C (middle and right) (LR=0.3, scaling factor 5 to lateral direction).

Conclusions

The proposed method gave promising results for the considered cases. However, further research is needed e.g. to validate the simplifications and to find the range of applications for the method. Moreover, the method should be extended to more general case where non-uniform loading and temperature distribution as well as semi-rigid joints could be applied.

References

[1] EN 1993-1-2, Eurocode 3: *Design of steel structures – Part 1-2: General rules. Structural fire design*, CEN, Brussels, 2005.

[2] Yin Y.Z., Wang Y.C., A numerical study of large deflection behaviour of restrained steel beams at elevated temperatures, *Journal of Constructional Steel Research* 60, 2004.

[3] Yin Y.Z., Wang Y.C., Analysis of catenary action in steel beams using a simplified hand calculation method, Part 1: theory and validation for uniform temperature distribution, *Journal of Constructional Steel Research* 61, 2005.

[4] Yin Y.Z., Wang Y.C., Analysis of catenary action in steel beams using a simplified hand calculation method, Part 2: validation for non-uniform temperature distribution, *Journal of Constructional Steel Research* 61, 2005.

[5] Wang Y.C., Yin Y.Z., Feasibility of utilising catenary action to eliminate fire protection to steel beams, *Advances in Steel Structures*, Vol. II, 2005.

[6] Ding J., Wang Y.C., Experimental study of structural fire behaviour of steel beam to concrete filled tubular column assemblies with different types of joints, *Engineering Structures* 29, 2007.

[7] Chen L., Wang Y.C., Methods of improving survivability of steel beam/column connections in fire, *Journal of Constructional Steel Research* 79, 2012.

[8] ABAQUS 6.10/CAE User's Manual, Dassault Systemes, 2010.

[9] EN 1993-1-5, Eurocode 3: *Design of steel structures – Part 1-5: Plated structural elements*, CEN, Brussels, 2005.

[10] Twilt L., *Design tools for the behaviour of multi-storey steel framed buildings exposed to natural fires*, 8th interim report, TNO report, TNO, 2002.

[11] EN 1991-1-7, Eurocode 1: *Actions on structures– Part 1-7: General actions – Accidental actions*, CEN, Brussels, 2006.

Mikko Salminen[a,b] and Markku Heinisuo[a]
Tampere University of Technology[a] and KPM-Engineering Oy[b]
Korkeakoulunkatu 10, 33720 Tampere
mikko.a.salminen@tut.fi

Jump conditions in surface tension problems with distributed torque

Mika Reivinen and Eero-Matti Salonen

Summary. The present article is a continuation of articles [1] and [2]. When the distributed torque has jumps in its value, edges can emerge on the interface surface. The article concentrates on deriving the jump conditions at the edges. The derivation is performed in the three-dimensional case. The two-dimensional case is obtained as a special case. In the two-dimensional case an exact solution with an edge is studied to show the satisfaction of the jump conditions. Further, a discrete solution is given, showing that also in it the jump conditions are satisfied rather accurately.

Key words: surface tension, crystal shape, jump conditions, virtual work

Introduction

The present article is an extension of articles [1] and [2]. The problem consists of the determination of the shape of the interface between two material phases with a non-constant surface tension. The final purpose is to be able to determine the equilibrium shapes of crystals. In [1] the phases considered were a liquid and a vapor. For continuity of presentation we will follow here again the notation of [1] and will thus still speak about the liquid and vapor phases although the physical assumption of an orientation dependent surface tension should actually be related to a solid.

Let us consider Figure 1. The basic setting consists of a liquid, surrounded by a vapor and resting in equilibrium on a solid surface. The task is to determine the position of the interface surface C between the liquid and the vapor. The shape of the solid surface is considered as given.

The position vector $\mathbf{r}$ to C is represented as

$$\mathbf{r} = \mathbf{r}\,(u^1, u^2), \tag{1}$$

where u^1 and u^2 are the surface parameters. Of course, the relationship (1) is originally unknown. Here and later we will follow rather closely the notations of reference [3] and also employ some relevant formulas presented there.

The surface tension σ is not constant but depends in a prescribed way on the orientation of the interface and consequently on position. The equilibrium of the interface is then not possible without a distributed torque loading $\mathbf{m}$.

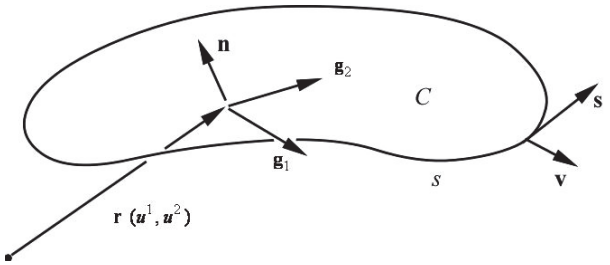

Figure 1. Interface surface C and some notations.

Virtual work

The determination of the position of the interface is based here in three dimensions similarly as in two dimensions on the principle of virtual work. This is the most useful approach for the discrete formulation. However, we must also show that the virtual work expressions used produce the correct differential equations. This has been done in [2] in two dimensions. Here in three dimensions we just give without details the appropriate virtual work equation and show how the jump conditions emerge from it.

The virtual work equation associated with interface can be represented as

$$\begin{aligned}\delta' W \equiv & -\int_{u^1,u^2} \sigma \left[(\mathbf{n}\times\mathbf{g}_1)\bullet\frac{\partial\delta\mathbf{r}}{\partial u^2} - (\mathbf{n}\times\mathbf{g}_2)\bullet\frac{\partial\delta\mathbf{r}}{\partial u^1}\right] \mathrm{d}u^1\mathrm{d}u^2 \\ & + \int_{u^1,u^2}\left(m_1\mathbf{n}\bullet\frac{\partial\delta\mathbf{r}}{\partial u^2} - m_2\mathbf{n}\bullet\frac{\partial\delta\mathbf{r}}{\partial u^1}\right)\mathrm{d}u^1\mathrm{d}u^2 \\ & + \int_{u^1,u^2}\sqrt{g}\,(p_1 - p_\mathrm{v})\,\mathbf{n}\bullet\delta\mathbf{r}\,\mathrm{d}u^1\mathrm{d}u^2 + bt = 0\,. \end{aligned} \tag{2}$$

Above, the first integral is the virtual work of the internal forces, the second integral is the external virtual work from the torque (moment per unit interface surface)

$$\mathbf{m} = m_\alpha \mathbf{g}^\alpha = m_1\mathbf{g}^1 + m_2\mathbf{g}^2\,, \tag{3}$$

and the third integral is the external virtual work from the pressure difference $p_1 - p_\mathrm{v}$. The term bt refers to the virtual work from the free boundary and is not given here in detail as it does not affect the jump conditions. Further explanations concerning equation (2) are as follows. The integrals are over the appropriate domain in the u^1u^2-plane. $\delta\mathbf{r}$ is the virtual movement from surface C to a varied surface C^*. $\mathbf{n}$ is the unit normal vector to C. $\mathbf{g}_1$ and $\mathbf{g}_2$ are the covariant and $\mathbf{g}^1$ and $\mathbf{g}^2$ the contravariant basis vectors and g is the discriminant of the covariant metric tensor.

In the terminology used especially in the finite element literature, e.g. [4], (2) is a weak formulation of the present problem. Based on the arbitrariness of the virtual movement $\delta\mathbf{r}$, we can deduce the so-called strong forms from it. Some development of the formula (1.13.61) in [5] gives the integration by parts formula

$$\int_{u^1,u^2} \mathbf{f}\bullet\frac{\partial \mathbf{h}}{\partial u^\alpha}\,\mathrm{d}u^1\mathrm{d}u^2 = -\int_{u^1,u^2} \frac{\partial \mathbf{f}}{\partial u^\alpha}\bullet\mathbf{h}\,\mathrm{d}u^1\mathrm{d}u^2 + \int_s \frac{v_\alpha}{\sqrt{g}}\mathbf{f}\bullet\mathbf{h}\,\mathrm{d}s\,. \tag{4}$$

It concerns two smooth vector functions $\mathbf{f}(u^1,u^2)$ and $\mathbf{h}(u^1,u^2)$. The line integral is over the boundary of *C*. Some additional notations are shown in Figure 1. The unit vector **s** is tangent to the boundary line. The unit vector **v** is in the tangent plane at the point in question and normal to the boundary line. It is represented as

$$\mathbf{v} = v_\alpha \mathbf{g}^\alpha = v_1\mathbf{g}^1 + v_2\mathbf{g}^2\,. \tag{5}$$

At the boundary, **n**, **v** and **s** form in this order a right-handed vector triad.

Jump conditions

For obtaining the strong forms corresponding to (2), the derivatives of $\delta\mathbf{r}$ with respect to u^1 and u^2 must be removed by integration by parts. This means manipulations with respect to the first and second integrals in (2). Integration by parts using formula (4) produces the line integral contribution

$$L \equiv -\int_s \frac{\sigma}{\sqrt{g}}\left[v_2\left(\mathbf{n}\times\mathbf{g}_1\right) - v_1\left(\mathbf{n}\times\mathbf{g}_2\right)\right]\bullet\delta\mathbf{r}\,\mathrm{d}s + \int_s \frac{1}{\sqrt{g}}\left[\left(v_2 m_1 - v_1 m_2\right)\mathbf{n}\right]\bullet\delta\mathbf{r}\,\mathrm{d}s\,. \tag{6}$$

We will not derive here all the strong forms following from (2). For our purpose it is enough to consider just (6) further. First,

$$\mathbf{n}\times\mathbf{g}_1 = \sqrt{g}\mathbf{g}^2, \quad \mathbf{n}\times\mathbf{g}_2 = -\sqrt{g}\mathbf{g}^1\,, \tag{7}$$

so

$$v_2\left(\mathbf{n}\times\mathbf{g}_1\right) - v_1\left(\mathbf{n}\times\mathbf{g}_2\right) = \sqrt{g}\left(v_2\mathbf{g}^2 + v_1\mathbf{g}^1\right) = \sqrt{g}\,\mathbf{v}\,. \tag{8}$$

Second,

$$\mathbf{s} = \mathbf{n}\times\mathbf{v} = \mathbf{n}\times\left(v_1\mathbf{g}^1 + v_2\mathbf{g}^2\right) = v_1\mathbf{n}\times\mathbf{g}^1 + v_2\mathbf{n}\times\mathbf{g}^2 = \frac{1}{\sqrt{g}}\left(v_1\mathbf{g}_2 - v_2\mathbf{g}_1\right) \tag{9}$$

and thus

$$\mathbf{m}\bullet\mathbf{s} = \left(m_1\mathbf{g}^1 + m_2\mathbf{g}^2\right)\bullet\frac{1}{\sqrt{g}}\left(v_1\mathbf{g}_2 - v_2\mathbf{g}_1\right) = \frac{1}{\sqrt{g}}\left(-m_1 v_2 + m_2 v_1\right). \tag{10}$$

When (7) and (10) are taken into account in (6), we arrive at the formula

$$L = -\int_s \left[\sigma\mathbf{v} + \left(\mathbf{m}\bullet\mathbf{s}\right)\mathbf{n}\right]\bullet\delta\mathbf{r}\,\mathrm{d}s\,. \tag{11}$$

The expression inside the brackets is physically rather transparent. Especially, the term $\mathbf{m}\bullet\mathbf{s}$ is the scalar component of the torque vector $\mathbf{m}$ along the boundary tangent direction.

The above result was obtained assuming that the surface C is smooth. Let us consider the case where there is an edge along a line c shown in Figure 2.

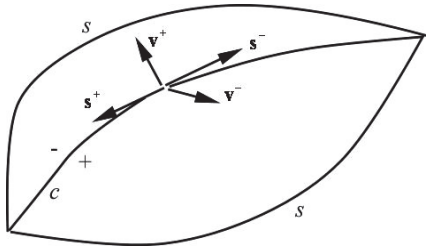

Figure 2. An edge.

Now the integration by parts manipulation must be performed in a piecewise manner. The values of the quantities on both sides of c are indicated by minus and plus superscripts as shown in the figure. (Here $\mathbf{s}^+ = -\mathbf{s}^-$. Vectors $\mathbf{n}^-$ and $\mathbf{n}^+$ are not drawn to keep the figure simple enough.) Two contributions like (11) appear along c and we obtain together the term

$$\int_c \left[-\sigma^- \mathbf{v}^- - \left(\mathbf{m}^- \bullet \mathbf{s}^- \right) \mathbf{n}^- - \sigma^+ \mathbf{v}^+ - \left(\mathbf{m}^+ \bullet \mathbf{s}^+ \right) \mathbf{n}^+ \right] \bullet \delta\mathbf{r} \, \mathrm{d}s \,. \tag{12}$$

As the virtual movement is arbitrary, the jump conditions on c become

$$-\sigma^- \mathbf{v}^- - \left(\mathbf{m}^- \bullet \mathbf{s}^- \right) \mathbf{n}^- - \sigma^+ \mathbf{v}^+ - \left(\mathbf{m}^+ \bullet \mathbf{s}^+ \right) \mathbf{n}^+ = \mathbf{0} \,. \tag{13}$$

Two dimensions

Figure 3 shows a cross-section of the interface at an angular point. Now $\mathbf{t}^-$ and $\mathbf{t}^+$ are the tangent unit vectors. The torque is here $\mathbf{m} = m\mathbf{j}$. Let $\mathbf{s}^- = \mathbf{j}$ and thus $\mathbf{s}^+ = -\mathbf{j}$. Then

$$\mathbf{m}^- \bullet \mathbf{s}^- = m^- \mathbf{j} \bullet \mathbf{j} = m^- , \quad \mathbf{m}^+ \bullet \mathbf{s}^+ = m^+ \mathbf{j} \bullet \left(-\mathbf{j} \right) = -m^+ . \tag{14}$$

Further, comparing Figures 2 and 3, $\mathbf{v}^- = \mathbf{t}^-$ and $\mathbf{v}^+ = -\mathbf{t}^+$. The jump conditions (13) obtain thus here finally the form

$$-\sigma^- \mathbf{t}^- - m^- \mathbf{n}^- + \sigma^+ \mathbf{t}^+ + m^+ \mathbf{n}^+ = \mathbf{0} \,. \tag{15}$$

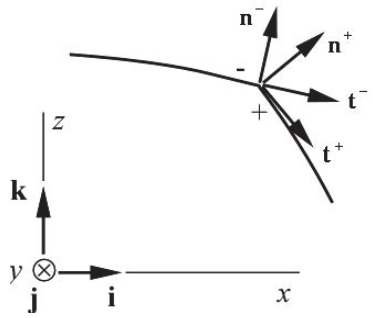

Figure 3. An angular point.

An example

In reference [6] a two-dimensional case with the surface tension expression

$$\sigma = \left(|\sin\psi| + |\cos\psi| + \frac{1}{2}\left|\sin\left(\frac{\pi}{4}+\psi\right)\right| + \frac{1}{2}\left|\cos\left(\frac{\pi}{4}+\psi\right)\right| \right)\sigma_0 \tag{16}$$

is considered. σ_0 is a reference surface tension value and ψ is the angle between **k** and **n**. The torque is obtained by, [2], $m = -\mathrm{d}\sigma / \mathrm{d}\psi$. Figure 4 (a) shows the corresponding solution. It has been obtained by the Wulff construction described in e.g. [7].

Let us consider the upper angular point in Figure 4 (a). We have

$$\mathbf{n}^- = \mathbf{k}, \quad \mathbf{t}^- = \mathbf{i}, \quad \mathbf{n}^+ = \frac{1}{\sqrt{2}}\mathbf{i} + \frac{1}{\sqrt{2}}\mathbf{k}, \quad \mathbf{t}^+ = \frac{1}{\sqrt{2}}\mathbf{i} - \frac{1}{\sqrt{2}}\mathbf{k}. \tag{17}$$

$$\sigma^- = \left(1 + \frac{1}{\sqrt{2}}\right)\sigma_0, \quad m^- = -\sigma_0, \quad \sigma^+ = \left(\frac{1}{2} + \sqrt{2}\right)\sigma_0, \quad m^+ = \frac{1}{2}\sigma_0. \tag{18}$$

When these values are substituted in (15), the equation is found to be satisfied.

The present problem has been solved also by the discrete approach described in [2]. The results of the calculations are shown in Figure 4 (b). The number of segments has been 14. The initial guess (the dashed line) for the interface is smooth. It is interesting to note that the solution process so to say automatically finds the angular solution in a rather satisfactory way.

Conclusions

The jump conditions in surface tension problems with distributed torque have been derived in the three-dimensional case. As a special case, the jump conditions are then obtained in the two-dimensional case. An example case in two dimensions with an exact solution is considered. It is found that the derived jump conditions are satisfied at the

angular points. It is also found that a discrete solution approach is able to mimic the angular behavior of the solution.

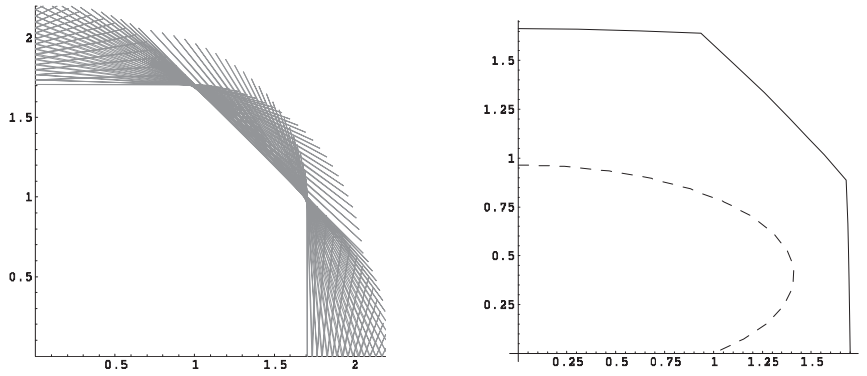

Figure 4. (a) Solution surface, (b) Discrete solution.

References

[1] M. Reivinen E.-M. Salonen, Surface tension problems, virtual work and free boundary. *Proceedings of the IX Finnish Mechanics Days*, Lappeenranta university of technology, June 13-14, 2006.

[2] M. Reivinen E.-M. Salonen, V.P. Vaskelainen, Surface tension problems with distributed torque. *Proceedings of the X Finnish Mechanics Days*, University of Jyväskylä, December 3-4, 2009.

[3] E. Kreyszig. *Differential Geometry*, Dover,1991.

[4] T. Belytschko, W. K. Liu, B.Moran, *Nonlinear Finite Elements for Continua and Structures*, Wiley, 2000.

[5] A. E. Green, W. Zerna, *Theoretical Elasticity*, second edition, Dover, 1968.

[6] H. Junes, *Liquid-Solid Interference of 3He Imaged Using a Fabry-Pérot Interferometer*, Master's Thesis, Helsinki University of Technology, 2004.

[7] P. Nozieres. Shape and growth of crystals, in *Solids far from equilibrium*, Cambridge University Press, edited by C. Godrèche, 1989.

Mika Reivinen, Eero-Matti Salonen
Aalto University, School of Engineering
P.O.Box 12100, FI-00076 Aalto, Finland
mika.reivinen@aalto.fi, eero-matti.salonen@aalto.fi

A nonlocal model of micro-displacement hysteresis for adhesive bonded frictional contact problems

A. Oinonen, G. Marquis

Summary. An approach to finite element analysis of cyclic micro-displacement responses of adhesive reinforced frictional contact is presented. The studied variational boundary value problem involves both the regularized friction and decohesion functionals. A nonlocal friction law is adapted to model deformation of contact asperities and a cohesive zone model governs the linear portion of the interfacial shear strength. Finite displacements are assumed and nonlinear finite elements are incorporated at the contact nodes. Experimental results are exploited for characterization of the suggested total response model.

Key words: cohesion, contact, finite element, friction, interface, variational method

Introduction

Recently, adhesive reinforced frictional interfaces (RFI) in steel have been focus of both experimental research and development of modelling [1-4]. There are many potential applications of RFI, e.g. shrink fits [1]. Hurme et al. [2] have used the specimen disks with ground contact surfaces in high strength steel (HSS) to experiment the shear strength properties of RFI under cyclic loading. In the recent studies [2-4], a fundamental testing method was used, i.e. the napkin ring test with an axial clamping property. See the previous work [1-4] for the special mechanical properties of RFI.

A review about the suggested models and computational aspects of interfacial friction has been published by Oden and Martins [5]. In addition, a nonlinear nonlocal model of micromechanical contact of non-bonded rough surfaces and physical arguments of friction have previously been studied by Oden and Pires [6]. Recently, Oinonen and Marquis [4] have applied the concept of cohesive zone (CZ) [7] to computational simulation of the growth of interfacial damage of RFI involving the significant axial clamping load. For cyclic loading conditions, the CZ contributes to the computed mechanical response of RFI at the nonlocal level of micro-deformation.

The objective of this study is to develop a finite element method (FEM) based analysis procedure for combined nonlocal micro-slip and cohesion of RFI under cyclic tangential loading. New details of interfacial modelling implemented in geometrically nonlinear FE theory [8] are introduced. The previously published cyclic responses [2] are characterized and a comparison of numerical results on the two-dimensional (2D) representative volume element (RVE) is made against the reference data. For simplicity, exclusively initial constant amplitude responses of the RFI are computed.

Principles of modeling

An assumption of finite sliding is made, i.e. large displacement FE analyses based on the updated Lagrangian formulation [8] are computed. Hence, the variational formulation corresponds to the Eulerian form of the principle of virtual velocities in engineering mechanics. The studied variational boundary value problem (BVP) involves both the regularized friction [6] and decohesion functionals, respectively. It is assumed that there are no body forces since FE analysis is quasi-static. The Newton-Raphson scheme is applied for the nonlinear solution of global equations.

For the setup of the RVE, four node quadrilateral plane stress continuum FE involving a reduced integration scheme, i.e. with the one point Gaussian quadrature, are used. In addition, nonlinear nodal FE are incorporated along the contact boundary $\partial\Omega^c$ of the RVE. A new nonlinear friction law is formulated and applied to model predominantly elastic deformation of contact asperities while the CZ model governs the linear portion of the interfacial tangential strength.

Nonlinear finite elements

For the updated Lagrangian approach [8], the discrete equations are formulated in the current configuration Ω_{k+1} which is assumed to be the new reference configuration Ω_k after update of variables at the total time $t = t + \Delta t$. The dependent variables are the Cauchy stress $\boldsymbol{\sigma}(\mathbf{x},t)$ and velocity $\mathbf{v}(\mathbf{x},t)$. We first introduce the symmetric strain rate tensor $\mathbf{D} = \left(\mathbf{L} + \mathbf{L}^{\mathrm{T}}\right)/2$ and spatial velocity field gradient $\mathbf{L} = \dot{\mathbf{F}}\mathbf{F}^{-1}$, where $\mathbf{F} = \partial\mathbf{x}/\partial\mathbf{X}$ is the deformation gradient; $\mathbf{x} \in \mathbf{R}^n$ is the vector of spatial coordinates and for material coordinates $\mathbf{X} \in \mathbf{R}^n$, respectively. The displacement field is defined by $\mathbf{u} = \mathbf{x}(\mathbf{X},t) - \mathbf{X}$.

The Hencky's strain is numerically computed from the spectral form of the logarithmic strain tensor [9]

$$\mathbf{E} = \sum_{i=1}^{n} \ln \lambda_i \, \mathbf{l}_i \otimes \mathbf{l}_i , \tag{1}$$

where λ_i are the principal stretches, $\mathbf{l}_i$ are the orthonormal eigenvectors of the positive definite Green's deformation tensor $\mathbf{U}^2 = \mathbf{F}^{\mathrm{T}}\mathbf{F}$ and $\mathbf{U}$ is the right stretch tensor. The material time derivative of $\mathbf{E}$ gives the strain rate

$$\dot{\mathbf{E}} = \sum_{i=1}^{n} \left(\dot{\lambda}_i \lambda_i^{-1} \mathbf{l}_i \otimes \mathbf{l}_i + \ln \lambda_i \left(\mathbf{l}_i \otimes \dot{\mathbf{l}}_i + \dot{\mathbf{l}}_i \otimes \mathbf{l}_i \right) \right). \tag{2}$$

A property of one-by-one mapping between $\dot{\mathbf{E}}$ and $\mathbf{D}$ is preserved since $\mathbf{D}$ is the stretching and $\dot{\mathbf{E}}$ is corotational, i.e. involving large displacements, $\mathbf{E}$ measured in Ω_{k+1} is infinitesimal. Importantly, $\mathbf{D}$ is the stress-strain pair of $\boldsymbol{\sigma}$, i.e. they conjugate in power [8,9], see Eq. (5).

Representative volume element

The macroscopically homogeneous result data is obtained based on a concept of the RVE [10]. Symmetry is exploited in the 2D RVE presented in Fig. 1. Thus, the elastic body $\Omega \subset \mathbf{R}^n$ ($n = 2$) is assumed to rest on the rigid foundation. The macroscopic stress and strain fields are obtained by the averages of the microscopic respective quantities

over the RVE with the volume $|\Omega_{k+1}|$. With reference to Fig. 1, the same assumption is applied to the uniform tractions $\mathbf{t}^n$.

$$\langle \boldsymbol{\sigma} \rangle = |\Omega_{k+1}|^{-1} \int_{\Omega_{k+1}} \boldsymbol{\sigma} d\Omega_{k+1}, \quad \langle \boldsymbol{\varepsilon} \rangle = |\Omega_{k+1}|^{-1} \int_{\Omega_{k+1}} \boldsymbol{\varepsilon} d\Omega_{k+1}, \quad \langle \mathbf{t}^n \rangle = |\partial\Omega^c_{k+1}|^{-1} \int_{\partial\Omega^c_{k+1}} \mathbf{t}^n d\partial\Omega^c_{k+1} \tag{3}$$

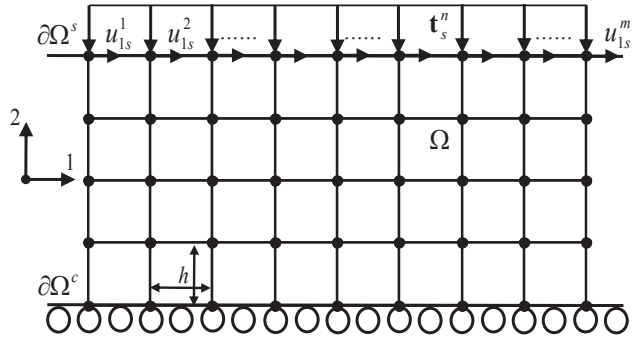

Figure 1. RVE of the elastic block $\Omega \subset \mathbf{R}^2$ with the frictional cohesive contact resting on the rigid foundation. The element size is h = 0.25 mm; the size of the RVE is then 2 x 1 mm. The uniform loading $\mathbf{t}^n_s$ and horizontal nodal displacements u^i_{1s} are applied on $\partial\Omega^s$, i = 1, 2,...., 9.

Variational formulation

The equilibrium equation of the BVP $\Omega \subset \mathbf{R}^2$ involving the boundary conditions (BC) of the regularized friction problem shown in Fig. 1 is defined as

$$\nabla \cdot \boldsymbol{\sigma} = 0, \qquad \forall \mathbf{x} \in \Omega \tag{4.1}$$

$$\boldsymbol{\sigma}\mathbf{n} = \mathbf{t}^n_s, \qquad \forall \mathbf{x} \in \partial\Omega^s \tag{4.2}$$

$$|\sigma_t| \mu(u_t) = \sigma_n, \qquad \forall \mathbf{x} \in \partial\Omega^c \tag{4.3}$$

$$u_2 = 0, \qquad \forall \mathbf{x} \in \partial\Omega^c \tag{4.4}$$

$$u_1 = f(\hat{\tau}), \qquad \forall \mathbf{x} \in \partial\Omega^s,\ \hat{\tau} \in [-1,1],\ \hat{\tau}_0 = 0, \tag{4.5}$$

where $f(\hat{\tau}) = u_a \hat{\tau}$ is the linear amplitude function of the horizontal displacement BC; Eq. (4.4) defines the symmetry BC. In Eq. (4.3), μ is the coefficient of friction.

The variational formulation is applied since the differential formulation of the equilibrium Eq. (4.1) is difficult to solve. In the updated Lagrangian form [8], the principle of virtual velocities gives the variational equality

$$\int_{\Omega_{k+1}} \boldsymbol{\sigma} : \delta\dot{\mathbf{E}} d\Omega_{k+1} = \int_{\partial\Omega^s_{k+1}} \mathbf{t}^n_s \cdot \delta\mathbf{v} d\partial\Omega^s_{k+1} + \int_{\partial\Omega^c_{k+1}} \mathbf{t}^t_f \cdot \delta\mathbf{v} d\partial\Omega^c_{k+1} + \int_{\partial\Omega^c_{k+1}} \mathbf{t}^t_c \cdot \delta\mathbf{v} d\partial\Omega^c_{k+1} + \int_{\partial\Omega^c_{k+1}} \mathbf{t}^n_c \cdot \delta\mathbf{v} d\partial\Omega^c_{k+1}, \tag{5}$$

where $\mathbf{t}^n_s$ is the applied surface traction loading; for $\partial\Omega^c$, $\mathbf{t}^t_f$ is the tangential traction due to friction, $\mathbf{t}^t_c$ is due to cohesion, respectively, and $\mathbf{t}^n_c$ is the prescribed normal contact traction. The last integral of Eq. (5) defines the virtual power of the normal contact.

Based on Eq. (5), the nonlocal problem [6] is to find **u** from the variational BVP

$$a(\mathbf{u}, \mathbf{v}) = f(\mathbf{v}) + j^\kappa_c(\mathbf{v}) + j^\kappa_f(\mathbf{v}), \quad \mathbf{u} \in \mathbf{V}, \quad \forall\, \mathbf{v} \in \mathbf{V}, \qquad j^\kappa_c + j^\kappa_f : \mathbf{V} \to \mathbf{R}, \tag{6}$$

where j_f^κ is the regularized friction functional and j_c^κ is due to cohesion, respectively. The linear functionals are defined as

$$f(\mathbf{v}) = \int_{\partial\Omega^s} \mathbf{t}_s^n \cdot \mathbf{v} ds + \int_{\partial\Omega^c} \mathbf{t}_c^n \cdot \mathbf{v} dc, \quad j_c^\kappa(\mathbf{v}) = \int_{\partial\Omega^c} \varphi_c(|\mathbf{v}_t|) dc, \quad j_f^\kappa(\mathbf{v}) = \int_{\partial\Omega^c} \varphi_f(|\mathbf{v}_t|) |\sigma_n| dc, \quad (7)$$

where σ_n is the prescribed normal stress, and both φ_f and φ_c are the mollifier functions. To this end, the initially solved σ_n used to form j_f^κ need not match the respective contact pressure which is obtained by solving the nonlinear nonlocal problem, Eq. (6), due to the iterative solution process involving a displacement residual based convergence criteria.

Nonlocal friction and cohesion laws

The frictional slip hardening law defines the first regularizing function of Eq. (6)

$$\varphi_f(u_t) = \mu_0 \left(2\coth 2\tanh\left(\left(u_{\max} + \dot{u}_t / |\dot{u}_t| u_t\right) / u_a\right) - 1\right), \quad u_t \in [0, u_a] \quad (8)$$

where μ_0 is the macroscopic friction coefficient, u_a is the amplitude of the displacement and $u_t = |\mathbf{u}_t|$ is the magnitude of the tangential displacements. The adapted linear CZ model defines the second regularizing function

$$\varphi_c(u_t) = \kappa_t u_t, \quad \kappa_t = t_a / u_a, \quad (9)$$

where t_a is the amplitude of the tangential traction stress due to cohesion and κ_t is stiffness, respectively.

The interface constant u_a was determined from the experimental data [2]. First, the constant μ_0 was determined by approximating the measured tangential shear stress quantity $\tau(0)$ and then t_a based on $\tau(u_a)$, respectively. The interface parameters are listed in Table 1 for four cases.

Table 1. Interface constants for the fine abraded epoxy adhesive RFI in HSS.

$\lvert\mathbf{t}_s^n\rvert$ (MPa)	50		150	
u_a (μm)	12.48	7.72	16.75	13.22
τ_a (MPa)	46.60	31.44	65.45	55.40
t_a (MPa)	36.1	30.5	54.8	54.0
μ_0	0.215	0.05	0.094	0.025

Results

Cyclic micro-displacements

In Figs. 2 and 3, the FE solutions $\langle \tau(u_h) \rangle, \forall \mathbf{x} \in \partial\Omega^s$ obtained for the representative example problem shown in Fig. 1 are presented for four cases involving $|\mathbf{t}_s^n| = \{50, 150\}$ MPa. A direct comparison to the corresponding reference results [2] can be done from Figs. 2 and 3.

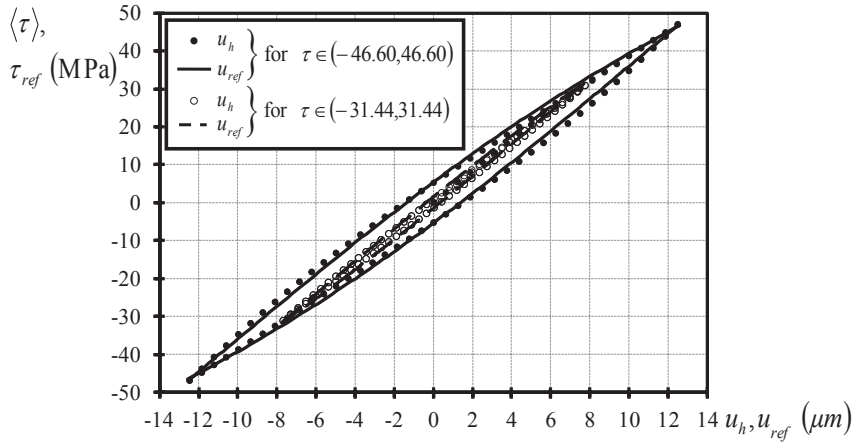

Figure 2. Tangential stress vs. relative micro-displacement for the case $\left|\mathbf{t}_s^n\right|$ = 50 MPa.

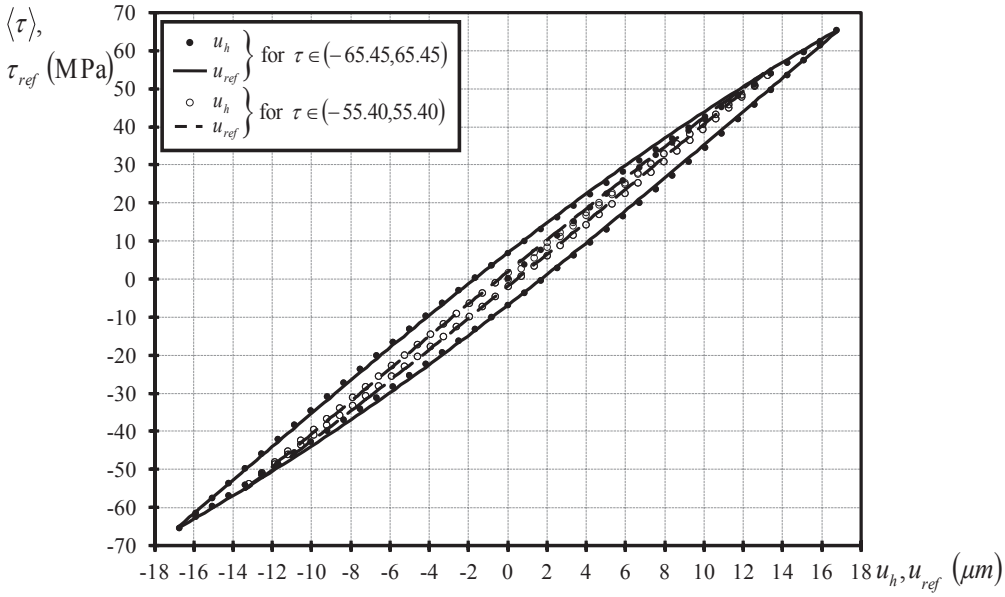

Figure 3. Tangential stress vs. relative micro-displacement for the case $\left|\mathbf{t}_s^n\right|$ = 150 MPa.

Discussion

Based on Figs. 2 and 3, $\langle\tau(u_h)\rangle$ is close to $(\tau(u))_{ref}$ for all computed cases. With reference to Table 1, μ_0 decreased for the cases with higher $\mathbf{t}_s^n$ and for smaller u_a. Thus, cohesion increasingly contributes to the mechanical responses of RFI if u_a is small and for high $\mathbf{t}_s^n$. Higher $\mathbf{t}_s^n$ causes interfacial sticking which shows in the increased value of t_a. Numerical results on the RVE did not show any separation of $\partial\Omega^c$ from the contact.

Conclusions

The computational procedure for the mechanical response of RFI has been developed and implemented. A new friction law for RFI has been suggested. The selected numerical examples have been solved in the MATLAB environment. The main findings of this work are summarized as follows.

1. The nonlocal response due to the combined micro-slipping and cohesion of RFI can be characterized based on the principle of superposition.
2. For the prescribed displacement and stress amplitudes, a nonlinear portion of the micro-displacement hysteresis of RFI can be approximated by the hyperbolic functions and weighted by the macroscopic coefficient of friction.
3. The suggested new interface model involves only few constants.

References

[1] T. Sawa, M. Yoneno, Y. Motegi. Stress analysis and strength evaluation of bonded shrink fitted joints subjected to torsional loads. *J Adhes Sci Technol*, 15:23-42, 2001.

[2] S. Hurme, A. Oinonen, G. Marquis. Fatigue of bonded steel interfaces under cyclic shear loading and static normal stress. *Engng Fract Mech*, 78:1644-56, 2011.

[3] A. Oinonen, G. Marquis. Shear decohesion of clamped abraded steel interfaces reinforced with epoxy adhesive. *Int J Adhes Adhes*, 31:550-8, 2011.

[4] A. Oinonen, G. Marquis. A parametric shear damage evolution model for combined clamped and adhesively bonded interfaces. *Engng Fract Mech*, 78:163-74, 2011.

[5] J.T. Oden, J.A.C. Martins. Models and computational methods for dynamic friction phenomena. *Comput Methods Appl Mech Engng*, 52:527-634, 1985.

[6] J.T. Oden, E.B. Pires. Nonlocal and nonlinear friction laws and variational principles for contact problems in elasticity. *J Appl Mech*, 50:67-76, 1983.

[7] G.I. Barenblatt. The mathematical theory of equilibrium cracks in brittle failure. *Adv Appl Mech*, 7:55-129, 1962.

[8] H.D. Hibbitt, P.V. Marcal, J.R. Rice. A finite element formulation for problems of large strain and large displacement. *Int J Solids Struct*, 6:1069-86, 1970.

[9] H. Xiao, O.T. Bruhns, A. Meyers. Logarithmic strain, logarithmic spin and logarithmic rate. *Acta Mech*, 124:89-105, 1997.

[10] R. Hill. The elastic behaviour of a crystalline aggregate. *Proc Phys Soc A*, 65:349-54, 1952.

Ahti Oinonen, Gary Marquis
Aalto University School of Engineering, Department of Applied Mechanics
PL 14300, Puumiehenkuja 5 A, 00076 Aalto
ahti.oinonen@aalto.fi, gary.marquis@aalto.fi

Systemaattinen menettelytapa taivutetun ja väännetyn palkin jännitysten määrittämiseksi

Jukka Aalto ja Eero-Matti Salonen

Tiivistelmä. Artikkelissa esitetään klassisen palkkiteorian otaksumia täydentävä poikkileikkauksen käyristymisen tavanomaista tarkemmin huomioonottava lähestymistapa, jolla taivutetun ja väännetyn palkin eri jännitysresultanteista aiheutuvat jännityskomponentit voidaan määrittää yhtenäisellä tavalla.

Avainsanat: palkkiteoria, taivutus, vääntö, käyristymisfunktio, jännitysresultantit, jännityskomponentit, reuna-arvotehtävä, elementtimenetelmä

Taivutusjännitysten määrittäminen

Tarkastellaan suoran palkin taivutusta. Tehdään tarkasteltavan poikkileikkauksen ympäristössä paikallisesti seuraavat otaksumat: Palkin akselin aksiaalinen siirtymä $u(x)$ on lineaarinen ja sen poikittaiset siirtymät $v(x)$ ja $w(x)$ (taipumat) kuubisia koordinaatin x funktioita. Yleisen pisteen aksiaalinen siirtymä on muotoa

$$\mathrm{u}(x,y,z) = u(x) - v'(x)y - w'(x)z - v'''\Psi_v(y,z) - w'''\Psi_w(y,z), \qquad (1)$$

missä Ψ_v ja Ψ_w ovat käyristymisfunktiot ja yleisen pisteen poikittaiset siirtymät ovat

$$\mathrm{v}(x,y,z) = v(x), \quad \mathrm{w}(x,y,z) = w(x). \qquad (2)$$

Lisäksi tehdään jännityksiä koskevat otaksumat $\sigma_y = \sigma_z = \tau_{yz} = 0$. Lähtien näistä otaksumista ja käyttäen hyväksi lineaarisesti kimmoisen, isotrooppisen aineen matemaattisen kimmoteorian yhtälöitä voidaan johtaa [1] seuraavassa esitettävät tulokset.

Reuna-arvotehtävät poikkileikkauksen käyristymisfunktioiden $\Psi_v(y,z)$ ja $\Psi_w(y,z)$ määrittämiseksi ovat

$$\begin{aligned} &\frac{\partial}{\partial y}\left(G\frac{\partial \Psi_v}{\partial y}\right) + \frac{\partial}{\partial z}\left(G\frac{\partial \Psi_v}{\partial z}\right) + Ey = 0 \ A:\text{ssa}, \quad n_y\frac{\partial \Psi_v}{\partial y} + n_z\frac{\partial \Psi_v}{\partial z} = 0 \ s:\text{llä}, \\ &\frac{\partial}{\partial y}\left(G\frac{\partial \Psi_w}{\partial y}\right) + \frac{\partial}{\partial z}\left(G\frac{\partial \Psi_w}{\partial z}\right) + Ez = 0 \ A:\text{ssa}, \quad n_y\frac{\partial \Psi_w}{\partial y} + n_z\frac{\partial \Psi_w}{\partial z} = 0 \ s:\text{llä}, \end{aligned} \qquad (3)$$

missä A on poikkipinnan alue, s sen reuna sekä n_y ja n_z ovat reunan yksikkönormaalivektorin komponentit. Puhtaan taivutuksen ehdosta $N = 0$ seuraa lisäyhtälöt

$$\int_A \Psi_v dA = 0, \quad \int_A \Psi_w dA = 0, \qquad (4)$$

jotka huomioiden funktiolle $\Psi_v(y,z)$ ja $\Psi_w(y,z)$ saadaan yksikäsitteiset ratkaisut.

Kun poikkileikkauksen jännitysresultantit normaalivoima N, leikkausvoimat Q_y ja Q_z sekä taivutusmomentit M_y ja M_z tunnetaan, saadaan jännityskomponentit $\sigma_x(y,z)$, $\tau_{xy}(y,z)$ ja $\tau_{xz}(y,z)$ lausekkeista

$$\sigma_x = E[\frac{N}{EA} + \frac{EI_y M_z - EI_{yz} M_y}{EI_y EI_z - (EI_{yz})^2} y + \frac{EI_z M_y - EI_{yz} M_z}{EI_y EI_z - (EI_{yz})^2} z],$$
$$\tau_{xy} = G[\frac{EI_y Q_y - EI_{yz} Q_z}{EI_y EI_z - (EI_{yz})^2} \frac{\partial \Psi_v}{\partial y} + \frac{EI_z Q_z - EI_{yz} Q_y}{EI_y EI_z - (EI_{yz})^2} \frac{\partial \Psi_w}{\partial y}], \quad (5)$$
$$\tau_{xz} = G[\frac{EI_y Q_y - EI_{yz} Q_z}{EI_y EI_z - (EI_{yz})^2} \frac{\partial \Psi_v}{\partial z} + \frac{EI_z Q_z - EI_{yz} Q_y}{EI_y EI_z - (EI_{yz})^2} \frac{\partial \Psi_w}{\partial z}].$$

Tässä EA on poikkileikkauksen aksiaalijäykkyys sekä EI_y, EI_z ja EI_{yz} ovat sen taivutusjäykkyydet ja tulojäykkyys. Kaavat (5) ovat voimassa sekä isotrooppiselle homogeeniselle että useammasta isotrooppisesta materiaalista koostuvalle palkille.

Taivutuksen jännitysresultantit ja leikkauskorjauskertoimet

Palkin taivutukseen liittyvät jännitysresultantit $N(x)$, $Q_y(x)$, $Q_z(x)$, $M_y(x)$ ja $M_z(x)$ voidaan määrittää käyttäen tavanomaisia rakenteiden mekaniikan menetelmiä. Yleensä palkin käyttäytymistä mallinnetaan käyttäen teknistä taivutusteoriaa (Bernoulli-Euler palkkiteoria), joka jättää leikkausmuodonmuutoksen vaikutuksen palkin siirtymiin huomiotta. Jos leikkausmuodonmuutoksen vaikutus on merkittävä, käytetään Timoshenkon palkkiteoriaa. Tässä yhteydessä täytyy edellä esillä olleiden poikkileikkaussuureiden lisäksi tuntea myös palkin leikkauskorjauskertoimet k_y, k_z, k_{yz} ja k_{zy}. Ne esiintyvät kaavoissa

$$Q_y = k_y GA\gamma_y + k_{yz} GA\gamma_z,$$
$$Q_z = k_{zy} GA\gamma_y + k_z GA\gamma_z, \quad (6)$$

missä γ_y ja γ_z ovat Timoshenkon palkkiteorian yhteydestä tutut liukumakulmat ja

$$GA = \int_A G dA. \quad (7)$$

Leikkauskorjauskertoimille voidaan johtaa lausekkeet vaatimalla, että leikkausjännitysten (5b) ja (5c) sekä leikkausvoimien tekemät virtuaaliset työt palkin pituutta kohti ovat vastaavasti yhtä suuret, eli

$$\int_A (\tau_{xy}\delta\gamma_{xy} + \tau_{xz}\delta\gamma_{xz}) dA = Q_y \delta\gamma_y + Q_z \delta\gamma_z. \quad (8)$$

Tulokseksi saadaan

$$\begin{bmatrix} k_y & k_{yz} \\ k_{zy} & k_z \end{bmatrix} = \frac{1}{GA} \begin{bmatrix} EI_z & EI_{yz} \\ EI_{yz} & EI_y \end{bmatrix} \begin{bmatrix} \int_A E\Psi_v y dA & \int_A E\Psi_v z dA \\ \int_A E\Psi_w y dA & \int_A E\Psi_w z dA \end{bmatrix}^{-1} \begin{bmatrix} EI_z & EI_{yz} \\ EI_{yz} & EI_y \end{bmatrix}, \quad (9)$$

missä $k_{zy} = k_{yz}$.

Vääntöjännitysten määrittäminen

Tarkastellaan suoran palkin vääntöä. Tehdään tarkasteltavan poikkileikkauksen ympäristössä paikallisesti seuraavat otaksumat: Palkin vääntökulma $\varphi(x)$ on kuubinen koordinaatin x funktio. Yleisen pisteen aksiaalinen siirtymä on muotoa

$$\mathrm{u}(x,y,z) = \varphi'(x)\bar{\Psi}(y,z) + \varphi'''\Phi(y,z), \tag{10}$$

missä $\bar{\Psi}$ ja Φ ovat käyristymisfunktiot. Lisäksi otaksutaan, että poikkileikkaus kiertyy vääntökeskiön T ympäri kuten jäykkä kappale, joten yleisen pisteen poikittaiset siirtymät ovat

$$\mathrm{v}(x,y,z) = -\varphi(x)(z - z_{\mathrm{T}}), \quad \mathrm{w}(x,y,z) = \varphi(x)(y - y_{\mathrm{T}}), \tag{11}$$

missä y_{T} ja z_{T} ovat vääntökeskiön koordinaatit. Edelleen tehdään jännitysotaksumat $\sigma_y = \sigma_z = \tau_{yz} = 0$. Käyristymisfunktio $\bar{\Psi}$ on jatkon kannalta tarkoituksenmukaista esittää vaihtoehtoisessa muodossa

$$\bar{\Psi}(y,z) = \Psi(y,z) + \Delta\Psi_0 - z_{\mathrm{T}}y + y_{\mathrm{T}}z, \tag{12}$$

missä $\Psi(y,z)$ on uusi käyristymisfunktio ja $\Delta\Psi_0$ on vakio. Lähtien näistä otaksumista ja käyttäen hyväksi lineaarisesti kimmoisen, isotrooppisen aineen matemaattisen kimmoteorian yhtälöitä, voidaan johtaa [2] seuraavassa esitettävät tulokset.

Reuna-arvotehtävät poikkileikkauksen käyristymisfunktioiden $\Psi(y,z)$ ja $\Phi(y,z)$ määrittämiseksi ovat

$$\begin{aligned}
&\frac{\partial}{\partial y}\left(G\frac{\partial\Psi}{\partial y}\right) + \frac{\partial}{\partial z}\left(G\frac{\partial\Psi}{\partial z}\right) + z\frac{\partial G}{\partial y} - y\frac{\partial G}{\partial z} = 0 \ A:\text{ssa}, \quad n_y\frac{\partial\Psi}{\partial y} + n_z\frac{\partial\Psi}{\partial z} = -n_y z + n_z y \ \ s:\text{llä},\\
&\frac{\partial}{\partial y}\left(G\frac{\partial\Phi}{\partial y}\right) + \frac{\partial}{\partial z}\left(G\frac{\partial\Phi}{\partial z}\right) + E\bar{\Psi} = 0 \ A:\text{ssa}, \qquad n_y\frac{\partial\Phi}{\partial y} + n_z\frac{\partial\Phi}{\partial z} = 0 \qquad s:\text{llä}.
\end{aligned} \tag{13}$$

Puhtaan väännön ehdosta $N = 0$ seuraa lisäyhtälöt

$$\int_A \Psi dA = 0, \quad \int_A \Phi dA = 0 \tag{14}$$

jotka huomioiden funktioille $\Psi(y,z)$ ja $\Phi(y,z)$ saadaan yksikäsitteiset ratkaisut.

Kun poikkileikkauksen jännitysresultantit, Saint-Venantin vääntömomentti T, bimomentti B ja sen derivaatta B' tunnetaan, saadaan jännityskomponentit $\sigma_x(y,z)$, $\tau_{xy}(y,z)$ ja $\tau_{xz}(y,z)$ lausekkeista

$$\begin{aligned}
&\sigma_x = -E\frac{B}{EI_\psi}\bar{\Psi},\\
&\tau_{xy} = G\left[\frac{T}{GJ}\left(\frac{\partial\Psi}{\partial y} - z\right) - \frac{B'}{EI_\psi}\frac{\partial\Phi}{\partial y}\right], \quad \tau_{xz} = G\left[\frac{T}{GJ}\left(\frac{\partial\Psi}{\partial z} + y\right) - \frac{B'}{EI_\psi}\frac{\partial\Phi}{\partial z}\right].
\end{aligned} \tag{15}$$

Tässä

$$GJ = \int_A G\left[-\left(\frac{\partial\Psi}{\partial y} - z\right)z + \left(\frac{\partial\Psi}{\partial z} + y\right)y\right]dA, \quad EI_\Psi = \int_A E\bar{\Psi}^2 dA \tag{16}$$

ovat poikkileikkauksen vääntöjäykkyys ja käyristymisjäykkyys. Kaavat (15) ovat voimassa sekä isotrooppiselle homogeeniselle että useammasta isotrooppisesta materiaalista koostuvalle palkille.

Vääntökeskiön koordinaatit ja väännön jännitysresultantit

Poikkileikkauksen vääntötehtävä voidaan nyt ratkaista siten, että ensin määritetään käyristymisfunktio Ψ probleeman (13a) ratkaisuna ja sitten käyristymisfunktio Φ probleeman (13b) ratkaisuna. Ennen jälkimmäisen tehtävän ratkaisemista täytyy käyristymisfunktio $\bar{\Psi}$ määrittää kaavalla (12), jossa esiintyy vakio $\Delta\Psi_0$ ja vääntökeskiön koordinaatit y_T and z_T. Käyttämällä hyväksi puhtaan väännön ehtoja $N=0$, $M_y=0$ and $M_z=0$ niille saadaan

$$\Delta\Psi_0=-\frac{ES_\Psi}{EA},\quad y_\mathrm{T}=-\frac{EI_zEI_{z\Psi}-EI_{yz}EI_{y\Psi}}{EI_yEI_z-EI_{yz}^2},\quad z_\mathrm{T}=\frac{EI_yEI_{y\Psi}-EI_{yz}EI_{z\Psi}}{EI_yEI_z-EI_{yz}^2}. \tag{17}$$

missä

$$ES_\Psi=\int_A E\Psi dA,\quad EI_{y\Psi}=\int_A Ey\Psi dA,\quad EI_{z\Psi}=\int_A Ez\Psi dA. \tag{18}$$

Palkin vääntöön liittyvien jännitysresultanttien $T(x)$, $B(x)$ ja $B'(x)$ määrittäminen tapahtuu avointen ohutseinämäisten palkkien osittain estetyn väännön vääntökulman differentiaaliyhtälöä soveltamalla. Siinä esiintyvät suureet GJ ja EI_Ψ saadaan kaavoista (16).

Esimerkki

Tarkastellaan kuvan 1a päistään haarukkalaakeroitua, keskipisteestään pistekuorman F kuormittamaa ja kahdesta materiaalista koostuvaa palkkia. Koska pistekuorma F sijaitsee etäisyydellä e_T vääntökeskiöstä T (kuva 1b), kohdistuu palkkiin myös sen keskipisteessä vaikuttava vääntävä pistemomentti $-F\cdot e_\mathrm{T}$.

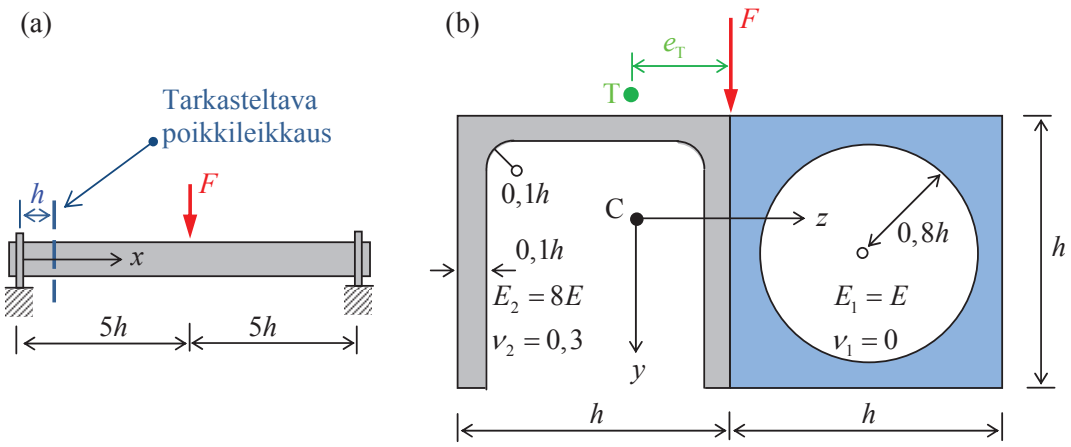

Kuva 1. (a) Keskipisteestään pistekuorman kuormittama päistään haarukkalaakeroitu palkki ja (b) sen kahdesta materiaalista koostuva poikkileikkaus.

Poikkileikkausanalyysi suoritettiin tässä elementtimenetelmällä lineaarisia kolmioelementtejä käyttäen. Sen tuloksena saatiin poikkileikkauksen taivutukseen liittyville jäykkyyksille $EA \approx 2,777Eh^2$, $EI_y \approx 0,8375Eh^4$, $EI_z \approx 0,2993Eh^4$, $EI_{yz} \approx 0,0543Eh^4$ ja $GA \approx 1,126Eh^2$ sekä leikkauskorjauskertoimille $k_y = 0,5447$, $k_z \approx 0,3235$ ja $k_{yz} \approx 0,0053$. Edelleen saatiin vääntöön liittyville jäykkyyksille $GJ \approx 0,07793Eh^4$ ja $EI_\Psi \approx 0,1352 \cdot Eh^4$ sekä vääntökeskiön asemalle $e_\mathrm{T} = 0,3278h$. Koska palkki on taivutuksen suhteen staattisesti määrätty, saatiin tarkasteltavan poikkileikkauksen taivutuksen jännitysresultanteille helposti $N = 0$, $Q_y = 0,5F$, $M_z = 0,5Fh$, $Q_z = 0$, $M_y = 0$. Palkin vääntötehtävä ratkaistiin analyyttisesti osittain estetyn väännön teoriaa soveltaen. Tulokseksi saatiin tarkasteltavan poikkileikkauksen väännön jännitysresultanteille $T \approx -0,1541Fh$, $B \approx -0,008300Fh^2$ ja $B' \approx -0,009837Fh$. Kuvissa 2 ja 3 on esitetty sekä (a) taivutuksesta että (b) väännöstä aiheutuvat normaalijännityksen σ_x ja leikkausjännityksen itseisarvon $\tau = \sqrt{\tau_{xy}^2 + \tau_{xz}^2}$ jakaumat tarkasteltavassa poikkileikkauksessa.

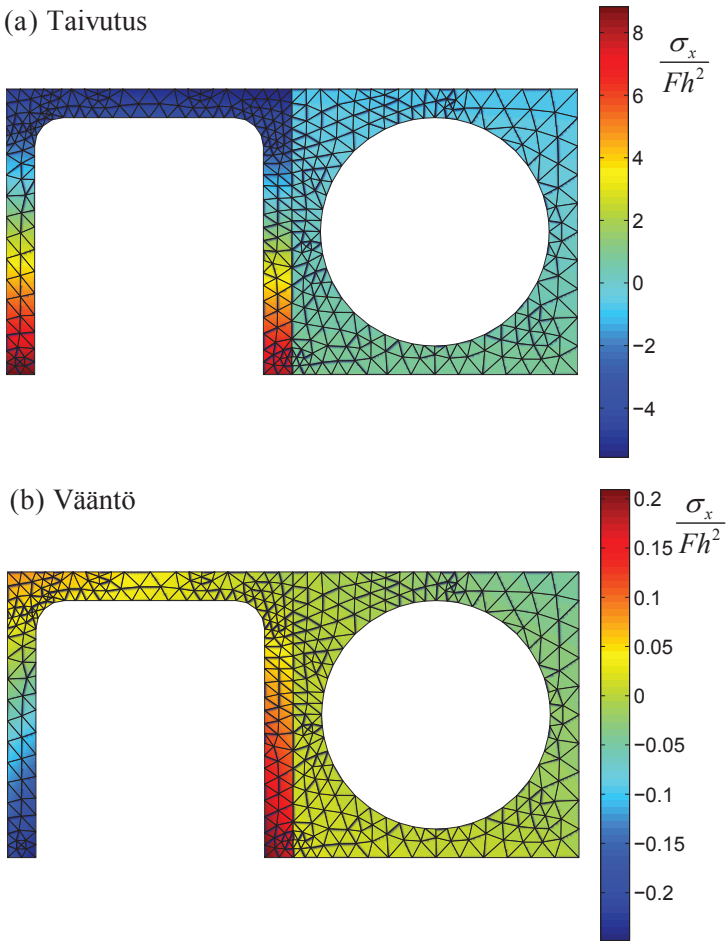

Kuva 2. (a) Taivutuksesta ja (b) väännöstä syntyvä normaalijännitys

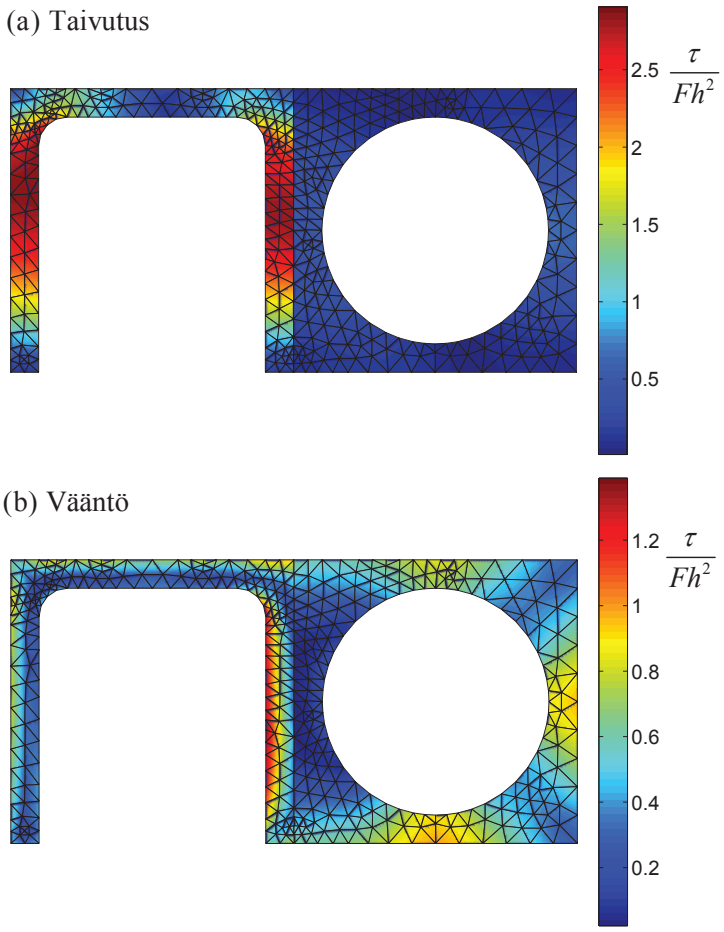

Kuva 3. (a) Taivutuksesta ja (b) väännöstä syntyvä leikkausjännitys

Johtopäätökset

Artikkelissa on esitetty teoria, jonka avulla taivutetun ja väännetyn palkin jännitystila voidaan määrittää systemaattisesti ja tarkasti. Oleellisena osana tätä teoriaa on poikkileikkaukseen liittyvien reuna-arvotehtävien mukaantulo. Nykyaikaisten tehokkaiden elementtimenetelmäohjelmistojen johdosta nämä lisätehtävät eivät kuitenkaan aiheuta käytännön ongelmia.

Viitteet

[1] J. Aalto, R. Syrjä ja C. Ribas, “Accurate stresses for homogeneous and composite beams”, Proceedings of the Eleventh International Conference on Computational Structures Technology, B.H.V. Topping, (Editor), Civil-Comp Press, Stirlingshire, Scotland, 2012.

[2] J. Aalto ja R. Syrjä, “A unified solution attempt for the torsion problem”, Proceedings of the 24th Nordic Seminar on Computational Mechanics, J. Freund and R. Kouhia (Eds.), Aalto University, 2011.

A novel approach for obtaining simulated stress history during multibody analysis

Tuomas Rantalainen and Aki Mikkola

Summary. Modern machine structures are often fabricated by welding. From a fatigue point of view, the structural details and especially, the welded details are the most prone to fatigue damage and failure. Even though, dynamic simulation of flexible bodies is already current method for analyzing structures, obtaining the stress history of a structural detail during dynamic simulation is a challenging task; especially when the detail has a complex geometry. In particular, analyzing the stress history of every structural detail within a single finite element model can be overwhelming since the amount of nodal degrees of freedom needed in the model may require an impractical amount of computational effort. The purpose of computer simulation is to reduce amount of prototypes and speed up the product development process. Also, to take operator influence into account, real time models, *i.e.* simplified and computationally efficient models are required. This in turn, requires stress computation to be efficient if it will be performed during dynamic simulation.

This paper combines suitable parts of multibody simulation and finite element method to form a new approach for efficient stress calculation. This paper proposes that, the problem of stress calculation during dynamic simulation can be greatly simplified by using a combination of Floating Frame of Reference Formulation with modal superposition and a sub-modeling approach. In practice, the approach can be used to efficiently generate the relevant fatigue assessment stress history for a structural detail during or after dynamic simulation. A novel approach is demonstrated with one numerical example.

Keywords: floating frame of reference, fatigue design, sub-modeling, flexible multibody dynamics

Introduction

In dynamically loaded components and structures, fatigue damage invariably initiates at local stress concentrations created by holes, welds, fillets, grooves, etc. Field measurements involving long sequences of stresses at structural discontinuities are expensive, time consuming and impossible for new product development when the machine or prototype does not exist. One method for obtaining stress history is the use of computer simulation based on multibody simulation approach [1, 2, 3]. In this approach, stress calculations are typically made after the dynamic simulation. In mobile machines, operators have a significant influence on the fatigue life of the machine. This must be accounted for in the design phase. A machine operator can theoretically be replaced by a real-time simulation. In this case the simulation, as well as stress calculations made during the simulation, must be computationally efficient.

Flexible multibody dynamic simulation based on the Floating Frame of Reference Formulation has great potential for obtaining stresses with sufficient accuracy. However, one of the largest challenges in this method is computational efficiency since dynamic simulation becomes impractical in case of large models. The Floating Frame of Reference

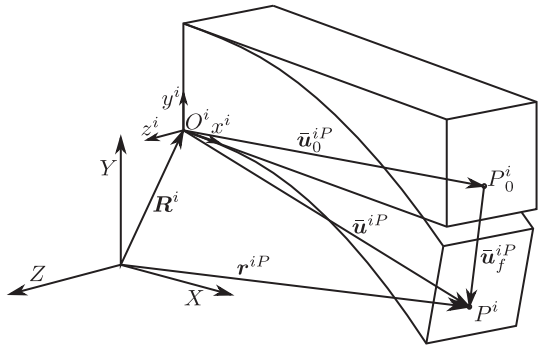

Figure 1. Position of particle P^i in a flexible body.

Formulation with modal reduction approach is poorly suited for examining local stresses. This is due to the fact that the deformation modes used in the floating frame of reference formulation typically describe deformation of the overall body where structural details are assumed to be negligible. Regardless of coordinate reduction, a problem remains that involves the need of a detailed finite element model for use as an initial model in the model reduction. In order to create such a model, locations of interest should be known *a priori*. This can be accomplished by separating global and local behavior with the use of sub-modeling. This assumption, in turn, gives the opportunity for describing global behavior with a simplified and reduced model.

Floating Frame of Reference

The Floating Frame of Reference Formulation is an often used approach for describing structural deformations in multibody applications. The formulation describes structural deformations by employing the local reference coordinate system. In this formulation, the dynamics of a flexible body can be considered to be generated by reference motion and deformation of the body. The interaction between reference motion and deformation can be accounted for with the description of inertia. [4]

In figure 1 particle P^i is depicted within the flexible body i. In a deformed configuration, the position of the particle in the local reference coordinate system of the body can be determined with vector $\bar{u}^{iP}$.

As body i is deformed (figure 1), the position of particle P^i changes according to the vector $\bar{\boldsymbol{u}}_f^{iP}$. The location of the particle in a global reference frame can be defined with the vector $\boldsymbol{r}^{iP}$ as follows:

$$\mathbf{r}^{iP} = \boldsymbol{R}^i + \mathbf{A}^i \left(\bar{\boldsymbol{u}}_0^{iP} + \bar{\boldsymbol{u}}_f^{iP} \right), \tag{1}$$

where $\boldsymbol{R}^i$ is translation of the local reference coordinate system of body i in the global coordinate system, and matrix $\mathbf{A}^i$ is the rotational matrix, which is expressed here in terms of four Euler parameters. In equation 1, $\bar{\boldsymbol{u}}_0^{iP}$ is the position vector of particle P^i in the local reference coordinate system for the undeformed configuration, and $\bar{\boldsymbol{u}}_f^{iP}$. In practical application, the vector $\bar{\boldsymbol{u}}_f^{iP}$ is described using the finite element method.

Using the model reduction method, the position of an arbitrary particle P^i in the global coordinate system can be expressed as.

$$\boldsymbol{r}^{iP} = \boldsymbol{R}^i + \mathbf{A}^i \left(\bar{\boldsymbol{u}}_0^{iP} + \boldsymbol{\Phi}_R^{iP} \boldsymbol{p}^i \right) \tag{2}$$

Equation 2 is determined using a collection of modes. The vector $\bar{\boldsymbol{u}}_0^{iP}$ and the modal matrix $\boldsymbol{\Phi}_R^{iP}$ are constant with time. Consequently, they only need to be calculated once, at the beginning of the simulation.

In Lagrangian way [4] equations of motion can be written as follows.

$$\mathbf{M}\ddot{\boldsymbol{q}} + \mathbf{C}_{\boldsymbol{q}}^{\mathrm{T}}\boldsymbol{\lambda} = \boldsymbol{Q}^e - \boldsymbol{Q}^v - \boldsymbol{Q}^f, \tag{3}$$

where $\mathbf{C}_{\boldsymbol{q}}$ is Jacobian matrix of constraint equations, $\mathbf{M}$ is the mass matrix, $\boldsymbol{Q}^e$ is the vector of generalized forces, $\boldsymbol{Q}^v$ is the quadratic velocity vector, $\boldsymbol{Q}^f$ is the vector of elastic forces, and $\boldsymbol{\lambda}$ is the vector of Lagrange multipliers.

Fatigue

Fatigue is a failure that occurs after cyclic loading, and it is a common cause of structural fracture. Fatigue damage is one of the most common faults in dynamically loaded structures. In principle, the entire development of fatigue damage can be described as follows: one or more cracks form in the material, and the cracks grow until fatigue failure takes place.

The fatigue life of a structure under dynamic load can be estimated by assuming it to have some initial amount of fatigue endurance and then assuming that one load cycle will result in fatigue damage of some amount. This idea is commonly known as Palmgren-Miner's rule. It was suggested that fatigue damage could be accumulated linearly for a certain amplitude value. Finally, when all fatigue endurance has been depleted, failure is expected. A large amount of fatigue test data can be found in the literature, and stress histories can be obtained experiments or by simulation.

Sub-modeling

Sub-modelling is an approach that is used together with the finite element method to combine two different finite element meshes. There are several reasons the sub-modelling approach is powerful. It can be used to connect finite models into a larger assembly. The approach does not require meshes to be similar and even element types can differ. Currently available methods do not require any coincident nodes. These beneficial features can be utilized to combine separately constructed models or refine the element mesh in a certain area without taking care of refining the mesh smoothly. In addition, a sub-model can be changed easily without modifying other parts of the model.

Coupling between the sub-model and the large-scale model is assumed to be one directional, *i.e.*, it is assumed that the behavior of the reduced model in dynamic simulation is not affected by the sub-model. That means, the large scale model is complemented with a sub-model of the desired detail and it does not affect the system's overall stiffness. This crucial simplification makes dynamic simulation and stress calculation independent from each other. Therefore, the computation can be straight forwardly parallelized. Displacement boundary conditions of the sub-model, however, are acquired from the large-scale model. In the proposed approach, during dynamic analysis the general behavior of the structure is calculated with a simplified model and details are examined as a separate problem. For assessing fatigue loads on a structure, this assumption is sufficient since any significant change in structural flexibility due to crack growth occurs only very late in the total life of a structure.

Table 1. Properties of the cantilever beam and the cross section.

property	value	unit
Height of the profile	0.1	m
Width of the profile	0.1	m
Thickness of the profile	0.01	m
Area of the profile	0.0036	m^2
Area moment of inertia	$0.492 \cdot 10^{-5}$	m^4
Shear correction factor	5/6	
Length of the cantilever beam	2.0	m
Elastic modulus	2.1	GPa
Poisson's ratio	0.3	

Stress in multibody dynamic simulation

A stress history from a multibody dynamics simulation can be used as initial data for component dimensioning. Furthermore, it can provide loading data for the analyst that is otherwise difficult to obtain. Finally, the stress history can be used as input for the fatigue analysis of the component. In such cases, one should make sure that simulated operations describe the operating conditions of the machine with sufficient accuracy. With simulation, it is difficult to describe the impact of statistical issues, such as component wear and operator usage habits, on component loading. On the other hand, simulation helps to understand the causes and effects related to loading. This allows the use of optimization routines in component dimensioning. Simulation and measurement on a real-life machine can thus be considered to support each other, and using them together can help to reach an optimal solution. For the proposed method, linear hot spot extrapolation [5] is selected, for both simplicity and robustness in use.

Numerical Example

As a numerical example, a cantilever beam with sinusoidal tip load is studied. The geometric values of the beam and cross sectional properties used in the numerical example are shown in table 1.

The beam model represents the center line of a structural component. The sub-model is attached to the interpolated locations of the reduced model via rigid and massless beams. Due to the use of rigid beam webs, the cross-section is assumed to remain planar at the boundary condition points. The effect of this assumption, with respect to stresses in notch, is negligible. In dynamic simulation, translational and rotational displacements are solved as boundary conditions for the sub-model. In general, sub-models are attached at arbitrary locations of the structural component, thus nodal displacement interpolation should be used. Note that only displacement boundary conditions are transferred to the sub-model. The coarse beam element model of the cantilever beam, shown in figure 2, is modeled with seven Timoshenko beams. Next, the beam model is reduced with the Craig-Bampton [6] method and structural flexibility is described with two deformation modes. The detailed finite element model is shown in figure 3 (left) and is used as reference. Furthermore, the finite element model contains a round attachment on the top surface in

the center of the beam. In case of the coarse beam model the center is described with a sub-model, shown in figure 3 (right).

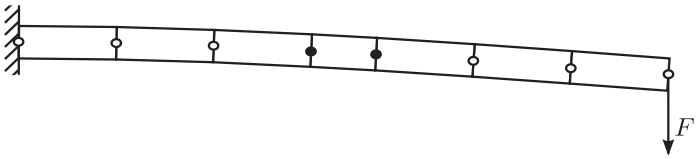

Figure 2. The coarse beam element model.

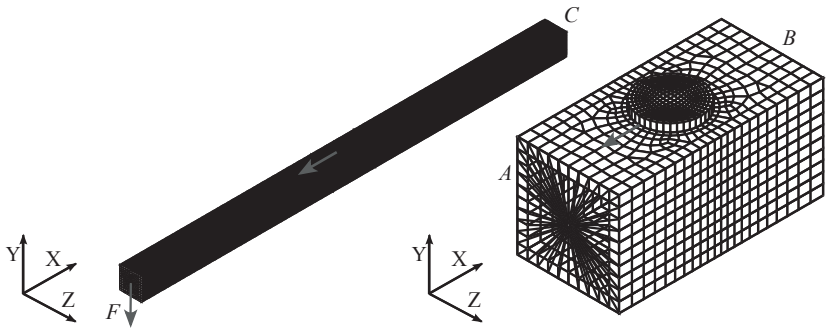

Figure 3. Detailed finite element model (left) and sub-model.

The finite element mesh of the sub-model has 2000 linear, brick elements and 400 rigid, massless beams. The detailed finite element model is modeled with 9000 solid elements. At end C, the model is fixed at all nodes. The black lines seen on side A, in figure 3 (right), represent rigid and massless beam webs and connect the cross section of the sub-model to the dynamical model. The use of rigid beam webs keeps the boundary cross section of the sub-model planar. This clearly simplifying assumption is made because in the beam model the cross-section is assumed to remains planar. In slender structures, cross sectional deformation due to axial forces caused by bending is insignificant.

A harmonic load with a frequency of $\omega = 3$ rad/s is applied to the cantilever beam shown figure 2. Parameters for the cantilever beam are shown in table 1. The cantilever beam is loaded on its free end with force F_h.

$$F_h = 10 \text{ kN} \cdot \sin(\omega t) \tag{4}$$

The detailed finite element in figure 3 (left) is loaded with the same force F_h as the reduced model in order to create a reference result. For fatigue assessment the hot spot or structural stress is often used [7]. Time history of hot spot stresses obtained using the detailed model and the sub-modeling approach are compared in figure 4. A constant time step of 10^{-4} s is used throughout the simulation.

It can be observed in figure 4 that the system reaches steady state rapidly. It is also seen that the reduced beam model with sub-modeling results in a structural stress approximately 6 % greater than with the reference model. This is due to an inaccurate

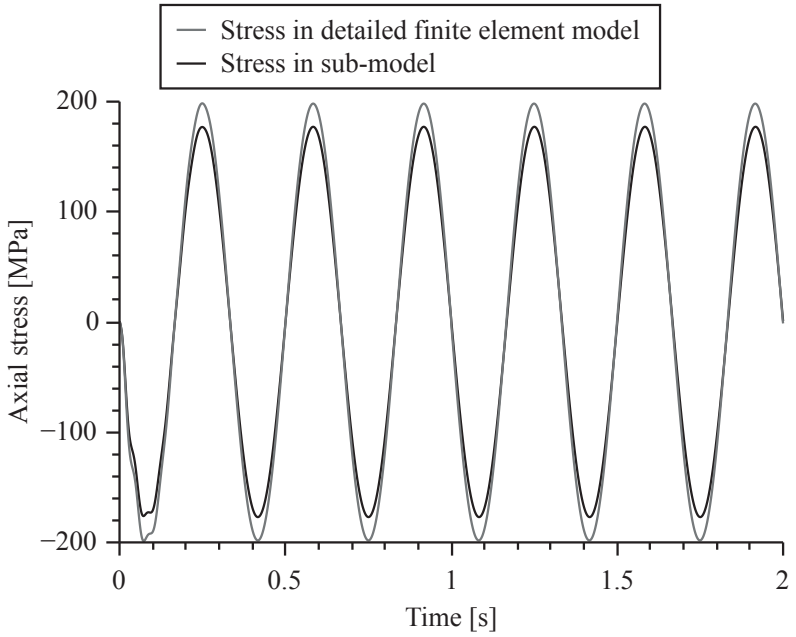

Figure 4. Stress comparison in harmonically loaded cantilever beam.

description of displacement field in the reduced model. Error can be diminished by using more deformation modes, with the cost of an increased computational burden.

Conclusions

In order to combine dynamic simulation and fatigue design this paper introduces a novel approach for efficiently obtaining stress history from dynamic simulation. In the proposed approach, the stress history for fatigue life estimation of an arbitrary structural discontinuity in a large-scale structure can be efficiently obtained in multibody simulation.

In the proposed approach the structure is modeled with structured elements (*i.e.* planes or beams) in order to get rid small structural details. After that model is further reduced using component mode synthesis [6] to minimize nodal degrees of freedom. This model is called as reduced model that is used to represent flexible body in multibody simulation. Small structural details are modeled separately and are attached to reduced model using suitable methods. In the presented example sub-model was attached to reduced model using rigid beam webs. Sub-model was analyzed quasi-statically within finite element codes using displacements, obtained from dynamic simulation, as boundary conditions. This analysis can be made during the dynamic simulation or in post-processing phase. Computations involving sub-modeling allow the fatigue assessment calculation to be separated from the dynamic simulation and structural details can be analyzed independently.

In future work the integration of fatigue analysis and produced stress history could be improved. The way how stress data is analyzed and compared to real fatigue test results differs from the stress results that can be straightforwardly obtained from dynamic simulation.

References

[1] H. Claus. A deformation approach to stress distribution in flexible multibody systems. *Multibody System Dynamics*, 6(2):143–161, 2001.

[2] C. Tobias and P. Eberhard. Stress recovery with Krylov-subspaces in reduced elastic multibody systems. *Multibody System Dynamics*, 25(4):377–393, 2011.

[3] P. Korkealaakso, A. Mikkola, and A. Rouvinen. Multi-body simulation approach for fault diagnosis of a reel. *Proceedings of the Institution of Mechanical Engineers, Part K: Journal of Multi-body Dynamics*, 220(1):9–19, 2006.

[4] A. A. Shabana. *Dynamics of Multibody Systems*. Cambridge University Press, Cambridge, 3rd edition, 2005.

[5] I. Poutiainen, P. Tanskanen, and G. Marquis. Finite element methods for structural hot spot stress determination - a comparison of procedures. *International Journal of Fatigue*, 26(11):1147–1157, 2004.

[6] R. R. Craig Jr. and M. C. C. Bampton. Coupling of substructures for dynamic analyses. *AIAA Journal*, 6(7):1313–1319, 1968.

[7] E. Niemi, W. Fricke, and S. J. Maddox. *Fatigue analysis of welded components: Designer's guide to the structural hot-spot stress approach*. Woodhead Publishing Ltd, Cambridge, 2006.

Tuomas Rantalainen, Aki Mikkola
Lappeenranta University of Technology
Laboratory of Machine Design
PL 20, 53851 Lappeenranta
tuomas.rantalainen@lut.fi, aki.mikkola@lut.fi

Fatigue behaviour of bonded high strength steel interfaces - The influence of clamping stress and surface roughness

Susanna Hurme, Gary Marquis

Summary. It is well known that the fatigue strength of a welded joint does not increase proportionally with steel strength. For this reason weld improvement technologies and alternative joining techniques for high strength steels are of great interest. Some studies have shown that hybrid joints, which combine mechanical fasteners and adhesives, have improved fatigue resistance as compared to welded joints. For reliable design, an in-depth understanding of the clamped and bonded interface under cyclic loading is needed. In this study, the napkin ring specimen geometry has been chosen for a series of constant amplitude fatigue tests. The test setup provides a bonded interface with well-defined normal and shear stress boundary conditions. This paper reports the fatigue strength values for interfaces under several different normal stress and surface roughness conditions.

Key words: hybrid joint, bonded joint, fatigue testing, interface fracture

Introduction

High strength steels (HSS) are increasingly used to provide light weight and improved strength in structures. However, the endurance of a HSS structure depends strongly on the welded joints, whose fatigue strength does not increase proportionally with the steel strength. Hybrid joints, where the good properties of adhesives and mechanical fasteners or spot welds are combined, provide potential joining alternatives for improved fatigue endurance in high strength steel structures. The current paper focuses on hybrid joints that combine adhesives and bolts. The research focuses solely on shear joints.

Even though the bonded/bolted joint has been shown to significantly improve the fatigue strength [1,2] of steel joints compared to welding, relevant data for design is still lacking. Most applications involve the use of the bonded/bolted hybrid joint in the fail-safe mode in which the bolts are designed to carry shear load only after the adhesive has failed [3]. To fully exploit the potential of the hybrid joint, where one method improves the performance of the other, in depth understanding of the behaviour of the clamped and bonded interface during quasi static as well as fatigue loading is needed.

There are no established test methods for bonded interfaces under static normal stress, and therefore one needs to be developed. The most common specimen geometry for measuring shear properties of adhesives is the thin-lap shear specimen (ASTM D1002). However, the specimen is not well suited for characterizing interfaces because of the stress concentrations and interactions of various stress components in the joint. Shear lag due to elastic deformations of the adherends causes stress concentrations at the ends of the overlap. Eccentricity in the lap joint causes bending, which introduces peel stresses at the ends of the overlap. The peel stresses can be reduced by using the double lap joint (ASTM D 3528) which has minimal load eccentricity and thus minimal

bending. Also the thick adherend specimen (ASTM D 5656) has significantly reduced peel stresses compared to the thin-lap joint specimen. Torsion methods such as napkin ring specimens [4] or butt-bonded hollow cylinders (EN 14869-1:2011) provide a practically uniform stress state in the adhesive layer. However, the testing equipment for torsion tests is rare in laboratories. Fatigue testing is usually done by the single lap shear test (ASTM D3166, EN ISO 9664:1995).

Previously the clamped and bonded interface under quasi static loading has been studied by Oinonen and Marquis [5,6]. They designed a specimen based on the classical napkin ring specimen [4] where two hollow cylinders are butt joined and loaded in torsion. The annular contact surface of the new specimen is narrow, which ensures virtually uniform shear stress distribution during torsion. The new napkin ring specimen was used for deriving cohesive zone model parameters and assessing the effect of surface roughness and clamping stress on the shear capacity of the interface [5,6]. The interface decohesion behaviour was successfully modelled using CZM.

The new napkin ring specimen has been used for fatigue tests by Hurme et al. [7, 8]. In [7] the fatigue behaviour of the bonded and clamped fine ground interface was reported. According to the results, fretting governs the fatigue endurance of such an interface. In [8] the effect of clamping stress on the fatigue strength of grit blasted interfaces was reported along with a qualitative analysis of the several damage phenomena in the clamped and bonded interface during fatigue loading. This paper adds to the results in [7] and [8] by considering three surface treatments and four clamping stress levels.

Experimental

Specimens

Test specimens were machined from HSS sheets (nominal yield strength 960 MPa) with thickness of 6 mm. Main dimensions of the specimens are shown in Fig. 1. The eight smaller holes visible in Fig. 1 were used for fixing the specimens in the testing machine. The 2 mm wide contact surface had one of the following surface finishes: grit blasted with medium grit aluminium silicate (R_a = 3.1 μm), fine ground (R_a = 0.4 μm) or coarse ground (R_a = 1.3 μm). A two component structural epoxy adhesive DP760 produced by 3M [9] was used for bonding the interfaces. Two specimen halves were glued together with the circular contact surface of one specimen opposing the contact surface of an identical specimen. During the assembly process, adhesive was applied to the contact surfaces of the specimens and clamping to the static pre-stress was immediately applied. The normal pre-stress was constant during the curing process and was not released until fatigue testing was complete.

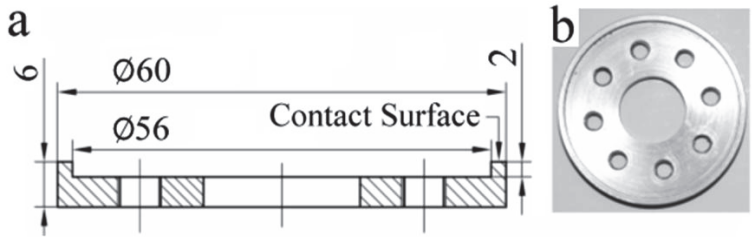

Figure 1. The napkin ring specimen and dimensions.

Laboratory testing procedure

Experiments were performed using a servo-hydraulic test machine which applied cyclic torsion across the circular glued interfaces. During testing, normal stress on the interfaces was maintained via a fine-threaded rod equipped with an axial load cell. Relative displacement (slippage) between the contact surfaces was measured by a high precision eddy current extensometer fixed to each side of the specimen pairs.

At least one static failure test was done for each specimen condition. The static tests were done following the procedure described in [5,6].

Constant amplitude fatigue testing was performed using load (torque) control with a fully reversed (R=-1) sinusoidal type signal at 13.5 Hz. Normal pre-stress levels were 4, 50, 100 and 150 MPa. The 4 MPa pre-stress was as close to zero as possible with the current test setup. Tests continued until fatigue failure occurred or until $2*10^6$ load cycles had been attained. Failure was defined as large (δ_a > 500 μm) relative displacement (slipping) of the specimen pairs measured by the eddy current extensometer. A more detailed description of the experimental setup can be found in [7].

Results

Shear fatigue strength

The shear fatigue strength, τ_f, corresponding to no failure at $N = 2*10^6$ cycles for each surface type / pre-stress combination was computed using the small sample staircase method [10-12]. The method provides an estimate of the mean fatigue strength, but no information about the scatter. This is a practical approach for a large number of test conditions and an exploratory test programme. An estimate of the mean fatigue strength can be calculated from a sequence of only 2-6 fatigue tests. Because some preliminary tests in the test programme were not originally planned for a staircase analysis, the artificial staircase method introduced by Nicholas [13] was used where needed. Shear fatigue strength values, τ_f, of each surface type / pre-stress combination are listed in Table 1. Some of the test series are still running when this paper is being written. Some series are not completed, but an initial estimate of the mean fatigue strength can be given (values in italics). For some series the stress amplitudes for non-failure response were so low that reliable tests could not be carried out with the current test setup (indicated by N/A).

Table 1. Mean shear fatigue strength, τ_f, obtained by the small sample staircase method.

q [MPa]	Grit blasted		Fine ground		Coarse ground	
	Bonded	Non-Bonded	Bonded	Non-Bonded	Bonded	Non-Bonded
4	21 MPa	-	*Running*	-	N/A	-
50	19 MPa	14 MPa	14 MPa	14 MPa	17 MPa	*Running*
100	32 MPa	34 MPa	49 MPa	42 MPa	37 MPa	32 MPa
150	62 MPa	66 MPa	*Running*	*68 MPa*	63 MPa	*58 MPa*

From table 1 it seems that no increase in the fatigue strength is observed upon applying the epoxy adhesive. For fine ground and coarse ground surface treatments a slight improvement in the fatigue strength of the bonded interfaces vs. non-bonded interfaces can be seen, but this falls within the accuracy of the results. This is a surprising result given that the static strength was found to increase nearly twofold by adding the adhesive [6]. It appears that the only improvement in the fatigue strength of the bonded interface comes from the very low clamping stress where the shear capacity of the non-bonded interface is inherently zero.

The fine ground surface roughness seems to yield the best fatigue strength under high clamping stress. This is in contradiction to the results from static tests, where the fine ground interface was weaker than the grit blasted interface [6]. Other than that, the three surface finishes seem to give very similar results for fatigue strength. However, there was an important difference in the failure of the low clamping stress (4 and 50 MPa) cases. The grit blasted specimen always failed cohesively, i.e. failure in the adhesive, whereas the coarse ground specimens failed in part cohesively and in part adhesively (failure in the interface between the adhesive and the steel). Adhesive failure should always be avoided in order to exploit the full strength of the adhesive. All specimens were treated identically before applying the adhesive. Therefore it can be suspected that the coarse ground interface is not suitable for the adhesive joint.

Failure mode

Two primary failure modes were identified in the test program: fretting fatigue and shear decohesion as evidenced by sudden relative slipping of the interfaces. With the higher pre-stresses (q = 100 MPa and q = 150 MPa) most of the failures were due to fretting fatigue for both bonded and non-bonded interfaces. For the lower pre-stresses (q = 4 MPa and q = 50 MPa) no fretting fatigue was observed. The bonded specimens with low pre-stress failed by shear decohesion and the non-bonded specimens with low pre-stress failed by progressive slipping.

Discussion

The unexpected result of this study was that adding the adhesive provides no improvement to the fatigue strength of the bonded and clamped interface. Explanation

to this lies in the micro-geometry of the interface. During the assembly when static normal stress is applied, some adhesive is left in the voids of the surface roughness while the metal asperities are brought to contact and deform plastically because of the high pressure. When shear stress is applied the contacting metal asperities resist slipping very efficiently. The stiffness of the adhesive (Young's modulus = 6 GPa) is small compared to the stiffness of the steel (Young's modulus = 210 GPa) and therefore with the small relative displacement amplitudes involved in fatigue loading, the adhesive has minimal effect on shear capacity. For large displacements (1 mm in static tests [5,6]) on the other hand, the adhesive has a significant role in carrying shear stress.

Considering the hybrid joint where both low and high clamping stresses exist at the interface depending on the distance from the bolt, the overall fatigue strength might be significantly improved by applying adhesive to the mildly clamped areas. If only the area under clamping is bonded, the expected fatigue strength should be identical to the fatigue strength of a non-bonded joint based on the results of this paper. Perhaps the best value for adding bolts to an adhesive joint is obtained if the bolts are positioned so that they minimize normal stresses that tend to open the adhesive interface. The next steps of this research program are to carry out fatigue tests on large scale joints and try to assess the fatigue strength of that joint based on the knowledge obtained from the napkin ring tests.

Conclusions

A series of constant amplitude fatigue tests have been done for bonded and non-bonded interfaces under four different static normal pre-stresses. The interfaces had the grit blasted, coarse ground or fine ground surface finish. The specimen geometry was similar to the napkin ring specimen, which assures uniform normal and shear stress conditions at the contact area. Fatigue strength values at $N = 2*10^6$ cycles for all static normal pre-stress / surface type combinations were determined by the small sample staircase method. The following conclusions can be drawn.

- The shear fatigue strength of the interfaces is not improved by the addition of epoxy adhesive. This is a surprising result given that a nearly twofold increase in strength was found by adding the adhesive during quasi-static loading [6].
- The failure mode with the higher clamping stresses (100 MPa and 150 MPa) was almost always fretting fatigue. No fretting fatigue was observed with the lower clamping stresses (4 MPa and 50 MPa) but instead all failures were due to shear decohesion and sudden slipping.

References

[1] Albrecht, P., Sahli, A.H. Fatigue strength of bolted and adhesive bonded structural steel joints. In: Potter J. M., (Ed.), *Fatigue in mechanically fastened composite and metallic joints*, ASTM STP 927, American Society for Testing and Materials, Philadelphia, 1986, pp. 72-94.

[2] Albrecht, P. Fatigue strength of adhesively bonded cover plates. *Journal of Structural Engineering*, 1987, Vol. 113, pp. 1236-1250.

[3] Weitzenböck, J.R., McGeorge, D. Science and Technology of Bolt-Adhesive Joints. In: da Silva, L.F.M., Pirondi, A., (Eds.), *Hybrid Adhesive Joints*. Springer-Verlag, Berlin Heidelberg. 2011. pp. 177-199.
[4] De Bruyne, N.A. The measurement of the strength of adhesive and cohesive joints. In: Weiss P, (Ed.), *Adhesion and Cohesion*. Proc Symp Adhes Cohes, GM Res Lab, Elsevier Publishing Company, Warren Michigan, 1962, pp. 47-64.
[5] Oinonen, A., Marquis, G. A parametric shear damage evolution model for combined clamped and adhesively bonded interfaces. *Engng Fract Mech*, 2011, Vol. 78, pp. 163-174.
[6] Oinonen, A., Marquis, G. Shear decohesion of clamped abraded steel interfaces reinforced with epoxy adhesive. *Int J Adhes Adhes*, 2011, Vol. 31, pp. 550-558.
[7] Hurme, S., Oinonen, A., Marquis, G. Fatigue of bonded steel interfaces under cyclic shear loading and static normal stress. *Engng Fract Mech*, 2011, Vol. 78, pp. 1644-1656
[8] Hurme, S., Marquis, G. The effect of clamping stress on the fatigue strength of bonded high strength steel interfaces. *(article in review)*
[9] 3M United Kingdom PLC. Scotch-Weld™ EPX™ Epoxy adhesive DP760 Product data sheet. 2001.
[10] Dixon, W. J., Mood, A. M. A method for obtaining and analyzing sensitivity data. *Journal of the American Statistical Association*, 1948, Vol. 43, pp. 109-126.
[11] Dixon, W. J. The up-and-down method for small samples. *Journal of the American Statistical Association*, 1965, Vol. 60, pp. 967-978.
[12] Little, R. E. The up-and-down method for small samples with extreme value response distributions. *Journal of the American Statistical Association*, 1974, Vol. 69, pp. 803-806.
[13] Nicholas, T. *High cycle fatigue*: A mechanics of materials perspective. Elsevier Ltd. 2006. pp. 105-106.

Susanna Hurme
Aalto University, Department of Applied Mechanics
Puumiehenkuja 5A, 00076 Aalto
susanna.hurme@aalto.fi

Gary Marquis
Aalto University, Department of Applied Mechanics
Puumiehenkuja 5A, 00076 Aalto
gary.marquis@aalto.fi

Fatigue Crack Growth of Arbitrary Planar Cracks Subjected to Non-Uniform Stress Fields

Pasi Lindroth, Gary Marquis, Grzegorz Glinka

Summary. Engineering components subjected to cyclic loads contain frequently imperfections which can be modeled as planar cracks. Cyclic loadings cause such cracks to grow and what may finally lead to component failure. Estimation of safe fatigue lives of mechanical components containing small flaws is rationally accomplished by fracture mechanics methods and the fatigue crack growth analysis. Fatigue crack growth models use the range and the maximum stress intensity factor to describe the severity of cyclic stresses at the crack tip. Unfortunately, determining the stress intensity factor is not trivial, especially if the stress field or the crack geometry is complex. Therefore the weight function method is often used to calculate the stress intensity factors.

Numerous different weight functions are available for different crack geometries. However, the most of the weight functions are valid only for one dimensional stress fields and specific crack geometries. Therefore, the general point load weight function has been developed. The general point load weight function is valid for arbitrary planar cracks subjected to two-dimensional stress field and, therefore, only one weight function is needed to analyze numerous crack geometry and loading configurations.

The fatigue crack growth is calculated by using a two-parameter fatigue crack growth model that is capable of predicting the effects of under- and overloads. This is accomplished by accounting for the residual stresses introduced by the cyclic plasticity around the crack tip. The plasticity effects are calculated accounting for the multiaxial stress state ahead of a moving crack tip. Therefore, the model is suitable for fatigue crack growth analysis induced by cyclic constant and variable amplitude loading processes.

Example of fatigue crack growth analyses and comparison with experimental data will be presented.

Key words: fatigue crack growth, fracture mechanics, variable amplitude

Introduction

Engineering materials and mechanical components frequently contain imperfection introduced during manufacturing processes or introduced during service, e.g. by fatigue. In most cases they appear as material discontinuities which can be modelled as planar cracks. Cyclic loading causes these cracks to grow and may lead ultimately to component failure. Estimation of the safe fatigue lives of mechanical components containing small flaws is rationally accomplished using a fracture mechanics method to asses fatigue crack growth.

The basic parameter used in such analyses is the stress intensity factor, K. Unfortunately, determining the stress intensity factor is not trivial in most practic1al engineering cases, especially when the stress field or the crack geometry is complex. Therefore a simplified crack geometry and stress field are usually assumed during fatigue analysis. After simplification, the stress intensity factor can be calculated based on handbook solutions or specific weight functions [1, 2]. However, simplification can lead to predictions of the growth of the cracks which are far from realistic and, therefore, methods to calculate the stress intensity factor which require far fewer simplifications have been developed.

The general point-load weight function, which can be used with arbitrary shaped cracks, is a powerful method for calculating stress intensity factors during fatigue crack growth analysis [3, 4]. The weight function method uses the stress field of the uncracked body and so that no stress field updates are needed as a crack advances [5, 6]. Hence, the stress intensity factor calculation is computationally efficient and very rapid in comparison to a fully FEA-based method.

In order to predict fatigue crack propagation rate, numerous empirical or semi-empirical equations have been proposed to relate fatigue crack growth rate data to the parameter ΔK. Among the proposed equations, the Paris-Erdogan relationship [7] is commonly accepted and used in practice for a wide range of mode I cracks. This relationship is given as

$$\frac{\mathrm{d}a}{\mathrm{d}N} = C(\Delta K_{appl})^m \tag{1}$$

where da/dN is the crack extension per cycle, ΔK is the stress intensity factor range and C and m are material constants.

Equation 1 excludes any information concerning the sequence of loading cycles. Especially for irregular load histories or load histories with large mean stress changes, load sequence can have a dramatic influence. Marquis [8] has presented a review of the most common variable amplitude crack growth prediction models.

In this paper, the general point-load weight function is combined with a crack tip plasticity based crack growth model proposed by Noroozi et al. [9]. The developed method was validated by comparing estimated fatigue lives to published experimental data. The validation showed that the combination of the general weight function and the advanced crack growth model is powerful tool to estimate the fatigue life of the complex cases.

General point load weight function

The weight function depends only on the geometry of the cracked body. Therefore, after the weight function is found, it can be used with any stress field. As mentioned, a significant advantage of the weight function is that the stress field of the uncracked body is used. For a 2D crack, the stress intensity factor is obtained by integrating the product of the weight function, $w(x, y)$, and the stress field of the uncracked body, $\sigma(x, y)$, over the crack area Ω_C.

$$K_A = \iint_{\Omega_C} \sigma(x, y) w_A(x, y)\, \mathrm{d}x\, \mathrm{d}y \tag{2}$$

The index A denotes the arbitrary point at the crack front Ω_C where the stress intensity factor is calculated.

Oore and Burns [3] proposed a general weight function for arbitrary shaped planar cracks based on their observation of stress intensity factor solutions of different crack geometries. The weight function depends on two parameter, the distance ρ between the load point $P(x_P, y_P)$ and the stress intensity factor point $A(x_A, y_A)$ and the line integral that includes the distance l from the load point $P(x_P, y_P)$ to each point of the crack front Ω_C.

$$w_A(x_P, y_P) = \frac{\sqrt{2}}{\pi\rho^2\sqrt{\oint_{\Omega_C} \frac{\mathrm{d}\Omega_C}{l^2}}} \tag{3}$$

The notation is illustrated in Fig 1. Glinka and Reinhardt [4] proposed simpler form of Eq. (3) by replacing the line integral by the length of the inverted crack contour, Γ_C. The new weight function also takes account the effect of the finite boundaries. This is done by including the length of the inverted external contour, Γ_B.

$$w_A(x_p, y_p) = \frac{\sqrt{2}}{\pi\rho^2}\frac{\sqrt{\Gamma_C + \Gamma_B}}{\Gamma_C} \tag{4}$$

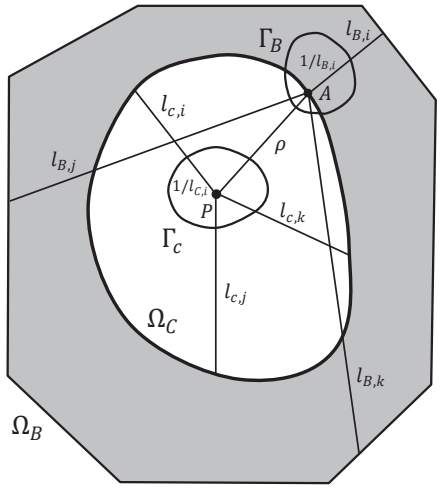

Figure 1. Notation for the general weight function for an arbitrary planar crack in a finite body.

Since the general weight function, $w_A(x, y)$, is known, Eq. (2) can be used to compute stress intensity factor for the arbitrary planar crack. Integrations were performed numerically which required that the problem is discretized. The crack front and the external boundary were described by using finite number of points and linear segments, Fig 2. The stress intensity factor is calculated at the middle of these segments. Jankowiak et al. [10] studied the influence of the angle γ between two adjoining segments for semi-elliptical cracks and concluded that angle should be at least 170°. Increasing the angle above 174° improves the accuracy only slightly but computation time increases significantly. This proposed limit of 170° may not always be practical for arbitrary cracks, e.g. for rectangular cracks. The crack area was divided into small rectangular or triangular regions and stress fields over these areas were replaced by the discrete point loads positioned at the middle of the areas.

A crack tip plasticity-based fatigue crack growth model

Noroozi et al. [9] developed a crack tip plasticity-based fatigue crack growth model to

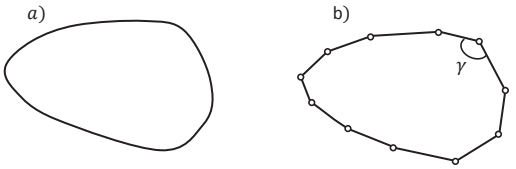

Figure 2. Continuous crack front, a), is replaced by using finite number of nodal points and linear segments, b).

include the effects of stress ratio and sequence effect during variable amplitude loading. Due to plasticity in front of the crack tip, blunting occurs and the crack tip remains open even when the crack faces are in contact. This is opposite to what is hypothesized in crack closure models [11]. This model has been previously verified [9, 12, 13] and could be used in the paper without further calibration. According to this model, the crack growth equation is:

$$\frac{\mathrm{d}a}{\mathrm{d}N} = C\left[(K_{max,tot})^p(\Delta K_{tot})^{1-p}\right]^m \tag{5}$$

The variables $(K_{max,tot})^p$ and $(\Delta K_{tot})^{1-p}$ include the effect of the residual stresses caused by the plastic deformation at the crack tip. That effect is included as a residual stress intensity factor, K_r.

$$\begin{array}{lcl} K_{max,tot} & = & K_{max} - K_r \\ \Delta K_{tot} & = & \Delta K - K_r \end{array} \tag{6}$$

In order to calculate K_r, the stress field around the crack tip must be known. The stress field can be calculated by assuming the blunt crack tip and using the Creager-Paris solution [14]. Noroozi et al. [9] proposed that the crack tip radius used to obtain stress field at the crack tip is a material constant, ρ^*. In order to determine ρ^* fatigue crack growth data is needed. The type of available data determines the method that can be used to estimate ρ^*. The best estimation for the ρ^* is obtained if several $\mathrm{d}a/\mathrm{d}N$ vs. ΔK curves with the different stress ratio R are available.

Stress intensity factor calculations and the Creager-Paris solutions are based on linear-elastic fracture mechanics. However, the actual elastic-plastic stress-strain history can be obtained from the linear-elastic solutions by using the Neuber rule [15]. This method is very time efficient because the calculations of complex elastic-plastic cracked body boundary problem for each load/stress reversal is avoided. More details to obtain ρ^*, calculate the residual stress field and the residual stress intensity factor are given in elsewhere [9, 12, 13].

Validation

The numerical crack growth simulation programme has been validated based on comparison with experimental result for a valve spring used in engines. The spring is developed for a very long fatigue life and typically failure occurs because of subsurface fatigue cracks that initiate from subsurface defects. Fracture surface was inspected and initial flaw size was 20 μm x 30 μm. The initial flaw was located at the depth of 250 μm below the surface. Diameter of the spring wire was 4 mm.

The load fluctuated from 298 N to 791 N with constant amplitude. Thus the load ratio was $R = 0.38$. The applied load induced internal torsion and direct shear. Therefore, the stress distribution over the cross-section of the spring wire was non-uniform. The principal normal stresses were found on the plane that was oriented in 45^o angle with respect to the wire longitudinal axis , Fig. 3.

The initial crack was modelled as an ellipse and fatigue crack growth was computed until the crack front reached the free surface, Fig 4. Based on the simulation, 59 million cycles were needed in order to break through the free surface. During the experiment, the spring failed after 78 million cycles.

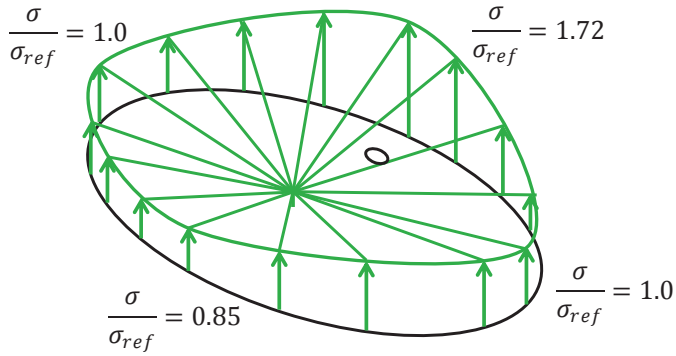

Figure 3. Stress field over the cross-section of the spring wire. $\sigma_{ref} = 582$ MPa (max).

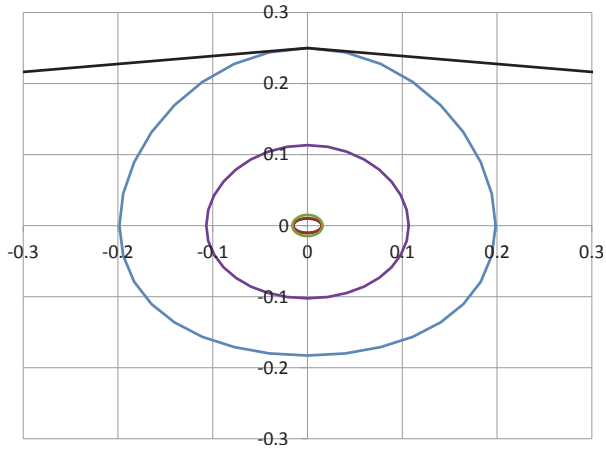

Figure 4. Simulated fatigue crack growth.

Conclusion

The fatigue crack growth model for arbitrary planar cracks has been proposed. Proposed model is able to estimate fatigue crack growth of surface, edge and embedded cracks in

both infinite and (semi-)finite bodies under complex stress field. Generality is obtained by using the general weight function for the stress intensity factor calculations.

In the proposed model, fatigue crack growth rate is calculated based on the crack tip plasticity model. The crack growth model includes the effects of stress ratio and sequence effect during variable amplitude loading. The crack growth model is based on an assumption that the radius of the crack tip is a material parameter.

The proposed model was verified by simulating fatigue crack growth and comparing results to the experimental crack growth data. The comparison resulted in confirming good accuracy of the proposed model.

Acknowledgements

Partial funding for this work was granted by the Finnish Funding Agency for Technology (TEKES). Partner organizations include Aalto University, Ruukki, VTT Technical Research Centre of Finland and Wärtsilä.

References

[1] Y. Murakami, editor. *Stress Intensity Factors Handbook*. Pergamon Press, Oxford, 1987.

[2] X. Niu and G. Glinka. Stress-intensity factors for semi-elliptical surface cracks in welded joints. *International Journal of Fracture*, pages 255–270, 1989.

[3] M. Oore and D. J. Burns. Estimation of stress intensity factors for embedded irregular cracks subjected to arbitrary normal stress fields. *Journal of Pressure Vessel Technology*, 102/211, 1980.

[4] G. Glinka and W. Reinhardt. Calculation of stress intensity factors for cracks of complex geometry and subjected to arbitrary nonlinear stress fields. *Fatigue and Fracture Mechanics*, 31, ASTM STP 1389:348–370, 2000.

[5] H. F. Bueckner. A novel principle for the computation of stress intensity factors. *Zeitschrift fur Angewandte Mathematic und Mechanik*, 50:529–546, 1970.

[6] J. R. Rice. Weight function theory for three-dimensional elastic crack analysis. *Fracture Mechanics: Perspectives and Directions (Twentieth Symposium)*, pages 29–57, 1989.

[7] P. C. Paris and F. Erdogan. A critical analysis of crack propagation laws. *J. Basic Engineering*, 85:528–534, 1963.

[8] G. Marquis. Variable amplitude loading. In A. MacDonald, K, editor, *Fracture and Fatigue of Welded Joints and Structures*, chapter 8, pages 208–238. Woodhead Publishing Ltd, Cambridge, 2011.

[9] A. H. Noroozi, G. Glinka, and S. Lambert. A two parameter driving force for fatigue crack growth analysis. *International Journal of Fatigue*, pages 1277–1296, 2005.

[10] A. Jankowiak, H. Jakubczak, and G Glinka. Fatigue crack growth analysis using 2-d weight function. *International Journal of Fatigue*, 31:1921–1927, 2009.

[11] J. C. Newman Jr. A crack-closure model for predicting fatigue crack growth under aircraft spectrum loading. In J. B. Chang and C. M. Hudson, editors, *Methods and Models for Predicting Fatigue Crack Growth under Random Loading*, ASTM STP 748, pages 53–84. ASTM, Philadelphia, PA, 1981.

[12] A. H. Noroozi, G. Glinka, and S Lambert. Prediction of fatigue crack growth under constant amplitude loading and a single overload based on elasto-plastic crack tip stresses and strains. *Engineering Fracture Mechanics*, pages 188–206, 2007.

[13] S. Mikheevskiy. *Elastic-Plastic Fatigue Crack Growth Analysis under Variable Amplitude Loading Spectra*. PhD thesis, University of Waterloo, 2009.

[14] M. Creager and P. C. Paris. Elastic field equations for blunt cracks with reference to stress corrosion cracking. *International Journal of Fracture*, 3(4):247–252, 1967.

[15] H. Neuber. Theory of stress concentration for shear-strained prismatic bodies with arbitrary nonlinear stress-strain law. *Journal of Applied Mechanics*, 28:544–551, 1961.

Pasi Lindroth, Gary Marquis
Aalto University, Department of Applied Mechanics
pasi.lindroth@aalto.fi

Grzegorz Glinka
University of Waterloo, Department of Mechanical and Mechatronics Engineering
Aalto University, Department of Applied Mechanics

PIENAHITSIEN STAATTISEN KESTÄVYYDEN MITOITUS PERINTEISESTI JA ERI REUNAEHTOIHIN PERUSTUVILLA PARANNETUILLA MITOITUSMALLEILLA

Timo Penttilä

Tiivistelmä. Tässä tutkimuksessa oli tavoitteena tarkastella analyyttisen laskennan keinoin pienahitsin mitoittamista ja selvittää käytännön kokeissa havaittu a-mitasta poikkeavan vauriotason sijainti poikittain kuormitetuissa pienahitseissä. Perinteinen laskentamallin tarkastelu laajennettiin koskemaan mielivaltaisessa kulmassa olevaa laskentatasoa ja suurimman yhdistetyn jännityksen perusteella löydettiin kriittisin leikkaus tasakylkisessä hitsissä. Lisäksi tarkasteltiin voimatasapainon huomioon ottamista mitoituksessa ja luotiin kaksi eri mallia tämän pohjalta. Kolme teoreettisesti oikeampaa mitoitusmallia täydennettiin kattamaan myös erikylkiset hitsit ja todettiin, että kaikilla mitoitusmalleilla erikylkiset hitsit ovat tilavuudeltaan optimaalisempia verrattaessa samanlujuisiin tasakylkisiin hitseihin.

Avainsanat: pienahitsi, mitoitus, a-mitta, äärikestävyys, kateettipoikkeama

Johdanto

Pienahitsit ovat yleisimpiä hitsausliitostyyppejä. Pienahitsien staattisen kestävyyden mitoitus perustuu Eurokoodi 3:n ohjeistukseen, joka määrää pienahitsin laskentapinnan a-mitan perusteella. Käytännön kokeissa on kuitenkin havaittu, että poikittain kuormitetuissa pienahitseissä vauriot eivät yleensä muodostu a-mitan määräämälle tasolle, vaan loivempaan kulmaan. Voidaan siis päätellä, että oletus a-mitasta vauriokohtana on virheellinen. Yleensä analyyttisesti mitoitettujen hitsien kestävyys on kuitenkin varmalla puolella, joten virheellisestä mitoitusperiaatteesta ei ole haittaa.

Pienahitsin poikkipinta-ala ja siten myös tilavuus kasvaa hitsin a-mitan neliössä, joten turhan suuria hitsejä tulisi välttää. Tämä korostuu etenkin lujien terästen hitsauksessa, joissa ylisuuri palko merkitsee perusaineen lujuudelle haitallista ylimääräistä lämmöntuontia. Hitsien mitoitus tai valmistus ylivarmoiksi voi tästä johtuen heikentää liitosten kapasiteettia, mikä pitää ottaa huomioon suunnittelussa ja valmistuksessa.

Tämän tutkimuksen tavoitteena on tarkastella pienahitsien mitoittamista pohjautuen suurimpaan yhdistettyyn jännitykseen mielivaltaisella laskentatasolla ja selittää tähän perustuen käytännössä havaitut loivemmat vauriokulmat. Tarkastelun pohjalta on luotu perinteisestä eroavia mitoitusmalleja, jotka ovat teoreettisesti oikeampia kuin perinteinen. Tässä artikkelissa esitetään mitoitusmallien johtaminen erikylkisille otsapienahitseille, joista saadaan tasakylkisen hitsin mitoitusyhtälöt erikoistapauksena.

Pienahitsin a-mitta

Pienahitsin a-mitta on aikaisemmin määritelty standardin SFS 3052 mukaan hitsin sisään piirretyn tasakylkisen kolmion korkeutena (Niemi & Kemppi, 1993, s. 14). Koska hitsin mitoitus perustuu a-mittaan, tämän määrittelyn perusteella ideaalinen hitsin muoto

on tasakylkinen kolmio, ns. tasahitsi. Tällöin hitsin poikkipinta-ala ja näin myös tilavuus ovat pienimmillään a-mitan funktiona. Nykyisten ohjeistuksien mukaan (SFS EN 1993-1-8, 2005, s. 45) hitsin efektiivinen a-mitta määritetään hitsin sisään piirretyn suurimman kolmion korkeutena. Tässä tapauksessa kolmio saa olla tasa- tai erikylkinen. Tämän ansiosta mahdollinen kateettipoikkeama voi tuoda hitsin a-mittaa lisää verrattuna aikaisempaan määritystapaan. Lisäksi erikylkisen hitsin a-mitan määrittämän leikkaustason kulma perusaineeseen nähden ei ole enää perinteinen 45°.

Pienahitsin mitoitus perinteisesti a-mitan määräämässä tasossa

Pienahitsit mitoitetaan yksinkertaista tai tarkempaa mitoitustapaa käyttäen. Yksinkertaisessa mitoituksessa hitsiin kohdistuvan voiman oletetaan aina aiheuttavan leikkausjännitystä a-mitan määräämässä laskentatasossa. Tarkemmassa mitoitustavassa hitsiin kohdistuva voima jaetaan komponentteihin. Voimakomponentit jaetaan a-mitan määräämällä laskentapinta-alalla ja näin saadaan vastaavat jännityskomponentit, jotka yhdistetään vakiomuodonvääristymisenergiahypoteesin (VMVEH) eli von Misesin hypoteesin avulla vertailujännitykseksi. Kuvassa 1 on esitetty pienahitsin jännityskomponentit.

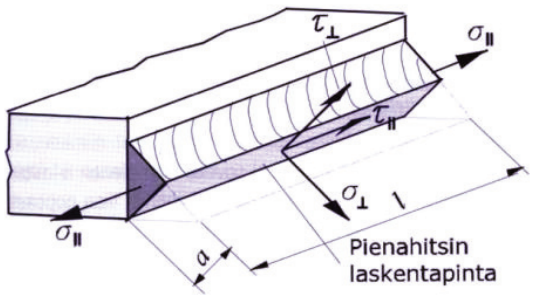

Kuva 1. Pienahitsin laskentapinnalla vaikuttavat jännityskomponentit. (Niemi, 2003, s. 68)

Tarkemman mitoitustavan mukaan pienahitsin jännityskomponenttien tulee täyttää yhtälöiden 1 ja 2 mukaiset ehdot. (SFS EN 1993-1-8, 2005, s. 46).

$$\sqrt{\sigma_\perp^2 + 3\tau_\perp^2 + 3\tau_\parallel^2} \leq \frac{f_u}{\beta_w \cdot \gamma_{M2}} \tag{1}$$

$$\sigma_\perp \leq 0{,}9\frac{f_u}{\gamma_{M2}} \tag{2}$$

Yhtälöissä 1 ja 2 $\sigma_\perp$, $\tau_\perp$ ja $\tau_\parallel$ ovat kuvan 1 mukaiset jännityskomponentit, f_u on heikomman liitettävän osan vetomurtolujuuden nimellisarvo, γ_{M2} on osavarmuusluku, jonka suositeltava arvo on 1,25 (SFS-EN 1993-1-8, 2005, s. 25) ja β_w on ns. korrelaatiokerroin, mikä kuvaa perusaineen ja hitsiaineen lujuuksien suhdetta. Hitsin pituussuuntaista normaalijännitystä $\sigma_\parallel$ ei oteta huomioon mitoituksessa.

Otsapienahitsiin kohdistuva voima F_w jaetaan a-mitan tasossa vaikuttaviin komponentteihin kuvan 2 mukaisesti. Näistä voimakomponenteista muodostetaan kuvan 1 mukaiset jännityskomponentit $\sigma_\perp$ ja $\tau_\perp$.

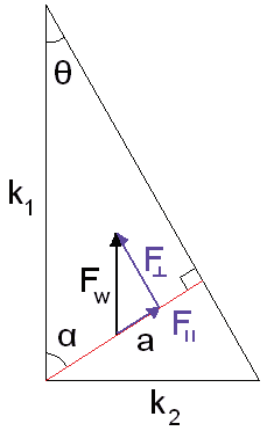

Kuva 2. Voimakomponenttien muodostuminen erikylkisessä otsapienahitsissä.

Muodostetaan voimakomponentit $F_\perp$ ja $F_\parallel$ voiman F_w projektioina kulman α avulla. Otetaan myös huomioon, että kulma α on kateettipoikkeamakulman θ komplementti, jolloin voimakomponentit saadaan esitettyä kulman θ funktiona. Muodostetaan nyt jännityskomponentit $\sigma_\perp$ ja $\tau_\perp$ a-mitan ja hitsin pituuden l määrittämässä leikkauksessa. Kun jännityskomponentit sijoitetaan yhtälöön 1, saadaan erikylkisen otsapienahitsin mitoitusyhtälö 3, joka on ehkä relevanteinta esittää kateettimitan k_1 suhteen ratkaistuna.

$$k_1 \geq \frac{\sqrt{1+3\tan^2\theta}}{\tan\theta} \cdot \frac{\beta_w \gamma_{M2} F_w}{f_u \cdot l} \tag{3}$$

Tasakylkisen hitsin tapauksessa ($\theta = 45°$) yhtälö 3 sievenee perinteiseksi otsapienahitsin mitoitusyhtälöksi 4, joka esitetään a-mitan suhteen ratkaistuna.

$$a \geq \sqrt{2} \cdot \frac{\beta_w \gamma_{M2} F_w}{l \cdot f_u} \tag{4}$$

Pienahitsin mitoitus suurimman yhdistetyn jännityksen mukaan

Edellä esitetty mitoitustapa perustuu oletukseen, että vaurio hitsissä muodostuu a-mitan määräämälle tasolle. Vaikka a-mitan määrittämä taso edustaa pinta-alaltaan pienintä leikkaustasoa hitsissä, ei suurin yhdistetty jännitys esiinny siellä. Laajennetaan mitoitusmalli mielivaltaisessa kulmassa α olevaan leikkaukseen s. Esitetään mitan s pituus kulmien α ja θ ja kateettimitan k_1 funktiona. Jaetaan voima F_w komponenteiksi $F_\perp$ ja $F_\parallel$ mitan s määräämälle tasolle ja muodostetaan voimakomponentteja vastaavat jännityskomponentit. Kuvassa 3 on esitetty erikylkisen hitsin geometria, jota hyödyntäen mitoitusyhtälö muodostetaan.

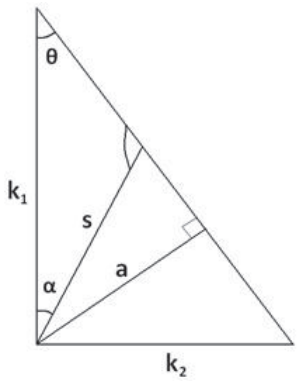

Kuva 3. Erikylkisen hitsin geometria ja laskentatason *s* määrittäminen.

Sijoittamalla mitan *s* määräämälle leikkaustasolle muodostetut jännityskomponentit hitsin mitoitusyhtälöön 1 saadaan yhtälö 5, joka mitoittaa kateettimitan k_1 kulmassa α olevan laskentatason yhdistetyn jännityksen mukaan.

$$k_1 \geq \left(\frac{\sin\alpha}{\tan\theta} + \cos\alpha\right)\sqrt{\sin^2\alpha + 3\cos^2\alpha} \cdot \frac{\beta_w \gamma_{M2} F_w}{l \cdot f_u} \tag{5}$$

Erotetaan yhtälöstä 5 kulmista α ja θ määräytyvä osuus ja muodostetaan tämän osittaisderivaatta kulman α suhteen. Osittaisderivaatan nollakohtien (yhtälö 6) perusteella saadaan muodostettua kulmien α ja θ välinen riippuvuus suurimpaan yhdistettyyn jännitykseen perustuen (yhtälö 7).

$$\frac{\partial}{\partial\alpha}\left[\left(\frac{\sin\alpha}{\tan\theta} + \cos\alpha\right)\sqrt{\sin^2\alpha + 3\cos^2\alpha}\right] = 0 \tag{6}$$

$$\Rightarrow \tan\theta \cdot \tan^3\alpha + \tan^2\alpha + 5\tan\theta \cdot \tan\alpha - 3 = 0 \tag{7}$$

Kulma α voitaisiin ratkaista yhtälöstä 7 kolmannen asteen yhtälön ratkaisukaavalla ja sijoittaa yhtälöön 5, jolloin saataisiin suurimpaan yhdistettyyn jännitykseen perustuen erikylkisen hitsin mitoitusyhtälö kateettipoikkeamakulman θ funktiona. Yhtälöt muodostuvat monimutkaisiksi, joten tyydytään osittain numeeriseen tarkasteluun.

Ratkaisemalla yhtälöstä 7 tan(θ):n arvo ja sijoittamalla tämä yhtälöön 5 saadaan mitoitusyhtälö esitettyä pelkästään kulman α funktiona (yhtälö 8).

$$k_1 \geq \frac{(\cos 2\alpha + 2)^{\frac{3}{2}}}{\cos 3\alpha + 2\cos\alpha} \cdot \frac{\beta_w \gamma_{M2} F_w}{l \cdot f_u} \tag{8}$$

Kulman α arvo voidaan ratkaista numeerisesti yhtälöstä 7, kun kateettipoikkeamakulman θ on tunnettu. Kun kyseessä on tasakylkinen hitsi, on kulman θ arvo 45° ja yhtälöstä 7 saadaan ratkaistua kulman α arvoksi 27,4°. Tämän kulman määräämässä tasossa esiintyy siis suurin yhdistetty jännitystila. Sijoitettaessa kulman α arvo mitoitusyhtälöön 8 saadaan tasakylkisen hitsin mitoitusyhtälö 9 a-mitan suhteen ratkaistuna:

$$a \geq 1{,}53 \cdot \frac{\beta_w \gamma_{M2} F_w}{l \cdot f_u} \tag{9}$$

Mitoitusmalli suurimpaan yhdistettyyn jännitykseen perustuen ennustaa tasakylkisen hitsin vauriokulmaksi vetokuormituksessa 27,4° ja mitoitettaessa tämän perusteella vaaditaan hitsiin n. 8 % suurempi a-mitta (1,53 / $\sqrt{2}$ ≈ 1,0819).

Voimatasapainon huomioon ottaminen mitoitusmallissa

Edellä esitetyissä mitoitustavoissa on huomattava yksinkertaistus hitsiä kuormittavan voiman F_w käsittelyssä. Tarkastellaan kuvan 4 mukaista pienahitsattua X-liitosta. Kuvan 4 kohdassa a liitos on esitetty täydellisenä ja kohdassa 4b hitsit ovat leikattu mitoitustasoa pitkin ja mitoittava voima on asetettu leikkaustason keskiöön. Tässä vaiheessa vapaakappalekuva on tasapainossa, mutta leikattaessa hitsi edelleen toista kateettia pitkin kuvan 4c mukaisesti ja tuotaessa voima kateettia pitkin leikkausvoimana eivät statiikan tasapainoyhtälöt enää täyty.

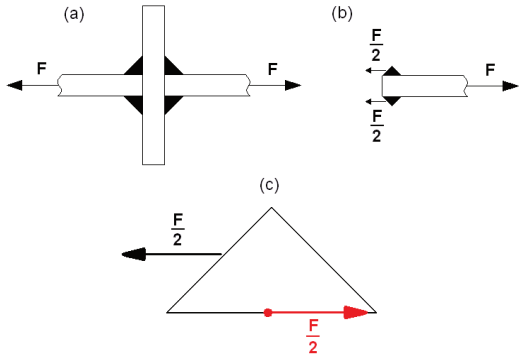

Kuva 4. Perinteinen voimien käsittely pienahitsin mitoituksessa ja staattinen epätasapaino.

Hitsin tasapainottamiseen tarvitaan siis momentti, joka voidaan esittää uutena sekundaarisena voimaparina kuvan 5 mukaisesti. Ongelmaksi muodostuu voimien sijaintien määrittäminen kateeteilla ja kriittisessä leikkauksessa. Voimakomponentti on seurausta jännitysjakaumasta pinta-alan yli, joten tehdään kaksi eri oletusta jakaumamuodoista, jolloin voimakomponenttien sijainnit saadaan lukittua.

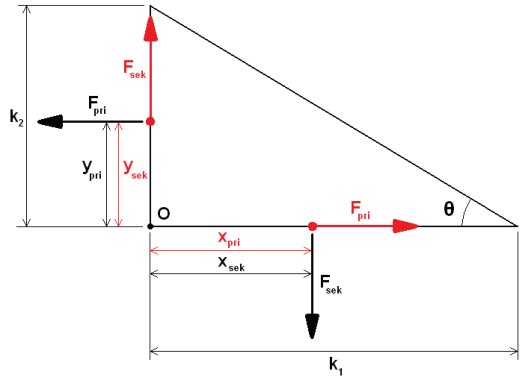

Kuva 5. Erikylkisen hitsin kateeteilla vaikuttavat voimat ja niiden etäisyydet pisteestä *O*.

Oletettaessa primaari- ja sekundaarivoiman aiheuttamien jännitysjakaumien olevan tasaisesti jakautuneita voimakomponentit vaikuttavat kateettien keskipisteissä. Tällöin voidaan osoittaa, että tasapaino toteutuu myös jokaisessa kulman α määräämässä leikkauksessa, kun voimakomponentit vaikuttavat leikkaustason keskiössä. Muodostetaan mitoitusyhtälö 10, joka ottaa huomioon sekundaarisen voimaparin vaikutuksen.

$$k_1 \geq \left(\frac{\sin\alpha}{\tan\theta} + \cos\alpha\right)\sqrt{(\sin\alpha + \cos\alpha\tan\theta)^2 + 3(\cos\alpha - \sin\alpha\tan\theta)^2} \cdot \frac{\beta_w \gamma_{M2} F_{pri}}{l \cdot f_u} \qquad (10)$$

Erottamalla yhtälöstä 10 kulmista α ja θ määräytyvä osuus, muodostamalla osittaisderivaatta kulman α suhteen ja ratkaisemalla tämän nollakohdat löydetään kaksi lokaalia jännitysmaksimitasoa, joilla voidaan osoittaa olevan yhtä suuret yhdistetyt jännitykset. Maksimijännitykset esiintyvät yhtälön 11 määräämissä kulmissa.

$$\tan\alpha = \frac{\pm\sqrt{3} - \tan\theta}{1 \pm \sqrt{3}\tan\theta} \qquad (11)$$

Sijoitettaessa toinen yhtälön 11 mukaisista ratkaisuista yhtälöön 10 saadaan mitoitusyhtälöksi:

$$k_1 \geq \frac{3\sqrt{2}}{4} \cdot \frac{\tan^2\theta + 1}{\tan\theta} \cdot \frac{\beta_w \gamma_{M2} F_{pri}}{l \cdot f_u} \qquad (12)$$

Tasakylkisen hitsin tapauksessa mitoitusyhtälö supistuu a-mitan suhteen ratkaistuna yhtälöksi 13 ja yhtälön 11 mukaiset vauriokulman α arvot ovat 15° ja 75°.

$$a \geq 1.5 \cdot \frac{\beta_w \gamma_{M2} F_{pri}}{l \cdot f_u} \qquad (13)$$

Oletus tasaisista jännitysjakaumista johtaa hitsin jännitystilan symmetrisyyteen a-mitan suhteen tasakylkisessä hitsissä, mikä näkyy kahtena mahdollisena vauriokulmana. Käytännön kokeissa ei tällaista käyttäytymistä ole kuitenkaan havaittu. Lähtökohtaisesti voidaan olettaa, että sekundaariset voimat eivät ole yhtä suuria kuin primaarinen voima. Kuvan 5 mukaisia voimien sijainteja saadaan säädettyä sekundaarivoimia pienentäviksi olettamalla kuvan 6 mukaiset kolmiomaiset normaalijännitysjakaumat. Kateeteilla vaikuttavien leikkausjännitysjakaumien muotoihin ei ole otettu kantaa, koska ne eivät vaikuta momenttitarkastelussa pisteen *O* suhteen.

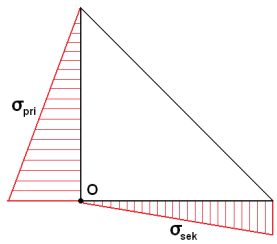

Kuva 6. Kolmionmuotoiset primaari- ja sekundaarivoimien normaalijännitysjakaumat.

Primaarisen ja sekundaarisen voiman sijainti on nyt määrätty kolmiomaisten jakaumien painopisteiden perusteella kateeteilla. Tarkasteltaessa hitsin sisäistä leikkaustasoa voidaan osoittaa, että tasapaino ei toteudu kaikilla kulman α arvoilla jos voimakom-

ponentit sijoitetaan leikkaustason keskipisteeseen. Tehdään tästä syystä olettamus, että kriittisellä vauriotasolla jännitykset ovat tasaisesti jakautuneita. Tällöin vauriotason kulma α ratkeaa tasapainon perusteella yhtälön 14 mukaiseksi.

$$\tan\alpha = \frac{1}{2}\tan\theta \tag{14}$$

Kolmiomaisilla jännitysjakaumilla sekundaarisen voiman suuruus on puolet primaarisesta voimasta ja mitoitusyhtälö muodostuu seuraavanlaiseksi:

$$k_1 \geq \left(\frac{\sin\alpha}{\tan\theta} + \cos\alpha\right)\sqrt{\left(\sin\alpha + \frac{1}{2}\cos\alpha\tan\theta\right)^2 + 3\left(\cos\alpha - \frac{1}{2}\sin\alpha\tan\theta\right)^2} \cdot \frac{\beta_w \gamma_{M2} F_{pri}}{l \cdot f_u} \tag{15}$$

Sijoitetaan tasapainon perusteella ratkaistu kriittinen vauriotason kulma α (yhtälö 14) yhtälöön 15, joka sievenee muotoon:

$$k_1 \geq \frac{3\tan\theta}{\tan^2\theta + 4}\sqrt{\frac{3}{4}\tan^2\theta + \frac{12}{\tan^2\theta} - 2} \cdot \frac{\beta_w \gamma_{M2} F_{pri}}{l \cdot f_u} \tag{16}$$

Tasakylkisen hitsin tapauksessa saadaan kulmaksi α n. 26,6° ja mitoitusyhtälö 16 supistuu tällöin a-mitan suhteen ratkaistuksi yhtälöksi 17.

$$a \geq \frac{3}{10}\sqrt{\frac{43}{2}} \cdot \frac{\beta_w \gamma_{M2} F_{pri}}{l \cdot f_u} \approx 1{,}39 \cdot \frac{\beta_w \gamma_{M2} F_{pri}}{l \cdot f_u} \tag{17}$$

Tulosten tarkastelu ja mitoitusmallien vertailu

Edellä on johdettu neljä erilaista poikittain kuormitetun pienahitsin mitoitusmallia erikylkisille hitseille ja esitetty myös näiden mukaiset mitoitusyhtälöt, kun hitsi on tasakylkinen. Verrattaessa tasakylkisen hitsin mitoitusyhtälöitä (yhtälöt 4, 9, 13 ja 17) keskenään nähdään, että äärikestävyyden kannalta erot eivät ole suuria. Kolmiomaisilla primaari- ja sekundaarivoiman jännitysjakaumilla (yhtälö 17) hitsin a-mitta tulee n. 1,6 % pienemmäksi verrattuna perinteiseen mitoitustapaan (yhtälö 4), mikä kertoo siitä, että tasapainottavien voimien huomioon ottaminen mitoitusmallissa voi muodostaa jännitystilan hitsissä suotuisammaksi. Oleellisempi havainto on se, että a-mitta ei ole kriittinen vauriotaso hitsissä muiden mitoitusmallien mukaan.

Verrattaessa mitoitusmallien käyttäytymistä ääritilanteissa ($\theta \rightarrow 0°$ tai $\theta \rightarrow 90°$) nähdään, että tasapainottavat voimat huomioon ottavat mallit eivät toimi samoin kuin perinteinen ja suurimpaan yhdistettyyn jännitykseen perustuva mitoitusyhtälö. Käytännön kannalta oleellisin tarkastelualue on $\theta = 45° \pm 0\ldots15°$ ja tällä alueella mitoitusyhtälöiden tuottamissa hitsin mitoissa ei ole suuria eroja.

Esitettäessä erikylkisen hitsin suhteellinen poikkipinta-ala (verrannollinen tilavuuteen) kateettipoikkeamankulman θ funktiona (kuva 7) nähdään, että optimaalisin hitsin muoto saavutetaan kuormituksen suuntaan pienemmällä kulman θ arvolla kuin 45° kaikilla mitoitusmalleilla. Kuvan 7 mukaisilla mitoitusmalleilla 1 ja 3 optimaalinen kulman θ arvo on 30° ja mitoitusyhtälöt antavat tällöin saman hitsin mitan. Mitoitusmallilla 2 optimaalinen kulman θ arvo on $\tan^{-1}[\sqrt{(2\sqrt{3} - 3)}] \approx 34{,}3°$. Mitoitusmallilla 4 ei ole käy-

tännössä optimaalista kulman θ arvoa, koska sen käyttäytyminen poikkeaa muista kulman θ lähentyessä arvoa 0°. Kuvan 7 perusteella poikkipinta-alan suhteen löytyy lokaali minimi, kun kulman θ arvo on n. 50°…55°.

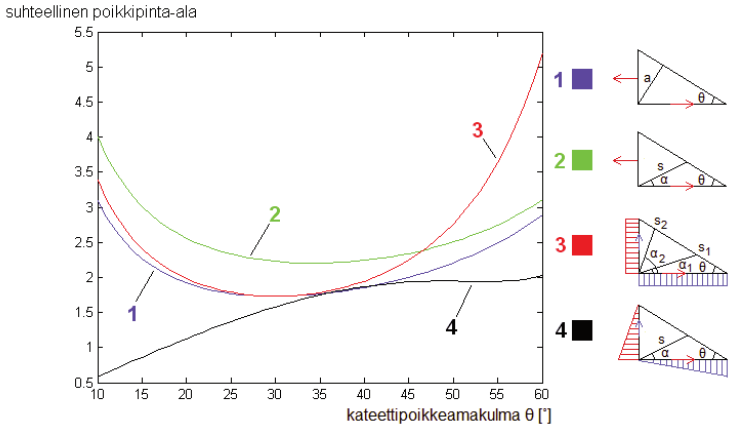

Kuva 7. Eri mitoitusmalleilla laskettujen samanlujuisten hitsien poikkipinta-alojen vertailua kateettipoikkeamakulman θ funktiona välillä 10°…60°.

Johtopäätökset

Eri reunaehdoin johdetut perinteisestä poikkeavat mitoitusmallit ennustavat tasakylkisessä poikittain kuormitetussa hitsissä a-mitasta poikkeavan vauriotason. Kahden parannetun mitoitusmallin ennustamat vauriokulmat (27,4° ja 26,6°) ovat erittäin lähellä toisiaan ja tasaisia jännitysjakaumia käyttävä malli indikoi myös loivempaa vauriokulmaa. Tasapainottavien voimien huomioon ottamisessa on ongelma voimakomponenttien sijaintien määrittämisessä ja mitoitusehdon muodostamisessa, joten tuloksien suhteen täytyy olla kriittinen. Kaikilla mitoitusmalleilla erikylkiset hitsit ovat optimaalisempia tilavuuden kannalta tarkasteltaessa.

Viitteet

Niemi, E. & Kemppi, J. 1993. Hitsatun rakenteen suunnittelun perusteet. Helsinki, Painatuskeskus Oy. 337 s.

Niemi, E. 2003. Levyrakenteiden suunnittelu. Tekninen tiedostus 2/2003. Helsinki, Teknologiainfo Teknova Oy. 136 s.

SFS-EN 1993-1-8. 2005. Eurokoodi 3. Teräsrakenteiden suunnittelu. Osa 1-8: Liitosten suunnittelu. Suomen standardoimisliitto SFS. 149 s.

Timo Penttilä
Lappeenrannan teknillinen yliopisto, Konetekniikan laitos, Teräsrakenteiden laboratorio
Skinnarilankatu 34, 53851 Lappeenranta
timo.penttila@lut.fi

Yksinkertainen J2-plastisuus-vauriomalli metalleille

Timo Saksala

Tiivistelmä. Tässä artikkelissa esitetään yksinkertainen materiaalimalli metallien plastisoitumisen ja vaurioitumisen kuvaukseen. Malli perustuu klassiseen J_2-plastisuusmalliin (von Mises), jota rikastetaan isotrooppisella vauriomallilla. Vauriomallin lisääminen plastisuusmalliin mahdollistaa kokeellisesti havaitun, plastiseen muodonmuutokseen liittyvän, jäykkyyden menetyksen mallinnuksen. Lujittumislait oletetaan epälineaarisiksi ja saturoituviksi. Plastisuusmallin ja vauriomallin kytkentä toteutetaan ns. tehollisessa jännitysavaruudessa, jolloin niihin liittyvät laskennat (jännityspalautus ja vauriomuuttujan päivitys) voidaan tehdä itsenäisesti. Tämä kytkentätapa johtaa erityisen helppoon tangenttijäykkyysmatriisin laskentakaavan. Laskentaesimerkkinä simuloidaan dynaamisesti yksiaksiaalista syklistä vetokoetta yhden elementin laskentamallilla.

Avainsanat: J_2-plastisuusmalli, istrooppinen vauriomalli, myötöväsyminen, jännitysintegrointi

Johdanto

Metallirakenteiden suunnittelussa ei perinteisesti ole sallittu myötörajan ylitystä. Plastisten muodonmuutosten ja vaurioitumisen mallintamista kuitenkin tarvitaan esimerkiksi kehärakenteiden sortumistarkasteluissa ja koneenosien myötöväsymisanalyyseissä. Metallien sitkeä vaurioituminen esiintyy samanaikaisesti plastisen muodonmuutoksen kanssa tietyn kynnysarvon jälkeen. Siten realistiseen vaurioitumisolosuhteiden ennustamiseen pyrkivän mallin täytyy ottaa huomioon sekä plastiset muodonmuutokset että niiden aikaansaama vaurio.

J_2-plastisuusmalli, eli von Mises-myötöfunktioon ja assosiatiiviseen myötösääntöön perustuva malli, on metallien plastisuusanalyyseissä tavallisimmin käytetty teoria. Kun klassiseen J_2-plastisuusmalliin lisätään vauriomalli, sillä voidaan ennustaa kokeissa havaittua materiaalin jäykkyyden ja lujuuden menetystä eli pehmenemistä. Jäykkyyden menetys (vaurio) johtuu metalleilla plastiseen virtaukseen liittyvästä dislokaatioiden pysähtymisestä seuraavasta atomisidosten katkeamisesta [1].

Tässä artikkelissa esitetään klassisen J_2-plastisuusmallin yksinkertainen laajennus liittämällä siihen isotrooppinen vauriomalli. Isotrooppinen ja kinemaattinen lujittuminen mallinnetaan saturoituvilla epälineaarisilla lujittumissäännöillä. Malli formuloidaan pienten venymien teoriaa käyttäen. Mallin ennustamaa materiaalin käyttäytymistä havainnollistetaan simuloimalla syklistä veto-puristuskoetta yhden elementin mallilla.

Mallin teoria

J_2-plastisuusmalli ja lujittumislait

Von Mises myötöfunktio kirjoitetaan tämän artikkelin tarpeisiin seuraavasti

$$\begin{aligned} f_{\text{vM}}(\boldsymbol{\xi}, R) &= \sqrt{J_2} - (\sigma_Y + R) \\ J_2 &= \tfrac{1}{2}\,\text{dev}(\boldsymbol{\xi}) : \text{dev}(\boldsymbol{\xi}) \end{aligned} \tag{1}$$

missä $\boldsymbol{\xi} = \boldsymbol{\sigma} - \mathbf{X}$, $\mathrm{dev}(\boldsymbol{\xi}) = \boldsymbol{\xi} - \frac{1}{3}\mathrm{tr}(\boldsymbol{\xi})\mathbf{I}$ ($\mathbf{I}$ on 2. kertaluvun identiteettitensori) on deviaattori, σ_Y on myötöraja, $\boldsymbol{\sigma}$ on jännitystensori, $\mathbf{X}$ on kinemaattiseen lujittumiseen liittyvä jännitys (engl. back stress) ja R on isotrooppinen lujittumismuuttuja. Lemaitrea [1] seuraten isotrooppisen ja kinemaattisen lujittumisfunktion oletetaan olevan muotoa

$$R = R_\infty\left(1 - \exp(-b\varepsilon^p_{\mathrm{eqv}})\right), \quad \mathbf{X} = X_\infty\left(1 - \exp(-\gamma\varepsilon^p_{\mathrm{eqv}})\right)\frac{\partial f_{\mathrm{vM}}}{\partial \boldsymbol{\sigma}} \tag{2}$$

missä R_∞ ja X_∞ ovat saturaatiojännitykset, b ja γ ovat kokeellisia lujittumisparametrejä, ja $\varepsilon^p_{\mathrm{eqv}}$ on ekvivalentti plastinen venymä, jonka määrittelee kaava

$$\dot{\varepsilon}^p_{\mathrm{eqv}} = \sqrt{\tfrac{2}{3}\dot{\boldsymbol{\varepsilon}}^p : \dot{\boldsymbol{\varepsilon}}^p} \tag{3}$$

Kaavassa (3) $\boldsymbol{\varepsilon}^p$ on plastinen venymätensori. Pienten venymien teorian mukaisesti on voimassa venymän additiivinen jako elastiseen ja plastiseen osaan, eli $\dot{\boldsymbol{\varepsilon}} = \dot{\boldsymbol{\varepsilon}}^e + \dot{\boldsymbol{\varepsilon}}^p$.

Plastisen venymän muutosnopeuden määrittelee assosiatiivinen virtaussääntö:

$$\dot{\boldsymbol{\varepsilon}}^p = \dot{\lambda}\frac{\partial f_{\mathrm{vM}}}{\partial \boldsymbol{\sigma}} = \dot{\lambda}\frac{\mathrm{dev}(\boldsymbol{\xi})}{\sqrt{J_2}} \tag{4}$$

missä $\dot{\lambda}$ on plastinen inkrementti.

Yhteyksien (3) ja (4) avulla voidaan lujittumislait nyt kirjoittaa lujittumisfunktioiden (2) derivaattoina. Siten ketjusäännön avulla saadaan

$$\begin{aligned} \dot{R} &= R_\infty b\exp(-b\varepsilon^p_{\mathrm{eqv}})\dot{\lambda}\sqrt{\tfrac{2}{3}\partial_{\boldsymbol{\sigma}} f_{\mathrm{vM}} : \partial_{\boldsymbol{\sigma}} f_{\mathrm{vM}}} = h_R(\boldsymbol{\xi}, \varepsilon^p_{\mathrm{eqv}})\dot{\lambda} \\ \dot{\mathbf{X}} &= X_\infty\gamma\exp(-\gamma\varepsilon^p_{\mathrm{eqv}})\dot{\lambda}\sqrt{\tfrac{2}{3}\partial_{\boldsymbol{\sigma}} f_{\mathrm{vM}} : \partial_{\boldsymbol{\sigma}} f_{\mathrm{vM}}}\partial_{\boldsymbol{\sigma}} f_{\mathrm{vM}} = h_X(\boldsymbol{\xi}, \varepsilon^p_{\mathrm{eqv}})\dot{\lambda}\partial_{\boldsymbol{\sigma}} f_{\mathrm{vM}} \end{aligned} \tag{5}$$

missä symboli $\partial_{\mathbf{x}}$ merkitsee derivaattaa suureen $\mathbf{x}$ (tensori) suhteen. Mallin laskennalliseen implementointiin tarvitaan vielä Kuhn-Tucker-muotoiset konsistenssiehdot:

$$f_{\mathrm{vM}} \le 0, \quad \dot{\lambda} \ge 0, \quad \dot{\lambda} f_{\mathrm{vM}} = 0, \quad \dot{\lambda}\dot{f}_{\mathrm{vM}} = 0 \tag{6}$$

Seuraavaksi esitetään vauriomalli.

Isotrooppinen vauriomalli

Mikrotasolla vauriomekanismi on atomisidosten pettäminen ja siitä seuraava mikrosäröily. Mesotasolla vaurio voi esiintyä hauraana, sitkeänä tai virumisvauriona riippuen kuormituksesta, lämpötilasta ja materiaalityypistä. Tässä artikkelissa tarkastellaan vain metallien sitkeätä vauriota.

Koska metalleja voidaan käsitellä usein isotrooppisina ja homogeenisina materiaaleina, oletetaan vaurio tässä isotrooppiseksi. Tällöin vaurion vaikutus materiaalilakiin voidaan käsitellä skalaarimuuttujan ω avulla. Isotrooppisen skalaarivauriomallin peruskomponentit ovat nimellisen ja tehollisen jännityksen kaava

$$\boldsymbol{\sigma} = (1-\omega)\overline{\boldsymbol{\sigma}} = (1-\omega)\mathbf{E} : (\boldsymbol{\varepsilon} - \boldsymbol{\varepsilon}^p) \tag{7}$$

missä **E** on lineaarinen kimmotensori. Normaalisti vauriomalli tarvitsee sallitut jännitystilat, joissa vaurioituminen ei etene, osoittavan vauriofunktion, mutta tässä artikkelissa mallinnetaan metallin vaurioitumista, jolloin vauriota ajaa plastinen venymä. Siten vauriofunktiota ei tarvita, vaan von Mises-myötöfunktio osoittaa myös vaurioon johtavan jännitystilan.

Vaurion kehitysfunktion oletetaan olevan lineaarinen seuraavasti:

$$\omega = g_{\mathrm{d}}(\varepsilon^{p}_{\mathrm{eqv}}) = \begin{cases} 0, \ \text{jos } \varepsilon^{p}_{\mathrm{eqv}} < \varepsilon_{\mathrm{pD}} \\ \omega_c \dfrac{\varepsilon^{p}_{\mathrm{eqv}} - \varepsilon_{\mathrm{pD}}}{\varepsilon_{\mathrm{pR}} - \varepsilon_{\mathrm{pD}}}, \ \text{jos } \varepsilon_{\mathrm{pD}} \le \varepsilon^{p}_{\mathrm{eqv}} < \varepsilon_{\mathrm{pR}} \\ \omega_c, \ \text{jos } \varepsilon^{p}_{\mathrm{eqv}} \ge \varepsilon_{\mathrm{pR}} \end{cases} \tag{8}$$

missä $\varepsilon_{\mathrm{pD}}$ ja $\varepsilon_{\mathrm{pR}}$ ovat vaurion kynnys- ja sortumisvenymät, vastaavasti, ja ω_c on kriittinen, sortumiseen johtava, vaurion arvo.

Mikrosäröt tai -kaviteetit aukeavat vetokuormituksessa, mutta puristuksessa niiden vaikutus on yleensä huomattavasti pienempi, jolloin materiaalin jäykkyys palautuu. Tätä efektiä mallinnetaan tässä, Lemaitrea seuraten [1], jakamalla jännitys positiiviseen ja negatiiviseen osaan:

$$\begin{aligned} &\boldsymbol{\sigma} = (1-\omega)\overline{\boldsymbol{\sigma}}_{+} - (1-h\omega)\overline{\boldsymbol{\sigma}}_{-} \quad (\overline{\boldsymbol{\sigma}} = \overline{\boldsymbol{\sigma}}_{+} - \overline{\boldsymbol{\sigma}}_{-}) \\ &\overline{\boldsymbol{\sigma}}_{+} = \sum_{i=1}^{3} \langle \overline{\sigma}_i \rangle \mathbf{n}_i \otimes \mathbf{n}_i, \ \overline{\boldsymbol{\sigma}}_{-} = \sum_{i=1}^{3} \langle -\overline{\sigma}_i \rangle \mathbf{n}_i \otimes \mathbf{n}_i \end{aligned} \tag{9}$$

missä <> ovat McAuley-sulkeet, $\overline{\sigma}_i$ ja $\mathbf{n}_i$ ovat tehollinen pääjännitys ja -suunta, ja h on särön sulkeutumisparametri. Lemaitren [1] mukaan tämän parametrin suuruus on samaa luokkaa kuin ω_c.

Mallin plastinen ja vaurio-osa yhdistetään tehollisessa jännitysavaruudessa niin, että ensin palautetaan myötöpinnalle myötöehtoa (von Mises) rikkova tehollinen ennustejännitys. Tämän jälkeen päivitetään vauriomuuttuja (8) ja lopuksi lasketaan nimellisjännitys kaavalla (9) [2].

Jännitysintegrointi ja tangenttijäykkyysmatriisi

Palautusalgoritmi

Jännityspalautusalgoritmiksi valitaan leikkaavan tason-algoritmi (engl. Cutting plane algorithm), koska se on eksplisiittinen ja se suppenee kvadraattisesti [3]. Tämä algoritmi, sovellettuna yllä esitettyyn J_2-plastisuusmalliin, on esitetty alla.

Kimmoinen ennuste

Annettu: $\boldsymbol{\varepsilon}_{n+1}, \boldsymbol{\varepsilon}^{p}_{n}, \mathbf{X}_n, R_n, \varepsilon^{p}_{\mathrm{eqv},n}$

Laske testitila: $\boldsymbol{\sigma}^{\mathrm{trial}}_{n+1} = \mathbf{E} : (\boldsymbol{\varepsilon}_{n+1} - \boldsymbol{\varepsilon}^{\mathrm{p}}_{n}), \boldsymbol{\xi}^{\mathrm{trial}}_{n+1} = \boldsymbol{\sigma}^{\mathrm{trial}}_{n+1} - \mathbf{X}_n, f^{\mathrm{trial}}_{\mathrm{vM}} = f_{\mathrm{vM}}(\boldsymbol{\xi}^{\mathrm{trial}}_{n+1}, R_n)$

Jos $f^{\mathrm{trial}}_{\mathrm{vM}} > 0$, aseta : $\boldsymbol{\varepsilon}^{p,(0)}_{n+1} = \boldsymbol{\varepsilon}^{p}_{n}, \mathbf{X}^{0}_{n+1} = \mathbf{X}_n, \boldsymbol{\sigma}^{0}_{n+1} = \boldsymbol{\sigma}^{\mathrm{trial}}_{n+1}, R^{0}_{n+1} = R_n, \varepsilon^{p,(0)}_{\mathrm{eqv},n+1} = \varepsilon^{p}_{\mathrm{eqv},n}$,

$k = 0$, ja suorita *Plastinen korjaus*. Muuten testitila on oikea.

Plastinen korjaus

1. $\Delta\lambda = \dfrac{f_{\mathrm{vM}}(\xi_{n+1}^{k}, R_{n+1}^{k})}{\partial_{\boldsymbol{\sigma}} f_{\mathrm{vM}} : \mathbf{E} : \partial_{\boldsymbol{\sigma}} f_{\mathrm{vM}} + h_R(\xi_{n+1}^{k}, \varepsilon_{\mathrm{eqv},n+1}^{p,(k)}) + h_X(\xi_{n+1}^{k}, \varepsilon_{\mathrm{eqv},n+1}^{p,(k)}) \partial_{\boldsymbol{\sigma}} f_{\mathrm{vM}} : \partial_{\boldsymbol{\sigma}} f_{\mathrm{vM}}}$
2. $\Delta\boldsymbol{\varepsilon}^{p} = \Delta\lambda \dfrac{\partial f_{\mathrm{vM}}(\xi_{n+1}^{k}, R_{n+1}^{k})}{\partial \boldsymbol{\sigma}}$
3. $R_{n+1}^{k+1} = R_{n+1}^{k} + h_R(\xi_{n+1}^{k}, \varepsilon_{\mathrm{eqv},n+1}^{p,(k)})\Delta\lambda$
4. $\mathbf{X}_{n+1}^{k+1} = \mathbf{X}_{n+1}^{k} + h_X(\xi_{n+1}^{k}, \varepsilon_{\mathrm{eqv},n+1}^{p,(k)})\Delta\boldsymbol{\varepsilon}^{p}$
5. $\boldsymbol{\sigma}_{n+1}^{k+1} = \boldsymbol{\sigma}_{n+1}^{k} - \mathbf{E} : \Delta\boldsymbol{\varepsilon}^{p}$, $\boldsymbol{\xi}_{n+1}^{k+1} = \boldsymbol{\sigma}_{n+1}^{k+1} - \mathbf{X}_{n+1}^{k+1}$
6. $\boldsymbol{\varepsilon}_{n+1}^{p,(k+1)} = \boldsymbol{\varepsilon}_{n+1}^{p,(k)} + \Delta\boldsymbol{\varepsilon}^{p}$, $\varepsilon_{\mathrm{eqv},n+1}^{p,(k+1)} = \varepsilon_{\mathrm{eqv},n+1}^{p,(k)} + \sqrt{\frac{2}{3}\Delta\boldsymbol{\varepsilon}^{p} : \Delta\boldsymbol{\varepsilon}^{p}}$

Jos $f_{\mathrm{vM}}(\xi_{n+1}^{k+1}, R_{n+1}^{k+1}) \le TOL$, lopeta.

Muuten aseta $k \leftarrow k+1$ ja mene askeleeseen 1.

Algoritmi suppenee yhdellä askeleella lujittumisfunktioiden (2) epälineaarisuudesta huolimatta. Tämä johtuu siitä, että J_2-plastisuusmallille löytyy tarkka ratkaisu ideaaliplastisessa ja lineaarisesti lujittuvassa tapauksessa. Nyt, koska plastisen korjauksen aikana lujittumismoduulit lasketaan *tässä algoritmissa* edellisen kierroksen k ekvivalentin plastisen venymän avulla (askeleet 3 ja 4), niin lujittuminen on käytännössä *paloittain lineaarista* ja tarkka ratkaisu saadaan yhdellä askeleella.

Konsistentti tangenttijäykkyysmatriisi

Konsistentti tangenttijäykkyysmatriisi tarvitaan systeemiyhtälöiden iteratiivisen ratkaisun kvadraattisen suppenemisen takaamiseksi. Mallin plastiselle osalle se on [3]:

$$\mathbf{E}^{\mathrm{epc}} = \mathbf{E}^{\mathrm{c}} - \frac{\mathbf{E}^{\mathrm{c}} : \dfrac{\partial f_{\mathrm{vM}}}{\partial \boldsymbol{\sigma}} \otimes \mathbf{E}^{\mathrm{c}} : \dfrac{\partial f_{\mathrm{vM}}}{\partial \boldsymbol{\sigma}}}{\dfrac{\partial f_{\mathrm{vM}}}{\partial \boldsymbol{\sigma}} : \mathbf{E}^{\mathrm{c}} : \dfrac{\partial f_{\mathrm{vM}}}{\partial \boldsymbol{\sigma}} + h_R + h_X \dfrac{\partial f_{\mathrm{vM}}}{\partial \boldsymbol{\sigma}} : \dfrac{\partial f_{\mathrm{vM}}}{\partial \boldsymbol{\sigma}}}, \quad \mathbf{E}^{\mathrm{c}} = \left(\mathbf{E}^{-1} + \Delta\lambda \frac{\partial^2 f_{\mathrm{vM}}}{\partial \boldsymbol{\sigma}^2} \right)^{-1} \tag{10}$$

Jotta vauriomallin osuus saadaan mukaan, yhtälöä (7) häiritään hieman:

$$\begin{aligned} \delta\boldsymbol{\sigma} &= (1-\omega)\delta\overline{\boldsymbol{\sigma}} - \delta\omega\overline{\boldsymbol{\sigma}} = (1-\omega)\mathbf{E}^{\mathrm{epc}} : \delta\boldsymbol{\varepsilon} - g_{\mathrm{d}}'(\varepsilon_{\mathrm{eqv}}^{p})\overline{\boldsymbol{\sigma}} \otimes \frac{\partial \varepsilon_{\mathrm{eqv}}^{p}}{\partial \boldsymbol{\varepsilon}^{p}} : \delta\boldsymbol{\varepsilon} \\ &= \left((1-\omega)\mathbf{E}^{\mathrm{epc}} - g_{\mathrm{d}}'(\varepsilon_{\mathrm{eqv}}^{p})\overline{\boldsymbol{\sigma}} \otimes \frac{\partial \varepsilon_{\mathrm{eqv}}^{p}}{\partial \boldsymbol{\varepsilon}^{p}} \right) : \delta\boldsymbol{\varepsilon} = \mathbf{E}^{\mathrm{epdc}} : \delta\boldsymbol{\varepsilon} \end{aligned} \tag{14}$$

missä $\mathbf{E}^{\mathrm{epdc}}$ vaurion sisältävä elastoplastinen tangenttijäykkyysmatriisi. Kun ekvivalentti plastinen venymä on pienempi kuin vaurioon liittyvä kynnysarvo, $\varepsilon_{\mathrm{pD}}$, käytetään elastoplastista jäykkyyttä $\mathbf{E}^{\mathrm{epc}}$. Kun kynnysarvo ylitetään, käytetään vaurion sisältävää jäykkyyttä $\mathbf{E}^{\mathrm{epdc}}$. Kimmoisen kuormituksen ja kuormanpoiston aikana käytetään jäykkyyttä $(1-\omega)\mathbf{E}$.

Numeeriset esimerkit

Mallin ennustetta testataan Kuvassa 1 esitetyn yhden 8-solmuisen elementin laskentamallin avulla. Huomattakoon, että käytetty malli- ja materiaalidata ei välttämättä edusta mitään todellista materiaalia. Ongelma ratkaistaan dynamiikan tehtävänä Newmarkin aikaintegrointimenetelmää käyttäen.

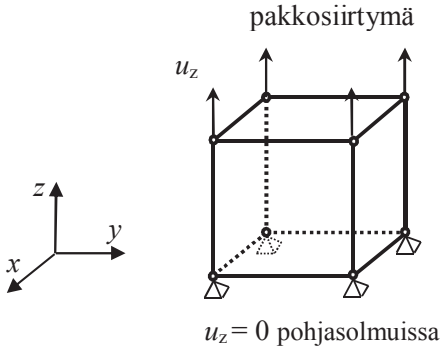

$E = 200\text{GPa}$, $\nu = 0.3$, $\sigma_Y = 200\text{MPa}$,
$R_\infty = 200\text{MPa}$, $X_\infty = 100\text{MPa}$,
$\rho = 7800\text{kg/m}$, $b = 200$, $\gamma = 100$
$\varepsilon_{pD} = 0.01$, $\varepsilon_{pR} = 0.05$, $\omega_c = 0.4$,
$d_{ele} = 0.01\text{m}$, $h = 0.2$

Kuva 1. Yhden elementin laskentamalli, reunaehdot ja materiaalidata.

Tarkoituksena on simuloida myötöväsymistä, kun kuormituksena on Kuvan 2a mukainen sini-muotoinen pakkovenymä, jonka amplitudi on 0.005. Kuvassa 2 on esitetty mallin ennustama vaste puhtaalle plastisuusmallille, kun kinemaattinen ja isotrooppinen lujittuminen on lineaarista (lujittumismoduulit $0.1E$) ja epälineaarista, ja yhdistetylle plastisuusvauriomallille, kun lujittuminen on epälineaarista.

Materiaalin käyttäytyminen on hyvin erilaista eri tapauksissa, mikä osoittaa mallikomponenttien tärkeyttä tulosten realistisuudelle. Lineaaristen lujittumislakien tuottama jatkuva syklinen lujittuminen on epärealistista (Kuva 2d). Huomattavasti realistisempi vaste saadaan epälineaarisilla lujittumislaeilla (2). Lujittuminen saturoituu muutaman syklin jälkeen (Kuva 2c), mutta kuormitus ja kuormanpoisto tapahtuu alkuperäisellä jäykkyydellä, mikä ei ole realistista.

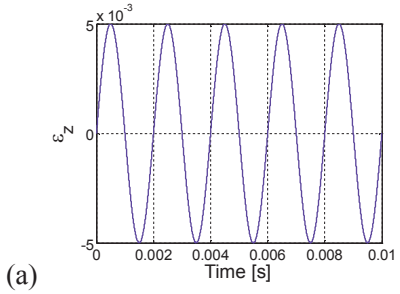

(a)

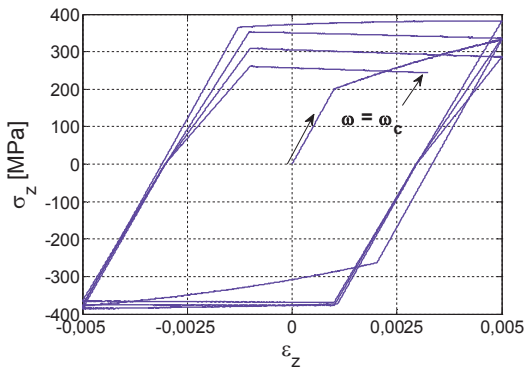

(b)

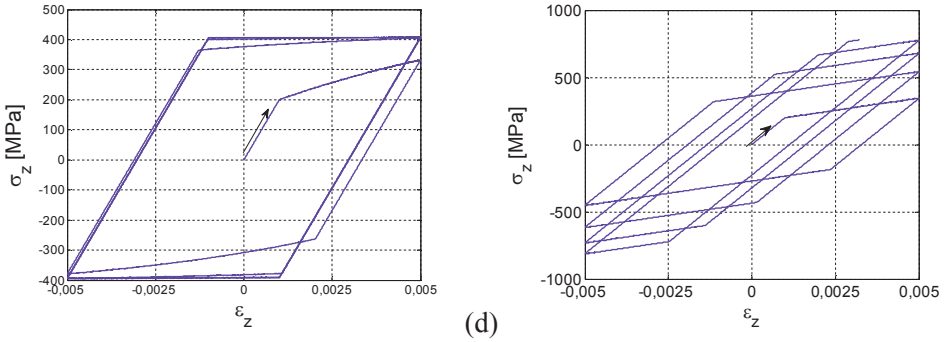

Kuva 2. Pakkosiirtymä (a), plastisuus-vauriomalli (epälineaarinen lujittuminen) (b) plastisuusmalli (epälineaarinen lujittuminen) (c) ja plastisuusmalli (lineaarinen lujittuminen) (d).

Vauriomallin lisääminen korjaa tämän puhtaan plastisuusmalliin heikkouden tuomalla mukaan jäykkyyden menetyksen, kuten Kuvasta 2b voidaan nähdä. Myös mikrosäröjen sulkeutumisefekti voidaan selvästi havaita puristus- ja vetopuolen käyrien epäsymmetrisyytenä. Mainitaan lopuksi, että Bauschinger-effekti voidaan havaita kaikissa Kuvan 2 tuloksissa.

Johtopäätökset

Tässä artikkelissa esitetty yksinkertainen J_2-plastisuus-vauriomalli varustettuna epälineaarisilla lujittumislaeilla kykenee mallintamaan useita metallien käyttäytymisen tärkeitä syklisessä kuormituksessa esiintyviä piirteitä. Näihin piirteisiin sisältyy isotrooppinen ja kinemaattinen lujittuminen, jotka ilmenevät myötölujuuden kasvamisena ja myötöpinnan siirtymisenä (Bauschinger-effekti), lujuudenmenetys eli pehmeneminen sekä jäykkyyden menetys eli vaurio. Ne ilmiöt, joita malli ei kykene ennustamaan, kuten kuroutuminen 1D-vetokokeessa, ovat pääosin pienten siirtymien teorian heikkouksia. Malli ei myöskään ennusta hystereesiä eikä vaurion indusoimaa anisotropiaa.

Lähteet

[1] J. Lemaitre, *A Course on Damage Mechanics*, Springer-Verlag, 1990.
[2] P. Grassl, M. Jirásek, Damage-plastic model for concrete failure, *International Journal of Solids and Structures*, 43: 7166-7196, 2006.
[3] J.C. Simo, T.J.R. Hughes, *Computational Inelasticity*, Springer, 2000.

Timo Saksala
Tampereen teknillinen yliopisto, konstruktiotekniikan laitos
PL 589, FI-33101, Tampere, Finland
timo.saksala@tut.fi

Screw dislocation in functionally graded layers with arbitrary gradation

S. M. Mousavi[1], S. J. Fariborz[2], J. Paavola[1]

[1]Department of Civil and Structural Engineering,
Aalto University, Finland
[2]Department of Mechanical Engineering,
Amirkabir University of Technology, Iran

Summary. Dislocation solutions can be utilized in the fracture analysis of materials via distributed dislocation technique (DDT). Recently, DDT was utilized in static and elastodynamic analysis of different functionally graded (FG) domains. The authors applied DDT for the analysis of a cracked FG layer, taking into account the energy dissipation in the material (Mousavi et al., 2011; Mousavi et al., 2012). The material properties in the above mentioned investigations were assumed to vary exponentially with the same rate. The assumption considerably simplifies the solution of ensuing differential equation. Nonetheless, it may cause a significant inaccuracy of the results. In this article, the assumption has been relaxed for static analysis allowing the solution of screw dislocation in FGM layers with arbitrary exponential gradation.

Key words: Screw dislocation, Functionally graded, Antiplane

Esitys on julkaistu *Rakenteiden mekaniikka lehdessä*: Vol. 45, 2012, Nro 3.

Two thermodynamically consistent formulations of a strain-rate dependent ductile-to-brittle transition model

Juha Hartikainen[1], Kari Kolari[2], Reijo Kouhia[3], and Saba Tahaei Yaghoubi[1]

[1]Aalto University Department of Civil and Structural Engineering,
P.O. Box 12100, FI-00076 Aalto, Finland
[2]VTT, P.O. Box 1806, 02044 VTT, Finland
[3]Department of Mechanics and Design, Tampere University of Technology
P.O. Box 589, FI-33101 Tampere, Finland

Summary. In this paper, two partially complementary formulations of a simple phenomenological constitutive model for ductile-to-brittle transition of rate-dependent solids are presented. The models are based on consistent thermodynamic formulation using proper expressions for the Helmholtz free energy or its complementary form of the dissipation potential. Basic features of the models as well as their implication to the numerical implementation are discussed.

Introduction

Most materials exhibit rate-dependent inelastic behaviour. Increasing strain-rate usually increases the yield stress thus enlarging the elastic range. However, the ductility is gradually lost and for some materials there exists a rather sharp transition strain-rate after which the material behaviour is completely brittle.

In the model first presented at the Finnish Mechanics Days, Lappeenranta 2006, the elastic behaviour is described by the Helmholtz free energy using elastic strain and damage variable as state variables. In addtion, the dissipation potential is additively split into damage and visco-plastic parts and the transition behaviour is obtained using a stress dependent damage potential.

In the new model, the Gibbs free energy function, which is a partial Legendre transform to the Helmholtz free energy function, and the stress and crack density as independent state variables are used to capture the elastic behaviour.

Thermodynamic formulation

Model based on Helmholtz free energy and dissipation potential

The constitutive model presented in [1] is derived using a thermodynamic formulation, in which the material behaviour is described through the Helmholz free energy and the dissipation potential in terms of the variables of state and dissipation and considering that the Clausius-Duhem inequality is satisfied

The Helmholtz free energy

$$\psi = \psi(\boldsymbol{\epsilon}_\mathrm{e}, \omega) \tag{1}$$

is assumed to be a function of the elastic strains, $\boldsymbol{\epsilon}_\mathrm{e}$, and the so-called continuity or integrity, ω. The elastic strains together with the inelastic strains, $\boldsymbol{\epsilon}_\mathrm{i}$, constitute the total

strains as

$$\boldsymbol{\epsilon} = \boldsymbol{\epsilon}_{\mathrm{e}} + \boldsymbol{\epsilon}_{\mathrm{i}}. \tag{2}$$

The continuity in turn is a function of the scalar damage parameter, D, as

$$\omega = 1 - D. \tag{3}$$

It is used instead of the damage parameter to simplify the notation.

As usual in the solid mechanics, the dissipation potential

$$\varphi = \varphi(\boldsymbol{\sigma}, Y) \tag{4}$$

is expressed in terms of the thermodynamic forces $\boldsymbol{\sigma}$ and Y dual to the fluxes $\dot{\boldsymbol{\epsilon}}_{\mathrm{i}}$ and $\dot{\omega}$, respectively. The dissipation potential is associated with the power of dissipation, γ, such that

$$\gamma = \frac{\partial \varphi}{\partial \boldsymbol{\sigma}} : \boldsymbol{\sigma} + \frac{\partial \varphi}{\partial Y} Y. \tag{5}$$

Convexity is not a prerequisite for the dissipation potential but the condition that the product $(\partial\varphi/\partial\boldsymbol{\sigma}) : \boldsymbol{\sigma} + (\partial\varphi/\partial Y)Y$ is non-negative.

In the absence of thermal effects, the dissipation power can be expressed as

$$\gamma = -\rho\dot{\psi} + \boldsymbol{\sigma} : \dot{\boldsymbol{\epsilon}}, \tag{6}$$

where ρ is the material density. The Clausius-Duhem inequality

$$\gamma \geq 0, \tag{7}$$

which has to be satisfied for every thermodynamically admissible process. Using definition (5) and the result (6) and defining that $\partial\psi/\partial\omega = Y$, gives

$$\left(\boldsymbol{\sigma} - \rho\frac{\partial \psi}{\partial \boldsymbol{\epsilon}_{\mathrm{e}}}\right) : \dot{\boldsymbol{\epsilon}}_{\mathrm{e}} + \left(\dot{\boldsymbol{\epsilon}}_{\mathrm{i}} - \frac{\partial \varphi}{\partial \boldsymbol{\sigma}}\right) : \boldsymbol{\sigma} + \left(-\dot{\omega} - \frac{\partial \varphi}{\partial Y}\right) Y = 0. \tag{8}$$

Then, if eq. (8) holds for any evolution of $\dot{\epsilon}_{\mathrm{e}}$, σ and Y, inequality (7) is satisfied and the following relevant constitutive relations are obtained:

$$\boldsymbol{\sigma} = \rho\frac{\partial \psi}{\partial \boldsymbol{\epsilon}_{\mathrm{e}}}, \qquad \dot{\boldsymbol{\epsilon}}_{\mathrm{i}} = \frac{\partial \varphi}{\partial \boldsymbol{\sigma}}, \qquad \dot{\omega} = -\frac{\partial \varphi}{\partial Y}. \tag{9}$$

To model the ductile-to-brittle transition due to increasing strain-rate, the dissipation potential is decomposed into the brittle damaging part, φ_{d}, and the ductile viscoplastic part, φ_{vp}, as

$$\varphi(\boldsymbol{\sigma}, Y) = \varphi_{\mathrm{d}}(Y)\varphi_{\mathrm{tr}}(\boldsymbol{\sigma}) + \varphi_{\mathrm{vp}}(\boldsymbol{\sigma}), \tag{10}$$

where the transition function, φ_{tr}, deals with the change in the mode of deformation when the strain-rate $\dot{\boldsymbol{\epsilon}}_{\mathrm{i}}$ increases.

Model based on Gibbs function and dissipation potential

In the new model, the elastic properties are capured by using the Gibbs function,

$$\psi^{\mathrm{c}} = \psi^{\mathrm{c}}(\boldsymbol{\sigma}, \alpha) \tag{11}$$

where the stress $\boldsymbol{\sigma}$ and the crack density α are independent state variables [2, 3]. The Helmholtz free energy and the Gibbs function are related by the partial Legendre transformation as [1]

$$\rho\psi + \rho\psi^{\mathrm{c}} = \boldsymbol{\sigma} : \boldsymbol{\epsilon}_{\mathrm{e}}. \tag{12}$$

Now the dissipation potential

$$\varphi^{\mathrm{c}} = \varphi^{\mathrm{c}}(\dot{\boldsymbol{\epsilon}}_{\mathrm{i}}, Z) = \varphi^{\mathrm{c}}_{\mathrm{d}}(Z)\varphi^{\mathrm{c}}_{\mathrm{tr}}(\dot{\boldsymbol{\epsilon}}_{\mathrm{i}}) + \varphi^{\mathrm{c}}_{\mathrm{vp}}(\dot{\boldsymbol{\epsilon}}_{\mathrm{i}}) \tag{13}$$

is expressed in terms of the dissipative flux $\dot{\boldsymbol{\epsilon}}_{\mathrm{i}}$ dual to $\boldsymbol{\sigma}$ and the thermodynamic force Z dual to the flux $\dot{\alpha}$, respectively. The dissipation potential is associated with the power of dissipation, γ, such that

$$\gamma = \frac{\partial\varphi^{\mathrm{c}}}{\partial\dot{\boldsymbol{\epsilon}}_{\mathrm{i}}} : \dot{\boldsymbol{\epsilon}}_{\mathrm{i}} + \frac{\partial\varphi^{\mathrm{c}}}{\partial Z} Z. \tag{14}$$

Differentiating equation (12) by parts with respect to time and assuming constant density, results in

$$\rho\dot{\psi} = \dot{\boldsymbol{\sigma}} : \boldsymbol{\epsilon}_{\mathrm{e}} + \boldsymbol{\sigma} : \dot{\boldsymbol{\epsilon}}_{\mathrm{e}} - \rho\dot{\psi}^{\mathrm{c}}, \tag{15}$$

and substituting it to the expression of dissipation (6) power gives

$$\gamma = \left(\rho\frac{\partial\psi^{\mathrm{c}}}{\partial\boldsymbol{\sigma}} - \boldsymbol{\epsilon}_{\mathrm{e}}\right)\dot{\boldsymbol{\sigma}} + \boldsymbol{\sigma} : \dot{\boldsymbol{\epsilon}}_{\mathrm{i}} + \frac{\partial\psi^{\mathrm{c}}}{\partial\alpha}\dot{\alpha}. \tag{16}$$

Combining equations (14) and (16) results in

$$\left(\rho\frac{\partial\psi^{\mathrm{c}}}{\partial\boldsymbol{\sigma}} - \boldsymbol{\epsilon}_{\mathrm{e}}\right)\dot{\boldsymbol{\sigma}} + \left(\boldsymbol{\sigma} - \frac{\partial\varphi^{\mathrm{c}}}{\partial\dot{\boldsymbol{\epsilon}}_{\mathrm{i}}}\right) + \left(\dot{\alpha} - \frac{\partial\varphi^{\mathrm{c}}}{\partial Z}\right) Z = 0, \tag{17}$$

and for any evolution of $\dot{\boldsymbol{\sigma}}, \dot{\boldsymbol{\epsilon}}_{\mathrm{p}}$ and Z, the following constitutive equations are obtained

$$\boldsymbol{\epsilon}_{\mathrm{e}} = \rho\frac{\partial\psi^{\mathrm{c}}}{\partial\boldsymbol{\sigma}}, \qquad \boldsymbol{\sigma} = \frac{\partial\varphi^{\mathrm{c}}}{\partial\dot{\boldsymbol{\epsilon}}_{\mathrm{i}}}, \qquad \dot{\alpha} = \frac{\partial\varphi^{\mathrm{c}}}{\partial Z}. \tag{18}$$

Particular models

Model based on Helmholtz free energy and dissipation potential

A particular expression for the free energy, describing the elastic material behaviour with the reduction effect due to damage, is given by

$$\rho\psi = \frac{1}{2}\omega\boldsymbol{\epsilon}_{\mathrm{e}} : \boldsymbol{C}_{\mathrm{e}} : \boldsymbol{\epsilon}_{\mathrm{e}} \tag{19}$$

where $\boldsymbol{C}_{\mathrm{e}}$ is the elasticity tensor.

Applying an overstress type of viscoplasticity [6–8] and the principle of strain equivalence [9,10], the following choices are made to characterize the inelastic material behaviour:

$$\varphi_{\mathrm{d}} = \frac{1}{r+1}\frac{Y_{\mathrm{r}}}{\tau_{\mathrm{d}}\omega}\left(\frac{Y}{Y_{\mathrm{r}}}\right)^{r+1}, \tag{20}$$

$$\varphi_{\mathrm{tr}} = \frac{1}{pn}\left[\frac{1}{\tau_{\mathrm{vp}}\eta}\left(\frac{\bar{\sigma}}{\omega\sigma_{\mathrm{r}}}\right)^{p}\right]^{n}, \tag{21}$$

$$\varphi_{\mathrm{vp}} = \frac{1}{p+1}\frac{\sigma_{\mathrm{r}}}{\tau_{\mathrm{vp}}}\left(\frac{\bar{\sigma}}{\omega\sigma_{\mathrm{r}}}\right)^{p+1}, \tag{22}$$

[1]Often the Gibbs function is defined as opposite to the present definition, e.g. [4, 5]. Here, the mathematical definition for the Legendre transformation is used.

where parameters τ_d, r and n are associated with the damage evolution, and parameters τ_vp and p with the visco-plastic flow. In addition, η denotes the inelastic transition strain-rate. The relaxation times τ_d and τ_vp have the dimension of time and the exponents $r, p \geq 0$ and $n \geq 1$ are dimensionless. $\bar{\sigma}$ is a scalar function of stress, e.g. the effective stress $\sigma_\mathrm{eff} = \sqrt{3J_2}$, where J_2 is the second invariant of the deviatoric stress. The reference values Y_r and σ_r can be chosen arbitrarily, and they are used to make the expressions dimensionally reasonable. Since only isotropic elasticity is considered, the reference value Y_r is chosen as $Y_\mathrm{r} = \sigma_\mathrm{r}^2/2E$, where E is the Young's modulus.

Making use of eqs. (2) and (9), choices (19)-(22) yield the following constitutive equations:

$$\boldsymbol{\sigma} = \omega \boldsymbol{C}_\mathrm{e} : (\boldsymbol{\epsilon} - \boldsymbol{\epsilon}_\mathrm{i}), \tag{23}$$

$$\dot{\boldsymbol{\epsilon}}_\mathrm{i} = \left[\frac{\varphi_\mathrm{d}}{(\tau_\mathrm{vp}\eta)^n \omega \sigma_\mathrm{r}} \left(\frac{\bar{\sigma}}{\omega \sigma_\mathrm{r}} \right)^{np-1} + \frac{1}{\tau_\mathrm{vp}\omega} \left(\frac{\bar{\sigma}}{\omega \sigma_\mathrm{r}} \right)^{p} \right] \frac{\partial \bar{\sigma}}{\partial \boldsymbol{\sigma}}, \tag{24}$$

$$\dot{\omega} = -\frac{\varphi_\mathrm{tr}}{\tau_\mathrm{d}\omega} \left(\frac{Y}{Y_\mathrm{r}} \right)^{r}. \tag{25}$$

Moreover,

$$Y = \rho \frac{\partial \psi}{\partial \omega} = \frac{1}{2} (\boldsymbol{\epsilon} - \boldsymbol{\epsilon}_\mathrm{i}) : \boldsymbol{C}_\mathrm{e} : (\boldsymbol{\epsilon} - \boldsymbol{\epsilon}_\mathrm{i}) = \frac{1}{2\omega^2} \boldsymbol{\sigma} : \boldsymbol{C}_\mathrm{e}^{-1} : \boldsymbol{\sigma}. \tag{26}$$

The general properties of this particular model are discussed in detail in [1].

Model based on Gibbs function and dissipation potential

A comparable expression to (19) describing the elastic material behaviour with the reduction effect due to damage can be given the Gibbs function

$$\rho \psi^\mathrm{c} = \frac{1}{2} (1+\alpha) \boldsymbol{\sigma} : \boldsymbol{C}_\mathrm{e}^{-1} : \boldsymbol{\sigma}. \tag{27}$$

For the dissipation potential the following expressions are used

$$\varphi_\mathrm{d}^\mathrm{c} = \frac{1}{r+1} \frac{(1+\alpha) Z_\mathrm{r}}{\tau_\mathrm{d}} \left(\frac{Z}{Z_\mathrm{r}} \right)^{r+1}, \tag{28}$$

$$\varphi_\mathrm{tr}^\mathrm{c} = \frac{1}{n} \left((1+\alpha) \frac{\|\dot{\boldsymbol{\epsilon}}_\mathrm{i}\|}{\eta} \right)^{n}, \tag{29}$$

$$\varphi_\mathrm{vp}^\mathrm{c} = \frac{p}{p+1} \frac{\sigma_\mathrm{r}}{\tau_\mathrm{vp}} \left[\tau_\mathrm{vp} (1+\alpha) \|\dot{\boldsymbol{\epsilon}}_\mathrm{i}\| \right]^{p+1}, \tag{30}$$

where the norm of the inelastic strain rate can be e.g. the equivalent inelastic strain rate $\dot{\bar{\epsilon}}_\mathrm{i} = \sqrt{(2/3) \dot{\boldsymbol{e}}_\mathrm{i} : \dot{\boldsymbol{e}}_\mathrm{i}}$, where $\dot{\boldsymbol{e}}_\mathrm{i}$ is the rate of the deviatoric inelastic strain. The reference values σ_r and Z_r can be chosen freely. In this work, the value $Z_\mathrm{r} = \sigma_\mathrm{r}/2E$ has been used. From equations (18) the following constitutive equations are obtained

$$\boldsymbol{\epsilon}_\mathrm{e} = (1+\alpha) \boldsymbol{C}_\mathrm{e}^{-1} : \boldsymbol{\sigma}, \tag{31}$$

$$\boldsymbol{\sigma} = \left[\frac{n}{\eta} \varphi_\mathrm{d}^\mathrm{c} \left((1+\alpha) \frac{\|\dot{\boldsymbol{\epsilon}}_\mathrm{i}\|}{\eta} \right)^{n-1} + \sigma_r [\tau_\mathrm{vp} (1+\alpha) \|\dot{\boldsymbol{\epsilon}}_\mathrm{i}\|]^{1/p} \right] \frac{\partial \|\dot{\boldsymbol{\epsilon}}_\mathrm{i}\|}{\partial \dot{\boldsymbol{\epsilon}}_\mathrm{i}}, \tag{32}$$

$$\dot{\alpha} = \frac{1+\alpha}{\tau_\mathrm{d}} \left(\frac{Z}{Z_\mathrm{r}} \right)^{r} \left((1+\alpha) \frac{\|\dot{\boldsymbol{\epsilon}}_\mathrm{i}\|}{\eta} \right)^{n}. \tag{33}$$

Furthermore, the thermodynamic force Z obtains the form

$$Z = \rho \frac{\partial \psi^c}{\partial \alpha} = \frac{1}{2} \boldsymbol{\sigma} : \boldsymbol{C}_{\mathrm{e}}^{-1} : \boldsymbol{\sigma} = \frac{1}{2(1+\alpha)^2} \boldsymbol{\epsilon}_{\mathrm{e}} : \boldsymbol{C}_{\mathrm{e}} : \boldsymbol{\epsilon}_{\mathrm{e}}. \tag{34}$$

On numerical integration

In plasticity and viscoplasticity the backward Euler time integration seems to be the most popular one, mostly due to its simplicity and good accuracy when finite size timesteps are used [11]. However, this practically very appealing accuracy property of the backward Euler scheme is lost when material degradation is coupled in the model [12,13]. Integration of the model (32)-(25) is discussed in refs. [1, 13]. It was found that the discontinuous Galerkin scheme with linear trial function has good accuracy also for large time steps, especially when the integrals are evaluated by the two point Gauss-Lobatto quadrature.

However, it is easy to see that the system (31)-(33) differs substantially from the system (32)-(25) since the equation (32) is an implicit differential equation. The stress driven format can be obtained from equation (31) by elimination the inelastic strain

$$\boldsymbol{\epsilon}_{\mathrm{i}} = \boldsymbol{\epsilon} - (1+\alpha) \boldsymbol{C}_{\mathrm{e}}^{-1} : \boldsymbol{\sigma}, \tag{35}$$

and thus the inelastic strain rate can be expressed as a function of stress, stress rate and strain rate

$$\dot{\boldsymbol{\epsilon}}_{\mathrm{i}} = \dot{\boldsymbol{\epsilon}} - (1+\alpha) \boldsymbol{C}_{\mathrm{e}}^{-1} : \dot{\boldsymbol{\sigma}} - \boldsymbol{C}_{\mathrm{e}}^{-1} : \boldsymbol{\sigma} \dot{\alpha}. \tag{36}$$

Solution of the implicit differential equation does not pose any particular problem. It is easy to see that the implicit differential equation

$$f(\dot{y}, y) = 0, \tag{37}$$

can be transformed to a diffrerential-algebraic equation (DAE) system by introducing an auxiliary variable $p = \dot{y}$. On the other hand, direct insertion of time discretization into (32) results in a non-linear algebraic equation which can be solved using the Newton's iteration.

Concluding remarks

A new formulation for a strain-rate dependent ductile-to brittle transition model is presented, where the dissipation potential is expressed in terms of inelastic strain rate and the thermodynamic force dual to the crack density rate. Such formulation is more natural to control strain-rate dependent deformation mechanisms. In addition, the elasticity is described by the Gibbs function, which facilitates the description of damage processes in non-isothermal case [14].

References

[1] Fortino, S., Hartikainen, J., Kolari, K., Kouhia, R. & Manninen, T. A constitutive model for strain-rate dependent ductile-to brittle-transition. In von Hertzen, R. & Halme, T. (eds.) *The IX Finnish Mechanics Days*, 652–662 (Lappeenranta University of Technology, Lappeenranta, 2006).

[2] Kachanov, M. Effective elastic properties of cracked solids: critical review of some basic concepts. *Applied Mechanics Review* **45**, 304–335 (1992).

[3] Basista, M. Micromechanics of damage in brittle solids. In Skrzypek, J. & Ganczarski, A. (eds.) *Anisotropic Behaviour of Damaged Materials*, vol. 9 of *Lecture Notes in Applied and Computational Mechanics*, 221–258 (Springer-Verlag, 2003).

[4] Malvern, L. *Introduction to the Mechanics of a Continuous Medium* (Prentice Hall, Englewood Cliffs, New Jersey, 1969).

[5] Holzapfel, G. *Nonlinear Solid Mechanics - A Continuum Approach for Engineering* (John Wiley & Sons, 2000).

[6] Perzyna, P. *Fundamental problems in viscoplasticity*, vol. 9 of *Advances in Applied Mechanics*, 243–377 (Academic Press, London, 1966).

[7] Duvault, G. & Lions, L. *Inequalities in Mechanics and Physics* (Springer, Berlin, 1972).

[8] Ristinmaa, M. & Ottosen, N. Consequences of dynamic yield surface in viscoplasticity. *International Journal of Solids and Structures* **37**, 4601–4622 (2000).

[9] Lemaitre, J. & Chaboche, J.-L. *Mechanics of Solid Materials* (Cambridge University Press, 1990).

[10] Lemaitre, J. *A Course on Damage Mechanics* (Springer-Verlag, Berlin, 1992).

[11] Kouhia, R., Marjamäki, P. & Kivilahti, J. On the implicit integration of inelastic constitutive equations. *International Journal for Numerical Methods in Engineering* **62**, 1832–1856 (2005).

[12] Wallin, M. & Ristinmaa, M. Accurate stress updating algorithm based on constant strain rate assumption. *Computer Methods in Applied Mechanics and Engineering* **190**, 5583–5601 (2001).

[13] Eirola, T., Hartikainen, J., Kouhia, R. & Manninen, T. Some observations on the integration of inelastic constitutive models with damage. In Dahlblom, O. *et al.* (eds.) *Proceedings of the 19th Nordic Seminar on Computational Mechanics*, 23–32 (Division of Structural Mechanics, LTH, Lund University, 2006).

[14] Hartikainen, J., Kouhia, R. & Manninen, T. A model for concrete at high temperatures. In von Hertzen, R. & Halme, T. (eds.) *The IX Finnish Mechanics Days*, 683–691 (Lappeenranta University of Technology, Lappeenranta, 2006).

Paineiskumallin soveltuminen sydän-verisuonisto-yhdistelmälle

Jari Mäkinen, Matti Huotari, Antti Ylinen

Tiivistelmä. Esityksessä tutkitaan hydrauliikan siirtolinjalle kehitetyn paineiskun käyttäytymistä kuvaavan laskentamallin soveltuvuutta sydän-verisuonistoyhdistelmälle. Hydrauliikan siirtolinjan laskentamallissa oletuksena on se, että siirtolinjaputken halkaisija on vakio ja sen seinämä on jäykkä. Verisuonistojen joustavuus voidaan siirtolinjamallissa ottaa huomioon efektiivisesti pienentämällä pulssiaallon etenemisnopeutta. Verisuonien ohentuminen otetaan huomioon paloittain suonien haarautuessa uusiksi suoniksi. Lisäksi tutkitaan kuinka suuren osan ihmisen verisuonistoa pitää mallintaa, että oleellisimmat ilmiöt saataisiin mallinnettua verisuoniston paine- ja fotopletysmografiesta pulssissa.

Avainsanat: paineisku, sydän-verisuonisto

Paineiskumallit

Tässä kappaleessa esitellään paineiskumallit, joita voidaan käyttää verisuonien sydämen aiheuttaman painesysäyksen mallintamiseen. Laplace-muunnetut liikeyhtälöt viskoosiselle kokoonpuristuvalle nesteelle ovat [1]:

$$\frac{dP(x,\bar{s})}{dx} = -\frac{Z_0 \Gamma^2(\bar{s})}{L\bar{s}} Q(x,\bar{s})$$
$$\frac{dQ(x,\bar{s})}{dx} = -\frac{\bar{s}}{LZ_0} P(x,\bar{s}) \qquad (x,\bar{s}) \in (0,L)\times \mathrm{C} \qquad (1a,1b)$$

missä impedanssi $Z_0 = \dfrac{\rho_0 c_0}{\pi r_0^2}$ ja $\bar{s} = Ts$, missä $T = L/c_0$.

Ensimmäinen yhtälö on yksinkertaistettu muoto Navierin ja Stokesin liikeyhtälöstä laminaarille virtaukselle sylinterikoordinaatistossa. Leviämisfunktion Γ^2 avulla kuvataan joko kitkatonta virtausta, taajuudesta riippumatonta viskoosista virtausta tai taajuudesta riippuvaa viskoosista virtausta. Tätä viimeistä mallia kutsutaan myös dissipatiiviseksi kitkamalliksi, koska siinä korkeat taajuuskomponentit vaimenevat nopeammin kuin hitaat. Jälkimmäinen yhtälöistä (1) on yhdistetty tila- ja jatkuvuusyhtälö. Muut suureet ovat: ρ_0 tiheys, c_0 äänennopeus, r_0 putken säde, L on siirtolinjan pituus.

Yhtälöt (1) pitävät sisällään seuraavat oletukset:

- neste toteuttaa Stokesin lain eli neste on newtonilaista.
- virtaus on laminaarista, i.e. Reynoldsin luku pienempi kuin 2300.
- virtaus on aksiaalisymmetristä. Tämä tarkoittaa, sitä että verisuonet ovat suoria ja poikkileikkaukseltaan ympyröitä.
- virtauksen säteensuuntainen liike voidaan ottaa huomiotta.
- materiaalisuureet ovat vakioita
- seinämät ovat jäykkiä. Verisuonelle tämä ei pidä tarkasti paikkansa, sillä oletus ei ota huomioon verenpaineen laajentavaa vaikutusta suonen halkaisijaan. Äänen etenemisnopeutta voidaan kuitenkin säätää, siten että verisuonten seinämien joustavuus otetaan efektiivisesti huomioon.

Eliminoimalla yhtälöistä (1) tilavuusvirta Q voidaan yhtälöt kirjoittaa pelkästään paineen P avulla:

$$-L^2 \frac{d^2 P(x)}{dx^2} + \Gamma^2 P(x) = 0 \qquad x \in (0, L) \tag{2}$$

Kolme erilaista reunaehtoa esiintyy putkivirtaukselle. Neumannin reunaehto

$$P'(0) = -\frac{Z_0 \Gamma^2}{L\bar{s}} Q_0, \qquad P'(L) = \frac{Z_0 \Gamma^2}{L\bar{s}} Q_1 \tag{3}$$

jossa on annettu verisuonen päässä tilavuusvirrat. Dirichletin reunaehto on

$$P(0) = P_0, \qquad P(L) = P_1 \tag{4}$$

jossa on annettu paineet verisuonen päissä. Lisäksi voidaan antaa Robinin reunaehto

$$P(0) = P_0, \qquad P'(L) = \frac{Z_0 \Gamma^2}{L\bar{s}} Q_1 \tag{5}$$

jossa toisessa päässä on annettu paine ja toisessa päässä tilavuusvirta.

Jos yhtälöistä (1) eliminoidaan paine, saadaan edelliselle duaalinen aaltotehtävä

$$-L^2 \frac{d^2 Q(x)}{dx^2} + \Gamma^2 Q(x) = 0 \qquad x \in (0, L) \tag{6}$$

Reunaehdot ovat tässä tapauksessa; Neumann:

$$Q'(0) = -\frac{\bar{s}}{LZ_0} P_0, \qquad Q'(L) = -\frac{\bar{s}}{LZ_0} P_1 \tag{7}$$

Dirichlet:

$$Q(0) = Q_0, \qquad Q(L) = -Q_1 \tag{8}$$

ja Robin:

$$Q(0) = Q_0, \qquad Q'(L) = -\frac{\bar{s}}{LZ_0} P_1 \tag{9}$$

Kaksi aaltoyhtälöä (2) ja (6) reunaehtoineen (3-5) ja (7-9) johtaa kuuteen erilaiseen siirtolinjamalliin. Seuraavaksi esitellään näiden siirtolinjamallien variaatiomuodot.

Aaltoyhtälön (2) variaatiomuoto Neumannin reunaehtolla (3) saadaan kertomalla aaltoyhtälö (2) testifunktiolla (virtuaalisella paineella) δP ja integoimalla putkilinjan yli ja lopuksi osoittaisinteroimalla

$$\int_0^L \left(L^2 P' \delta P' + \Gamma^2 P \, \delta P \right) dx = L Z_0 \frac{\Gamma^2}{\bar{s}} \left(Q_1 \, \delta P_1 + Q_0 \, \delta P_0 \right) \tag{10}$$

Saman aaltoyhtälön (2) variaatiomuoto Dirichletin reunaehdolla (4) on vastaavasti

$$\int_0^L \left(L^2 P' \delta P' + \Gamma^2 P \, \delta P \right) dx = 0, \tag{11}$$

missä δP toteuttaa nollareunaehdot. Vastaavasti Robinin reunaehtoilla (5)

$$\int_0^L \left(L^2 P' \delta P' + \Gamma^2 P \, \delta P \right) dx = L Z_0 \frac{\Gamma^2}{\bar{s}} \left(Q_1 \, \delta P_1 \right), \tag{12}$$

missä δP toteuttaa nollareunaehdon: $\delta P(0) = 0$.

Duaaliselle ongelmalle (6) Neumannin reunaehdolla (7) variaatiomuoto on

$$\int_0^L \left(L^2 Q' \delta Q' + \Gamma^2 Q \, \delta Q \right) dx = \frac{L \bar{s}}{Z_0} \left(P_1 \delta Q_1 + P_0 \delta Q_0 \right), \tag{13}$$

Dirichletin reunaehtoilla (8) variaatiomuoto on

$$\int_0^L \left(L^2 Q' \delta Q' + \Gamma^2 Q \, \delta Q \right) dx = 0, \tag{14}$$

missä δQ toteuttaa nollareunaehtot. Robinin reunaehdoilla variaatiomuoto on

$$\int_0^L \left(L^2 Q' \delta Q' + \Gamma^2 Q \, \delta Q \right) dx = \frac{L \bar{s}}{Z_0} P_1 \delta Q_1, \tag{15}$$

Lähteessä [1] on yksityiskohtaisesti kuvattu, miten näistä variaatiomuodoista saadaan siirtofunktiomallit. Variaatiomuotoihin voidaan sijoittaa paine- tai tilavuusvirta-yritteenä kunkin tehtävän ominaismuotofunktiot. Tällöin on mahdollista vaimentaa korkeampia taajuuksia vahvemmin kuin matalia taajuuksia.

Leviämisfunktio

Lineaarinen kitkamalli (1D) olettaa parabolisen nopeusjakauman putkivirtaukselle. 2D kitkamalli vaimentaa korkeampia taajuuksia voimakkaammin kuin matalia taajuuksia, jolloin vaimennus muuttaa aaltoprofiilia huomattavasti.

Leviämisfunktiolle Γ^2 voidaan eri tilanteessa käyttää seuraavia arvoja [1]

$$\Gamma^2(\bar{s}) = \begin{cases} \bar{s}^2, & \text{kitkaton virtaus} \\ \bar{s}^2 + \varepsilon\bar{s}, & \text{1D kitkamalli} \\ \dfrac{\bar{s}^2}{1 - \dfrac{2J_1(\kappa)}{\kappa J_0(\kappa)}}, & \text{2D kitkamalli} \end{cases} \tag{16}$$

missä $\kappa^2 = -8\frac{\bar{s}}{\varepsilon}$ ja kitkakerroin $\varepsilon = \frac{8\nu_0 L}{r_0^2 c_0}$. J_1 ja J_0 ovat Besselin funktioita.

Paineiskumallien siirtofunktiossa [1] esiintyy jakajassa termejä, jotka approksimoidaan

$$\Gamma^2(\bar{s}) + \alpha_i^2 \approx \bar{s}^2 + \bar{s}\varepsilon_i + \omega_i^2 \tag{17}$$

jossa ominaiskulmataajuus ω_i ja moodivaimennus ε_i saadaan kaavasta

$$\begin{aligned} \omega_i &= \alpha_i - \frac{1}{4}\sqrt{\alpha_i\varepsilon} + \frac{1}{16}\varepsilon, \qquad i = 1,2,\ldots,n \\ \varepsilon_i &= \frac{1}{2}\sqrt{\alpha_i\varepsilon} + \frac{1}{8}\varepsilon \qquad i = 1,2,\ldots,n \end{aligned} \tag{18}$$

Johtopäätökset

Tässä esityksessä on lyhyesti kuvattu ne paineiskumallit, joita on kehitetty hydrauliikan siirtolinjojen paineiskujen mallintamiseen ja paineiskujen simulointiin. Paineiskun aaltotehtävä voidaan esittää joko primäärisenä, jolloin perustuntemattomana kenttäsuureena on paine, tai duaalisen, jolloin perustuntemattomana on tilavuusvirta. Oleellista on äänen etenemisnopeuden säätäminen siten, että se vastaa joustavan verisuonen häiriön etenemisnopeutta. Toinen tärkeä ominaisuus on dissipatiivisen 2D-kitkamallin käyttö, jolla saadaan muutettua paineaallon muotoa.

Viitteet

[1] J. Mäkinen, R. Piché, A. Ellman, Fluid Transmission Line Modeling Using a Variational Method, *ASME Journal of Dynamic Systems, Measurement, and Control*, 122(1), pp. 153-162, 2000

Jari Mäkinen,
TTY/Rakennustekniikan laitos,
jari.m.makinen@tut.fi

Antti Ylinen
TTY/Konstruktiotekniikan laitos
antti.ylinen@tut.fi

Matti Huotari
OY/Tietotekniikan osasto
matti.huotari@ee.oulu.fi

Suurikaliiperisten ruutiaseiden tuliputkien lujuus- ja materiaaliteknisiä kehitysnäkymiä

Seppo Moilanen

Tiivistelmä. Kirjoitelmassa esitetään lyhyt katsaus raskaiden ruutiaseiden tuliputkien lujuusopillisiin ja materiaaliteknisiin suunnitteluperusteisiin ja -menetelmiin sekä arvioidaan niiden mahdollisia kehitysnäkymiä lähitulevaisuudessa kirjallisuustutkimukseen perustuen.

Avainsanat: Tykit, tuliputket, autofretointi, pinnoitus, väsyminen, kuluminen.

Taustaa

Nykyisten ja tulevaisuuden raskaiden asejärjestelmien kehitystä ohjaavat suorituskykyvaatimuksina mm: Lyhyt vasteaika uhkahavaintoon, hyvä operointikyky, asevaikutus ja liikkuvuus, yhteensopivuus muiden ase-, tiedustelu, tulenjohto- jne. järjestelmien kanssa sekä niiden edellyttämä ns. korkean teknologian järjestelmien hyödyntäminen. Monipuolisten ja osittain ristiriitaisten käyttäjävaatimuksien seurauksena raskaan aseen tuliputken suunnittelussa ja valmistuksessa on huomioitava laukaussyklin ääriolosuhteina samanaikaiset korkea ja nopea painekuormitus, palokaasujen korkea lämpötila ja niiden aiheuttama kemiallinen eroosio, ammuksen ja tuliputken vuorovaikutus ja sen muutokset putken eriosissa jne. sekä aseen rakenteellisina vaatimuksina painon ja tilantarpeen minimointi yhdistettynä vakauteen, korkeaan toimintavarmuuteen ja –turvallisuuteen, käyttäjäystävällisyyteen ja yhteensopivuuteen sekä olemassa olevien että kehitteillä olevien, tulevaisuuden ampumatarvikkeiden kanssa [1, 2].

Suurikaliiperisten (kaliiperi tyypillisesti > 40 mm) asejärjestelmien painetermit ja niiden väliset suhteet on määritetty viitteen [3] Nato-standardissa, jota käytetään suunnitteluperusteena laajalti myös Nato-maiden ulkopuolella.

Teräs tuliputkimateriaalina

Kiivaasta tutkimuksesta huolimatta toistaiseksi ei ole löytynyt suurikaliiperisen ruutiaseen tuliputken materiaaliksi teräksen veroista kilpailijaa. Pääsyinä lienevät teräksen ja muidenkin metallien ylivoimainen sitkeys, erinomainen isku- ja murtumissitkeyden sekä lujuuden yhdistelmä keraameihin ja komposiitteihin nähden, stabiili ja laskennallisesti hyvin ennustettava väsymiskäyttäytyminen, hyvä ympäristöolosuhteiden ja kovakouraisen käytön sieto ja kaikki nämä yhdistettynä kustannustehokkaasti sekä materiaali- että valmistustekniikan osalta [4]. Suuret asetuottajamaat ovat standardoineet raskai-

den aseiden osien valmistukseen liittyviä seikkoja teräslaadut ja niiden keskeiset ominaisuudet mukaan lukien. Briteillä on DEF-standardit [8] ja Yhdysvalloissa MIL-standardit [9].

Terästoimittajan valmistustekniikasta riippuen tuliputkien taeaihiot valmistetaan sulattamalla raaka-aine ensin sähköuunissa, jonka jälkeen joko metallurgisilla sulan tyhjökäsittelyillä tai huomattavasti kalliimmilla uudelleensulatustekniikoilla kuten sähkö- tai vakuumisulatuksilla (ESR electro-slag re-melting tai VAR Vacuum-argon re-melting) [25] saavutetaan haluttu laatu taeaihion valokselle. Taulukossa 1 on esitetty muutamia aseiden painetta sulkevien osien ja erityisesti tuliputken materiaaliksi soveltuvien teräksien tyypillisiä mekaanisia arvoja valmiina, lämpökäsiteltynä takeena.

Taulukko 1. Tuliputkiteräksien tyypillisiä myötölujuuden R_e, murtovenymän A, iskusitkeyden KV ja murtumissitkeyden K_{IC} (tai K_q)vaatimusarvoja tai toimittajan ilmoittamia alarajoja. Murtolujuusvaatimus on tyypillisesti $R_m > R_e$+60 MPa.

Teräs, ohjeellinen seos	R_e MPa	A %	KV J	K_{IC}, K_q MPa $m^{1/2}$	Viite	HUOM.
3 % NiCrMoV	1 100		50 (-40°C)	150 (-40°C)	[4]	
4335 mod.	(1 180)	(10)	(8) (-40°C)	(74)	[5]	a
ASTM A723	1 100			140	[5]	b
35NiCrMoV12 5	1 100	13	35 (-40°C)	120 (-40°C)	N/A	
30NiCrMoV14	1 100	13	35 (-40°C)	120 (-40°C)	[7]	HBR, c
33NiCrMoV15	1 200	13	31 (-40°C)	120 (-40°C)	[7]	HB3, c
40NiCrMoV15	1 250	11	28 (-40°C)	110 (-40°C)	[7]	HB7, c
40NiCrMoV15	1 250	13	31 (-40°C)	110 (-40°C)	[7]	HB7ESR, c

HUOM:

a) Suluissa esitetyt arvot on mitattu Vietnamin sodan aikana palveluskäytössä murtuneesta 175 mm:n kenttätykin tuliputkesta (1966), [5, 6] sekä tuntematon lähde.
b) Tyypillinen nykyinen USA:n raskaiden aseiden tuliputkiteräs.
c) ”HBx”-merkintä on Aubert&Duval:n kauppalaatumerkintä ko. teräkselle.

Tuliputken lujuuslaskenta ja tuliputkirakenteita

Tuliputken lujuusopillisen mitoituksen tavoitteena on kevyt sekä väsymis- että kulumisominaisuuksiltaan kestävä ja suorituskykyvaatimukset täyttävä rakenne. Pääkuormitus on ruutikaasunpaine. Rihlatuilla aseilla ammuksen johtorenkaan putken välinen puristus saattaa aiheuttaa kaasunpaineeseen nähden ennakoimattoman suuren kosketuspainepiikin tuliputken sisäpintaan [18-20]. Tuliputket on perinteisesti mitoitettu käsilaskentamenetelmin ”yritä ja todenna, try and true” periaatteella [10-12] ja nykyisin hyödyntäen tietokoneiden tarjoamaa laskentakapasiteettia. Ensin määritetään laskennalliset staattiset painerajat ja sen jälkeen esim. lineaarista murtumismekaniikkaa soveltaen väsymispainerajat ja tuloksia verrataan ampumatarvikkeiden painearvoihin [17]. Kokemuksien myötä todentaminen on kehittynyt rutiininomaiseksi testaamiseksi, mutta resurssivaatimuksiltaan raskaaksi prosessiksi [6, 13-15], johon pienten maiden valmiudet eivät riitä yksinään eivätkä edes aina usean pienen maan yhteistyönäkään, vaikka testaamistarve on ilmeinen [2].

Sisäpuolisella paineella kuormitetun paksuseinämäisen sylinterin seinämän materiaali on lujuusopillisesti huonosti hyödynnetty, joten seinämän jännitysjakaumaa ja erityisesti kehäjännitysjakaumaa pyritään tuliputkissa tasoittamaan:

- Monikerrosrakenteilla, joissa on kaksi tai useampia sisäkkäisiä putkia joko:
  - vapaasti (välyssovitteella, jännityksetön lepotilassa) tai
  - puristussovitteella
- Autofretoimalla
- Kuitukomposiittikerrosrakenteilla metallisen sisäputken ulkopuolella
- Edellisten yhdistelmillä.

Välyssovitteinen monikerrosrakenne on ollut käytössä vanhojen raskaiden laivakanuunoiden tuliputkissa kuluneen sisäputken vaihdon mahdollistamiseksi, mutta nykyisin laivatykit ovat korvautuneet ohjusaseilla. Puristussovitteisia monikerrosrakenteita käytetään edelleen panoskammion alueella korvamaan puuttuvaa autofretointia ja niitä tutkitaan jäähdytetyn tuliputkien rakennevaihtoehtona, jossa kerrosputkien rajapintaan on koneistettu jäähdytysnesteen virtausurat. Kokoamisvaiheessa ulko- ja sisäputken lämpötilaeron avulla ei saada riittävää puristuspainetta eikä putkien keskinäistä lukitusta aikaiseksi, joten hydraulisia liitostekniikkoja on kehitelty puristuksen kasvattamiseksi [16].

Autofretointi

Autofretoinnissa putken seinämään synnytetään pysyvä muodonmuutos-/jännitystila ylipaineella, jonka jälkeen kuormittamattoman seinämän sisäosassa on kehän suuntainen puristusjännitys ja ulko-osalla vetojännitys [21, 22]. Teollisia autofretointitekniikkoja on kaksi; hydraulinen autofretointi nestepaineella (hydrostatic autofretage) ja karaautofretointi, jossa ylisuuri kara työnnetään putken läpi (swage autofretage). Karaautofretointi on nopea menetelmä ja se soveltuu hyvin sarjatuotantoon. Hydraulinen autofretointi on menetelmänä hidas, mutta se tarjoaa hyvät putki- tai materiaalikohtaiset räätälöintimahdollisuudet ja sen mittaustuloksia voidaan hyödyntää valmistuksen laadunvalvonnassa [24]. Autofretoinnin etuina saavutetaan:

- Jäännosjännityskenttä pienentää laukauksen aikana esiintyvää tuliputken kriittisen sisäpinnan jännitysmaksimia, -vaihtelua, jännitysintensiteetin arvoa ja vaihtelua
- Putken painerajat ja kestoikä laukauksina kasvavat. Tyypillisesti autofretoidun tuliputken kestoikä on (2…4) –kertainen autofretoimattomaan putkeen nähden
- Tuliputki voidaan valmistaa a) kevyemmäksi, b) matalalujuuksisemmasta ja sitkeämmästä teräksestä ja/tai c) voidaan sallia suurempia ja NDT-menetelmin helpommin havaittavia säröjä verrattuna autofetoimattomaan tuliputkeen
- Autofretoidun tuliputken läpimurtumista edeltää plastinen sitkeä muodonmuutosvaihe, koska tasomuodonmuutostilaa ei synny särön eteen jäävään loppukannakseen, (”yield-before-break, leak-before-break” [23]), joten vaurioitumisvaara on ehkä havaittavissa etukäteen.

Autofretoinnin haittoja ovat:

- Autofretointi on teknisesti vaativa lisätyövaihe tuliputken valmistuksessa ja se edellyttää resurssipanostusta laitteisiin sekä suunnittelu- ja valmistustekniikkaan

- Metalleilla esiintyvän Bauschinger-efektin vuoksi autofretoinnin lopputuloksen hallinta on hankalaa puristuspuolen myötölujuuden laskiessa
- Ainettapoistavat autofretoinnin jälkeiset tuliputken valmistusvaiheet kuten rihlaus, mahdolliset savunpoistimen virtausreikien poraukset tai loppukoneistus muuttavat seinämän jäännösjännityskenttää, jolloin autofretoinnin hyötyä menetetään
- Autofretoinnin jälkeisissä työvaiheissa tuliputkea ei voida lämmittää yli $t \approx 360\ ^{o}\mathrm{C}$, jotta autofretoinnin jäännösjännitykset eivät laukea. Tämä rajoittaa putken pinnoitusmenetelmien ja -tekniikoiden valintaa [31].

Kuitulujitteinen tuliputki

USA:ssa on Benet Labs:n johdolla tehty tutkimusta kuitulujitetun tuliputken valmistamiseksi 1980 ja 1990 luvuilla ja jälleen 2000 luvulla. Useita peräkkäisiä laukauksia ampuvan suurikaliiperisen aseen tuliputken komposiittirakenteissa on perinteisesti ollut kaksi pääongelmaa:

- Korkea käyttölämpötila ja ruutikaasujen eroosiovaikutus. Metallinen sisäputki on tarpeen eristeenä ja kaasukosketuksen esteenä
- Lämpölaajenemiskertoimien eroavuus teräksen arvoihin nähden, joka aiheuttaa komposiittivaipan irtoamisen teräsputken pinnasta komposiitin ”paiston” aikana ja viimeistään laukaus- ja palveluskuormituksien alaisena.

Edellisten lisäksi ongelmia ovat tuottaneet:

- Teräksen ja komposiitin kemiallinen yhteensopivuus (korroosio, syöpyminen)
- Kuitulujitteista tuliputkea ei voi autofretoida, koska komposiitit eivät kestä autofretoinnin jälkeistä jännitysten tasaamishehkutusta, $t \approx 360\ ^{o}\mathrm{C}$
- Kuitulujitteista putkea ei voi kromata, koska prosessissa syntyvä kromihappo tuhoaa komposiitin ja yhteisvaikutus likaa varsinaisen kromipinnoitteen
- Autofretoinnin aiheuttamat suuret säteensuuntaiset jännitykset, joita vain kehä- ja aksiaalisuunnassa kuitulujitettu komposiittirakenne ei kestä
- Vaikeudet autofretointia korvaavan, riittävän esijännityksen aikaansaamisessa.
- Komposiittirakenteen viruminen, etenkin esijännitetyn rakenteen tapauksessa
- Kuiturakenteen ballistisen iskun jälkeinen rakenteellinen kestävyys.

Em. ongelmien voittamiseksi on kehitetty paikallisen sulattamisen ”Cure in Place” valmistusmenetelmä, jossa komposiittimatriisi saadaan välittömästi lujitettua autofretoidun ja kromipinnoitetun teräsputken pintaan paikallisesti ilman autoklaaviuunikäsittelyä [26]. Kiedottavien kuitujen esijännityksellä, kylmän sisäputken ja lämpimän kiedottavan kuidun lämpötilaerolla kompensoidaan ohennetun teräsputken autofretointihyödyn vajetta. Komposiitissa on IM7-hiilikuitu polyeetterieetteriketoni (PEEK) matriisissa. Valinnan perusteena ovat kuidun lujuus 2,07 GPa ja kimmomoduuli E=138 GPa kuidun suunnassa, komposiitin sitkeys (muihin termoplastisiin rakenteisiin nähden), korkea sulamispiste t_s=345 ^{o}C sekä hyvä kemiallinen kestävyys petrokemiallisten nesteiden suhteen. Hiilikuidun ja teräksen välinen kalvaaninen korrosio on estetty kietomalla teräksen pintaan ensin pari S2/PEEK -lasikuitukerrosta eristeeksi. Näin on saatu aikaan ennustettavasti käyttäytyvä, 120 mm panssarivaunukanuunan tuliputki (3 testiputkea), joka on n. 15 % keveämpi kokoteräksiseen perinteiseen putkirakenteeseen näh-

den. Viitejulkaisun [26] mukaan tuliputken perusrakenne on valittu USA:n Future Combat Systems – Mounted Combat Systems ajoneuvon pääaseen perustaksi.

Sisäpuolinen pinnoitus

Tuliputken sisäpuolisen pinnoituksen tai vuorauksen tarkoituksena on vähentää palokaasujen lämpö- ja eroosiovaikutusta perusmateriaaliin ja kasvattaa tuliputken kulumiskestävyyttä. Pinnoitteelta tai vuoraukselta vaaditaan hyvää kuumien lämpötilojen kestoa sekä mekaanisia että kemiallisia rasituksia vastaan, kykyä toimia eristeenä (huono lämmönjohtavuus, korkea ominaislämpökapasiteetti), hyvää tarttuvuutta perusaineeseen ja sen säilyvyyttä laukauksen aikana esiintyvissä lämpötiloissa ja lämpötilajakaumissa, jne. [28]. Pinnoitemateriaalia, jonka ominaisuudet täyttävät em. vaatimukset, ei toistaiseksi ole saatu aikaan. Mahdolliset vaihtoehdot ovat valikoituneet kahteen pääluokkaan eli refraktorimetalleihin (Cr, Nb, Mo, Ta, W, Re) ja keraameihin.

Perinteisesti tuliputket on pinnoitettu sähkökemiallisesti kromaamalla, mutta kromin sulamispiste $t_{sCr}\approx1850^oC$ (teräkselle $t_{sFe}=1530^oC$) ei ole riittävä tulevaisuuden ampumatarvikkeille, joiden korkeaenergiset ajoaineet sekä suuri lataustiheys kasvattavat tuliputken lämpökuormaa. Ohut kerrospaksuus ei estä riittävästi lämmönsiirtoa perusaineeseen lämpösäröytymisen kannalta haitallisen teräksen ”martensiitti ($t > 730^oC$)→ austeniitti (nopea jäähtyminen)→ kova ja hauras martensiitti” -muutoksen välttämiseksi. Kromipinnoite on hauras ja se säröytyy melko nopeasti, jonka jälkeen ruudin palokaasut huuhtovat terästä kromin alta kunnes se irtoaa putken pinnasta. Palonarvet ovat potentiaalisia väsymissärön alkamiskohtia sekä laajetessaan myös kulumisvaurioiden kasvukohtia. Sähkökemiallinen kromausprosessi on ympäristövaarallinen myrkyllisten päästöjensä vuoksi.

Kromauksen korvaavaa pinnoitusmenetelmää ei ole vielä saatu aikaan ainakaan teollisessa mittakaavassa, vaikka tutkimus on ollut aktiivista sekä materiaalien että valmistusmenetelmien suhteen [27-34]. Refraktorimetalleista ominaisuuksiensa puolesta lupaavimmat kromia korvaavat pinnoitekanditaatit ovat tantaali ($t_s\approx2990^oC$) ja Rhenium ($t_s\approx3190^oC$), mutta valitettavasti niiden suhteellinen raaka-ainehinta on 5- ja 100-kertainen kromiin nähden [28] ja pinnoitteen valmistusmenetelmät (terminen ruiskutus, pulverimetallurgiset menetelmät jne.) ovat sähkökemiallista kromausta mutkikkaampia.

Päätelmä

Suurikaliiperisten ruutiaseiden tuliputkimateriaalit ja -konstruktiot ovat pitkän suunnittelu-, valmistus- ja käyttöhistorian kehityksen myötä optimoituneet [12], joten käänteentekevien uusien materiaali- tai rakennetekniikoiden löytäminen tai käyttöönotto lienevät melko epätodennäköisiä lyhyellä aikajänteellä [28]. Kuitulujitteista komposiittirakennettakin on tutkittu ja kehitetty jo yli 30 vuotta välillä luopuen, taas uudelleen aloittaen ja vasta nyt on näköpiirissä mahdollinen teollinen tuotanto [26]. Vaihtoehtoisia ratkaisuja etsittäessä voidaan palata ennakkoluulottomasti perinteisen asetekniikan uusiosovelluksiin, vaikkapa jo uskontotunneilta mieleen jääneen ja hyvin dokumentoidun Daavidin ja Goljatin yhteenotosta tuttuun linkoon [35, 36].

Viitteet

[1] M. Perl, Third special section on pressure vessel technology applied on gun tubes, Editorial, *Journal of Pressure Vessel Technology*, 134, 040201, 2012.

[2] S. Henttinen, Aseiden ja ampumatarvikkeiden turvallisuus, *MPDI 40v 1963-2003*: 17-21, 2003.

[3] *Definition of pressure terms and their interrelationship for use in the design and proof of cannons and mortars and ammunitions, Stanag 4110*, North Atlantic Treaty Organization, Standardization Agreement.

[4] A. Doig, *Military metallurgy*, Reprinted edition, Maney Publishing, 2002.

[5] J.H. Underwood and E. Troiano. Critical fracture process in army cannons: A review, *Gun tubes conference 2002, 15–18 September 2002*, Keble College Oxford, Hosted by Cranfield Univ., RMCS, Shrivenham, Paper S3/P12. 2002.

[6] D.C. Smith. 175mm M113 Cannon: Historical Perspective on the Cannon that changed our Cannon Design Process, *NDIA Joints Armaments Symposi*um, 14-17 May, 2012.

[7] *Steels and alloys for defence applications, Heavy gun barrels*, Aubert&Duval 803002-A brochure.

[8] *Steel Forgings for Guns, DEF STAN 10-13/4.* Ministry of Defence, UK. 2005.

[9] *Steel forgings, tubular parts for guns, MIL-S-46119C,* US Army, 2000

[10] D.E. Carlucci and S.S. Jacobson, *Ballistics, Theory and design of guns and ammunitions*, CRC Press, 2008.

[11] H. Peter, *Mechanical Engineering, Principles of Armament Design*. Trafford Publishing, 2004.

[12] *Research and Development of Materiel, Engineering Design Handbook, Gun Series, Gun Tubes, AMCP 706-252*, U.S. Army Materiel Command, Washington DC, 1964.

[13] D.C. Smith and E.E. Coppola, *Safe maximum pressure determination for the M829E3/M256 cannon qualification program*, U.S. Army ARDEC, Benet Laboratories, Technical Report ARCCB-TR-02013, Watervliet, NY, 2002.

[14] D.C. Smith, *Gun Assembly Safety Certification – US Approach*, 2009. http://www.dtic.mil/ndia/2009gunmissile/SmithEmertechtuesday.pdf (21.10.2012).

[15] T.D. Andrews and F.E. Brine, Hydraulic testing of ordnance components*, Journal of Pressure Vessel Technology*, 128(2):162-167, 2006.

[16] T.D. Andrews, Assembly of compound tubes under hydraulic pressures*, Journal of Pressure Vessel Technology*, 128(2):208-211, 2006.

[17] J. Toivola ja S. Moilanen, Aseen tuliputken lujuusteknisen mitoituksen ohjelmointi, *IX Suomen mekaniikkapäivät, 13.-14.6.2006*, Lappeenrannan teknillinen yliopisto, Konetekniikan osasto raportti 17: 692-698, 2006.

[18] T.D. Andrews, Projectile driving band interactions with gun barrels, *Journal of Pressure Vessel Technology*, 128(2):273-278, 2006.

[19] H. Keinänen, S. Moilanen, J. Tervokoski and J. Toivola, Influence of Rotating band construction on gun tube loading -part I: Numerical approach*, Journal of Pressure Vessel Technology*, 134(4): 041006, 2012.

[20] J. Toivola, S. Moilanen, J. Tervokoski and H. Keinänen, Influence of rotating band construction on gun tube loading - part II: Measurement and analysis*, Journal of Pressure Vessel Technology*, 134(4): 041007, 2012.

[21] M.C. Gibson, *Determination of Residual Stress Distributions in Autofrettaged Thick-Walled Cylinders*. PhD Thesis. Cranfield University, DA-CMT, 2008.
[22] K.J. Korane, *Understanding the basics of autofrettage,* 2011, http://machinedesign.com/article/understanding-the-basics-of-autofrettage-0405E (21.10.2012).
[23] J.H. Underwood, R.A. Farrara and M.J. Audino, *Yield-before-break fracture mechanics analysis of high strength steel pressure vessels*, U.S. Army ARDEC, Benet Laboratories, Technical Report ARCCB-TR-94017, Watervliet, NY, 1994.
[24] W. Lanz and R. Knobel. Hydraulic autofrettage experience as a barrel steel quality control instrument, *Gun tubes conference 2002, 15–18 September 2002*, Keble College Oxford, Hosted by Cranfield Univ., RMCS, Shrivenham, Paper S1/P5. 2002
[25] J. Hölzle, R. Knobel and W. Lanz, Practical parameters of gun steel selections, *Gun tubes conference 2005, 10–14 April 2005*, Keble College Oxford, Hosted by Cranfield Univ., RMCS, Shrivenham, Paper S5/P20. 2005
[26] A.G. Littlefield and E.J. Hyland, 120 mm Pre-Stressed Carbon Fiber/Thermo-plastic Overwrapped Gun Tubes, *Journal of Pressure Vessel Technology*, 134(4): 041008, 2012.
[27] P.J. Conroy, P. Weinacht and M.J. Nusca, *Gun Tube Coatings in Distress*, U.S Army Research Laboratory, ARL-TR-2393, Aberdeen Proving Ground, MD, 2001.
[28] J.S. Montgomery and R.L. Ellis. Large Caliber Gun Tube Materials Systems Design. *10th U.S. Army Gun Dynamics Symposium Proceedings*: 385-397, 2001.
[29] L.F. Rusch et. al. *Tri-Service Green Gun Barrel (PP 074), Final Report*, U.S. Army Tank-Automotive Command, Benet Laboratories, Watervliet, NY, 2003.
[30] R.G. Hasenbein, *Wear and Erosion in Large Caliber Guns*, U.S.Army ARDEC, Benet Laboratories, RTO-MP-AVT-109, Watervliet, 2004.
[31] K. Truszkowska, Elimination of Chromium Electrodeposition from Large Caliber Launch Systems, *Hard Chrome Alternatives Team, 20-21 July, 2004, Utah*, U.S. Army ARDEC, Benet Laboratories, 2004.
[32] M.J. Audino, Use of Electroplated Chromium in Gun Barrels, *DoD Metal Finishing Workhop*, Washington, DC, 22-23 May, 2006.
[33] W. Garrett, A.J. Sherman and J. Stiglich, Rhenium as a Hard Chrome Replacement for Gun Tubes, *Materials and Manufacturing Processes*, 21: 618-620, 2006.
[34] L. Burton et. al. Army Targets Age Old Problems with New Gun Barrel Materials. *AMPTIAC Quarterly*, 8 (4): 49-56, 2004. http://ammtiac.alionscience.com/pdf/AMPQ8_4ART08.pdf (21.10.2012)
[35] http://www.slingatron.com/publications.htm (21.10.2012).
[36] D.A. Tidman, Slingraton Overview, *Briefing to Air Force Future Concepts,* 2005. http://www.highfrontier.org/Archive/hf/Pentagon%20Future%20AF%20Concepts.pdf (21.10.2012).

Seppo Moilanen
Patria Land Systems Oy
PL 12
38801 SASTAMALA
seppo.moilanen(at)patria.fi

Teknillisen mekaniikan verkkosivusto opetuksen apuna

Anni Mäkelä ja Heikki Marjamäki

Tiivistelmä. Artikkelissa esitetään teknillisen mekaniikan opetuksen avuksi toteutettua tarkastussivustoa. Opiskelija voi sivuston avulla tarkastaa harjoitustöidensä välituloksia. Lisäksi sivustoon on ohjelmoitu JavaScript-pohjainen elementtimenetelmäohjelma, johon on tällä hetkellä ohjelmoitu tasosauva- ja palkkielementit. Sivuston dynaaminen sisältö toteutettiin käyttämällä PHP-ohjelmointikieltä ja ulkoasu käyttämällä HTML-kuvauskieltä sekä CSS-tyylikieltä.

Avainsanat: Opetus, Open Access, PHP, SVG, HTML, JavaScript

Johdanto

Tampereen teknillisellä yliopistolla kesällä 2010 aloitettiin hanke teknillisen mekaniikan verkkopohjaisen sivuston uudistamisesta. Tarkoituksena oli tukea, ei niinkään korvata muita perinteisempiä opetusmuotoja, kuten luennointia. Lähtökohtana projektille oli peruskursseilla opiskelevien suurten opiskelijamäärien opiskelun sekä kursseilla opettavan henkilökunnan työn tehostaminen.

Projekti toteutettiin kolmessa eri vaiheessa, jotka ajoittuivat vuosille 2010-2012. Ensimmäisessä vaiheessa laadittiin dynamiikan perusteet -kurssille harjoitustyön tarkistussivu. Sivun avulla opiskelijat voivat esitarkistaa omat tuloksensa ja paikantaa virheensä, jolloin opetushenkilökunnan aikaa säästyy kurssin varsinaiseen asiasisältöön liittyvään neuvontaan.

Kesän 2011 aikana vastaavat tarkistussivut toteutettiin myös Lujuusopin perusteet -kurssin neljälle eri harjoitustyölle. Sivuston dynaaminen sisältö toteutettiin käyttämällä PHP-ohjelmointikieltä ja ulkoasu käyttämällä HTML-kuvauskieltä sekä CSS-tyylikieltä.

Projektin kolmannessa vaiheessa kesällä 2012 toteutettiin sivustolle JavaScript-pohjainen elementtimenetelmäohjelma, jolla opiskelijoille voidaan luoda interaktiivisia esimerkkitehtäviä. Ohjelman kaksiulotteinen grafiikka piirretään käyttäen SVG-kuvauskieltä. Sovelluksessa opiskelija voi muuntaa päälle/pois- periaatteella tehtävän parametreja. Esimerkiksi opiskelija voi esimerkin avulla tutkia painovoiman tai lämpötilan vaikutusta kappaleen siirtymiin. Sovellus laskee ja piirtää kunkin tehtävän siirtymä-, normaalivoima-, leikkausvoima- sekä taivutusmomenttikuvion. Kaikki tehdyt verkkosovellukset toteutettiin käyttäen ilmaisohjelmistoja, jotka löytyvät internetistä.

Käytetyt työkalut

Työkalujen valinta on tärkeä osa verkkosivuston suunnittelua, sillä se vaikuttaa koko tulevaan projektiin. Valitsemalla alussa vääränlaiset työkalut voi koko hankkeen onnistuminen olla vaarassa. Jo suunnitteluvaiheessa haluttiin löytää työkalut, joita voitaisiin käyttää projektissa myös tulevaisuudessa.

Yksi tärkeä kriteeri työkalujen valinnalle oli hinta. Käytettävien ohjelmien tuli olla ilmaisia, sillä projektilla ei ollut rahoitusta, jolla kustantaa maksullisien ohjelmien käyttö. Myöskään projektin tulevaisuutta ei haluttu sitoa rahoituksen saamiseen, joten ilmaisohjelmien valitseminen oli luonnollinen valinta.

HTML

HTML:ää käytetään internetsivujen rakenteen luomiseen. HTML:llä merkitään internetsivujen tekstin rakenne ja muotoilu, kuten otsikot ja fontit. HTML-asiakirjojen etuna on niiden muuttumattomuus käytettäessä eri selaimia. Joidenkin valmistajien selaimet ovat epästandardin mukaisia, mikä usein aiheuttaa sivujen ulkonäön muuttumisen selainta vaihdettaessa.

PHP

PHP on palvelinpohjainen ohjelmointikieli. PHP:n käyttö sopii erityisesti dynaamisten nettisivujen luontiin Web-palvelinympäristössä. Kielenä PHP on niin kutsuttu komentosarjakieli, mikä tarkoittaa että ohjelman koodi tulkataan vasta ohjelman suoritusvaiheessa. PHP on alustariippumaton kieli.

PHP-kielellä ohjelmoidut osat upotetaan yleensä HTML:n sekaan, kuten pilottihankkeessakin on tehty. PHP-osio merkitään muusta HTML-koodista erilleen aloittamalla merkinnällä `<?php` ja päättämällä merkintään `?>`.

MAXIMA

Maxima on Macsyma-ohjelmaan perustuva symbolisen laskennan matematiikkaohjelma. Symbolisen laskennan lisäksi Maxima tarjoaa myös mahdollisuuden numeeriseen laskentaan. Ohjelma ei sisällä kaikkia muunnoksia, joita sen edeltäjä kaupallinen Macsyma sisälsi, mutta on silti täysin toimiva ilmainen matematiikkaohjelma. Ohjelmaa voidaan käyttää eri käyttöjärjestelmillä. Ohjelmasta on saatavilla myös erillinen versio wxMaxima graafisella käyttöliittymällä.

JavaScript

JavaScript on alun perin Netscape Communications Corporationin kehittämä pääasiassa Web-ympäristössä käytettävä komentosarjakieli. JavaScriptin tärkein sovellus on mahdollisuus lisätä Web-sivuille dynaamista toiminnallisuutta. Erona PHP-kieleen JavaScript-ohjelma suoritetaan käyttäjän tietokoneella ja käyttäjä näkee halutessaan suoritettavan ohjelman koodin.

SVG

SVG (lyhenne sanoista Scalable Vector Graphics) on kaksiulotteisten vektorikuvien kuvauskieli, joka perustuu World Wide Web Consortiumin kehittämään avoimeen kuvatiedostostandardiin. Teknisesti SVG-kuvatiedostot on tehty XML-merkintäkielellä. Kuvissa on mahdollista esittää myös liikettä. Uusimmat selaimet tukevat SVG kuvauskieltä, mutta vanhemmilla selaimilla, kuten Internet Explorer 8 tuki puuttuu.

Dynamiikan harjoitustyö

Tarve teknisen laskennan verkkopohjaiselle oppimisympäristölle lähti suurista osallistujamääristä teknillisen mekaniikan peruskursseilla. Tampereen teknillisen yliopiston konstruktiotekniikan laitos järjestää vuosittain useita konetekniikkaan liittyviä kursseja, jotka kuuluvat monille yliopistomme opiskelijoille pakollisiin perusopintoihin, jonka seurauksena kursseilla osallistujamäärät kasvavat usein hyvin suuriksi. Laitoksella järjestettäviä kursseja ovat muun muassa Dynamiikan perusteet, Lujuusopin perusteet ja Teknillisen mekaniikan perusteet.
Opiskelijoille halutaan suurista osallistujamääristä huolimatta tarjota laadukasta opetusta ja mahdollisuus henkilökohtaiseen neuvontaan. Tällä hetkellä opetuksessa käytetään luentoja, laskuharjoituksia, kotitehtäviä ja harjoitustöitä. Esimerkiksi Lujuusopin perusteiden ja Dynamiikan perusteiden kursseilla on koettu hyväksi, että harjoitustyöt palautetaan henkilökohtaisesti, jolloin kurssin vetäjä tai assistentti näkee heti kurssilaisten oppimisen etenemisen. Vastavuoroisesti opiskelijat saavat suoraa palautetta ja kysymysten esittämisen mahdollisuus madaltuu.

Teknisen laskennan verkkopohjaisella oppimisympäristöllä halutaan tarjota opiskelijoille mahdollisuus kehittää omaa oppimistansa luentojen ulkopuolella. Kurssin vastuu henkilöille verkkopohjainen oppimisympäristö antaa mahdollisuuden jakaa opiskelijoille kurssiin liittyvää lisämateriaalia ja aikaa antaa enemmän henkilökohtaista neuvontaa. Rajoitetuista resursseista johtuen joudutaan monilla kursseilla tyytymään rajalliseen määrään harjoitusryhmiä. Harjoitusryhmien vähäisyys kasvattaa ryhmien kokoa, mikä saattaa johtaa opetuksen laadun heikkenemiseen.

Lujuusopin harjoitustyöt

Teknillisen mekaniikan verkkopohjaisen oppimisympäristön kehitysprojektin toisessa vaiheessa kesällä 2011 toteutettiin Lujuusopin perusteet -kurssin neljän harjoitustyön tarkistussivut. Kuvassa 1 on nähtävissä harjoitustyön 2 tarkistussivu.

Tavoitteena oli vähentää aikaa, joka opetushenkilökunnalta kuluu tavanomaisten laskuvirheiden jäljittämiseen. Tarkistussivujen avulla opiskelija voi itse havaita virheelliset tulokset, jolloin opetushenkilökunnan aikaa säästyy kurssin varsinaiseen asiasisältöön liittyvään neuvontaan.

Harjoitustöiden tehtävänannot perustuvat kunkin opiskelijan omaan opiskelijanumeroon, joten laskettava tehtävä on yksilöllinen. Tämän vuoksi tarkistussivun on pystyttävä laskemaan tarvittavat tulokset sille annetun opiskelija-

numeron perusteella. Tarkistussivulle haluttiin myös tuloksia havainnollistavia dynaamisia kuvia.

Kehitystyö tapahtui käyttäen XAMPP-palvelinohjelmistoa Windows-pohjaisessa ympäristössä. Dynaamisen sisällön tuottamisessa käytettiin PHP-ohjelmointikieltä ja ulkoasu toteutettiin HTML:llä. Tarkistussivu koostuu useista tiedostoista. Näitä tiedostoja ovat päätiedosto, joka sisältää sivun HTML-koodin ja laskennan suorittavan PHP-koodin, staattiset kuvat, dynaamisia kuvia luovat tiedostot ja erilaisia itse kirjoitettuja PHP-funktioita sisältävät tiedostot.

Tarvittavan opiskelijanumeron välittämiseen sivulle on käytetty HTML-lomaketta. Lomakkeeseen syötetyn opiskelijanumeron perusteella lasketaan tarvittavat tulokset käyttäen PHP-kieltä. Dynaamisten kuvien tuottamiseen käytettiin PHP-kielen GD-funktiokirjastoa. Lisäksi kirjoitettiin myös useita omia funktioita.

Sivun ulkoasussa hyödynnettiin HTML-taulukoita. Numeeristen tulosten esittämiseen käytettiin samankaltaisia taulukoita kaikissa neljässä tarkistussivussa ja tarvittavan HTML-elementin luomista varten kirjoitettiin oma PHP-funktio.

Tarkistussivun testaaminen aloitettiin heti kehitystyön alkuvaiheessa mahdollisimman pieni pala kerrallaan. Tällä tavalla virheiden paikallistaminen on helpompaa. Loppuvaiheen testaus jäi ajan puutteen vuoksi kuitenkin valitettavan vähiin. Tulevissa projekteissa kannattaakin varata riittävästi aikaa lähes valmiin sivuston testaamiselle. Itse testaaminenkin kannattaisi suunnitella hyvissä ajoin etukäteen ja dokumentoida se huolellisesti.

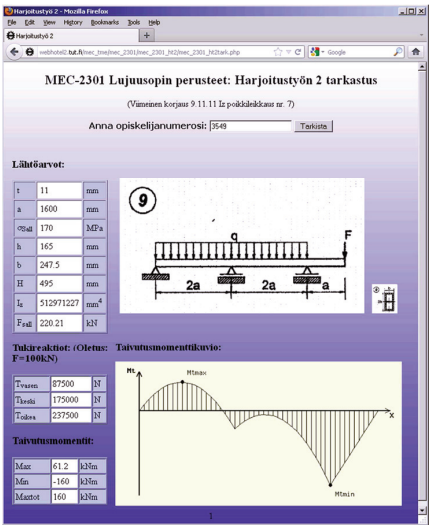

Kuva 1. Esimerkki harjoitustyön tarkistussivusta.

Elementtimenetelmäohjelmiston toteutus

Hankkeen kolmannessa vaiheessa toteutettiin JavaScript pohjainen elementtimenetelmäohjelma. Ohjelmaan voidaan tehdä opiskelijoille esimerkkitehtäviä, kuten kuvassa 2. Tavoitteena oli havainnollistaa opiskelijoille menetelmän toimintaa erilaisilla rakenteilla, kuten sauvoilla ja palkeilla.

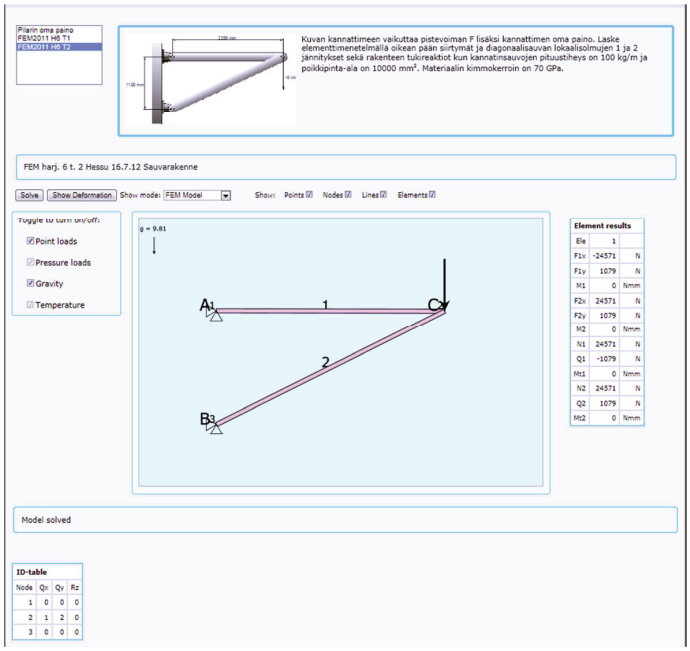

Kuva 2. Esimerkki JavaScript-pohjaisesta elementtimenetelmäohjelmiston prototyypistä.

Opiskelijapalaute

Opiskelijat pääsivät käyttämään Dynamiikan harjoitustyön tarkistussovellusta heti kurssin ensimmäisessä harjoitustyössä keväällä 2011. Sovelluksen julkistamisesta lähtien sovellus sai opiskelijoilta positiivista suullista palautetta.

Kurssin lopussa opiskelijat saivat mahdollisuuden antaa sovelluksesta nimetöntä palautetta numeerisella arvostelulla. Palautelomakkeella kysyttiin opiskelijan kokemuksia ohjelmasta. Numeerisen arvion lisäksi opiskelijoilla oli mahdollisuus antaa sanallista palautetta sovelluksen toiminnasta sekä tulevia ohjelmia varten kehitysehdotuksia.

Tarkastusohjelman toimivuuteen opiskelijat olivat palautteiden mukaan tyytyväisiä. Arvosteluasteikolla yhdestä viiteen opiskelijat antoivat toimivuudesta keskimäärin 4,4. Palautetta antaneiden opiskelijoiden mukaan tarkastusohjelma koettiin hyödylliseksi.

Kaikki annetut palautteet olivat viitosia ja nelosia, viitosen merkitessä todella hyödyllistä.

Kaikki vastaajat toivoisivat vastaavia tarkistusohjelmia myös muille kursseille. Palautteissa eri arvosanoja saaneiden välillä ei ollut merkittävää eroa. Hyvän arvosanan saaneet ja huonompia arvosanoja saaneet opiskelijat arvioivat kaikki ohjelman keskimäärin yhtä hyväksi, hyödylliseksi ja helppokäyttöiseksi. Vastauksista voidaan päätellä, että tarkastusohjelmasta oli hyötyä vastaajille vastaajan taidoista riippumatta.

Yhteenveto

Hankkeessa laadittu sivusto tulee olemaan pysyvä ja sitä pyritään kehitettämään mahdollisuuksien mukaan. Sivustoa laajennetaan tulevaisuudessa vakinaisen henkilökunnan panostuksen lisäksi opinnäytetöiden avulla. Hankkeesta kirjoitetaan opetukseen liittyvä lehtiartikkeli, jossa kuvataan tehtyjä parametrisoituja visualisointeja sekä vihjeistettyjä esimerkkilaskuja, esittäen myös loppukäyttäjien näkökulmia. Hankketta kehitetään yhteistyössä TTY:n tietohallinnon ja Hypermedialaboratorion kanssa, jolloin hankkeen edetessä saatuja kokemuksia on helpointa raportoida TTY:n laajuisesti.

Hankkeessa kehitettyjä osioita, jotka toimivat asiakkaan omassa koneessa voi vapaasti käyttää, muuttaa ja edelleenkehittää kuka tahansa sovelluksen käyttäjä. Mitään lisenssimaksuja ei tarvita.

Viitteet

[1] A. Mäkelä, *Teknillisen mekaniikan verkkopohjainen oppimisympäristö*, Kandidaatintyö, Tampereen teknillinen yliopisto, Konstruktiotekniikan laitos, 2011.

[2] L. Karppi, *Lujuusopin perusteet -kurssin verkkopohjaisten tarkistussivujen toteutus*, Kandidaatintyö, Tampereen teknillinen yliopisto, Konstruktiotekniikan laitos, 2012.

Anni Mäkelä, Heikki Marjamäki,
Tampereen teknillinen yliopisto,
Konstruktiotekniikan laitos,
PL 527, 33101 Tampere
anni.m.makela@tut.fi
heikki.marjamaki@tut.fi